

# **Climate Impacts of Marine Cloud Brightening**

Benjamin James Parkes

Submitted in accordance with the requirements for the degree of  
Doctor of Philosophy

The University of Leeds  
School of Earth and Environment  
July 2012

# Declaration of Authorship

The candidate confirms that the work submitted is his own, except where work which has formed part of jointly-authored publications has been included. The contribution of the candidate and the other authors to this work has been explicitly indicated below. The candidate confirms that appropriate credit has been given within the thesis where reference has been made to the work of others.

Section 2 of Latham et al. (2012) was based upon the simulations described in Table 4.1. Latham et al. (2012) contains plots based on the data used in Section 3.2.2 and the ice cover plots used in Chapter 5.

Parkes et al. (2012) is based upon the simulations described in Table 4.1. The work in Parkes et al. (2012) is based on work shown in Chapter 5.

This copy has been supplied on the understanding that it is copyright material and that no quotation from the thesis may be published without proper acknowledgment.

The right of Ben Parkes to be identified as Author of this work has been asserted by him in accordance with the Copyright, Designs and Patents Act 1988.

©2012 The University of Leeds and Ben Parkes.

# Acknowledgements

I would like to thank countless people and organisations for their help in making this work possible. First and foremost my family to whom I dedicate this thesis. I would like to thank my supervisor Dr Alan Gadian who's advice has been invaluable during my PhD. I also wish to thank Alan Blyth, John Latham and Jim McQuaid for their guidance during my PhD. Special thanks go to Richard Rigby for his help with the Leeds Linux system which made many aspects of my work possible.

Support for this research was provided by the Fund for Innovative Climate and Energy Research, FICER, at the University of Calgary. This work made use of the facilities of HECToR, the UK's national high-performance computing service, which is provided by UoE HPCx Ltd at the University of Edinburgh, Cray Inc and NAG Ltd, and funded by the Office of Science and Technology through NERC's High End Computing Programme. I would like to thank the National Centre of Atmospheric Science (NCAS) Computer Modelling Service (CMS) for their contributions to this work. During work on my thesis I also made use of data provided by NCAR/EOL under sponsorship of the National Science Foundation and the British Atmospheric Data Centre (BADC) which is the Natural Environment Research Council's (NERC) Designated Data Centre for the Atmospheric Sciences. I would also like to extend my thanks to the University of Manchester (UK) and the UK Met Office who processed and provided data from the VOCALs-REx field campaign.

Any project as long as a PhD would be impossible without the support of friends, credit goes out to the varied denizens of rooms 3.09 Chemistry and 10.128. I wish to thank Sarah-Jane L, Lindsay B, Ryan H, Pope 1.0 and Anja S for reading chapters of this work and providing extremely useful feedback. Matt W is commended for going beyond the levels of any sane masochist to read four chapters. I also wish to thank Tom B, Mike H, Swallace and Rob W for making my time in Leeds both entertaining and disturbing in equal quantities. Finally I want to thank Eimear for distracting me from this PhD long enough to retain some measure of sanity.

# Abstract

Marine Cloud Brightening (MCB) is one of several Solar Radiation Management (SRM) geoengineering schemes that have been proposed to counter the global warming associated with climate change. Herein an in-depth investigation of some of the climatological impacts of MCB are presented.

The proposed operation of MCB is located in both the sub-tropical and tropical regions, where reflection of solar radiation from marine cloud-tops is a maximum. Work described in many publications shows that polar regions are cooled by tropical seeding. The cooling of polar regions as a result of MCB leads to an increase in polar sea-ice cover and thickness. A possible explanation for cooling the poles by seeding in the tropics is an associated change in the Meridional Heat Flux (see Chapter 5 for details).

Further work has been performed to assess the effectiveness of MCB as a technique for weakening tropical cyclones, which are predicted to become more severe with climate change. Reducing sea surface temperatures decreases the amount of energy available to the convective processes which power a tropical cyclone. A second investigation concerns the impact of lowering sea surface temperatures via MCB on coral reefs, which are known to be vulnerable to changes in both temperature and nutrient quantities within the ocean systems. The hypothesis is that MCB could counter the temperature-increase associated with climate-change, and thus prevent coral bleaching.

Simulations of MCB often seed different areas, and an attempt is made herein to use pseudo-random seeding to identify optimal seeding regions. This technique also enables assessment of the impacts of seeding any given region on several remote locations.



# Contents

<b>Declaration of Authorship</b>	<b>i</b>
<b>Acknowledgements</b>	<b>ii</b>
<b>Abstract</b>	<b>iii</b>
<b>List of Figures</b>	<b>viii</b>
<b>List of Tables</b>	<b>xiv</b>
<b>Abbreviations</b>	<b>xvii</b>
<b>1 Introduction</b>	<b>1</b>
1.1 Motivation . . . . .	1
1.2 Climate Change . . . . .	2
1.2.1 Responses to climate change . . . . .	3
1.2.2 Polar amplification . . . . .	5
1.3 Stratocumulus clouds . . . . .	7
1.3.1 Formation . . . . .	8
1.3.2 Dissipation . . . . .	9
1.3.3 Aerosol effects . . . . .	10
1.4 Geoengineering . . . . .	13
1.4.1 Models used to simulate geoengineering . . . . .	14
1.4.2 Carbon Dioxide Removal . . . . .	15
1.4.2.1 Ocean fertilisation . . . . .	15
1.4.2.2 Forest management . . . . .	17
1.4.2.3 Air capture . . . . .	17
1.4.3 Solar Radiation Management . . . . .	18
1.4.3.1 Space Mirrors and Reduced Insolation . . . . .	19
1.4.3.2 Sulphate aerosol seeding . . . . .	22
1.4.3.3 Land use change . . . . .	29
1.4.3.4 Oceanic microbubbles . . . . .	30
1.4.3.5 Marine Cloud Brightening . . . . .	30

1.4.4	Assessing the effectiveness of geoengineering . . . . .	36
1.5	Thesis aims . . . . .	36
<b>2</b>	<b>The microphysical and radiative properties of clouds observed during the VOCALs-REx field campaign</b>	<b>38</b>
2.1	Results from the VOCALs-REx field campaign . . . . .	39
2.2	Aircraft used during the VOCALs-REx field campaign . . . . .	40
2.2.1	Dornier 228 . . . . .	40
2.2.2	BAe-146 . . . . .	42
2.3	Multiple instrument albedo investigation . . . . .	42
2.3.1	Cloud Droplet Probe . . . . .	42
2.3.2	Pyranometers . . . . .	44
2.3.3	2D-S Droplet Imager . . . . .	45
2.3.4	Flight legs . . . . .	46
2.3.5	Microphysical albedo calculation . . . . .	48
2.3.6	Satellite - Aircraft albedo comparison . . . . .	50
2.3.7	Aircraft shortwave - CDP albedo comparison . . . . .	51
2.3.8	Aircraft shortwave - 2D-S albedo comparison . . . . .	55
2.4	Cloud droplet number concentration - shortwave albedo comparison .	56
2.5	Summary . . . . .	59
<b>3</b>	<b>HadGEM1 model description</b>	<b>61</b>
3.1	Components of HadGEM1 . . . . .	61
3.1.1	Dynamics . . . . .	61
3.1.2	Radiation . . . . .	63
3.1.3	Microphysics and Precipitation . . . . .	63
3.1.4	Aerosol Processes . . . . .	64
3.1.5	Boundary layer . . . . .	65
3.1.6	Convection . . . . .	65
3.1.7	Ocean . . . . .	66
3.2	Comparison with datasets . . . . .	66
3.2.1	Sea surface temperature . . . . .	67
3.2.2	Precipitation . . . . .	67
3.3	Summary . . . . .	68
<b>4</b>	<b>Geoengineering, comparison of results with previous work</b>	<b>70</b>
4.1	Experiment description . . . . .	70
4.2	Previous work . . . . .	72
4.2.1	Temperature, precipitation and sea ice cover . . . . .	74
4.2.1.1	Surface temperature . . . . .	74
4.2.1.2	Precipitation . . . . .	76
4.2.1.3	Sea ice cover . . . . .	79
4.2.2	Radiative fields . . . . .	82
4.2.2.1	Radiative flux difference . . . . .	82

4.2.2.2	Albedo . . . . .	85
4.3	Discussion . . . . .	87
4.4	Summary . . . . .	89
<b>5</b>	<b>The Impacts of Marine Cloud Brightening on the Polar regions and the Meridional Heat Flux</b>	<b>90</b>
5.1	Climate impacts of Marine Cloud Brightening . . . . .	90
5.1.1	Variable selection . . . . .	91
5.1.2	Impact of doubling preindustrial carbon dioxide concentrations	92
5.1.3	Impact of seeding three regions of marine clouds in a double carbon dioxide atmosphere . . . . .	95
5.1.4	Impact of seeding the entire marine atmosphere in a double carbon dioxide atmosphere . . . . .	97
5.2	Meridional Heat Flux . . . . .	99
5.2.1	Meridional Heat Flux in HadGEM1 . . . . .	101
5.2.2	Changes in the MHF as a result of MCB . . . . .	102
5.3	Discussion and Summary . . . . .	104
<b>6</b>	<b>Impacts of MCB on two aspects the tropical climate</b>	<b>107</b>
6.1	Tropical cyclones . . . . .	107
6.1.1	Life cycle . . . . .	109
6.1.2	Impacts . . . . .	110
6.1.3	Impacts of climate change and MCB on surface temperatures in tropical cyclone basins . . . . .	111
6.1.3.1	Impacts of increasing greenhouse gas concentrations on sea surface temperatures in tropical cyclone basins . . . . .	112
6.1.3.2	Impacts of MCB on sea surface temperatures in tropical cyclone basins . . . . .	113
6.1.3.3	Impacts of MCB in an increased carbon dioxide atmosphere on sea surface temperatures in tropical cyclone basins . . . . .	115
6.1.4	Discussion and summary of the impacts of climate change and MCB on tropical cyclones . . . . .	118
6.2	Coral bleaching . . . . .	121
6.2.1	Coral reef locations . . . . .	123
6.2.2	Impacts of climate change and MCB on sea surface temperatures in regions containing coral reefs . . . . .	123
6.2.3	Discussion and summary of the impacts of climate change and MCB on regions containing coral reefs . . . . .	124
<b>7</b>	<b>Pseudo-random seeding in a climate model</b>	<b>127</b>
7.1	Method . . . . .	127
7.2	Climate model results . . . . .	131
7.2.1	Results from 10 day mean data . . . . .	131

---

7.2.2	Results from 1 day mean data . . . . .	136
7.2.3	Inverse plotting from 1 day mean data . . . . .	138
7.3	Discussion . . . . .	141
7.4	Summary . . . . .	143
<b>8</b>	<b>Conclusions</b>	<b>145</b>
8.1	Major findings . . . . .	145
8.2	Implications of this work . . . . .	147
8.3	Future work . . . . .	148
	<b>References</b>	<b>150</b>
	<b>Appendix A. Differences between climate models</b>	<b>166</b>
	<b>Appendix B. Flow chart of method used in Chapter 7</b>	<b>169</b>

# List of Figures

1.1	The change in atmospheric concentration of three long lived greenhouse gases, carbon dioxide (ppm), methane (ppb), nitrous oxide (ppb). Changes in greenhouse gas concentrations since 1750 are attributed to anthropogenic sources. Copied from Forster et al. (2007).	4
1.2	The change in radiative forcing ( $\text{W m}^{-2}$ ) as a result of either anthropogenic or natural processes. Results show the change in radiative forcing from the preindustrial era to 2005. Positive values result in a warming of the climate whereas negative values cool the climate. Copied from Forster et al. (2007).	5
1.3	Schematic of several aerosol effects on the climate. Black dots, open circles, straight lines and wavy lines represent aerosol particles, cloud droplets, solar radiation and terrestrial radiation respectively. A large number of smaller cloud droplets exists in a perturbed cloud as both anthropogenic and natural aerosol can form cloud condensation nuclei. Originally published in Forster et al. (2007). See also Section 1.3.3.	6
1.4	Sea ice cover for the month of August for each year between 1979 and 2011. The black data points show satellite derived sea ice cover, the blue line shows a least squares regression of the trend.	8
1.5	Series of infrared satellite photos from Channel 4 ( $10.7 \mu\text{m}$ ) of the GOES-10 satellite showing the breakup and reformation of a stratocumulus deck during the day. Images were recorded during the VOCALs-REx field campaign. Brightness temperature shown on the right hand side of each plot with the data range between 270 K and 295 K. All times are UTC, where local time is UTC-4.	11
1.6	Satellite photo of a ship track and the change in droplet effective radius observed near the ship track. Originally published in Segrin et al. (2007).	12
1.7	The potential impacts of increasing global mean annual surface temperature. The red line shows the historical track with two potential climate scenarios shown in grey. Colours indicate the temperature changes with the black text on the right showing the expected impacts at each temperature level (Parry et al., 2007). White text is used to replace the original black text for the top four lines to increase readability.	13

- 1.8 Schematic of several geoengineering methods. SRM methods reflect away solar radiation and CDR methods sequester carbon dioxide from the atmosphere. Solid arrows, hollow arrows, downward grey arrows, upwards grey arrows and dotted vertical arrows represent solar radiation, enhanced natural carbon flows, engineered carbon flows, engineered water flows and sources of cloud condensation nuclei respectively. Copied from Lenton and Vaughan (2009). . . . . 14
- 1.9 A modified version of Figure 1.2 displaying the desired changes to the radiative forcing ( $\text{W m}^{-2}$ ) caused by CDR. The green bar shows the possible effects of geoengineering and the orange bar in the final row shows the total changes. This figure is not balanced and does not take into account any secondary effects of reducing carbon dioxide. The change made is arbitrary and is designed solely to indicate the desired impacts of CDR. . . . . 16
- 1.10 A modified version of Figure 1.2 displaying the desired changes to the radiative forcing ( $\text{W m}^{-2}$ ) caused by some SRM methods. The green bars show the possible effects of geoengineering and the orange bar in the final row shows the total changes. This figure is not balanced and does not take into account any secondary effects of increasing aerosol fractions. The change made is arbitrary and is designed solely to indicate the desired impacts of SRM. . . . . 19
- 1.11 Change in near surface temperature (K) as a result of doubling carbon dioxide and as a result of reducing insolation by 1.84 % in a double carbon dioxide atmosphere, originally published in Caldeira and Wood (2008). . . . . 21
- 1.12 Global average surface air temperature anomaly (K) from 1951-1980 mean for four climate simulations. Observations shown in green, A1B in red, Arctic 3 Mt/yr in blue, tropical 5 Mt/yr in black and tropical 10 Mt/yr in brown. Copied from Robock et al. (2008). . . . . 27
- 1.13 The change in radiative flux difference ( $\text{W m}^{-2}$ ) as a result of either seeding 2.5 Tg/yr sulphate (Figure 1.13(a)) or increasing the CDNC to  $375 \text{ cm}^{-3}$  in three marine regions (Figure 1.13(b)). These figures were copied from Jones et al. (2011). . . . . 29
- 1.14 Artists impression of a ship designed to disperse sea salt particles to act as condensation nuclei within clouds (Salter et al., 2008). The three masts are clockwise rotating Flettner rotors with Thom fences. The prevailing wind is from the right of the image and the ship would move to the left. . . . . 32
- 1.15 The temperature anomaly for three geoengineering simulations, A1B in red, MCB in three regions of marine stratocumulus clouds in blue and MCB in three regions of marine stratocumulus clouds ceasing after 25 years in green. Originally published in Jones et al. (2009). . . . . 33
- 2.1 A schematic of several climate features of the South East Pacific investigated as part of the VOCALS-REx field campaign (Wood et al., 2011). The cold water transport line follows  $20^\circ \text{ S}$  when it straightens. . . . . 39

2.2	An example image generated from uncalibrated radiances of one band of the AISA Dual hyperspectral imager mounted on the Dornier 228 during VOCALs-REx. . . . .	41
2.3	A diagram showing the operation of the CDP. Image copied from Droplet Measurement Technologies (2009). . . . .	43
2.4	Example outputs from the CDP using data from the VOCALs-REx field campaign. The data used in this plot was recorded during Flight B417, which occurred on 9 <sup>th</sup> November 2008. . . . .	44
2.5	Example output data from the shortwave pyranometers using data recorded during the VOCALs-REx field campaign. The data used in this plot was recorded during Flight B417, which occurred on 9 <sup>th</sup> November 2008. . . . .	45
2.6	The logic system used in the stereo 2D-S droplet imager for particles passing through both laser beams. Image copied from Lawson et al. (2006). . . . .	46
2.7	An altitude track of an example flight leg, where the analysed data is shown in red. The altitude track outside the analysed region is in blue and the cloud start and end times are indicated by dashed black lines. . . . .	48
2.8	Satellite photos from the GOES-10 1 km visible radiation channel for four clean cloud events. The flight track from the BAe-146 is shown in red for the times shown in Table 2.2. . . . .	49
2.9	A comparison between GOES-10 satellite albedo and the shortwave albedo from the BAe-146 during the VOCALs-REx field campaign. Data is from four clean clouds described in Table 2.2. The dashed black line shows a 1:1 relationship. . . . .	52
2.10	A comparison between CDP microphysical albedo ( $g = 0.85$ ) and the shortwave albedo from the BAe-146 during the VOCALs-REx field campaign. Data is from four clean clouds described in Table 2.2. All results are ten second averages. The dashed black line shows a 1:1 relationship. . . . .	53
2.11	Investigation into the optimal asymmetry factor 'g' and averaging time for use in Equation 2.3. Darker colours indicate an increase in the gradient of the line of the best fit as shown in Figure 2.10. . . . .	54
2.12	As Figure 2.10 with an updated microphysical albedo calculation using data shown in Figure 2.11. The new equation has an asymmetry factor ( $g = 0.91$ ) and averages data over 12 second blocks. . . . .	54
2.13	As Figure 2.10 but for results from the 2D-S droplet imager. . . . .	56
2.14	As Figure 2.10 showing results from the 2D-S droplet imager for two separate research flights. . . . .	57
2.15	A comparison between the number concentration ( $\text{cm}^{-3}$ ) from two microphysical instruments Figure 2.15(a) the CDP and Figure 2.15(b) the 2D-S, and the shortwave albedo from the BAe-146 during the VOCALs-REx field campaign. Data is from the four clean clouds described in Table 2.2. All results are ten second averages. . . . .	58

3.1	A diagram of the scheme used within HadGEM1 to move water within the atmosphere system. Boxes show the four phases of water within the model and arrows show the transfer mechanisms simulated. Image copied from Wilson and Ballard (1999). . . . .	64
3.2	Difference between HadGEM1 and NOAA recorded annual average sea surface temperature (K). . . . .	68
3.3	Difference between HadGEM1 model annual average precipitation and CMAP observed and modelled precipitation (mm/day). . . . .	69
4.1	Carbon dioxide levels used in the simulations described in Table 4.1. The green line shows the carbon dioxide fraction in control atmospheres, the red line shows the carbon dioxide fraction in double preindustrial carbon dioxide concentration atmospheres and the blue line shows the preindustrial carbon dioxide level of 280 ppm. The vertical dashed black line shows the start of the analysis period for the simulations. . . . .	72
4.2	Seeding maps used in the simulations described in Table 4.1. Turquoise regions indicate the area of the marine atmosphere seeded to a CDNC of $N=375 \text{ cm}^{-3}$ . . . . .	73
4.3	Comparison of effects of increased greenhouse gas concentrations on surface temperature (K) from Bala et al. (2011); Jones et al. (2011); Rasch et al. (2010) with this work. . . . .	76
4.4	Comparison of effects of seeding in an increased greenhouse gas concentrations on surface temperature (K) from Bala et al. (2011); Jones et al. (2011); Rasch et al. (2010) with this work. . . . .	77
4.5	Comparison of effects of increased greenhouse gas concentrations on precipitation (mm/day except Bala et al. (2011) cm/year) rate from Bala et al. (2011); Jones et al. (2009, 2011); Rasch et al. (2010) with this work. . . . .	80
4.6	Comparison of effects of seeding in an increased greenhouse gas concentration atmosphere on precipitation (mm/day except Bala et al. (2011) cm/year) rate from Bala et al. (2011); Jones et al. (2009, 2011); Rasch et al. (2010) with this work. . . . .	81
4.7	Comparison of effects of increased greenhouse gas concentrations on sea ice cover from Jones et al. (2011); Rasch et al. (2010) with this work. . . . .	83
4.8	Comparison of effects of MCB in an increased greenhouse gas concentration atmosphere on sea ice cover from Jones et al. (2011); Rasch et al. (2010) with this work. . . . .	84
4.9	Comparison of effects of MCB in an increased greenhouse gas concentrations atmosphere on radiative flux difference ( $\text{W m}^{-2}$ ) between Jones et al. (2011) and this work. . . . .	85
4.10	Comparison of effects on albedo in increased carbon dioxide concentration atmospheres with and without seeding between (Bala et al., 2011) and this work. . . . .	86



5.1	Comparison of the CDNC ( $\text{cm}^{-3}$ ), shortwave forcing ( $\text{W m}^{-2}$ ), surface temperature (K), precipitation rate (mm/day) and polar ice cover between the $2\text{CO}_2$ and CON simulations described in Table 5.1. . . .	96
5.2	Comparison of the CDNC ( $\text{cm}^{-3}$ ), shortwave forcing ( $\text{W m}^{-2}$ ), surface temperature (K), precipitation rate (mm/day) and polar ice cover between the MCB3_2CO <sub>2</sub> and CON simulations described in Table 5.1. . . .	98
5.3	Comparison of the CDNC ( $\text{cm}^{-3}$ ), shortwave forcing ( $\text{W m}^{-2}$ ), surface temperature (K), precipitation rate (mm/day) and polar ice cover between the MCBA_2CO <sub>2</sub> and CON simulations described in Table 5.1. . . .	100
5.4	A comparison of the radiative flux difference at the top of the atmosphere ( $\text{W m}^{-2}$ ), the latitude weighted radiative power (W) and the radiative MHF (PW) for the ERBE dataset in Wunsch (2005) and this work. . . . .	103
5.5	The total radiative MHF (PW) calculated for four climate simulations described in Table 4.1. . . . .	104
6.1	Locations of seven oceanic basins where investigations are performed into the effectiveness of using MCB as a tool to reduce the intensity of tropical cyclones. Contoured data shows annual average sea surface temperature (K) from the CON simulation described in Table 4.1. . . .	108
6.2	A photograph of Hurricane Isabel (2003) in the Atlantic Ocean where the eye can clearly be seen at the centre of the image. Photograph taken by Astronaut Ed Lu aboard the International Space Station. Image released to the public domain by NASA. . . . .	110
6.3	Change in SST (K) during peak tropical cyclone season for the seven tropical cyclone basins described in Figure 6.1. For each plot the dashed box shows the tropical cyclone basin of interest. . . . .	114
6.4	Change in SST (K) during peak tropical cyclone season for the North Atlantic, Northeast Pacific, Northwest Pacific and North Indian ocean basins as a result of MCB in three regions (left panels) or MCB over the entire ocean surface (right panels). For each plot the dashed box shows the tropical cyclone basin of interest. . . . .	116
6.5	Change in SST (K) during peak tropical cyclone season for the Southwest Pacific, Southeast Indian and Southwest Indian ocean basins as a result of MCB in three regions (left panels) or MCB over the entire ocean surface (right panels). For each plot the dashed box shows the tropical cyclone basin of interest. . . . .	117
6.6	Change in SST (K) during peak tropical cyclone season for the North Atlantic, Northeast Pacific, Northwest Pacific and North Indian ocean basins as a result of MCB in three regions (left panels) or MCB over the entire ocean surface (right panels) in an increased carbon dioxide atmosphere. For each plot the dashed box shows the tropical cyclone basin of interest. . . . .	119

6.7	Change in SST (K) during peak tropical cyclone season for the Southwest Pacific, Southeast Indian and Southwest Indian ocean basins as a result of MCB in three regions (left panels) or MCB over the entire ocean surface (right panels) in an increased carbon dioxide atmosphere. For each plot the dashed box shows the tropical cyclone basin of interest. . . . .	120
6.8	Location of coral reefs generated from data collected by the Millennium Coral Reef Landsat Archive project undertaken by NASA. . . .	123
6.9	Difference in annual average sea surface temperature (K) between five climate scenarios and a control scenario in tropical regions between 30° N and 30° S. . . . .	125
7.1	Seeding and analysis maps used in development and analysis of pseudo-random seeding of a climate model. . . . .	129
7.2	An example of randomly generated cloud droplet numbers (blue), the average of the random series (cyan), a pseudo-random sequence (green) and the average of the random sequence multiplied by the pseudo-random sequence (black). . . . .	130
7.3	Example pseudo-random seeding result from the HadGEM1 climate model. Showing a temperature track from a Fixed CDNC simulation, a pseudo-random simulation. The difference between the tracks, the difference between the tracks with a mean of zero. The track after switching according to a pseudo-random number track and the pseudo-random number track used to perform the switching. . . . .	132
7.4	Transfer functions for ten day average precipitation within a climate model to six analysis regions. . . . .	135
7.5	Transfer functions for ten day average precipitation within a climate model to four analysis regions. . . . .	136
7.6	Transfer functions for surface temperature within a climate model on six polar regions. . . . .	137
7.7	Transfer functions for one day mean precipitation within a climate model to six analysis regions. . . . .	139
7.8	Transfer functions for one day mean average precipitation within a climate model to four analysis regions. . . . .	140
7.9	A comparison between seeding three regions permanently and pseudo-randomly. The fixed results are copied from Figure 8 of Jones et al. (2009). All results are for precipitation, with the left panels in mm/day and the right panels in mm/day/ % change in CDNC. Note the scale is symmetrical with asymmetric labelling to prevent overlapping numbers. . . . .	142
1	A flowchart showing the method used in Chapter 7 for analysis of transfer functions in the HadGEM1 GCM. . . . .	169

# List of Tables

1.1	Model results showing the effects of differing volumes of sulphate seeding on precipitation and sea ice fraction from Brovkin et al. (2009); Crutzen (2006); Jones et al. (2011, 2010); Rasch et al. (2008); Robock et al. (2008); Tilmes et al. (2009). Within the sulphate volume column, burdens are shown in plain text while rates are in italics. Precipitation is shown either in mm/day or percentage change, the precipitation results for Jones et al. (2010) are for the months of June, July and August (JJA). Sea ice changes are qualitative with the exception of results from Tilmes et al. (2009) and Jones et al. (2010). . . . .	28
2.1	Clouds investigated by the BAe-146 during the VOCALs-REx field campaign. Start and end times are in seconds and relative to the start time of the flight data. Cloud thickness is approximated by taking the height difference between the top and bottom of the cloud from CDP data. . . . .	47
2.2	Clean cloud subset analysed in the albedo investigation. All fields are the same as in Table 2.1. . . . .	48
4.1	The various climate scenario simulations run using HadGEM1 to investigate the climate effects of geoengineering via MCB. Where CON is the Control simulation and 2CO <sub>2</sub> gradually increases carbon dioxide levels to double preindustrial levels. MCB3_2CO <sub>2</sub> and MCBA_2CO <sub>2</sub> are geoengineering simulations using MCB in the same atmospheric conditions as 2CO <sub>2</sub> . MCB3 and MCBA are MCB simulations run in the control atmosphere without the effects of doubling preindustrial carbon dioxide. The carbon dioxide fractions are graphed in Figure 4.1. . . . .	71
4.2	The model, resolution, background atmospheric conditions, seeding mechanisms and analysis time used in four publications on MCB and this work. . . . .	75

4.3	Numerical results from several fields as presented in publications on the climate impacts of increasing greenhouse gas concentrations (above the line) or geoengineering in an increased greenhouse gas concentration atmosphere (below the line). Sea ice values for Rasch et al. (2010) and Bala et al. (2011) are percentage changes relative to the control simulation and not changes in the total ice cover. Both Rasch et al. (2010) and this work have multiple seeding fractions, therefore the fraction of the ocean seeded is shown in bold next to the values they apply to. . . . .	75
5.1	Section of Table 4.1 used to assess the climate impacts of MCB. Where CON is the Control simulation and 2CO <sub>2</sub> gradually increases carbon dioxide levels to double preindustrial levels. MCB3_2CO <sub>2</sub> and MCBA_2CO <sub>2</sub> are geoengineering simulations using MCB in the same atmospheric conditions as 2CO <sub>2</sub> . The carbon dioxide fractions are graphed in Figure 4.1. . . . .	91
5.2	Numerical results detailing the global annual average control levels and the differences in the simulations described in Table 5.1. . . . .	93
6.1	The tropical cyclone season, peak season and basin specific name for several ocean basins. The numbers relate to the numbered basins in Figure 6.1. . . . .	108
6.2	The various climate scenario simulations run using HadGEM1 to investigate the climate effects of geoengineering via MCB. Where CON is the Control simulation and 2CO <sub>2</sub> gradually increases carbon dioxide levels to double preindustrial levels. MCB3 and MCBA are MCB simulations run in the control atmosphere without the effects of doubling preindustrial carbon dioxide. MCB3_2CO <sub>2</sub> and MCBA_2CO <sub>2</sub> are geoengineering simulations using MCB in the same atmospheric conditions as 2CO <sub>2</sub> . This is a reordered version of Table 4.1. . . . .	112
6.3	Difference in sea surface temperature (K) between five climate scenarios and a control in seven tropical cyclone development regions during peak tropical cyclone season. . . . .	122
1	The similarities and differences between climate models HadCM3, HadGEM1, HadGEM2 and the NCAR CCM3. HadCM3 was the precursor to HadGEM1 (See Chapter 3) and HadGEM1, HadGEM2 and the NCAR CCM3 were used for comparison in Chapter 4. HadCM3 and HadGEM1 described in Martin et al. (2006), HadGEM2 in Martin et al. (2011), CCSM3 in Collins et al. (2006). Part one of table continued in Table 2. . . . .	167

- 
- 2    The similarities and differences between climate models HadCM3, HadGEM1, HadGEM2 and the NCAR CCM3. HadCM3 was the precursor to HadGEM1 (See Chapter 3) and HadGEM1, HadGEM2 and the NCAR CCM3 were used for comparison in Chapter 4. HadCM3 and HadGEM1 described in Martin et al. (2006), HadGEM2 in Martin et al. (2011), CCSM3 in Collins et al. (2006). Part two of table continued from Table 1. . . . . 168

# Abbreviations

Acronym	What it means
AMS	Aerosol Mass Spectrometer
BC	Black Carbon
CAM	Community Atmosphere Model
CCM	Community Climate Model
CCN	Cloud Condensation Nuclei
CCSM	Community Climate System Model
CDNC	Cloud Droplet Number Concentration
CDP	Cloud Droplet Probe
CDR	Carbon Dioxide Removal
CMAP	CPC Merged Analysis of Precipitation
CON	Control simulation described in Table 4.1
CPC	Climate Prediction Center
DMS	Dimethyl Sulphide (C <sub>2</sub> H <sub>6</sub> S)
ENSO	El Niño Southern Oscillation
ERBE	Earth Radiation Budget Experiment
GCM	Global Climate / General Circulation Model
GISS	Goddard Institute for Space Studies
GLOBE	Global Land One-kilometer Base Elevation
GLOMAP	Global Model of Aerosol Processes
GOES	Geostationary Operational Environmental Satellite
HadCM3	Hadley Centre Climate Model version 3
HadGAM	Hadley Centre Global Atmosphere Model version 1

---

HadGEM1	Hadley Centre Global Environment Model version 1
HadGOM	Hadley Centre Global Ocean Model version 1
HadGEM2	Hadley Centre Global Environment Model version 2
IPCC	Intergovernmental Panel on Climate Change
MCB	Marine Cloud Brightening
MHF	Meridional Heat Flux
MODIS	Moderate - Resolution Imaging Spectroradiometer
NaN	Not a Number
NASA	National Aeronautics and Space Administration
NCAR	National Center for Atmospheric Research
NCEP	National Centre for Environmental Prediction
NERC	Natural Environment Research Council
NOAA	National Oceanic and Atmospheric Administration
POC	Pocket of Open Cells
PPM	Parts Per Million
SRM	Solar Radiation Management
SST	Sea Surface Temperature
SWCF	Shortwave Cloud Forcing
TOA	Top Of Atmosphere
UM	Unified Model
VACC	Volatile Aerosol Concentration and Composition
VAMOS	Variability of the American Monsoon System
VOCALs	VAMOS Ocean Cloud Atmosphere Land study
VOCALs-REx	VOCALs - Regional Experiment
WACCM	Whole Atmosphere Community Climate Model

# Chapter 1

## Introduction

### 1.1 Motivation

The climate system is essential for all life on Earth, from plants engaging in photosynthesis to polar bears in the Arctic and humanity distributed across the globe. The climate is an extremely complex system of physical and chemical processes, which is affected by radiation, heat and pressure amongst other quantities. Numerous publications, including in the most recent IPCC report (in 2007), show evidence that the climate system is warming as a response to changes in atmospheric greenhouse gas concentrations (Forster et al., 2007). The human race exists within the climate system and is technologically capable of causing a significant change in the climate. Changes in the climate system could have a significant impact on the human race. Example changes include sea level rise or changes in precipitation rates.

This work aims to investigate some of the potential climate impacts of the marine cloud brightening (MCB), solar radiation management (SRM) geoengineering scheme. Clouds, especially stratocumulus clouds are of interest to people investigating MCB as they have a large impact upon the planetary albedo (Hanson, 1991)



and hence the climate and are susceptible to modification in the form of seeding. Using climate models, several geoengineering schemes have been shown to be able to recover global average surface or near surface temperatures (Crutzen, 2006; Govindasamy and Caldeira, 2000). With newer, higher resolution models, investigations have expanded into regional effects where geoengineering schemes are found to be producing undesirable changes. This project aims to investigate some of the changes resulting from MCB as the concept is now in the public domain and therefore requires careful scientific analysis before any deployment can be attempted.

## **1.2 Climate Change**

The primary driver for the change in climate is the increase in atmospheric greenhouse gas concentrations as a result of human consumption of fossil fuels since the start of the industrial revolution. In the last 150 years the carbon dioxide concentration within the atmosphere has increased from 280 ppm to 390 ppm. The change in concentration of three key greenhouse gases (carbon dioxide, methane and nitrous oxides) are shown in Figure 1.1. The impacts of these changes in greenhouse gases are modelled in several studies and detailed model intercomparisons (Forster et al., 2007). The IPCC report in 2007 contained a bar plot of anthropogenic contributors to climate change where greenhouse gases are found to be the largest and best understood effect (Forster et al., 2007). The effect of these gases and several others is shown in terms of a radiative forcing displayed in an IPCC plot reproduced in Figure 1.2. Carbon dioxide is a long lived gas that is assumed to be uniformly distributed over the globe. In the atmosphere, carbon dioxide absorbs longwave radiation emitted from the surface. The emission of the radiative energy is in all directions from the warmed air and therefore approximately half of the radiation will be reflected back to the surface.

Within the climate change scenario there are several possible feedback mechanisms which can act to increase global temperatures. An example of a potential positive feedback mechanism is the release of methane from permafrost. Methane is an extremely effective greenhouse gas and it is estimated that over 1500 Pg of carbon is currently held in permafrost soils. With increasing planetary temperatures the Arctic permafrost could melt. It is suggested that if the permafrost retreats some methane would be liberated to the atmosphere which could cause significant further warming (Koven et al., 2011). The polar regions of the globe are found to warm more than the tropics and this is termed polar amplification. Section 1.2.2 details polar amplification and some of the mechanisms responsible for the associated additional warming. As can be seen from Figure 1.2 the largest uncertainty is in the aerosol effects on the climate. Several of the effects that aerosol can have on the climate are shown in Figure 1.3. These direct and indirect aerosol effects range from scattering radiation to modifying the microphysical properties of clouds. Some of the indirect effects of aerosols on clouds will be described in Section 1.3.3.

### **1.2.1 Responses to climate change**

The overall positive radiative balance total from Figure 1.2 adds energy to the climate system which is generally stored as heat. This additional energy in the climate system leads to a melting of polar ice caps and the warming of both the land surface and on a longer timescale the oceans. A plot showing the change in Arctic ice cover for the month of August between 1979 and 2011 is shown in Figure 1.4. Sea levels are impacted by melting of glaciers and thermal expansion as the oceans warms. An increase in mean sea levels impacts strongly on low lying countries such as the Seychelles, Mauritius, the Netherlands and Bangladesh which have a significant fraction of their population and territory close to or even below sea level.

With these scenarios in mind several schemes have been proposed to mitigate climate change. These include the application of carbon budgets, development of renewable energy sources and financial incentives to improve energy efficiency.

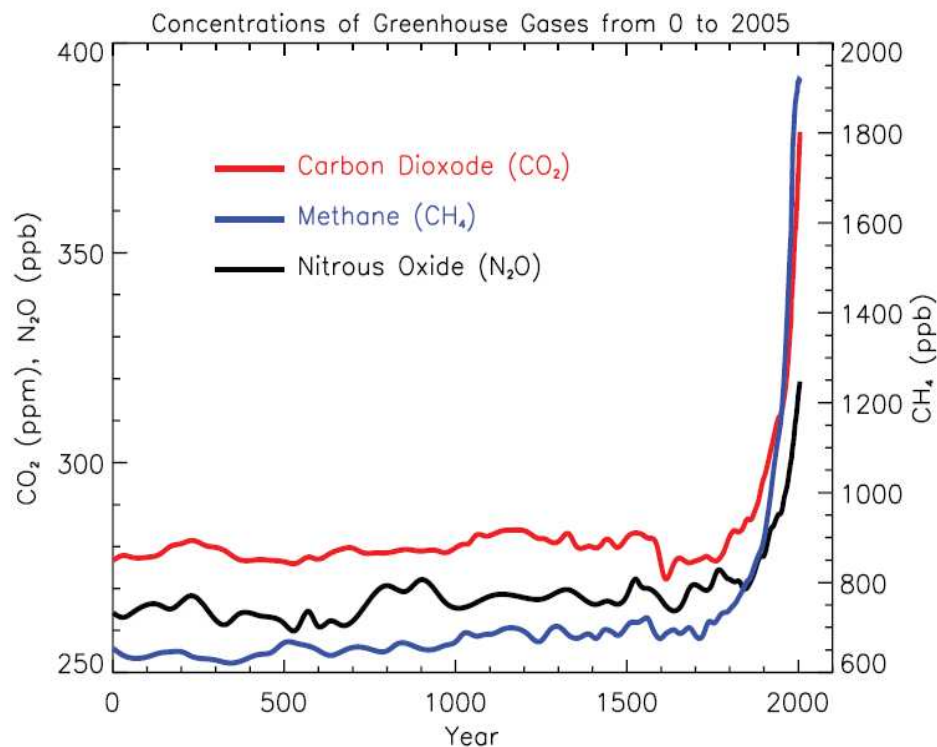


FIGURE 1.1: The change in atmospheric concentration of three long lived greenhouse gases, carbon dioxide (ppm), methane (ppb), nitrous oxide (ppb). Changes in greenhouse gas concentrations since 1750 are attributed to anthropogenic sources. Copied from Forster et al. (2007).

Beyond these mitigation strategies there are methods designed to tackle climate change directly, these are collectively known as geoengineering. Two groups of geoengineering methods are defined, carbon dioxide removal (CDR) and solar radiation management (SRM), they are discussed in Sections 1.4.2 and 1.4.3 respectively. Care should be taken with the use of the term geoengineering as it is possible to describe anthropogenic climate change as an engineered result. To prevent confusion, in this work geomodification is used to describe the unintentional changes to the climate system with geoengineering reserved for active attempts to remedy the problem of climate changes. An example of geomodification is the desertification of various areas by overzealous grazing, or the construction of the Hoover Dam which altered the flow of the Colorado river. The increase in evaporation from the newly formed Lake Mead may have lasting climatic impacts that were not the desired end result, instead the changes are byproducts of the construction of the

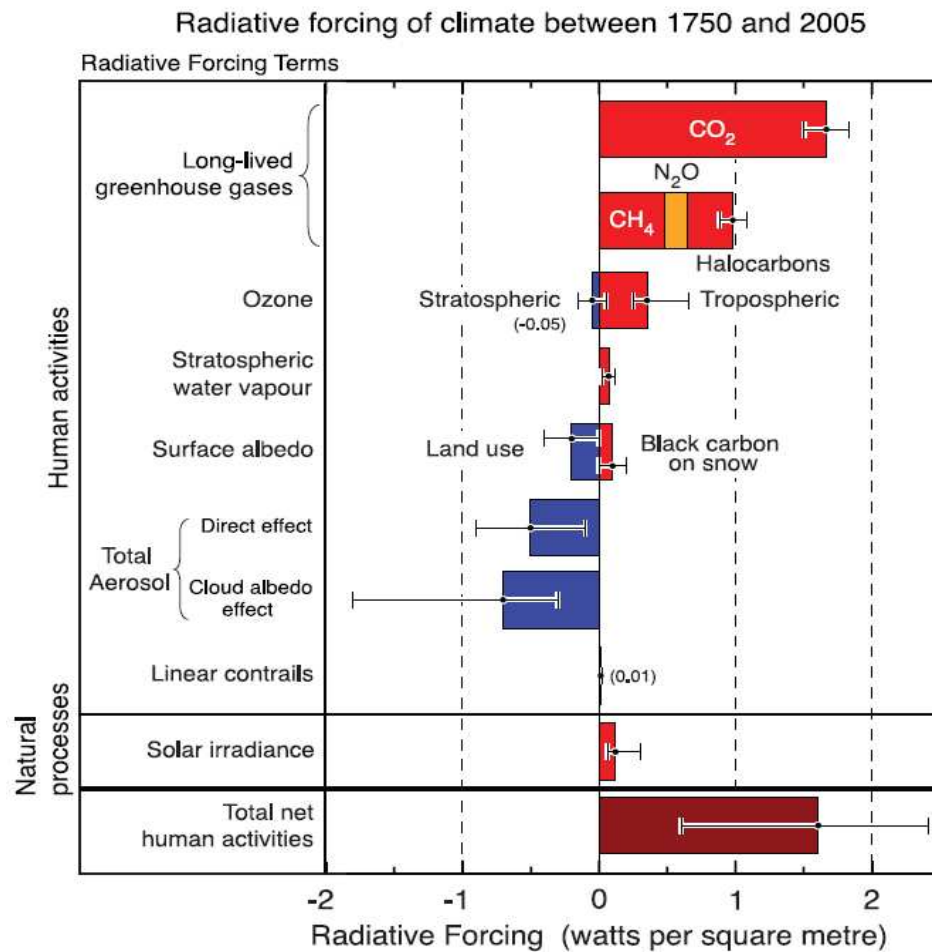


FIGURE 1.2: The change in radiative forcing ( $\text{W m}^{-2}$ ) as a result of either anthropogenic or natural processes. Results show the change in radiative forcing from the preindustrial era to 2005. Positive values result in a warming of the climate whereas negative values cool the climate. Copied from Forster et al. (2007).

dam. In contrast geoengineering is geared towards making an active change to the climate.

### 1.2.2 Polar amplification

Several publications, including papers on geoengineering, find that polar regions are preferentially warmed over the tropics as a result of increasing greenhouse gas concentrations in the atmosphere (Bala et al., 2011; Caldeira and Wood, 2008; Jones et al., 2009, 2011; Rasch et al., 2010). This phenomenon is known as polar

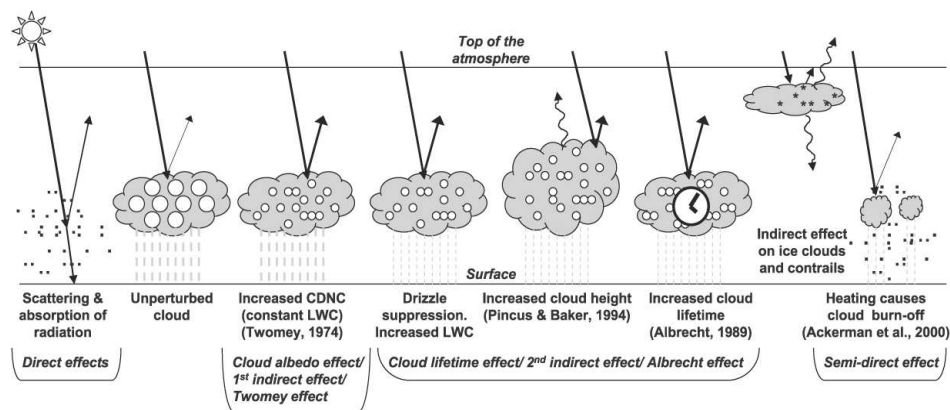


FIGURE 1.3: Schematic of several aerosol effects on the climate. Black dots, open circles, straight lines and wavy lines represent aerosol particles, cloud droplets, solar radiation and terrestrial radiation respectively. A large number of smaller cloud droplets exists in a perturbed cloud as both anthropogenic and natural aerosol can form cloud condensation nuclei. Originally published in Forster et al. (2007). See also Section 1.3.3.

amplification. Several observed and theoretical results investigating polar amplification are described in Curry et al. (1996).

There are multiple coupled mechanisms which exert an influence on the polar regions. As the global temperatures increase, sea ice cover is reduced which in turn reduces the albedo and allows more shortwave radiation to be absorbed by the newly revealed sea surface. This absorption increases the warming and forms a positive feedback loop (Curry et al., 1996). Results of this feedback loop include the reduction of sea ice as shown in Figure 1.4. The data in Figure 1.4 were recorded and plotted by the National Snow and Ice Data Center<sup>1</sup>. A second feedback loop described by Curry et al. (1996) is based upon the increased evaporation in a warmer atmosphere. Water vapour is a greenhouse gas and this can in turn continue to warm the atmosphere. With a reduction in ice cover and an exposure of more sea surface to solar radiation it is possible that water vapour levels in the Arctic will increase rapidly and cause significant further warming.

<sup>1</sup><http://nsidc.org/arcticseaicenews/>

An investigation by Holland and Bitz (2003) with doubling atmospheric carbon dioxide concentration in 15 climate models found that all predicted a temperature increase at 90° N that was at least 150 % of the global average. Of these models six of them had over 300 % average warming in the high latitudes (Holland and Bitz, 2003). The ice-albedo feedback process proposed by Curry et al. (1996) is supported by the results in Holland and Bitz (2003) where the highly sensitive models are found to have a thin polar ice layer in their control experiment. The results in Holland and Bitz (2003) are in contrast to Alexeev et al. (2005) where polar amplification of temperatures is still found despite the removal of the sea ice-albedo feedback loop. These publications suggest that there are multiple mechanisms behind polar amplification including changes in cloud cover and changes to the meridional heat flux (Alexeev et al., 2005; Curry et al., 1996). A model independent approach is used in Hudson (2011) where it is found that the sea ice albedo feedback proposed by Curry et al. (1996) produces a change in radiative forcing of  $0.11 \text{ W m}^{-2}$ . This value increases to  $0.7 \text{ W m}^{-2}$  if all northern hemisphere ice were lost for one month of the year.

### 1.3 Stratocumulus clouds

Stratocumulus clouds are long-lived clouds often capped with an inversion and generally found at altitudes between 1 km and 3 km. Persistent marine stratocumulus clouds are found on the west coast of Peru, California and Angola (Hanson, 1991). These regions have been suggested as a target for geoengineering as described in Section 1.4.3.5. Marine stratocumulus clouds are important to the earth's climate, they cover  $\sim 20$  % of the earth's surface and are responsible for reflecting  $\sim 30$  % of incoming solar radiation back into space (Borg and Bennartz, 2007). Once a stratocumulus deck is formed the cloud layer is maintained by cooler waters below and is responsible for cooling the waters, this leads to a positive feedback cooling the local climate (Hanson, 1991; Randall and Suarez, 1984). The deck cools the waters below by reflecting away solar radiation as clouds have a higher albedo than

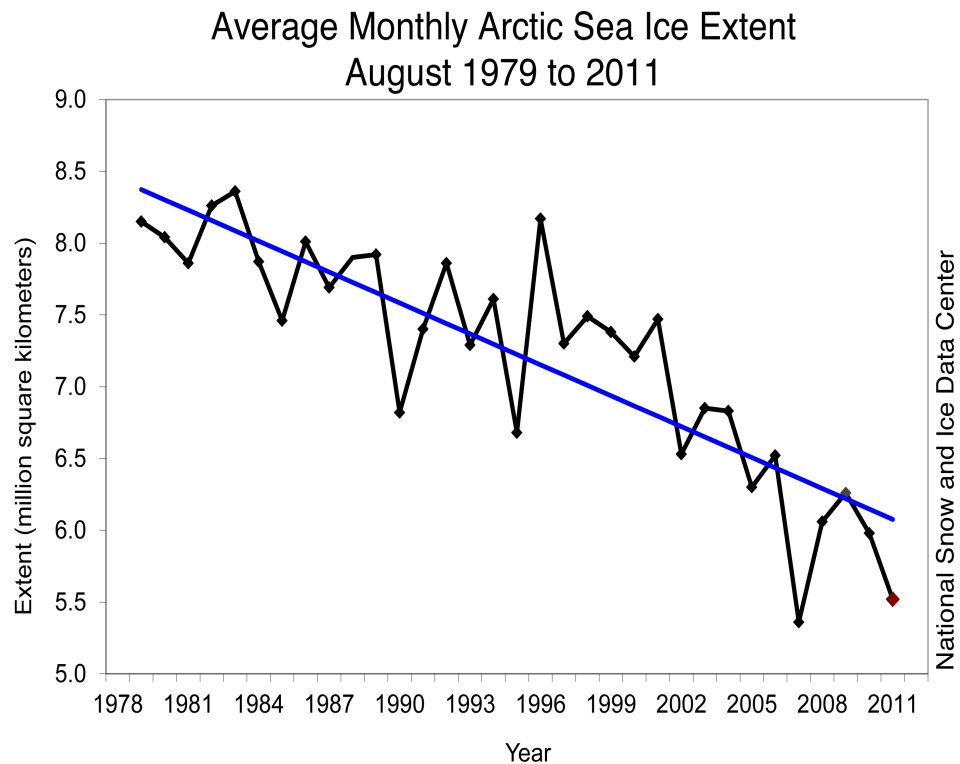


FIGURE 1.4: Sea ice cover for the month of August for each year between 1979 and 2011. The black data points show satellite derived sea ice cover, the blue line shows a least squares regression of the trend.

the sea surface. There is a large volume of research into the structure of pockets of open cells (POC) and the associated break up of stratocumulus decks (Haman, 2009; Stevens et al., 2005; Wood et al., 2008). There are several field campaigns looking into the mechanisms within stratocumulus clouds (Hogan et al., 2009; Randall et al., 1985; Slingo et al., 1982; Wood et al., 2011). Results from one such study, the VOCALS-REx field campaign (Wood et al., 2011), are examined in Chapter 2.

### 1.3.1 Formation

Marine stratocumulus clouds are formed in the atmospheric boundary layer over oceans. Within this layer there is turbulent mixing which brings moist air into contact with cooler air and condenses water vapour onto condensation nuclei. Above



the turbulent cloud layer there is an inversion, where warm dry air is maintained by dynamical forces above the cool moist boundary layer air (Hanson, 1991). Upwelling cool waters also reduce the local temperature with respect to the zonal mean and supplies cool moist air to the boundary layer. The cooling of the surface and the strength of the inversion above prevent deep convection and form layered clouds (Hanson, 1991). The moist air under the inversion is then able to form cloud droplets about a condensation nucleus. These nuclei are known as cloud condensation nuclei (CCN) and are formed from many sources including, sea salt aerosol, dimethyl sulphide (DMS), sulphate aerosol and mineral dust. Typical important nuclei in droplets of stratocumulus clouds are organic sulphates including DMS and sea salt particles.

### **1.3.2 Dissipation**

The stratocumulus cloud life cycle is complex and can be broken up by several mechanisms including pollution, precipitation, evaporation, pockets of open cell (POC) formation and dry air entrainment (Haman, 2009; Sorooshian et al., 2010; Stevens et al., 2005; Wood et al., 2008; Xue and Feingold, 2006). Dry air entrainment and turbulent mixing from above brings in air which can in certain circumstance cause the formation of cloud holes. This idea is expanded upon using modelling studies by Haman (2009). One heavily researched topic is the formation of POCs within the cloud sheets (Haman, 2009; Stevens et al., 2005; Wang and Feingold, 2009; Wood et al., 2008). It is suggested that the formation of POCs is related to convection and the local aerosol content (Wang and Feingold, 2009) and the fraction of water vapour below the cloud (Haman, 2009; Stevens et al., 2005).

Precipitation occurs when the droplets grow to a size where they are no longer dynamically supported by the cloud updrafts and gravity dominates. This causes a reduction in liquid-water path, thinning the cloud as water is removed from the layer and this in turn can reduce reflectivity and increase evaporation. Furthermore

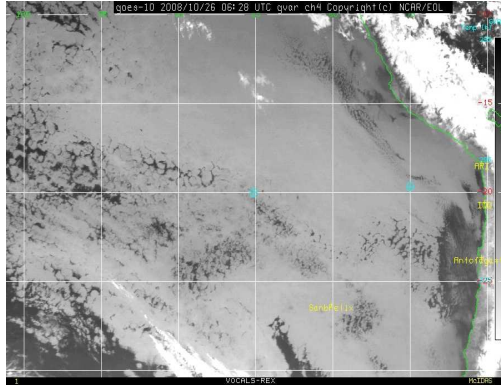


precipitation is capable of starting a cool air downdraft (Stevens et al., 2005; Wood et al., 2008).

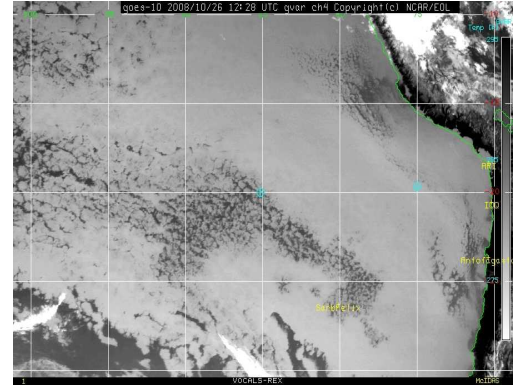
It was noted during the VOCALs-REx field campaign that the stratocumulus decks form during the night. The deck breaks up during the day into an open cellular system by the afternoon and reforms into a complete sheet during the night as shown in Figure 1.5. The deck forms during the night and persists through the morning. By noon local time the cloud deck begins to break up into a closed cellular structure (Figure 1.5(c)). By afternoon local time the deck is almost completely broken into open cellular clouds as (Figure 1.5(d)). In the evening and into the night the deck reforms (Figure 1.5(f)). Over night it is possible for the boundary layer to become decoupled from the surface layer (Wood and Bretherton, 2004), as the longwave radiation cools the surface and forms a stable layer, the decoupling breaks down in the morning when solar radiation warms the surface and warm air parcels begin to rise. The initiation of closed cellular convection (Figure 1.5(c)) is also noted in Stevens et al. (2005) where an increase in precipitation is also recorded. It is noted in simulations performed in Wang and Feingold (2009) that open cells do not form in the polluted regime.

### **1.3.3 Aerosol effects**

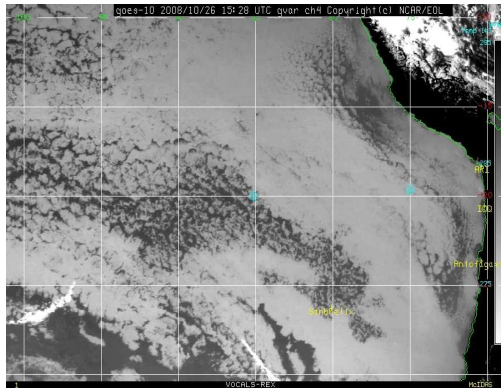
Aerosols effects on clouds are complex and have been studied in depth by both observations and modelling studies (Sorooshian et al., 2010). Indirect effects of aerosols were suggested by Twomey (1974). It is postulated that aerosol particles could increase the albedo of clouds by increasing the number of droplets while leaving the original liquid water content unaffected. This concept is then expanded upon in Twomey (1977) where impacts on optical thickness are investigated. These processes can however lead to a shorter cloud lifetime as the cloud droplets can be reduced to a size where they are readily evaporated and cause the cloud to dissipate (see Figure 1.3). A second indirect effect is proposed by Albrecht (1989) whereby the larger number of smaller droplets would take longer to form large droplets and



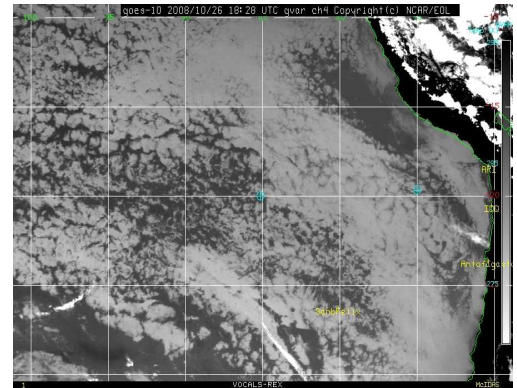
(a) Infrared image from GOES-10 over the VOCALS-REx experimental region taken at 06:28 UTC 26<sup>th</sup> October 2008.



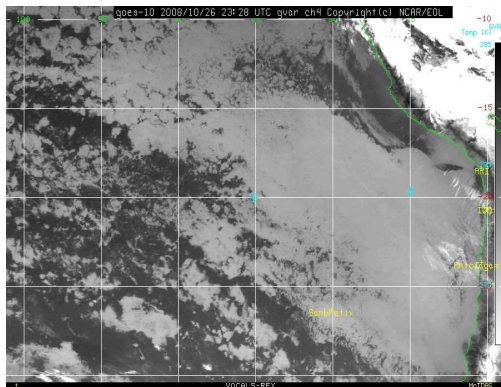
(b) Infrared image from GOES-10 over the VOCALS-REx experimental region taken at 12:28 UTC 26<sup>th</sup> October 2008.



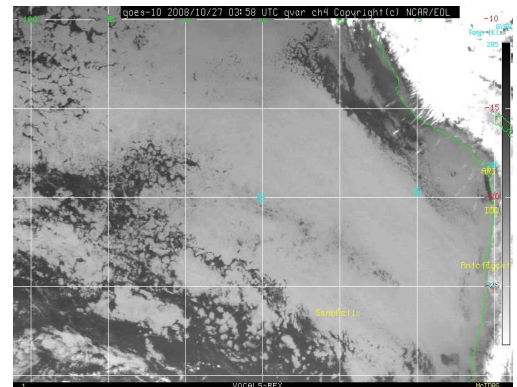
(c) Infrared image from GOES-10 over the VOCALS-REx experimental region taken at 15:28 UTC 26<sup>th</sup> October 2008.



(d) Infrared image from GOES-10 over the VOCALS-REx experimental region taken at 18:28 UTC 26<sup>th</sup> October 2008.

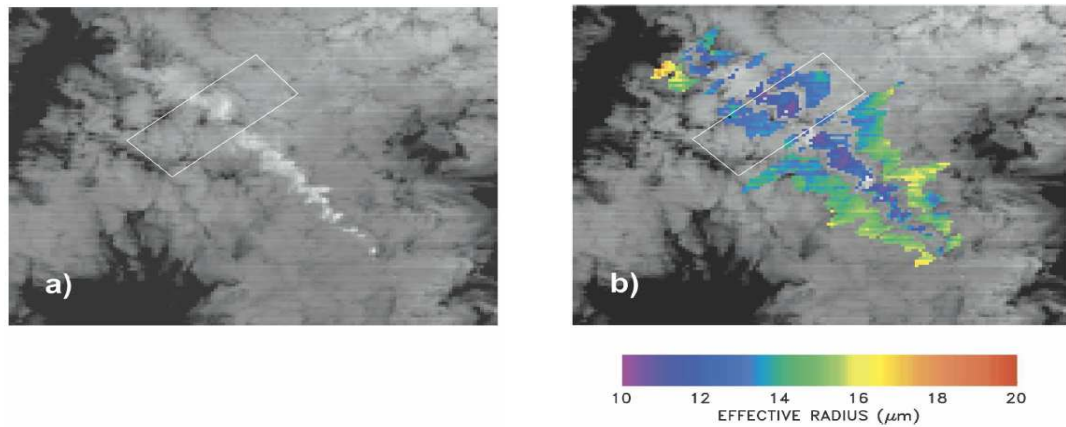


(e) Infrared image from GOES-10 over the VOCALS-REx experimental region taken at 23:28 UTC 26<sup>th</sup> October 2008.



(f) Infrared image from GOES-10 over the VOCALS-REx experimental region taken at 03:58 UTC 27<sup>th</sup> October 2008.

FIGURE 1.5: Series of infrared satellite photos from Channel 4 ( $10.7 \mu\text{m}$ ) of the GOES-10 satellite showing the breakup and reformation of a stratocumulus deck during the day. Images were recorded during the VOCALS-REx field campaign. Brightness temperature shown on the right hand side of each plot with the data range between 270 K and 295 K. All times are UTC, where local time is UTC-4.



(a) Image recorded using  $2.1 \mu\text{m}$  satellite band showing a ship track.

(b) The cloud droplet effective radius calculated using a  $2.1 \mu\text{m}$  satellite image. The polluted areas are shown with a smaller droplet radius than the unpolluted area away from the ship track.

FIGURE 1.6: Satellite photo of a ship track and the change in droplet effective radius observed near the ship track. Originally published in Segrin et al. (2007).

rain out. This lengthens the lifetime of the cloud. The first and second indirect effects of aerosols on clouds are noted in the legend in Figure 1.3. The work of Albrecht (1989) is investigated in Lee and Penner (2011) where it was found that paramtrisations which only include the response of clouds to the liquid water path are incorrect and that these could lead to large errors in climate model predictions. An example of the first indirect effect is the phenomenon of ship tracks where the exhausts from shipping are a source of aerosol which then pollutes the clouds and brightens them (Segrin et al., 2007). An example ship track and the effect of pollution on the cloud droplet effective radius is shown in Figure 1.6. It can be clearly seen in Figure 1.6 that the droplet effective radius is reduced nearer the ship track. Ship tracks are shown to increase the cloud top height, liquid water path and optical depth (Christensen and Stephens, 2011). It is found in one study that increasing the number of droplets within a cloud does lengthen the cloud lifetime but only to a point; if a cloud becomes over polluted then an entrainment-evaporation feedback can start and evaporate the cloud significantly faster (Xue and Feingold, 2006). Aerosol effects are pinpointed as a key component of the formation of POCs and it is found that in the case of a highly polluted environment that POCs do not form as readily (Wang and Feingold, 2009).

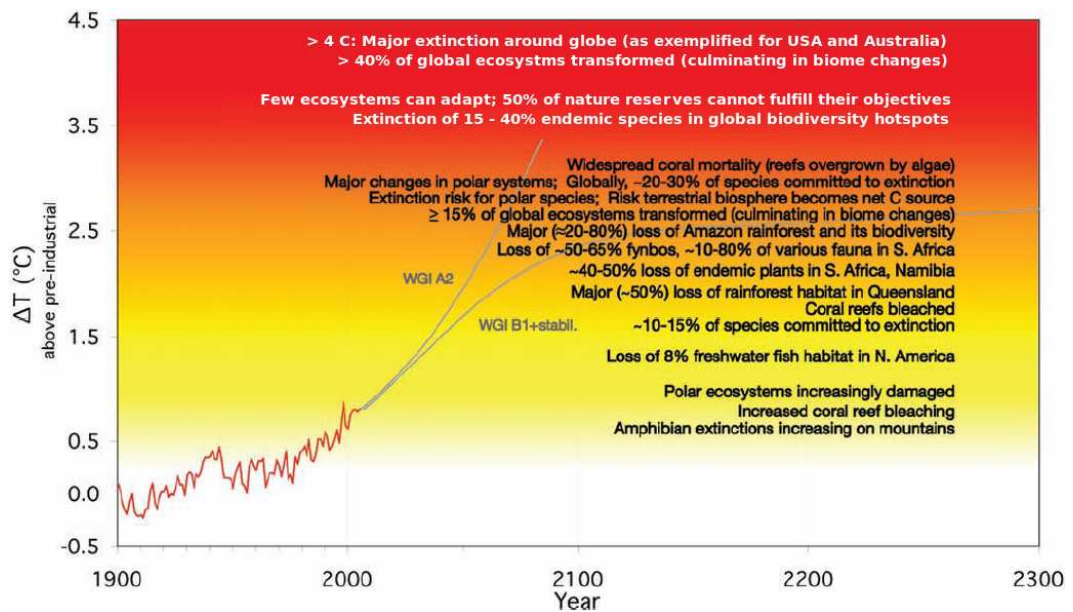


FIGURE 1.7: The potential impacts of increasing global mean annual surface temperature. The red line shows the historical track with two potential climate scenarios shown in grey. Colours indicate the temperature changes with the black text on the right showing the expected impacts at each temperature level (Parry et al., 2007). White text is used to replace the original black text for the top four lines to increase readability.

## 1.4 Geoengineering

Geoengineering is the term used to describe an active modification of the climate to achieve a set goal. A goal could be removing greenhouse gases or restoring the polar ice caps to preindustrial levels. Geoengineering can be considered an active approach to slowing global warming with the aim of reducing the damage done by meteorological disasters such as droughts or severe storms, or undoing damage done by anthropogenic pollution. An example of the potential changes as a result of climate change is shown in Figure 1.7 (Parry et al., 2007). It can be seen from Figure 1.7 that a temperature increase of as little as 2 K could lead to extinctions, coral bleaching and reduction in rainforests.

There are two distinct styles of geoengineering each with several possible implementations. Techniques termed Carbon Dioxide Removal (CDR) involve removing the greenhouse gases from the atmosphere while Solar Radiation Management



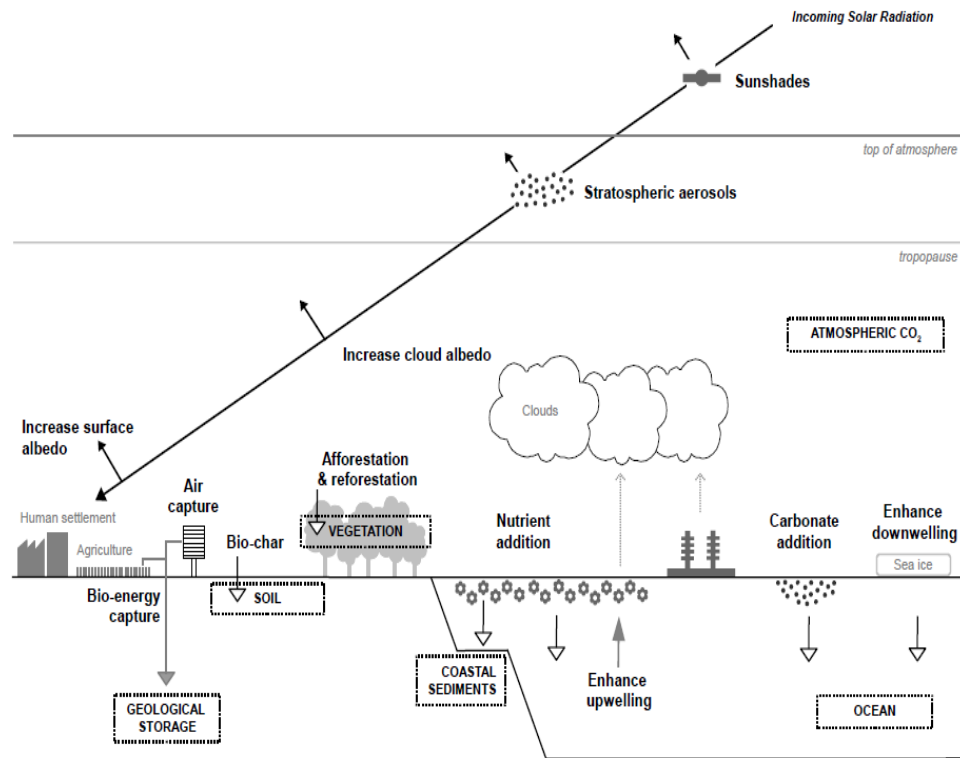


FIGURE 1.8: Schematic of several geoengineering methods. SRM methods reflect away solar radiation and CDR methods sequester carbon dioxide from the atmosphere. Solid arrows, hollow arrows, downward grey arrows, upwards grey arrows and dotted vertical arrows represent solar radiation, enhanced natural carbon flows, engineered carbon flows, engineered water flows and sources of cloud condensation nuclei respectively. Copied from Lenton and Vaughan (2009).

(SRM) methods reduce incoming radiation and provide a stop-gap against the most damaging effects of climate change. A schematic of several geoengineering methods is shown in Figure 1.8.

### 1.4.1 Models used to simulate geoengineering

Many models and model types are used to analyse the climate impacts of geoengineering. Models may simulate the atmosphere, ocean, land surface, carbon cycle, vegetation, ice cover or a combination of these. When analysing the ocean there is also the option of using either a slab ocean or a full ocean. Reducing the number of components in the model reduces the time taken to run numerical experiments

at the expense of reliability. The majority of models use one of an atmosphere only, atmosphere and slab ocean or atmosphere and full ocean. An atmosphere only model contains set fluxes from the surface and changes cannot affect ice or water temperatures. A slab ocean responds to atmospheric heating and provides dynamic moisture fluxes but does not simulate changes to large scale circulation. A full ocean contains oceanic overturning and the ability for ice and temperature changes to feedback into the atmosphere. The differences between the HadGEM1, HadGEM2, HadCM3 and NCAR CCM models are discussed in Appendix 1.

A known weakness of climate models is the representation of the tropical climate, especially precipitation. An investigation into the ability of the HadGEM1 model used in this work to represent global precipitation is shown in Section 3.2.2 and is discussed in Section 2 of Latham et al. (2012).

## **1.4.2 Carbon Dioxide Removal**

Carbon Dioxide Removal techniques include air capture (Lackner et al., 1999), ocean fertilisation (Martin, 1990) and forest management (Read et al., 2001). These methods have the added advantage that if they are successful then the problem of increased levels of atmospheric carbon dioxide is 'resolved'. These methods do not directly affect the methane burden in the atmosphere nor do they remove other warming gases. An example of a modified version of Figure 1.2 is shown in Figure 1.9, this plot shows the possible radiative impacts of reducing the atmospheric carbon dioxide fraction.

### **1.4.2.1 Ocean fertilisation**

Ocean fertilisation removes carbon dioxide from the atmosphere increasing the amount of carbon dioxide taken up by phytoplankton in the ocean. The amount of plankton in the ocean is limited by nutrient fraction, the commonly lacking nutrients are iron (Fe), phosphorous (P) and nitrogen (N) (Lampitt et al., 2008). The

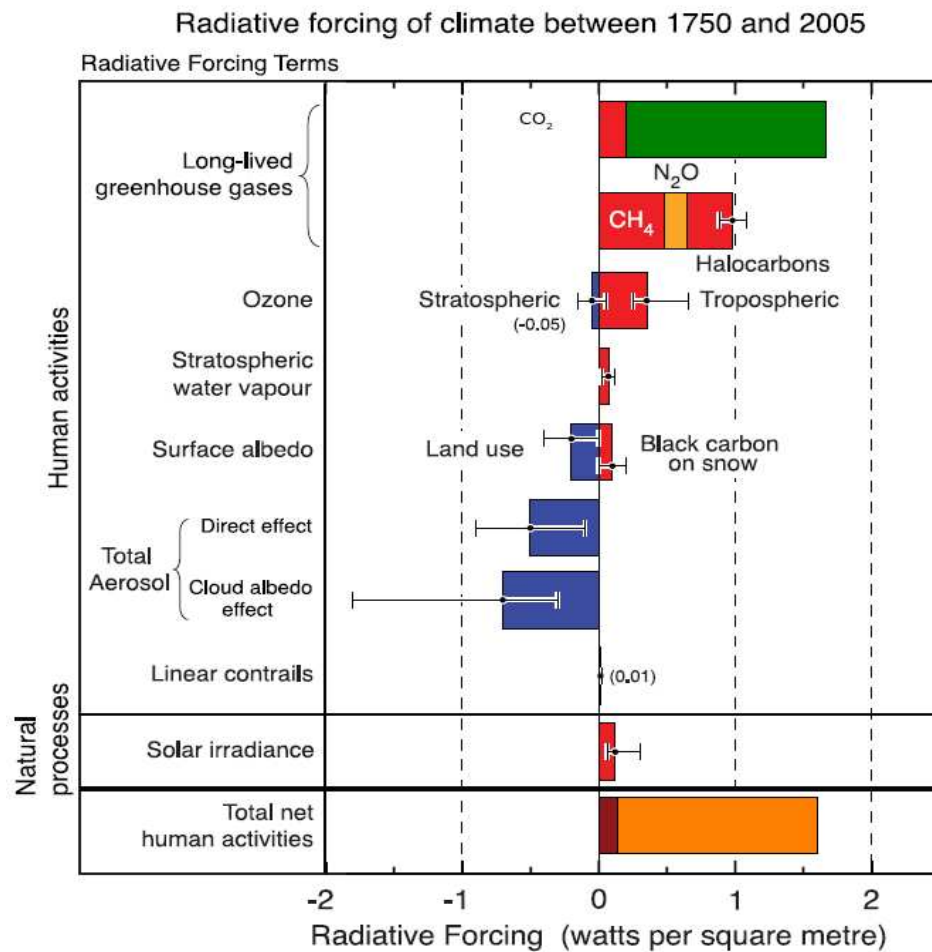


FIGURE 1.9: A modified version of Figure 1.2 displaying the desired changes to the radiative forcing ( $\text{W m}^{-2}$ ) caused by CDR. The green bar shows the possible effects of geoengineering and the orange bar in the final row shows the total changes. This figure is not balanced and does not take into account any secondary effects of reducing carbon dioxide. The change made is arbitrary and is designed solely to indicate the desired impacts of CDR.

ratio of these elements in algal tissues is 106:16:1:0.001 C:N:P:Fe (Redfield, 1934). The effects of adding iron to an iron poor environment would increase the plankton amount and reduce the volume of nitrogen and phosphorous available downstream of the seeding region (Lampitt et al., 2008). This could have a devastating effect on the marine ecosystem and lead to the creation of dead zones within the ocean (Diaz and Rosenberg, 2008). It is further found that a global seeding program would be required to remove up to 1 Gt carbon/yr from the atmosphere, while anthropogenic activities are adding 8.5 Gt carbon/yr (The Royal Society, 2009). Therefore any

deployment of ocean fertilisation requires additional CDR techniques be used concurrently to achieve a carbon neutral result.

#### **1.4.2.2 Forest management**

Forest management is another method of CDR based around enhancing photosynthesis rates. Within the forest system it is possible to increase the volume of carbon dioxide removed by reforesting deforested areas, afforesting previous barren areas, increasing the efficiency of forests at removing carbon dioxide or reducing degradation. Each of these methods is mentioned and described in Canadell and Raupach (2008). It is found that tropical deforestation is responsible for emissions of 1.5 Pg carbon/yr ( $1\text{Pg} \equiv 1\text{Gt}$ ) (Canadell and Raupach, 2008). Tropical forests are known to hold approximately 550 Gt carbon and are capable of sequestering carbon at a relatively high rate (Naidoo et al., 2008). As reforestation is relatively well understood certain schemes can be started with little delay and it is possible to remove 0.4 Gt carbon/yr by 2030, however this result is still dependent on investment (Canadell and Raupach, 2008). Several of the strategies within forest management could be considered mitigation techniques. However as with active geoengineering, large scale deployment of a mitigation technique requires careful study. An issue with reforestation or afforestation is the creation of organic aerosol products which can lead to a warming of the local region. These aerosol are commonly formed from isoprene and other related aromatic compounds which may in turn seed clouds (Claeys et al., 2004).

#### **1.4.2.3 Air capture**

Air capture reduces the amount of carbon dioxide in the atmosphere directly. The fraction of carbon dioxide in ambient air is found to be  $\approx 390$  ppm. It is possible to deploy air capture over a large area while not denying the use of the land for other purposes (Lackner et al., 1999). An example of this would be mounting the capturing devices in farmland or uninhabitable regions. It is proposed that air capture



be done using either highly alkaline solutions (Stolaroff et al., 2008), moderately alkaline solutions with the aid of enzymes (Bao and Trachtenberg, 2006) or onto solids (Lackner, 2009). Each method has advantages and disadvantages primarily related to availability of the raw materials. Furthermore the captured carbon dioxide will need storage and this has not been fully explored (The Royal Society, 2009). Suggested storage locations include former oil and gas fields. Another use for the captured carbon is to create a carbon neutral economy or energy sector, where the captured carbon is used as a fuel source however this proposal requires further investigation (The Royal Society, 2009). Capture direct from a power plant can be done in a relatively high carbon dioxide atmosphere at the source which will not require deployment over a large area.

### **1.4.3 Solar Radiation Management**

The second approach to geoengineering centres on reducing the amount of incoming solar radiation to balance the warming effects of greenhouse gases. These methods do not have the advantage of CDR as they are treating the symptoms not the problem but they allow the 'buying of time' to reduce the amount of greenhouse gases in the atmosphere. SRM geoengineering schemes include space mirrors (Govindasamy and Caldeira, 2000), sulphate aerosol injection (Crutzen, 2006), land surface change (Lenton and Vaughan, 2009), oceanic microbubbles (Seitz, 2011) and MCB (Latham, 1990). The blue bars shown in Figure 1.2 are the aerosol impacts on the climate system split into direct and indirect effects. SRM schemes such as sulphate aerosol and MCB are designed to increase the size of these blue bars to counteract the warming caused by greenhouse gases. An example of a modified version of Figure 1.2 is shown in Figure 1.10, where projected changes in aerosol forcings are used to balance the warming caused by an increase in anthropogenic greenhouse gas concentrations. These effects act to raise the planetary albedo by a small but significant amount. It is suggested that a change of 1 % in

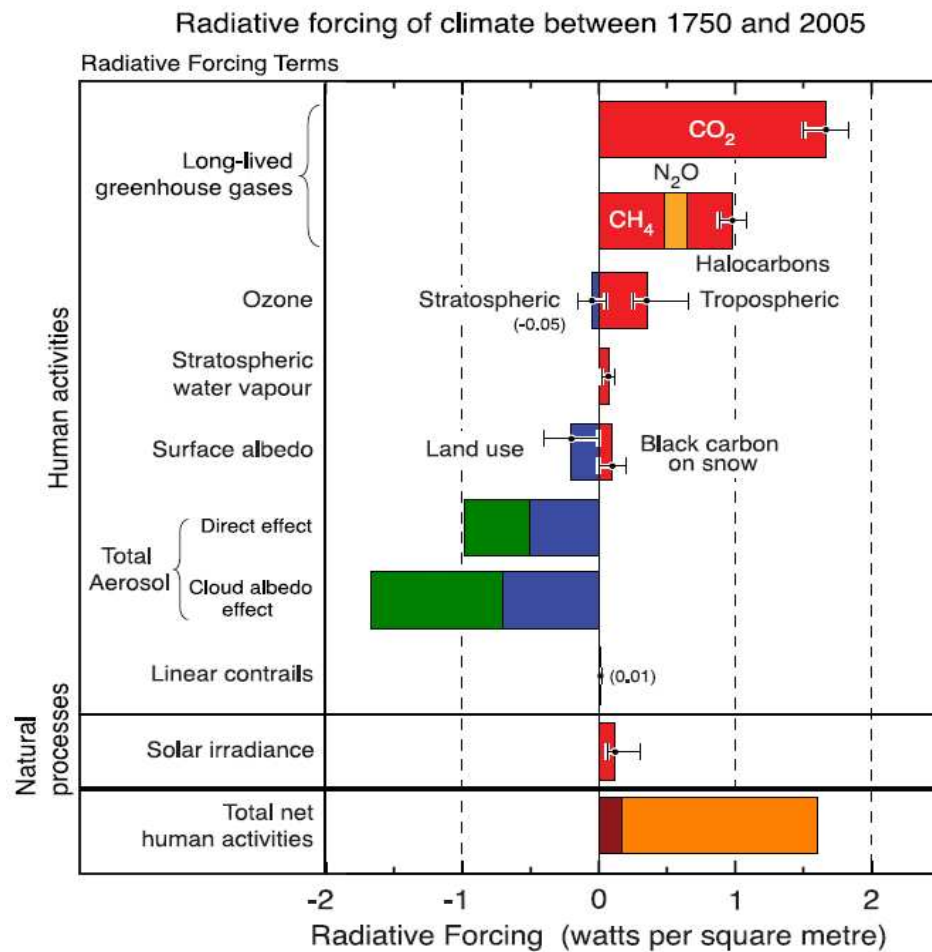


FIGURE 1.10: A modified version of Figure 1.2 displaying the desired changes to the radiative forcing ( $\text{W m}^{-2}$ ) caused by some SRM methods. The green bars show the possible effects of geoengineering and the orange bar in the final row shows the total changes. This figure is not balanced and does not take into account any secondary effects of increasing aerosol fractions. The change made is arbitrary and is designed solely to indicate the desired impacts of SRM.

the planetary albedo would be sufficient to offset the  $3.7 \text{ W m}^{-2}$  warming resulting from the doubling carbon dioxide (Donohoe and Battisti, 2011).

#### 1.4.3.1 Space Mirrors and Reduced Insolation

Space mirrors reduce incoming solar radiation by deflecting a portion of the radiation away from the earth. A possible position for the mirrors would be at Lagrange point 1 which is around 1.5 million km from the Earth, as it is an energetically

favourable position for the mirrors and will prolong their lifetime (Govindasamy and Caldeira, 2000). Lagrange point 1 is a region where there is a minima in the gravitational potential of a body in the Earth-Sun system. According to model work done by Govindasamy and Caldeira (2000) a reduction of incoming radiation of 1.8 % would be sufficient to negate the radiative forcing increase caused by doubling carbon dioxide from 280 ppm to 560 ppm. The results from the slab ocean - atmosphere version of the NCAR CCM v3 show that in a double carbon dioxide concentration atmosphere with reduced insolation the surface temperature, total daily precipitation and sea ice fraction are relatively unchanged with respect to a control atmosphere with standard insolation. It is however found that the reduction of solar radiation causes a cooling of the stratosphere which could further exacerbate ozone depletion. This work is expanded upon in Govindasamy et al. (2003) and Lunt et al. (2008) who suggest a reduction in solar radiation of 3.6 % and 4.8 % respectively. It is possible to tune the reduction of the solar constant using the 2 m global average temperature, however this does not ensure that temperatures at 2 m are all the same as the control (Lunt et al., 2008). There is a distribution of the temperature change, with a cooling compared to the control in the tropics and a warming in the high latitudes, the latter of these leading to a reduction in sea ice. Both Govindasamy et al. (2003) and Lunt et al. (2008) find a reduction in precipitation rates. However, in Govindasamy et al. (2003) this reduction is found to be less than the change in precipitation caused by quadrupling atmospheric carbon dioxide concentrations. The simulations in Lunt et al. (2008) are found to be too short to assess changes in oceanic circulation while increasing the strength of the Walker circulation in the atmosphere.

Further work presented in Caldeira and Wood (2008) shows the use of the NCAR CAM v3.1 which contains a full atmosphere model an interactive land surface model and a thermodynamic ice sheet model. The absence of an ocean within the model prevents influences from oceanic circulation and the long timescale changes that are associated with oceanic overturning. They perform simulations including a control, a doubled carbon dioxide atmosphere and geoengineered runs based on the

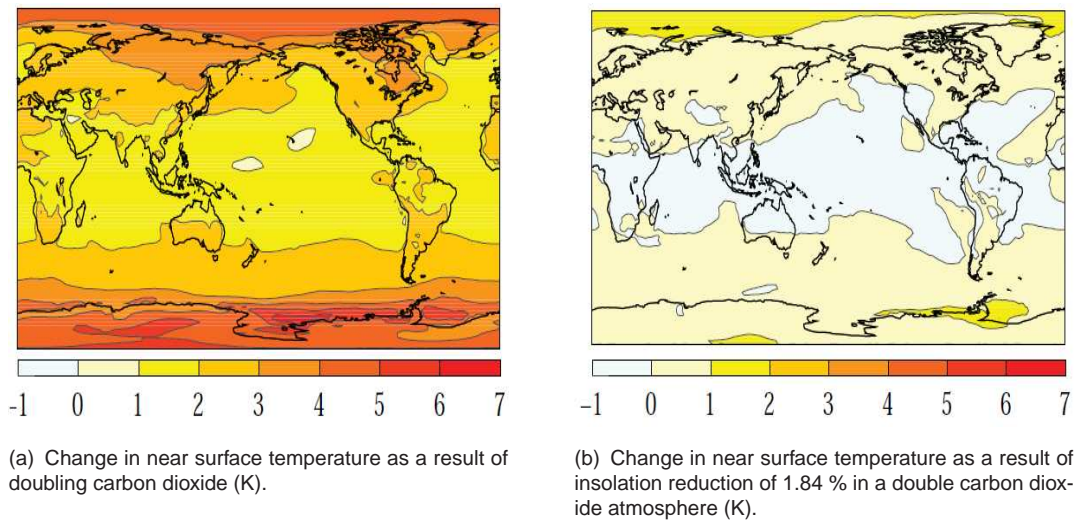


FIGURE 1.11: Change in near surface temperature (K) as a result of doubling carbon dioxide and as a result of reducing insolation by 1.84 % in a double carbon dioxide atmosphere, originally published in Caldeira and Wood (2008).

double carbon dioxide atmosphere with a reduction in solar insolation at various locations across the globe. In a different approach to previous studies, regional seeding is investigated in the Northern hemisphere between  $61^\circ$  or  $71^\circ$  N and the North pole. The global insolation reduction required to counteract doubling of carbon dioxide is found to be 1.84 % and this formed the base for some of the regional studies. All regional studies are done from either  $61^\circ$  or  $71^\circ$  N to the pole, in each study the insolation is reduced and the model is left to run under the new conditions. Arctic studies are done to investigate the possibility of using geoengineering to return the Arctic climate to a preindustrial state. Results showing the temperature effects of doubling carbon dioxide and geoengineering a double carbon dioxide atmosphere are shown in Figure 1.11. Doubling carbon dioxide is found to cause a significant increase in temperature at higher latitudes when compared to a control run (Caldeira and Wood, 2008). Global seeding patterns tend to reduce temperatures uniformly and a warming of the higher latitudes remains under these scenarios. The sea ice fraction follows the temperature pattern and it can be seen in the results that the control sea ice fraction can be maintained by any of the Arctic seeding patterns.

#### 1.4.3.2 Sulphate aerosol seeding

The use of sulphate aerosol to reflect solar radiation as proposed in *Global Warming and Ice Ages: I. Prospects for Physics-Based Modulation of Global Change*. (1997) is modelled in several papers (Brovkin et al., 2009; Jones et al., 2011, 2010; Rasch et al., 2008; Robock et al., 2008; Tilmes et al., 2009). Sulphate aerosol seeding aims to increase the earth's albedo by increasing the aerosol direct effect, which is shown as the sixth bar down in Figure 1.10. The method relies on deploying either hydrogen sulphide, sulphur dioxide or sulphuric acid to the upper troposphere or lower stratosphere where reactions with water forms sulphate aerosol. Across the literature the impacts of changing the volume of sulphate, the injection height and the aerosol distribution are investigated. Sulphate seeding utilises the aerosol first direct effect (See Figure 1.3). This effect works by using the aerosol to scatter the incoming radiation. From the scattering, some of the incident radiation is reflected back into space and this reduces the overall energy in the climate system. The dispersion of sulphate is dependent on the seeding location and time of year: seeding in the tropics uses atmospheric circulation to distribute the particles, while polar seeding restricts sulphate aerosol to a smaller region.

The earlier work on sulphate seeding suggests sulphate aerosol seeding as a response to the change in the radiation balance resulting from the use of clean coal. The desulphurisation was implemented to reduce damaging effects on the health of populations downwind of coal-fired power stations. This reduction of available sulphur reduced the sulphate aerosol burden in the atmosphere and led to a warming of up to  $1.4 \text{ W m}^{-2}$  (Crutzen, 2006). To correct for this warming it is suggested that 1.9 Tg sulphur could be placed into the upper atmosphere increasing the optical depth by 1.3 %. To maintain 1.9 Tg sulphur between 1-2 Tg would need to be added every year (Crutzen, 2006). This method is then further expanded to counteract the  $4 \text{ W m}^{-2}$  as a result of doubling carbon dioxide in the atmosphere. This is estimated to require a sulphate loading of 5.3 Tg which would increase optical depth by 4 %. This volume of sulphate is predicted to alter the colouring of the sky and cause a change in sunrises and sunsets (Crutzen, 2006).

A coupled climate-carbon cycle model including a biosphere is used in Brovkin et al. (2009) to expand on earlier work of Crutzen (2006). To hold surface temperatures static under a doubled carbon dioxide atmosphere it is estimated that a loading of 13 Tg S would be required. If an upper limit of 2 K of warming is set then this burden is reduced to 9 Tg sulphur. With global average temperatures brought back to a desired value by the aerosol, the local effects are analysed. It is found that with 13 Tg sulphur added to the atmosphere that polar winter temperatures would increase by more than 1 K while northern continental June, July, August average temperatures decrease by a similar amount. Globally the precipitation is generally not altered by more than 0.3 mm/day anywhere during the months of December, January and February. However, in the northern hemisphere summer there is an increase over much of India and Polynesia, with a decrease over the southern tip of the subcontinent, South East Asia and the tropics of America. This change in precipitation could have a drastic impact on billions of people and their livelihoods. The warming of surface temperatures in polar regions could lead to an increase in melting of the polar ice caps. The vulnerability of SRM to an unexpected cessation is highlighted in both Brovkin et al. (2009) and Jones et al. (2009), if the sulphate is no longer seeded then within 30 years it is found that Arctic winters are up to 6 K warmer and the global average temperature rapidly asymptotes to their control run (Brovkin et al., 2009).

Simulations using the GISS atmosphere model were performed to observe the effects of different sulphate loadings in varying regions of the atmosphere in Robock et al. (2008). The simulations are run for 40 years with the first 20 seeded, the second decade of seeding is used for analysis and the remaining time is used to investigate the effects of stopping seeding. Like Brovkin et al. (2009), they find that stopping geoengineering leads to rapid warming in the subsequent years and it takes around 30 years for the simulation to start matching the control run. These results are shown in Figure 1.12. Injection of sulphur dioxide at a rate of 5 Tg/yr in the tropics provides a stronger reduction in surface air temperature than 3 Tg/yr



across the Arctic, with both having a negligible effect on precipitation. This correlates with the change in September snow and ice fraction found over the Arctic during the second decade of seeding in the experiment. The use of temporal and global averages smooths over the local and time dependent effects that geoengineering could have. Over the northern hemisphere summer Arctic seeding warms the Antarctic, North Africa, North India and western Russia while causing a cooling over central Russia. Tropical seeding for the same time period results in a near uniform cooling over the globe with hot spots over India and Antarctica. In the northern winter, Arctic seeding has a significant warming effect on the Arctic climate while under tropical seeding the cooling is more uniform with the exception of the Labrador Sea (Robock et al., 2008).

Rasch et al. (2008) investigate the effects of particle sizes within sulphate aerosol seeding. Using the NCAR CAM3 model, a full atmosphere is coupled to a slab ocean. It is found that injection of 1 Tg sulphur/yr of small particles is almost as effective at cooling the climate as 2 Tg sulphur/yr of large particles. The larger number of smaller particles are more effective at reflecting away solar radiation than the larger particles. The large particles in the model have a mean effective radius that is close to 2.5 times that of the small particles ( $0.43\ \mu\text{m}$  and  $0.17\ \mu\text{m}$  respectively). A cooling of 0.8 K is found using 2 Tg sulphur/yr of small particles in a double carbon dioxide atmosphere, whereas using the same flux of large particles there is still a warming of 0.7 K when compared to a control atmosphere. Seeding with 1 Tg sulphur/yr provides a moderate value of cooling compared to the control run, but the cooling is insufficient to prevent ice loss and surface temperature increase. Doubling this seeding rate provides a cooling of surface temperatures and increases the sea ice fraction.

The addition of sulphate to the atmosphere can have an effect on the chemistry present and this is investigated in Tilmes et al. (2009). The WACCM3 model, a fully interactive chemistry climate model with a slab ocean is used to investigate the effects of stratospheric aerosol on several quantities. A seeding of 2 Tg sulphur/yr is used to simulate geoengineering the atmosphere. Sulphate seeding is found



to cool the atmosphere between the surface and 15 km but induce a warming between heights of 20 km and 30 km which can exacerbate ozone loss. The WACCM3 model contains stratospheric chemistry which is not present in CAM3. The addition of chemistry results in warmer surface temperatures in the model and significantly reduces the cooling present in Antarctica when compared with CAM3 results. Despite this warming found with the chemistry scheme there is still an increase in northern polar sea ice fraction. The addition of sulphur into the stratosphere also reduces ozone fractions and this in turn influences other chemical species. It is noted that the injection of 2 Tg sulphur/yr is able to delay warming by roughly 40 years as a result of continuing increases in the atmospheric carbon dioxide concentration.

The Met Office Unified Model Version 6.6 (known as HadGEM2) is a fully coupled atmosphere - ocean model. HadGEM2 is used in Jones et al. (2011) to investigate the impacts of SRM via sulphur dioxide (SO<sub>2</sub>) and MCB (see Section 1.4.3.5). Stratospheric sulphate seeding is found to reduce global average temperatures, this acts against the warming as a result of increasing greenhouse gas levels. In the decade where a balance is achieved between the increasing temperatures from greenhouse gases and the decreasing temperatures from stratospheric sulphate the analysis is performed. In a comparison between the geoengineered system and the control system it is found that there is a greater warming of the poles than the mid latitudes, furthermore there is a noticeable drop in precipitation over the Amazon and South East China. In line with the increasing temperatures there is a reduction in sea ice fraction in both the North and South poles. The radiative flux perturbations as a result of geoengineering via stratospheric sulphate or MCB are shown in Figure 1.13. This highlights the near uniform nature of the cooling due to stratospheric seeding.

The HadGEM2 and GISS ModelE models are compared in Jones et al. (2010). Both models are seeded with 5 Tg sulphur/yr and it is found that HadGEM2 retains a loading of about 70 % of that of GISS ModelE, indicated that deposition rates are higher in HadGEM2. The higher loading in GISS ModelE is reflected

in both the aerosol optical depth and the change in shortwave radiation. The effect of stopping geoengineering is investigated in Jones et al. (2010) where it is found that HadGEM2 warms quickly to the original A1B simulation. After stopping geoengineering the GISS ModelE simulates a quick warming for seven years and then warms at a slower rate until the geoengineered simulation matches A1B. The changes in annual surface temperature and June, July, August precipitation rate are shown in Jones et al. (2010) where the results from HadGEM2 show a larger cooling and less drying than the GISS ModelE results. The changes in ice cover as a result of sulphate seeding are also investigated. However only results from HadGEM2 are published. The results show an increase in both northern and southern hemisphere ice cover (Jones et al., 2010).

The HadCM3L model is used by Ricke et al. (2010) to perform multiple simulations of potential sulphate seeding schemes with time dependent changes in optical depth. The purpose of the work is to identify if it is possible to use a SRM method to restore both surface air temperature and precipitation over 23 large regions. An increase in aerosol optical depth results in a reduction in both surface air temperature and precipitation with precipitation continuing to decline while temperatures remain stable. (Ricke et al., 2010).

Work by Volodin et al. (2011) investigates the impacts of changing the height of sulphate aerosol seeding using the INMCM model. The model is seeded with 2 Tg/yr sulphate at varying heights and latitudes with temperature, precipitation and ozone change recorded. The results show that injections in 2 km bands between 20 km and 28 km between 0° and 10° latitude are most effective at cooling the planet. Furthermore Volodin et al. (2011) like Tilmes et al. (2009) shows a warming of the stratosphere while cooling the troposphere.

The idea of sulphate seeding is introduced to counter the reduction in aerosol number density as a result of clean coal regulations. Cleaning the sulphur from coal burned in power stations removed a source of sulphur dioxide which is known to have an adverse effect on health and the biosphere. The result of this is a significant reduction in the amount of sulphate aerosol in the atmosphere, this in turn leads

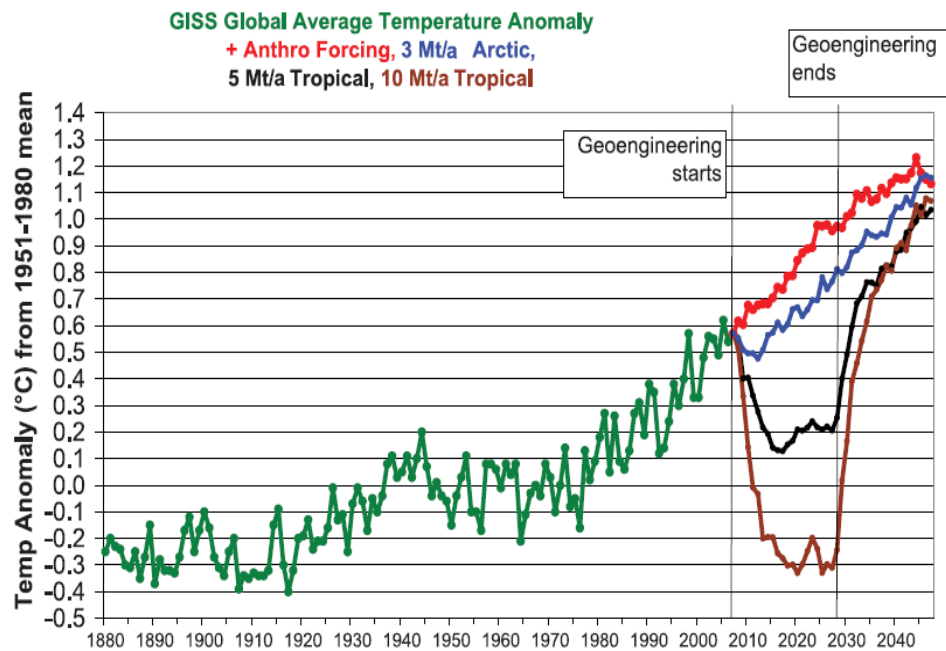


FIGURE 1.12: Global average surface air temperature anomaly (K) from 1951-1980 mean for four climate simulations. Observations shown in green, A1B in red, Arctic 3 Mt/yr in blue, tropical 5 Mt/yr in black and tropical 10 Mt/yr in brown. Copied from Robock et al. (2008).

to an increase in solar radiation reaching the surface. The results from Brovkin et al. (2009); Jones et al. (2011, 2010); Rasch et al. (2008); Robock et al. (2008); Tilmes et al. (2009) can be found in Table 1.1. The loadings required to counter climate change vary between 5.5 Tg in Rasch et al. (2008) and 9 Tg from Brovkin et al. (2009). Work by Jones et al. (2011, 2010); Rasch et al. (2008); Robock et al. (2008); Tilmes et al. (2009) produce a rate of sulphate addition instead of a total loading. This rate is found to be as high as 5 Tg/yr from Jones et al. (2010); Robock et al. (2008) and as low as 2 Tg/yr in Rasch et al. (2008); Tilmes et al. (2009). The lower rate is supported in work by Jones et al. (2011) where 2.5 Tg/yr is capable of returning an IPCC A1B (Defined in Solomon et al. (2007)) increase in greenhouse gases to the same temperature as a control atmosphere after 35 years.

Publication	Model	Sulphate volume	Precipitation effects	Sea ice change
Brovkin et al. (2009)	CLIMBER 2.3	9 Tg	-1 %	N/A
Robock et al. (2008)	GISS-E	<i>5 Tg/yr</i>	1.7 %	Increase
Tilmes et al. (2009)	WACCM3	<i>2 Tg/yr</i>	< -0.1 mm/day	± 5 %
Rasch et al. (2008)	NCAR CAM3	5.5 Tg <i>2 Tg/yr</i>	N/A	Increase
Jones et al. (2010)	HadGEM 2	<i>5 Tg/yr</i>	-0.041 mm/day (JJA)	NH + 0.011 SH + 0.004
Jones et al. (2010)	GISS-E	<i>5 Tg/yr</i>	-0.061 mm/day (JJA)	N/A
Jones et al. (2011)	HadGEM 2	<i>2.5 Tg/yr</i>	-0.065 mm/day	Decrease

TABLE 1.1: Model results showing the effects of differing volumes of sulphate seeding on precipitation and sea ice fraction from Brovkin et al. (2009); Crutzen (2006); Jones et al. (2011, 2010); Rasch et al. (2008); Robock et al. (2008); Tilmes et al. (2009). Within the sulphate volume column, burdens are shown in plain text while rates are in italics. Precipitation is shown either in mm/day or percentage change, the precipitation results for Jones et al. (2010) are for the months of June, July and August (JJA). Sea ice changes are qualitative with the exception of results from Tilmes et al. (2009) and Jones et al. (2010).

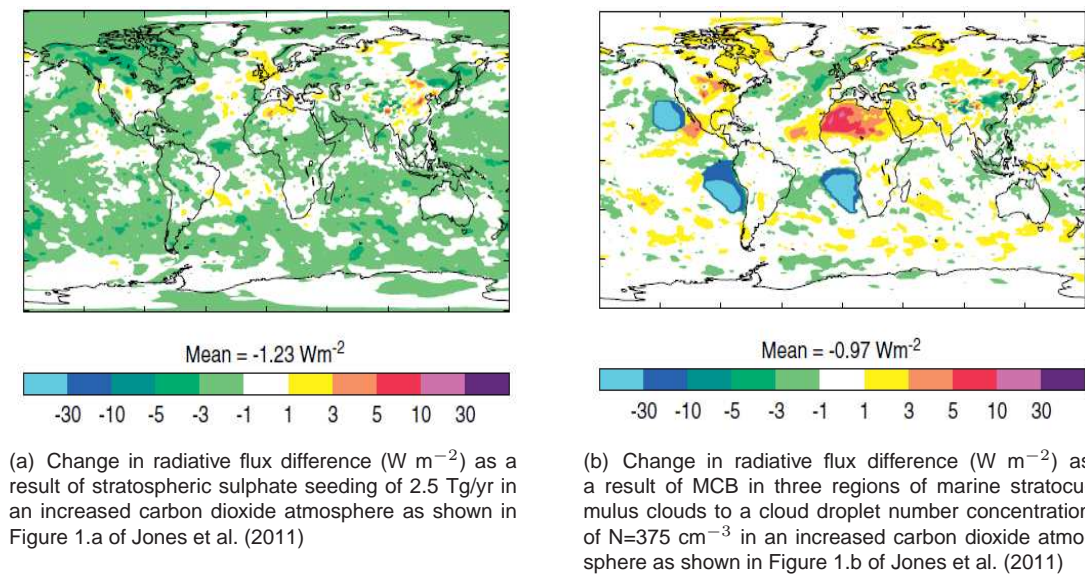


FIGURE 1.13: The change in radiative flux difference ( $\text{W m}^{-2}$ ) as a result of either seeding 2.5 Tg/yr sulphate (Figure 1.13(a)) or increasing the CDNC to  $375 \text{ cm}^{-3}$  in three marine regions (Figure 1.13(b)). These figures were copied from Jones et al. (2011).

### 1.4.3.3 Land use change

Land use change is the concept of altering the surface of the Earth to exert a change on the radiative balance of the climate system. Several approaches are suggested, including increasing the albedo of deserts, grasslands, crops and fully developed urban environs. All of the above are investigated in both The Royal Society special report on geoengineering (The Royal Society, 2009) and Lenton and Vaughan (2009). Both publications arrive at the conclusion that changing urban regions will not achieve a noticeable reduction in radiative forcing. If larger scale areas such as deserts are modified then it is found by Lenton and Vaughan (2009) that a change of  $2.12 \text{ W m}^{-2}$  is possible. The suggested method for altering the albedo of a desert is to manufacture and deploy a white polythene sheet over an aluminium base (Lenton and Vaughan, 2009).

#### **1.4.3.4 Oceanic microbubbles**

Oceanic microbubbles is the sea based equivalent of land use change where the albedo of the oceans is increased. The ocean absorbs a large fraction of the incoming solar radiation and if this is reduced it would be possible to cool the globe (Seitz, 2011). The NCAR CAM3 is used to investigate the impacts of changing ocean surface albedo by 0.05. The increase in ocean surface albedo resulted in a change in clear sky albedo of 0.031 and reduced global average temperatures by 2.7 K in a double carbon dioxide concentration atmosphere (Seitz, 2011). The impacts of using an atmosphere only model as opposed to a coupled full atmosphere - ocean model are discussed in Section 1.4.1.

#### **1.4.3.5 Marine Cloud Brightening**

Marine Cloud Brightening (also known as cloud whitening or cloud brightening) is a geoengineering scheme originally proposed by John Latham in a letter to *Nature* (Latham, 1990). Marine cloud brightening counteracts the decrease in long-wave radiation from increasing greenhouse gas concentration by increasing the outgoing shortwave radiation flux by creating brighter, more reflective clouds. A large fraction of the modelling work discussing MCB uses the Met Office Unified Model (UM) series of models (Jones et al., 2009, 2011; Latham et al., 2012, 2008). The NCAR CCM3 used in Rasch et al. (2008) is also used in Bala et al. (2011); Rasch et al. (2010) while GLOMAP is used by Korhonen et al. (2010). MCB is modelled in two distinct manners, either a modification of the global marine atmosphere or in specific regions. Work done in Latham et al. (2008) suggests doubling carbon dioxide would decrease upwelling longwave radiation at the top of the atmosphere by  $4 \text{ W m}^{-2}$ .

Results from the HadGAM model suggest that seeding stratocumulus clouds over the entire ocean would lead to a reduction in radiative forcing which is induced by

doubling carbon dioxide (Latham et al., 2008). The seeding of all marine stratocumulus clouds leads to a significant reduction in the cloud drop effective radius and an associated increase in the liquid water path, brought on by the reduction in evaporation from brighter clouds. Seeding three regions of marine stratocumulus cloud is also shown to reduce the radiative forcing locally, a result repeated in Jones et al. (2011). In the same paper using the NCAR CAM, it was found that seeding 75 % of the ocean would be the most efficient method for increasing shortwave cloud forcing (Latham et al., 2008) however reasons for this result were still under investigation. The work of Latham et al. (2008) on the technological requirements of MCB is expanded upon in Salter et al. (2008).

A proposed method of achieving the required change in CDNC for MCB is using wind-powered GPS guided ships to disperse small droplets to act as nuclei. An artists impression of one such vessel is shown in Figure 1.14. The ships would use Flettner rotors as a power source, the rotor design enables the vessel to sail more directly into the wind than a sail based ship, stop, and turn about its own axis (Salter et al., 2008). In addition the rotors require far less rigging than an sail of equivalent area. The goal of the ship design includes an inboard spray generation system which will create  $0.8\ \mu\text{m}$  monodisperse water droplets to act as CCN. The spray system is also designed to be self cleaning and resistant to biological build ups (Salter et al., 2008).

For MCB smaller regions have been investigated that for sulphate seeding, one example is three region seeding. The three regions can be seen in blue in Figure 1.13(b). Three region seeding applies to 5 % of the marine stratocumulus clouds (3.3 % of the global surface). These regions are later used in Jones et al. (2011). The HadGEM2 model is used and sets the cloud droplet number concentration to  $N=375\ \text{cm}^{-3}$  (Jones et al., 2009). MCB reduces the global average temperature while increased carbon dioxide increases temperatures. Temperature anomalies are measured against values taken as preindustrial. In an investigation of the impacts of cessation of geoengineering a simulation is run where geoengineering stops when the increase in temperature from greenhouse gases equals the



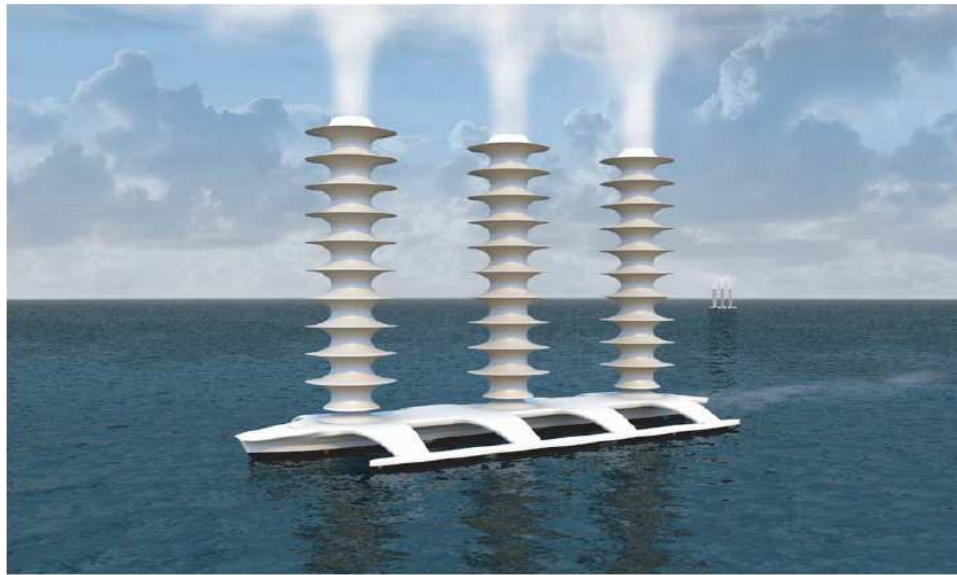


FIGURE 1.14: Artists impression of a ship designed to disperse sea salt particles to act as condensation nuclei within clouds (Salter et al., 2008). The three masts are clockwise rotating Flettner rotors with Thom fences. The prevailing wind is from the right of the image and the ship would move to the left.

decrease in temperature from MCB. In this case it is found that it takes less than 25 years for the global average temperatures to return to the levels in the A1B scenario (Jones et al., 2009). A plot showing the temperature tracks for three simulations, MCB, MCB turned off and A1B is shown in Figure 1.15.

Further work in Jones et al. (2011) uses the same model as their previous paper and shows the change in short wave cloud forcing (SWCF) as a result of seeding in three regions. When the global average temperatures of the geoengineered scenario are the same as the 1990 - 2000 average again it is found that cooling is strongest in the Arctic but it is not strong enough to overcome the warming from doubling carbon dioxide. The change in sea ice fraction responds to the temperature and in the case of increasing carbon dioxide the sea ice fraction is reduced. However when MCB is used the sea ice fraction does increase. The radiative flux perturbation from these experiments is shown in Figure 1.13(b).

The NCAR CCSM is used in Rasch et al. (2010) where instead of seeding three fixed regions the approach selected the clouds with the lowest CDNC. The NCAR CCSM runs at a slightly lower resolution than the HadGEM2 model used by Jones

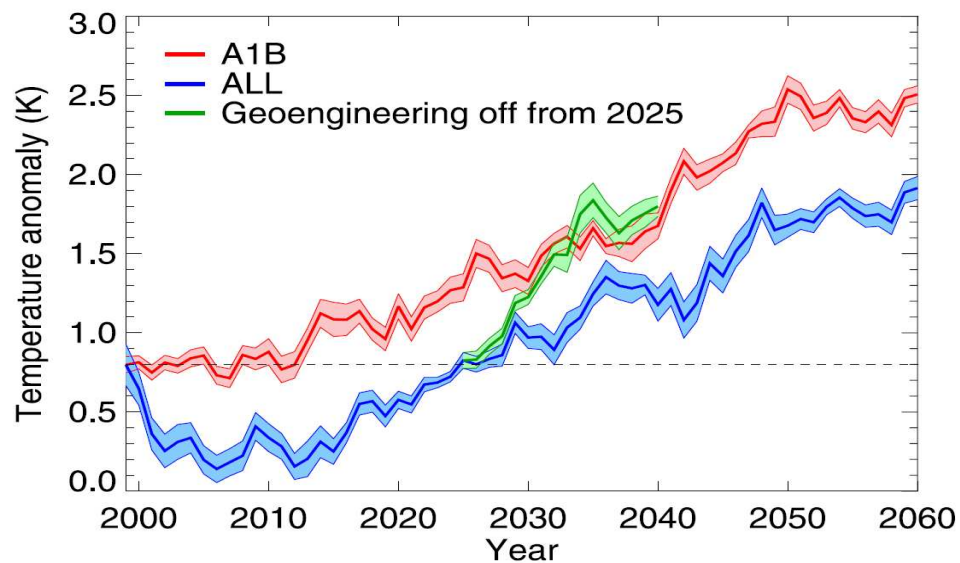


FIGURE 1.15: The temperature anomaly for three geoengineering simulations, A1B in red, MCB in three regions of marine stratocumulus clouds in blue and MCB in three regions of marine stratocumulus clouds ceasing after 25 years in green. Originally published in Jones et al. (2009).

et al. (2009, 2011) (See Appendix 1). Modification of the CDNC is to a value of  $1000 \text{ cm}^{-3}$  and the distribution of modified clouds changes for each month. In addition to a control and a double carbon dioxide simulation four seeding scenarios are investigated, seeding 20 %, 30 %, 40 % and 70 % of the ocean surface. Doubling atmospheric carbon dioxide concentration increases the polar temperatures more than the tropics and this in turn has a large effect on the sea ice fraction at the poles. Investigating the effects of 20 % seeding is restricted to the change in surface temperature where the majority of the cooling follows the seeding pattern. The 40 % seeding case reduces magnitude of sea ice lost as a result of increasing temperatures. When 70 % of the ocean is seeded then the surface temperature is reduced below the control experiment and a significant amount of sea ice was reformed around Antarctica.

Changes to the marine cloud droplet effective radius were investigated in Bala et al. (2011), this is an alternative approach to changing the cloud droplet number to a fixed value. Within the NCAR CAM the effective radius of a droplet is given to be  $14 \mu\text{m}$ , this is reduced to  $12 \mu\text{m}$ ,  $11.5 \mu\text{m}$  and  $11 \mu\text{m}$  in a series of experiments.

It is found that altering the effective radius to  $11.5 \mu\text{m}$  in a double carbon dioxide atmosphere had the least departure from the control experiment global average surface temperature. In a comparison between the control run and the  $11.5 \mu\text{m}$  geoengineered run it is found that there is a radiative forcing difference of  $0.35 \text{ W m}^{-2}$ . The  $11.5 \mu\text{m}$  geoengineered run contains a similar global average surface temperature to the control run however there are differences across the land and sea surfaces. The land surface is warmed by  $0.37 \text{ K}$  as a result of the doubling of atmospheric carbon dioxide concentrations while the seeding cools the ocean surface by  $0.07 \text{ K}$ . The seeding also causes a global reduction in precipitation but this is restricted to the ocean surface while the land surface is subject to a  $3.5 \%$  increase in annual average precipitation.

A different approach is taken by Korhonen et al. (2010), instead of using a GCM the GLOMAP aerosol process model is used. GLOMAP is driven by offline wind and thermodynamic fields. The mean droplet size detailed in Latham (2002) is used as the basis for aerosol which were then processed within the model. A second experiment is run with five times the defined rate ( $5^*\text{GEO}$ ). Within the simulations four regions were seeded, three similar to those from Jones et al. (2009) and one more in the Indian ocean, all are regions with low levels of condensation nuclei in the control model experiments. The CDNC is found to generally increase when compared to background levels for both cases, but in the geoengineered case there is a slight drop in North Pacific CDNC. The values of the background number of CDNC is investigated in Section 1 of Latham et al. (2012) where MODIS derived values are found to be significantly smaller than those assumed in Korhonen et al. (2010). The rate of emission of aerosol is linked to the wind speed with a maximum at  $7 \text{ ms}^{-1}$ , and is also dependent on the assumed vertical velocity probability density function (pdf). If the vertical velocities are too low then no amount of seeding will result in a large enough change in CDNC. With external thermodynamics it is not possible for the clouds to adapt to the change in aerosol loading. In both cases there is a spike in the aerosol size distribution between  $10^{-7} \text{ m}$  and  $10^{-6} \text{ m}$  with the  $5^*\text{GEO}$  case being significantly higher. It is also found that in the process of

forming extra cloud droplets the sulphur dioxide and sulphuric acid concentrations in the seeded area dropped significantly.

Analysis of satellite data to identify appropriate regions for seeding is performed by Alterskjær et al. (2012) using the MODIS satellite instrument and the NorESM global climate model. The susceptibility of clouds to MCB is calculated using both satellite and model data where it is shown that the three regions specified in Jones et al. (2009); Latham et al. (2008) are potential seeding sites. In addition to the three regions in Jones et al. (2009) there are also regions in the Western Pacific and the Indian Ocean, as shown in Korhonen et al. (2010), where deployment of MCB is possible. The work in Alterskjær et al. (2012) shows a reduction in sulphate aerosol concentration as a result of MCB which agrees with results from Korhonen et al. (2010).

Latham et al. (2012) is a collection of work across several groups on MCB including results from GCMs, high resolution cloud models and discussions on potential tests of a MCB scheme. The work in Latham et al. (2012) suggests that MCB is capable of recovering both North and South polar sea ice cover and depth. The GCM work also finds a reduction in precipitation over the Amazon, which is consistent with work in Bala et al. (2011); Jones et al. (2009, 2011). High resolution cloud modelling is performed to assess the impact of ship tracks on clouds with relatively high or low droplet numbers. The use of high resolution models allowed the investigation of the impacts of MCB on individual clouds. Modelling the impact of sea salt on clouds is performed to assess the optimum volume of sea salt to be added to a cloud to attain a desired albedo change. In addition to the modelling of sea salt impacts on clouds, work is performed on the design of the seeding ships shown in Figure 1.14. A potential field campaign is also discussed in Latham et al. (2012) where three phases are used to gradually increase the size of the experimental region.

#### **1.4.4 Assessing the effectiveness of geoengineering**

The climate system is complex and subject to multiple feedbacks. This uncertainty coupled with the experimental nature of any geoengineering scheme means that testing a potential geoengineering method is difficult. Testing of geoengineering via solar insolation reduction, a proxy for sulphate seeding, is performed using the HadCM3L model (MacMynowski et al., 2011). To identify a signal in the climate system there are three factors: the confidence in the result, the length of the experiment and the magnitude of forcing change simulated by the experiment. To identify a signal with appropriate confidence a balance between the amplitude of the change in forcing and the length of the experiment is required. A signal from a small change in forcing requires a longer experiment than for a larger forcing change and this has ramifications on the design of any potential test of geoengineering (MacMynowski et al., 2011).

### **1.5 Thesis aims**

The aim of this thesis is to investigate the impacts, effectiveness and mechanisms within the MCB geoengineering scheme. This work is an extension on numerous previous publications on the subject of MCB including Bala et al. (2011); Jones et al. (2009, 2011); Korhonen et al. (2010); Latham et al. (2012, 2008); Rasch et al. (2010). A short investigation into the microphysical properties of clouds using data from the VOCALs field campaign is shown in Chapter 2.

The bulk of this dissertation is based upon climate modelling work performed using the HadGEM1 coupled atmosphere-ocean climate model on the HECToR super-computer. A description of HadGEM1 is presented in Chapter 3 which description contains information condensed from three model description papers (Johns et al., 2006; Martin et al., 2006; Ringer et al., 2006). The main thesis aims are as follows.

1. How well does this work compare with previous results (Chapter 4)?

- a) Does HadGEM1 produce results consistent with previous work for simulations of climate change?
  - b) Does HadGEM1 produce results consistent with previous work for simulations of MCB?
2. What mechanism causes MCB to preferentially cool polar temperatures while only modifying clouds in the tropics (Chapter 5)?
  - a) Do the simulations described in Chapter 4 show a cooling of polar regions as found in Bala et al. (2011); Jones et al. (2011); Rasch et al. (2010)?
  - b) Is it possible to identify a mechanism for this change in polar temperatures?
3. What are the impacts of MCB on the tropical climate Chapter 6?
  - a) How does MCB affect tropical cyclone intensity?
  - b) How does MCB affect temperatures in regions containing coral reefs
4. Can pseudo-random seeding of a climate model be used to identify an optimal set of seeding regions Chapter 7?
  - a) Can signals from pseudo-random seeding of regions of the atmosphere be resolved in a climate model?
  - b) Are these signals the same as previous results?

## **Chapter 2**

# **The microphysical and radiative properties of clouds observed during the VOCALs-REx field campaign**

The VAMOS project is a collaborative effort between multiple universities, research institutions and funding agencies designed to investigate American monsoon systems. The VOCALs-REx field campaign took place throughout October and November 2008 (Wood et al., 2011). An image displaying several features of the climate system investigated in the VOCALs-REx field campaign is shown in Figure 2.1. VOCALs-UK is the UK element of the VOCALs-REx field campaign which involved people from several institutions and two research aircraft: the FAAM BAe-146 and the NERC Dornier 228 (Allen and Abel, 2009). An investigation into the persistent stratocumulus deck found in the VOCALs-REx field campaign was performed to provide experimental evidence into the effects of pollution on clouds.



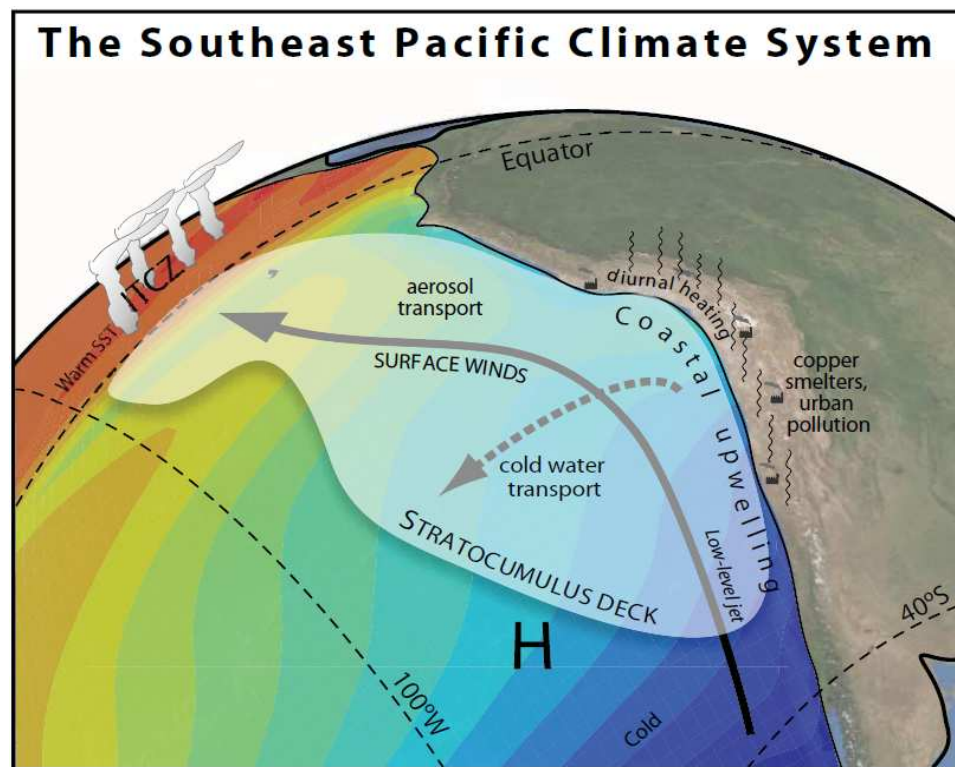


FIGURE 2.1: A schematic of several climate features of the South East Pacific investigated as part of the VOCALs-REx field campaign (Wood et al., 2011). The cold water transport line follows 20° S when it straightens.

## 2.1 Results from the VOCALs-REx field campaign

In the VOCALs-REx field campaign several flights were made along 20° S from 72° W to 86° W. The platforms include several aircraft, the Ronald H. Brown research vessel and soundings based at Iquique (Bretherton et al., 2010). Close to the coast the boundary layer is approximately 1 km in depth with cloud droplet numbers up to  $250 \text{ cm}^{-3}$  and a limited amount of drizzle. Back trajectories from this region found source air parcels from the Chilean coast indicating polluted air masses made up the clouds (Bretherton et al., 2010). In contrast to this, regions west of 75° W are rarely found to be made up of air parcels from the coast. In this cleaner region the cloud droplet number decreases to  $100 \text{ cm}^{-3}$  from  $250 \text{ cm}^{-3}$  and drizzle is more prevalent (Bretherton et al., 2010). In addition to these differences there is more evidence of boundary layer decoupling further from the coast (Bretherton et al., 2010). The 20° S flights are also part of an investigation into the marine boundary

layer. During the campaign there was an anticyclone above the boundary layer which produced a steady offshore wind. Below the boundary layer there was a reduction in sea surface temperature from North to South, which did not appear to change the atmospheric boundary layer depth (Rahn and Garreaud, 2010).

## **2.2 Aircraft used during the VOCALs-REx field campaign**

One possible use of the VOCALs-REx data is to provide evidence to assess the possibility of utilising this region as a site for MCB geoengineering as described in Section 1.4.3.5. Cross over events between the BAe-146 and the Dornier 228, where the aircraft are flying close together could be used to investigate the micro-physical and optical properties of the clouds simultaneously and possibly derive a relationship from the resulting data.

### **2.2.1 Dornier 228**

The NERC Dornier 228 provided remote sensing data using the AISA Dual radiometer, an instrument consisting of the AISA Eagle and the AISA Hawk radiometers (Wood et al., 2011). The instrument is a hyperspectral imager providing data from significantly more wavelengths than in a multispectral imager as found on satellites. The Eagle records images in the 400 nm - 970 nm range and at a frequency of 30 Hz (Makisara et al., 1993). The Hawk has an optical range of 970 - 2500 nm within the shortwave infrared spectrum (Spectral Imaging Ltd., 2009). When operated together as a single instrument the processing power available is a constraining factor on the output resolutions. The Eagle is capable of producing images 1024 pixels wide and the Hawk can produce images up to 320 pixels wide. The resolution in the direction of the flight path is dependent on the speed of the

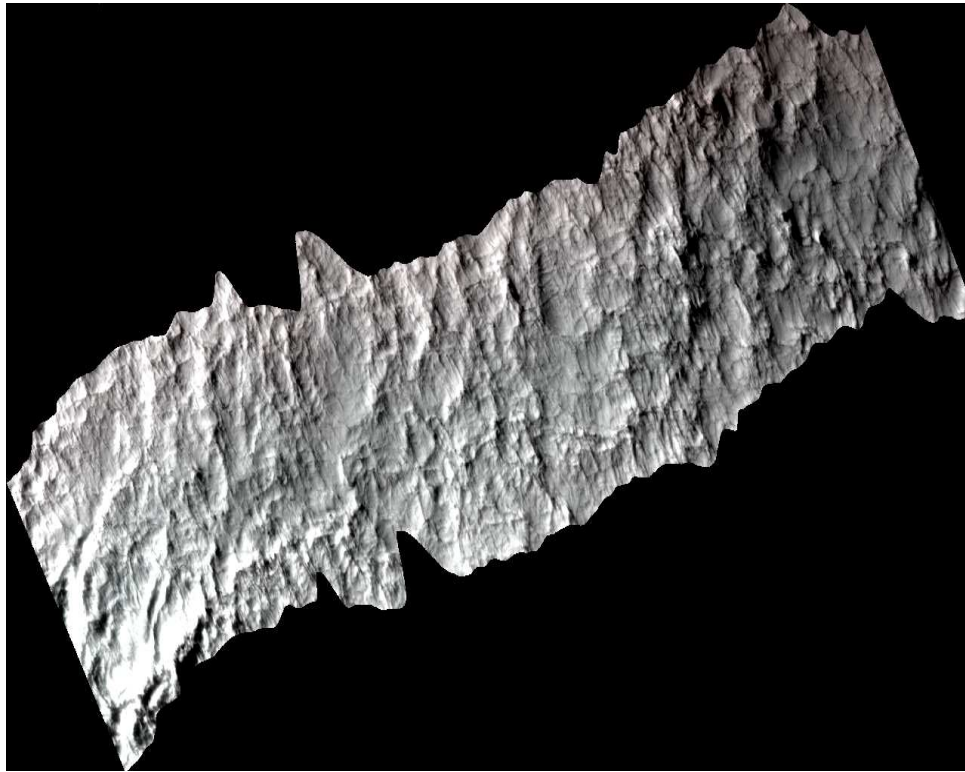


FIGURE 2.2: An example image generated from uncalibrated radiances of one band of the AISA Dual hyperspectral imager mounted on the Dornier 228 during VOCALs-REx.

aircraft, where increasing speeds reduce the resolution. The Dual sensor is capable of producing up to 500 spectral bands across the full 400 - 2500 nm range of the component instruments (Spectral Imaging Ltd., 2009). An example flight leg is shown in Figure 2.2. The plot in Figure 2.2 contains uncalibrated data at a temporal resolution of 30 Hz where the horizontal resolution is dependent on the airspeed and altitude of the aircraft. As a result of constraints on time it was decided that there would be no further investigation into the hyperspectral data. Future work in this area could look into cross over events and assigning them to flight legs before finding the albedo using a parametrisation or a radiative flux model.

### 2.2.2 BAe-146

The FAAM BAe-146 collected both remote sensing and in situ data during the VOCALs-REx field campaign. Several in situ instruments are used to provide verification and redundancies in case of faults. The primary instrument for microphysical data is the Cloud Droplet Probe (CDP), while the 2D-S is also used to record similar data. The BAe-146 is also equipped to record radiometric data using a series of broadband radiometers. To record shortwave radiation fluxes, two upward and downward facing clear-domed pyranometers are used (Wood et al., 2011).

## 2.3 Multiple instrument albedo investigation

During the VOCALs-REx field campaign the BAe-146 flew several in-cloud flight legs where it is possible to record microphysical data. There are several cross over events with the Dornier 228 which could be used to perform a comparison between the optical albedo from the Dornier and the in situ microphysics measurements. There is also scope for investigating the comparison between high resolution data from the Dornier 228 and the BAe-146 with the GOES-10 or MODIS satellites. As described in Section 2.2.1 there are issues with the Dornier data therefore a new approach was devised.

### 2.3.1 Cloud Droplet Probe

The CDP uses a single laser beam of wavelength 658 nm to analyse the particles passing through a focus region. For the VOCALs-REx field campaign the instrument was set to a 1 Hz data frequency with 30 size bins ranging between 1.7  $\mu\text{m}$  and 48  $\mu\text{m}$ . An image showing the path of a laser after a particle is detected is shown in Figure 2.3. Any particles incident with the beam outside the ‘depth of field’ produce either insufficient ( $<4^\circ$ ) or excessive ( $>12^\circ$ ) scatter and are automatically ignored by the instrument. The CDP instrument is compared against other

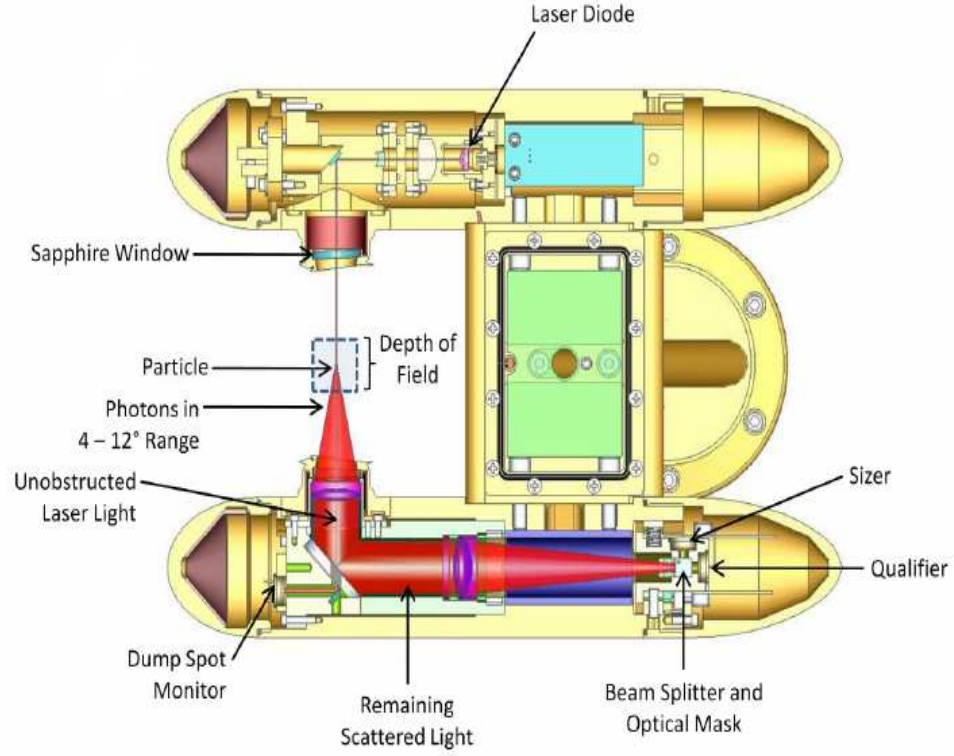
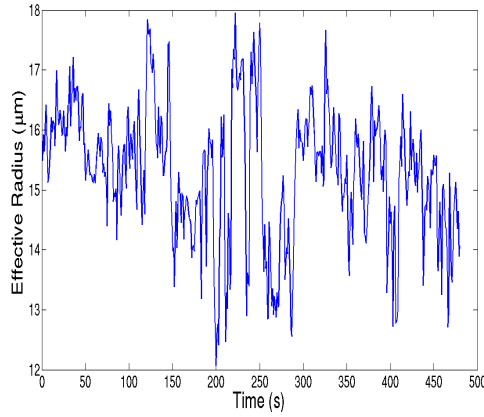


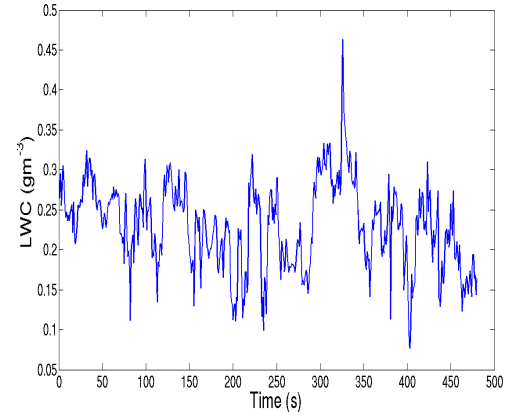
FIGURE 2.3: A diagram showing the operation of the CDP. Image copied from Droplet Measurement Technologies (2009).

instruments and is found to be susceptible to increasing liquid water content in clouds with a droplet concentration over  $200 \text{ cm}^{-3}$  (Lance et al., 2010). The CDP can also oversize smaller droplets. However this can be corrected within calibration (Lance et al., 2010). Example data from the VOCALs-REx field campaign is shown in Figure 2.4. The effective radius is defined in Equation 2.1. The effective radius is an area weighted radius of a droplet and is a component of the albedo parametrisation used in Section 2.3.5. The results in Figure 2.4(a) show that the effective radius varies between  $12 \mu\text{m}$  and  $18 \mu\text{m}$  while the results in Figure 2.4(b) show that the liquid water content ranges between  $0.15 \text{ gm}^{-3}$  and  $0.35 \text{ gm}^{-3}$ . The results in Figure 2.4 show little correlation between the effective radius and the liquid water content.

$$r_e = \frac{\int_{r_1}^{r_2} \pi r^3 n(r) dr}{\int_{r_1}^{r_2} \pi r^2 n(r) dr} \quad (2.1)$$



(a) Example time series of the effective radius ( $\mu\text{m}$ ) from the CDP instrument.



(b) Example time series of the liquid water content ( $\text{gm}^{-3}$ ) from the CDP instrument.

FIGURE 2.4: Example outputs from the CDP using data from the VOCALs-REx field campaign. The data used in this plot was recorded during Flight B417, which occurred on 9<sup>th</sup> November 2008.

### 2.3.2 Pyranometers

Pyranometers are devices that convert incident radiation into an electrical current that can be measured. The pyranometers are produced by Epply Laboratory and cast in aluminium to reduce weight when attached to the aircraft (FAAM, 2011). Radiation entering the instrument strikes a thermopile that converts the heat into an electrical current, which in turn is recorded. The thermopile is shielded from convection with two glass domes, which also restrict the signal to wavelengths of between  $0.3 \mu\text{m}$  and  $3 \mu\text{m}$  without blocking the field of use. Beyond the clear domed pyranometers there are two red domed instruments that focus on different wavelengths of light. An example set of upwelling and downwelling results are shown in Figure 2.5 for the same cloud leg as in Figure 2.4. The downwelling radiation shown in Figure 2.5(a) ranges between  $100 \text{ W m}^{-2}$  and  $140 \text{ W m}^{-2}$  while the upwelling radiation varies between  $15 \text{ W m}^{-2}$  and  $45 \text{ W m}^{-2}$ .



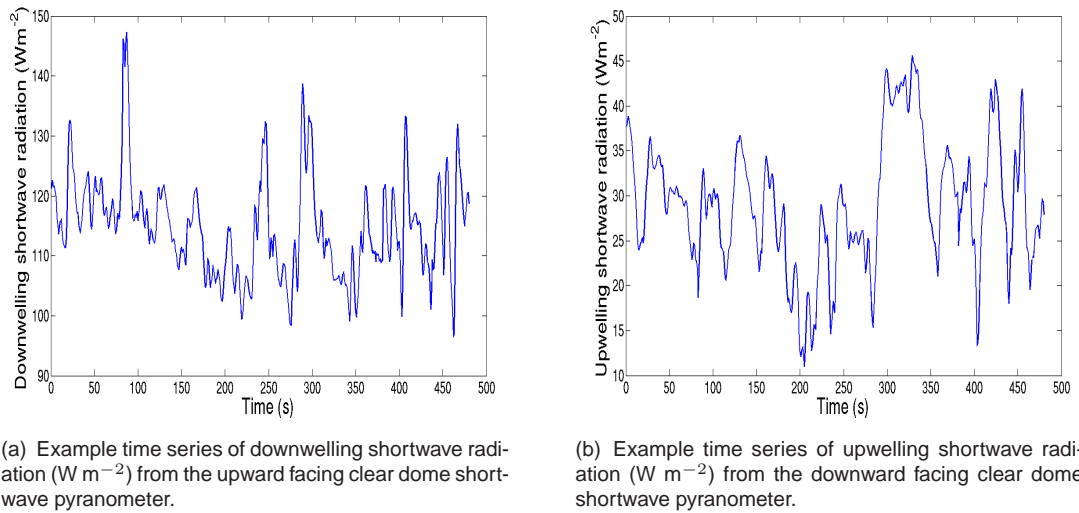


FIGURE 2.5: Example output data from the shortwave pyranometers using data recorded during the VOCALs-REx field campaign. The data used in this plot was recorded during Flight B417, which occurred on 9<sup>th</sup> November 2008.

### 2.3.3 2D-S Droplet Imager

The 2D-S Droplet Imager is either a mono or stereo probe designed to observe small particles such as cloud droplets. The mono version of the 2D-S operates in a similar manner to the CDP described in Section 2.3.1. The stereo version of the 2D-S has two orthogonal beams which cross at the detection point (Lawson et al., 2006). The stereo system is designed to ignore any events when only one beam is interrupted ensuring that all recorded events are stereo. The 2D-S is capable of generating images and recording numeric data. An image showing the 2D-S system for removing events which interrupt only one beam is shown in Figure 2.6. As can be seen from Figure 2.6 the instrument has a threshold of interference required to register a reading. Only the event shown in Figure 2.6 (a) will be recorded in the final output, while the two coincident small particles in Figure 2.6 (b) are too small to overcome the threshold. The large particle in Figure 2.6 (c) is only incident on one photodiode array and therefore is ignored by the stereo instrument (Lawson et al., 2006). For the VOCALs-REx campaign the 2D-S instrument operated with 200 size bins ranging from  $15 \mu\text{m}$  to  $2005 \mu\text{m}$  in a mono configuration.



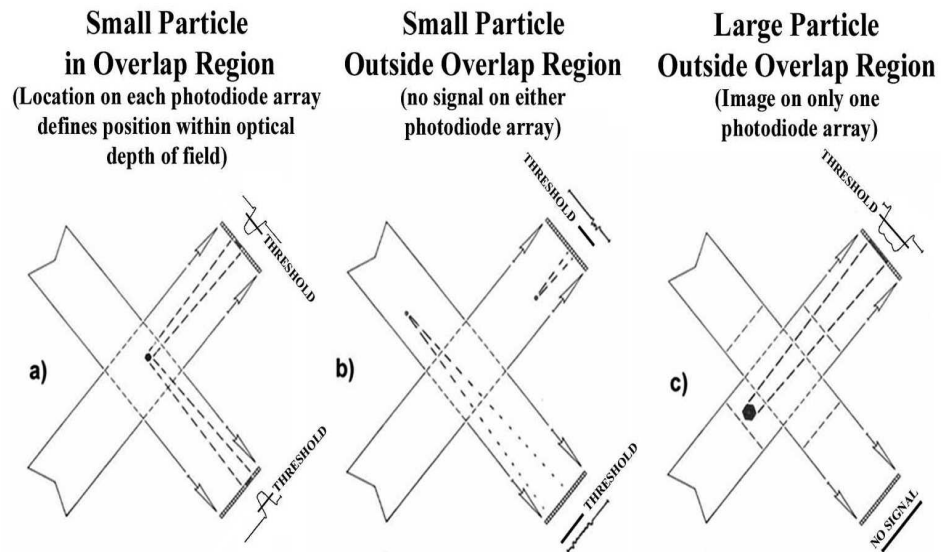


FIGURE 2.6: The logic system used in the stereo 2D-S droplet imager for particles passing through both laser beams. Image copied from Lawson et al. (2006).

### 2.3.4 Flight legs

The BAe-146 is equipped with both optical and microphysical sensors and a comparison between albedos derived from both, while in-cloud is attempted. During the campaign each flight leg took 10 minutes to allow use of the VACC instrument. Each cloud is defined as a period of time where the BAe-146 is recording microphysical data for a minimum of 5 minutes; 19 such clouds are identified. The clouds are then refined to remove polluted data, broken cloud or events without satellite photos. Each of the clouds and the reason for any removal of data is included in Table 2.1. The data from flights B408, B409, B410, B412, B413, B414 and B418 are rejected for a variety of reasons. Flights investigating pollution are not suitable for analysing clean clouds (B413, B418). The presence of sulphate in the Aerosol Mass Spectrometer (AMS) indicated coastal air parcels which are more likely to be polluted and therefore B408 is rejected. Missing satellite, shortwave radiometric or microphysical (2D-S) data requires the rejection of data from flights B410, B412, B413 and one leg of flight B417. Two legs of flight B419 are rejected as they are in regions of broken cloud and cloud legs of sufficient length are not possible. The

Flight	Start time (s)	End time (s)	Thickness (m)	Removal reason
B408	12975	13645	263.8	Sulphate in AMS
B408	15506	16202	359.4	Sulphate in AMS
B408	19371	20102	316.5	Sulphate in AMS
B410	10578	11333	552.9	Bad SW data
B412	16719	17428	473.0	2D-S data missing
B412	18228	18959	419.2	2D-S data missing
B413	20552	21200	267.6	Pollution flight
B413	22674	23331	262.2	Pollution flight
B414	18068	18728	319.0	No GOES data
B417	13319	14144	558.9	Bad SW data
B417	15504	16184	464.6	<b>Good data</b>
B417	18058	18769	523.1	<b>Good data</b>
B418	14237	15071	445.7	Pollution flight
B418	12534	13227	364.7	Pollution flight
B418	23034	24049	226.4	Pollution flight
B419	10148	10492	151.7	Broken cloud
B419	11962	12672	394.6	Broken cloud
B419	14072	15422	402.3	<b>Good data</b>
B419	16250	17565	428.2	<b>Good data</b>

TABLE 2.1: Clouds investigated by the BAe-146 during the VOCALs-REx field campaign. Start and end times are in seconds and relative to the start time of the flight data. Cloud thickness is approximated by taking the height difference between the top and bottom of the cloud from CDP data.

remaining four flight legs, two each from flights B417 and B419 are selected as good data and used in the comparisons in Sections 2.3.6, 2.3.7 and 2.3.8.

With four clean clouds identified they are further refined to remove large changes in altitude, which involved removing the start and end of the sections flight legs. An image showing the data retained and removed from one flight leg is shown in Figure 2.7. As is shown in Figure 2.7 the final flight leg is much flatter than a leg covering the entire length of the in-cloud run. The four in-cloud flight runs with good data are shown in Table 2.2. A satellite photo from the GOES-10 1 km visible radiation channel for each of the four clean cloud events is shown in Figure 2.8, where the flight leg is shown in red. For each cloud the shortwave albedo is assumed to be the ratio of downwelling to upwelling shortwave radiation. The microphysical albedo is derived using a method described in Twohy et al. (2005) based upon

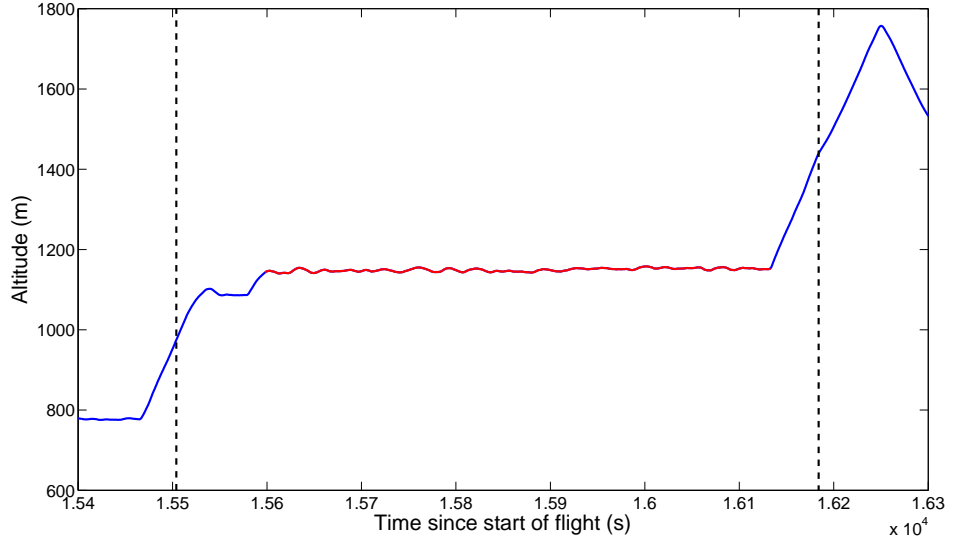


FIGURE 2.7: An altitude track of an example flight leg, where the analysed data is shown in red. The altitude track outside the analysed region is in blue and the cloud start and end times are indicated by dashed black lines.

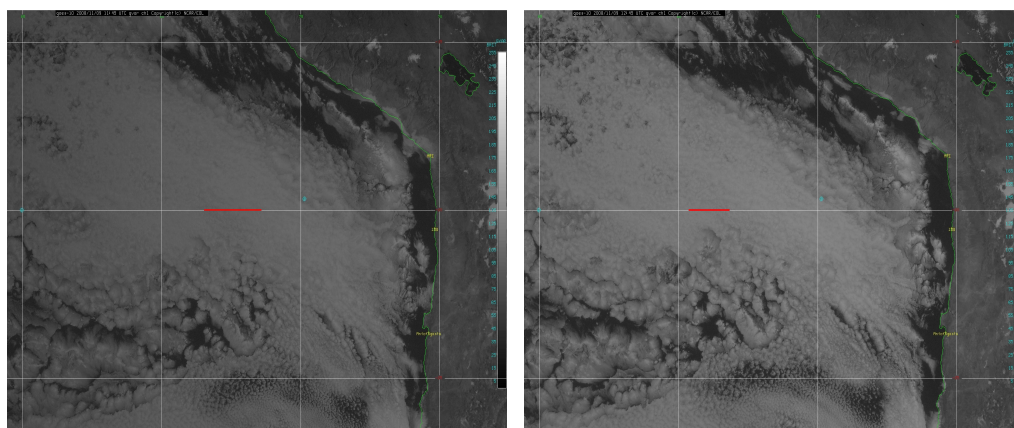
Flight	Start time (s)	End time (s)	Thickness (m)
B417	15598	16133	464.6
B417	18136	18739	523.1
B419	14191	15396	402.3
B419	16311	17521	428.2

TABLE 2.2: Clean cloud subset analysed in the albedo investigation. All fields are the same as in Table 2.1.

the Eddington approximation. The microphysical albedo derivation is described in Section 2.3.5.

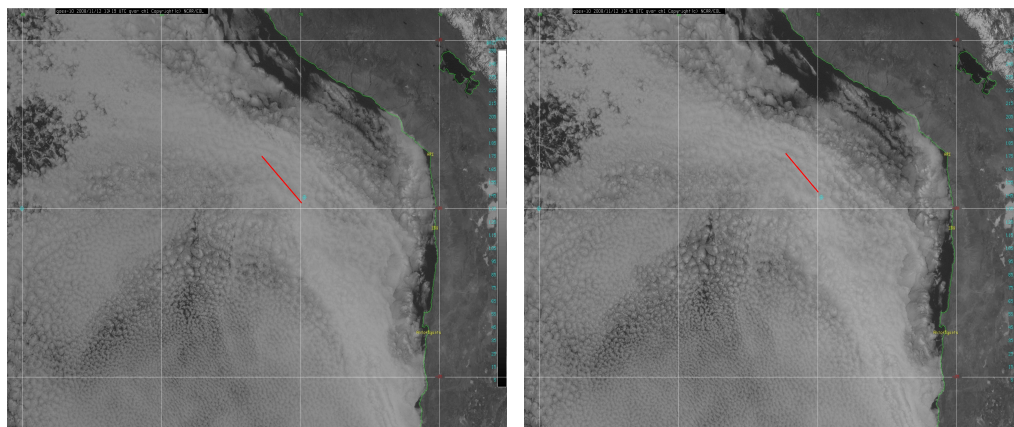
### 2.3.5 Microphysical albedo calculation

The microphysical albedo ( $A_c$ ) is calculated using Equation 2.4 which is a result of combining and evaluating constants from Equation 2.2 and Equation 2.3, where  $\tau^*$  is the optical thickness, LWP is the liquid water path,  $\rho_w$  is the density of water,  $r_e$  is the effective radius and  $g$  is an asymmetry factor.



(a) Satellite photo from the GOES-10 visible radiation imager of clean cloud event 1, the satellite photo was recorded at 11:45 UTC on 9th November 2008. The flight track of the BAe-146 during the clean cloud event is shown in red.

(b) Satellite photo from the GOES-10 visible radiation imager of clean cloud event 2, the satellite photo was recorded at 12:45 UTC on 9th November 2008. The flight track of the BAe-146 during the clean cloud event is shown in red.



(c) Satellite photo from the GOES-10 visible radiation imager of clean cloud event 3, the satellite photo was recorded at 13:15 UTC on 12th November 2008. The flight track of the BAe-146 during the clean cloud event is shown in red.

(d) Satellite photo from the GOES-10 visible radiation imager of clean cloud event 4, the satellite photo was recorded at 13:45 UTC on 12th November 2008. The flight track of the BAe-146 during the clean cloud event is shown in red.

FIGURE 2.8: Satellite photos from the GOES-10 1 km visible radiation channel for four clean cloud events. The flight track from the BAe-146 is shown in red for the times shown in Table 2.2.

$$\tau^* = \frac{3LWP}{2\rho_w r_e} \quad (2.2)$$

$$A_c = \frac{0.75(1-g)\tau^*}{1 + 0.75(1-g)\tau^*} \quad (2.3)$$

$$A_c = \frac{\frac{9(1-g)}{8} \frac{LWP}{\rho_w r_e}}{1 + \frac{9(1-g)}{8} \frac{LWP}{\rho_w r_e}} \quad (2.4)$$

Each equation is dependent on a set of assumptions and requirements that need to be met for the result to be valid. In Equation 2.2 the liquid water path is assumed to be constant across the depth of the cloud and the droplets are assumed to be uniform in size and shape (Stephens, 1978). In this work the liquid water path is assumed to be the liquid water content multiplied by the cloud depth. The cloud depth is found by taking the difference between the highest and lowest altitude where the CDP is recording data. As this requires the aircraft to pass through the entire cloud this reduces the number of clouds available in Table 2.2. The Eddington approximation is shown in Equation 2.3 with an asymmetry factor of 0.85 (Twohy et al., 2005). The Eddington approximation is shown to be weak at high values of  $\tau^*$ . However as the nature of the clouds in question results in low values of  $\tau^*$ , the equation is found to be suitable.

### 2.3.6 Satellite - Aircraft albedo comparison

Data is collected from satellites during the campaign including GOES-10, Terra and Aqua. The MODIS instrument is mounted on the Terra and Aqua satellites, however the satellites were not over the VOCALs-REx region for the clean clouds described in Table 2.2. The remaining source of data used is the GOES-10 satellite, a geostationary satellite based at 0° N and 60° W. The data from the satellite covers a non-Cartesian grid and images take several minutes to be recorded. With this in mind data is extracted as close as possible in time and space to the clean clouds. As a result of the relatively coarse non-Cartesian satellite grid the BAe-146 results

are averaged over several points to enable a comparison. The results of this comparison are shown in Figure 2.9 and it can be seen that there is very little agreement between the aircraft shortwave albedo and the GOES-10 albedo. The equation of the dashed line in Figure 2.9 is shown in Equation 2.5. Possible reasons for the poor correlation include the difficulty in aligning two separate grids and the time lag between the start and end of the satellite image. The satellite did not take the whole image at once, instead it focused on specific points and recorded the data before realigning on the next point. Therefore it is possible that the BAe-146 may not be in the clean cloud region while the image is being recorded. Furthermore the GOES-10 albedo is a broadband albedo and not a narrowband shortwave one and thus will take into account longwave emissions, which are not recorded by the shortwave radiometers used on the BAe-146.

$$A_{SW} = -0.12A_{GOES} + 0.60 \quad (2.5)$$

$$R^2 = 0.0319 \quad (2.6)$$

### 2.3.7 Aircraft shortwave - CDP albedo comparison

A comparison of the albedo from the shortwave radiometers and the CDP is shown in Figure 2.10. Uncertainties in the shortwave albedo are shown as three standard deviations from the mean value. Several assumptions are made in Equation 2.4 which extend the uncertainty of the result. Both the effective radius and the liquid water content carry uncertainties that have to be propagated through the parametrisation. Furthermore the assumption that the liquid water path is equal to the liquid water content multiplied by the thickness leads to a large uncertainty. This is exacerbated as the thickness is only found once and is based on two readings which are several minutes apart. As a result of these assumptions a 20 % uncertainty in the optical thickness is passed through to the final result. The line of fit between

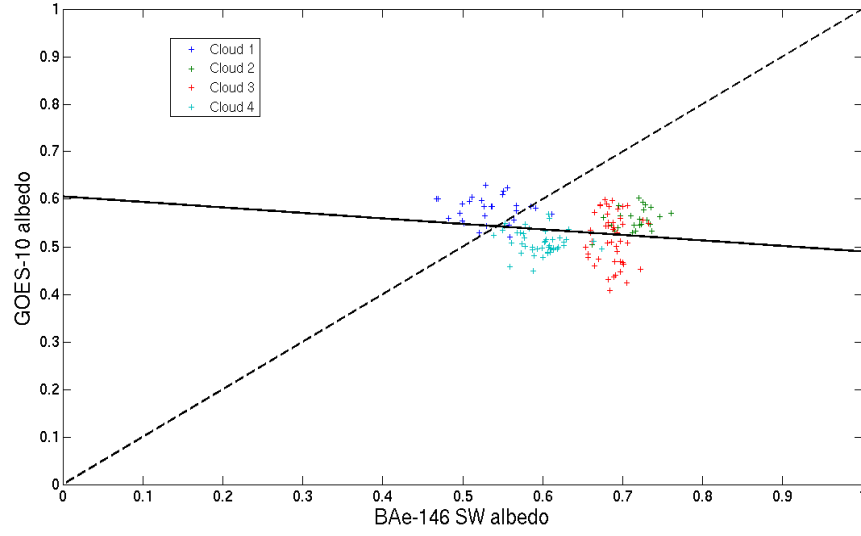


FIGURE 2.9: A comparison between GOES-10 satellite albedo and the shortwave albedo from the BAe-146 during the VOCALs-REx field campaign. Data is from four clean clouds described in Table 2.2. The dashed black line shows a 1:1 relationship.

the results is shown in Equation 2.7. Despite the large uncertainties in the results there is a good correlation found for data based on Equation 2.4 with a  $R^2$  value of 0.87.

$$A_{CDP} = 0.53A_{SW} + 0.38 \quad (2.7)$$

$$R^2 = 0.87 \quad (2.8)$$

The albedo approximation shown in Equation 2.3 has an asymmetry factor of 0.85 however the CDP described in Section 2.3.1 uniformly reflective particles. As the results are both dependent on the asymmetry factor and the time averaging used, a short investigation is performed on the optimum asymmetry and time averaging. Time averaging allows the removal of extremely short scale or short lifetime events, while increasing the asymmetry factor produces more uniformly reflective particles as expected by the CDP. An exploration of the ‘time averaging - asymmetry factor’ vector space is shown in Figure 2.11. The asymmetry factor varies between



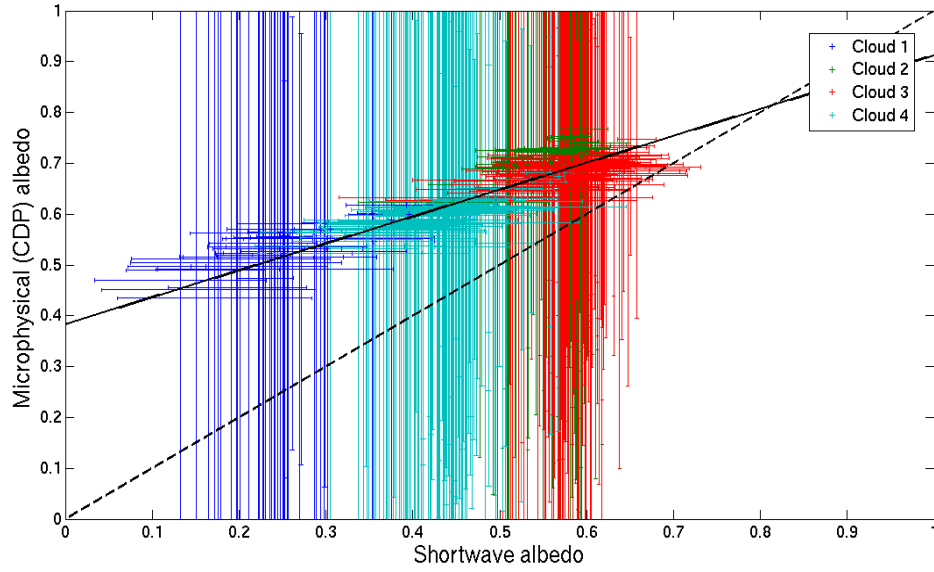


FIGURE 2.10: A comparison between CDP microphysical albedo ( $g = 0.85$ ) and the shortwave albedo from the BAe-146 during the VOCALs-REx field campaign. Data is from four clean clouds described in Table 2.2. All results are ten second averages. The dashed black line shows a 1:1 relationship.

0.70 and 0.95 in steps of 0.01 while the time averaged over is varied between 10 seconds and 30 seconds with 1 second intervals. The aim of the exploration is to optimise the gradient of the line of fit shown in Equation 2.7. The results in Figure 2.11 show that the asymmetry factor should be set to 0.91 to find a balance between the original equation from Twohy et al. (2005) and the assumptions of uniformly reflective particles used in the CDP instrument. The time averaging of 12 seconds is also found to be optimal.

An updated version of Figure 2.10 with the new asymmetry factor and time averaging is shown in Figure 2.12. The equation of the line of fit on Figure 2.12 is displayed in Equation 2.9. The results in Figure 2.12 could be further improved with a more accurate measure of the cloud thickness, which in turn improves the estimate of the liquid water path, as this is the greatest source of error. The results in Figure 2.12 slightly reduce the quality of the correlation from  $R^2 = 0.87$  in Figure 2.10 to  $R^2 = 0.86$  in Figure 2.12.

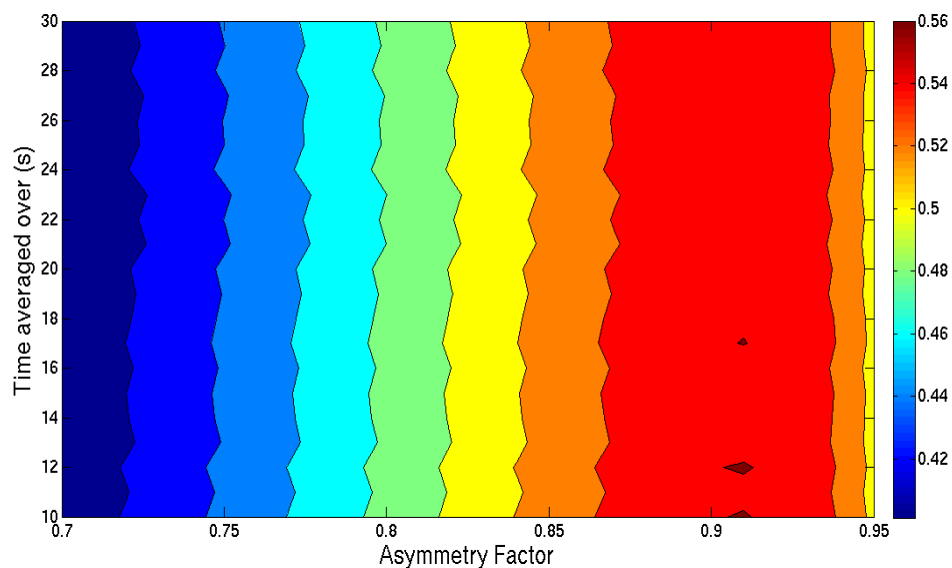


FIGURE 2.11: Investigation into the optimal asymmetry factor 'g' and averaging time for use in Equation 2.3. Darker colours indicate an increase in the gradient of the line of the best fit as shown in Figure 2.10.

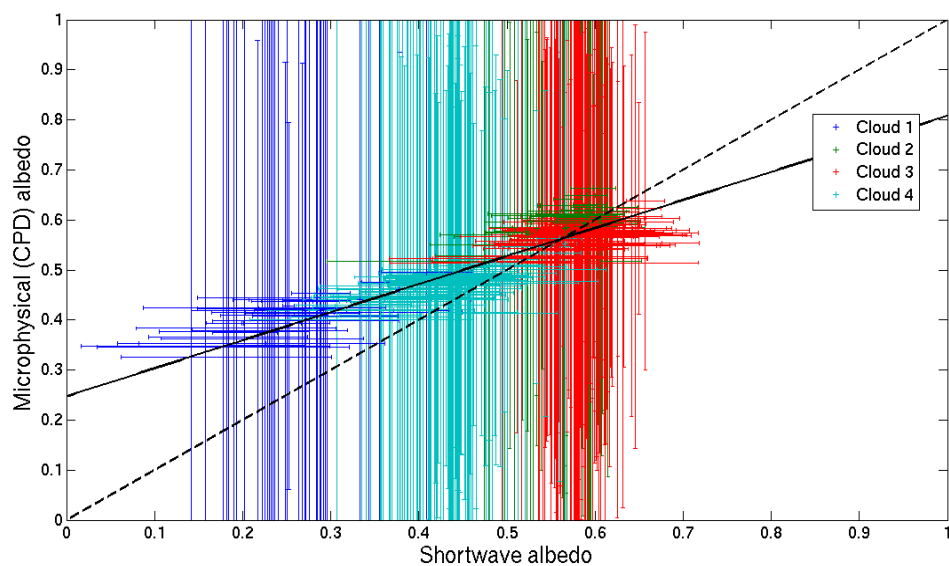


FIGURE 2.12: As Figure 2.10 with an updated microphysical albedo calculation using data shown in Figure 2.11. The new equation has an asymmetry factor ( $g = 0.91$ ) and averages data over 12 second blocks.

$$A_{CDP} = 0.56A_{SW} + 0.25 \quad (2.9)$$

$$R^2 = 0.86 \quad (2.10)$$

### 2.3.8 Aircraft shortwave - 2D-S albedo comparison

The method used to calculate the microphysical albedo from the CDP data is reused with the 2D-S data, (see Section 2.3.3). The formulation used is the same as when using the CDP data shown in Equation 2.4. As the same approach is used the assumptions in Section 2.3.7 are reused. The first few channels of the 2D-S are found to be noisy and therefore are removed from the calculation, the smallest size bin analysed is the  $35 \mu\text{m}$  bin. The initial results from an investigation into the use of the 2D-S derived microphysical albedo are shown in Figure 2.13. It can be clearly seen that the clouds are in two different regimes, above and below the 1:1 dashed line. The regimes correspond to two different flights on different days. Therefore the flight days are separated and are shown in Figure 2.14. The equations of the black lines shown in Figures 2.14(a) and 2.14(b) are shown in Equations 2.11 and 2.13. The results from Figure 2.14 indicate that further work is required to find a suitable method for calculating the microphysical albedo within clouds using the 2D-S instrument. The current method does appear to be able to find well correlated ( $R^2$  values above 0.8 in both cases) data for two days but it is unsuitable for identifying an equation for use across an entire campaign or as a general case.

$$A_{2D-S} = 0.55A_{SW} + 0.38 \quad (2.11)$$

$$R^2 = 0.94 \quad (2.12)$$

$$A_{2D-S} = 0.59A_{SW} - 0.013 \quad (2.13)$$

$$R^2 = 0.90 \quad (2.14)$$

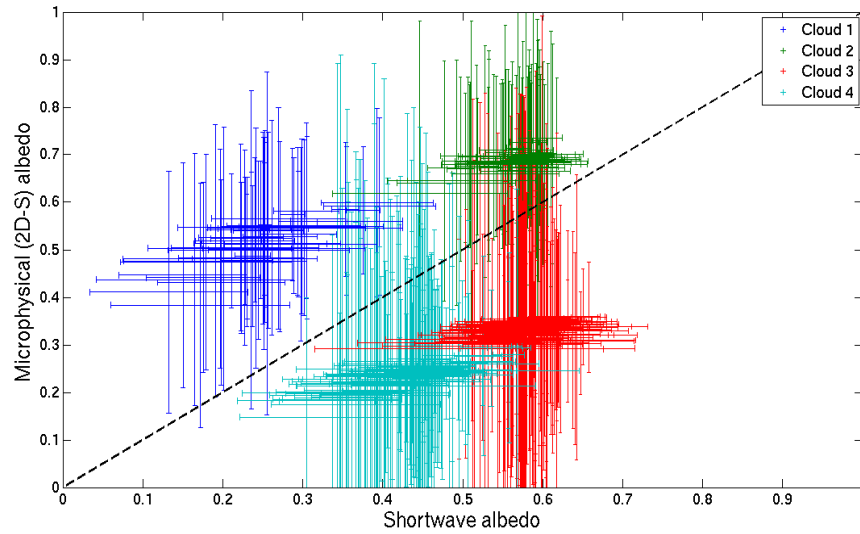
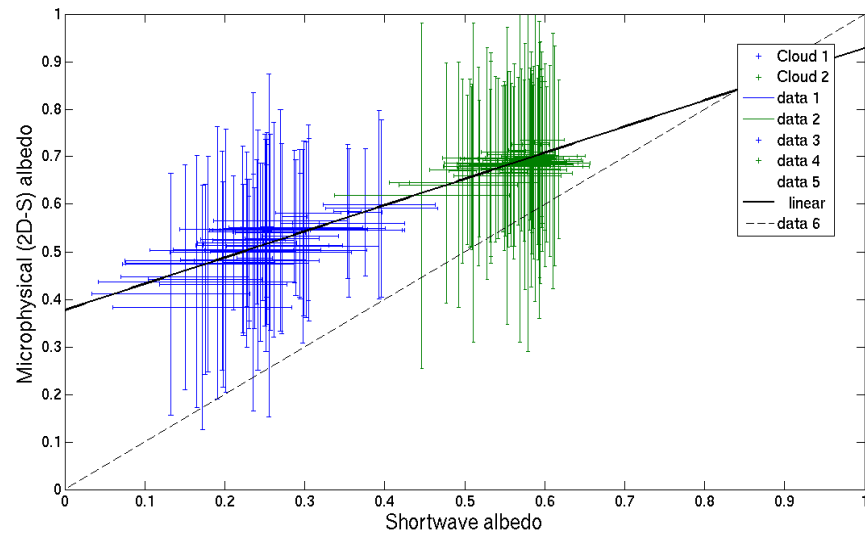


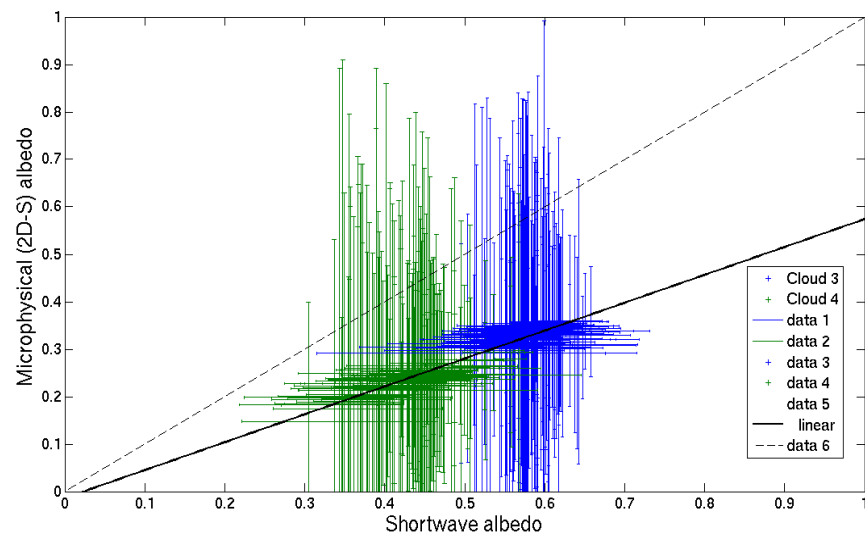
FIGURE 2.13: As Figure 2.10 but for results from the 2D-S droplet imager.

## 2.4 Cloud droplet number concentration - shortwave albedo comparison

The work described in Twomey (1977) suggests that increasing the cloud droplet number concentration increases the optical depth and thus the cloud albedo. The principle used in MCB is that the cloud albedo could be artificially enhanced by increasing the CDNC in set regions (See Section 1.4.3.5). The results shown in Figure 2.15 from both the CDP (Figure 2.15(a)) and the 2D-S (Figure 2.15(b)) show that the shortwave albedo does increase with increasing CDNC. The 2D-S operates over a large size range and indicates that a maximum albedo is reached at a concentration close to  $250 \text{ cm}^{-3}$ , however the maximum remains the same to concentrations of over  $300 \text{ cm}^{-3}$ .

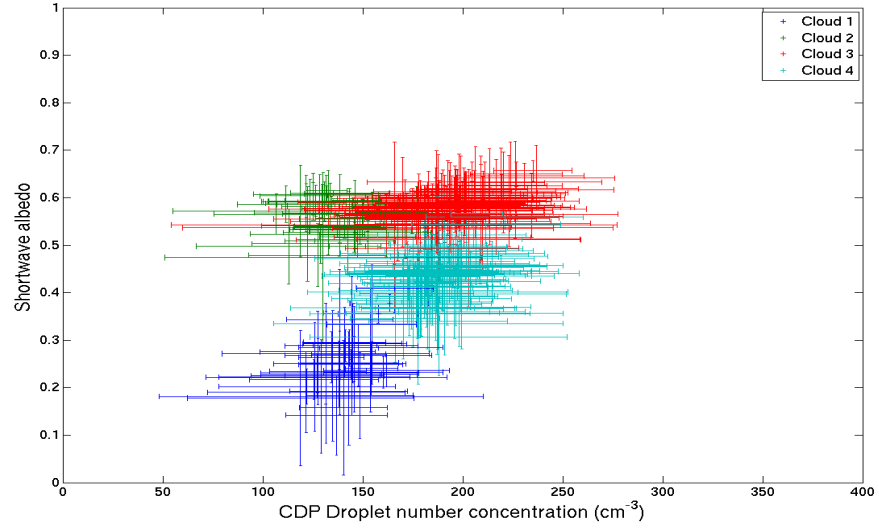


(a) As Figure 2.13 showing Clouds 1 and 2 which were recorded during research flight B417. The equation of fit is shown in Equation 2.11.

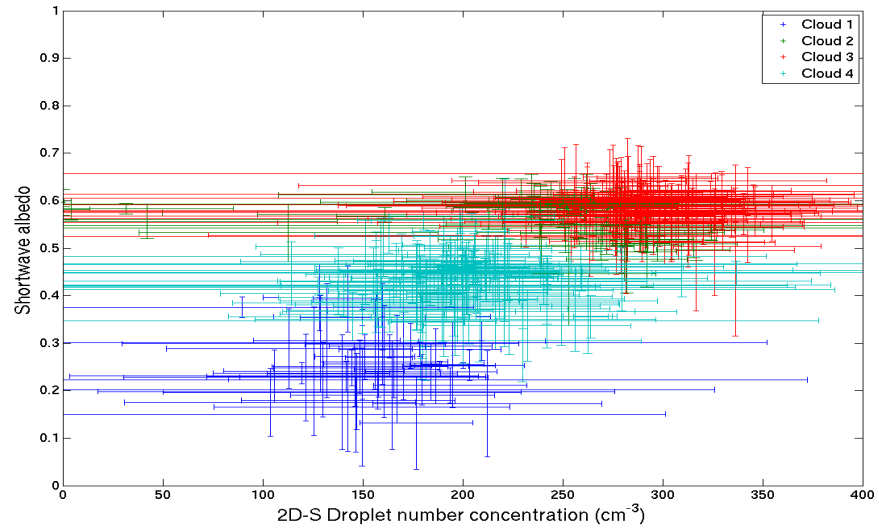


(b) As Figure 2.13 showing Clouds 3 and 4 which were recorded during research flight B419. The equation of fit is shown in Equation 2.13.

FIGURE 2.14: As Figure 2.10 showing results from the 2D-S droplet imager for two separate research flights.



(a) A comparison between the CDP droplet number concentration ( $\text{cm}^{-3}$ ) and the shortwave albedo from the BAe-146 during the VOCALs-REx field campaign. Data is from four clean clouds described in Table 2.2.



(b) A comparison between the 2D-S droplet number concentration ( $\text{cm}^{-3}$ ) and the shortwave albedo from the BAe-146 during the VOCALs-REx field campaign. Data is from four clean clouds described in Table 2.2.

FIGURE 2.15: A comparison between the number concentration ( $\text{cm}^{-3}$ ) from two microphysical instruments Figure 2.15(a) the CDP and Figure 2.15(b) the 2D-S, and the shortwave albedo from the BAe-146 during the VOCALs-REx field campaign. Data is from the four clean clouds described in Table 2.2. All results are ten second averages.

## 2.5 Summary

This chapter has provided an initial investigation into the albedo of stratocumulus clouds found in the South East Pacific during the VOCALs-REx field campaign. The NERC Dornier 228 provides a large quantity of data, despite this there are difficulties in completing the analysis. If numerical data could be derived from the Dornier 228 radiances then an investigation of multiple aircraft cross over events, looking at both radiometric and microphysical data, would be possible. The MODIS satellites are not used in Section 2.3.6 as there are no events where the BAe-146 is in cloud during a satellite overpass. However work by Painemal and Zuidema (2011) finds several events where the NCAR C-130 is in cloud during a MODIS overpass. The results from Painemal and Zuidema (2011) find that MODIS generally overestimates the effective radius of cloud droplets and this is reflected in the derived liquid water path.

It is possible to generate microphysical and shortwave radiative albedos using data recorded on the FAAM BAe-146 aircraft. The shortwave albedo is calculated from the ratio of upwelling and downwelling shortwave radiation measured using clear domed pyranometers. The computed microphysical albedo is based on several assumptions including the shape of droplets and a uniform distribution of water within a cloud (Stephens, 1978; Twohy et al., 2005). A comparison between the shortwave radiative albedo and the satellite derived broadband albedo yielded poor correlation with a  $R^2$  value of 0.013. This result is attributed to the difference in resolution between the satellite and the aircraft in addition to the difficulties aligning the grids both temporally and spatially.

A comparison between the microphysical and shortwave albedo is made using pyranometers and two microphysical probes. The line of best fit for CDP results from four clean clouds is shown in Equation 2.7. An expansion on the result shown in Equation 2.7 involving the time and asymmetry parameters is undertaken and a plot of the vector space is shown in Figure 2.11. From this exploration a new set of parameters is found and the new line of best fit is shown in Equation 2.9. Improving



the gradient of the line of fit does however slightly reduce the quality of correlation between shortwave and microphysical albedos with the  $R^2$  value falling from 0.87 to 0.86 when the gradient increases from 0.53 to 0.56.

A second investigation using data from the 2D-S droplet imager splits the data in two. As shown in Figure 2.13 there are distinct differences in the microphysical albedo between flights B417 and B419. The results using two separate datasets, one for each flight show good correlation ( $R^2 > 0.8$ ). The splitting of the dataset into two separate flight days indicated that this method would be unsuitable for use over an entire field campaign or as a general case. There is an inherent issue using data collected from the CDP and 2D-S (mono configuration) with Equation 2.4; the instruments assume uniformly reflective data however the equation requires non uniform inputs.

MCB is based on the assumption that seeding clouds in remote marine regions would lead to an increase in the CDNC and thus the albedo. The work shown in Figure 2.15 supports the idea that increasing the cloud droplet number in unpoluted clouds, such as those away from continental coasts, leads to an increase in albedo. The results in Figure 2.15(a) show that in the case of the VOCALs-REx field campaign a maximum albedo is reached at a CDNC of about  $250 \text{ cm}^{-3}$ .

## **Chapter 3**

# **HadGEM1 model description**

The Hadley Centre Global Environment Model, generally known by the acronym HadGEM1, is version 6.1 of the Met Office Unified Model. HadGEM1 is described in three papers- Johns et al. (2006); Martin et al. (2006); Ringer et al. (2006) each of which references several other publications that detail the many schemes used in the model. HadGEM1 is the successor to the HadCM3 model (Martin et al., 2006) and precedes HadGEM2. HadGEM1 is the coupled model comprising HadGAM and HadGOM the Global Atmosphere and Global Ocean Models respectively. The differences between the atmospheric components of HadCM3 and HadGEM1 are shown in Appendix A. HadGEM1 is used in the IPCC 4th Assessment report (Forster et al., 2007) as one of the many models used to simulate potential climate scenarios.

## **3.1 Components of HadGEM1**

### **3.1.1 Dynamics**

One major modification to previous versions of the model is the inclusion of a new dynamical core described by Davies et al. (2005). The new dynamics also brought

in the use of a higher resolution for the model, doubling the number of grid points in latitude, longitude and altitude. HadGEM1 runs at an atmospheric resolution of  $1.25^\circ$  latitude and  $1.875^\circ$  longitude with 38 unevenly spaced vertical levels ranging in size between 20 m and 7 km with a lid at about 39 km. The main features of the dynamical core in HadGEM1 are described in Davies et al. (2005).

The atmosphere is described as nonhydrostatic and fully compressible. Nonhydrostatic means that the atmosphere in the model is not required to follow the equation for hydrostatic equilibrium  $\frac{\partial P}{\partial z} + \rho g = 0$ . Hydrostatic equilibrium is found when a parcel of a fluid is held stationary by the forces above and below it, in this case the weight of the fluid above, the weight of the parcel itself and the upwards pressure of the fluid below. Fully compressible means the density of the fluid, in this case the atmosphere is able to change (e.g. with pressure).

The model grid is terrain following, which means that the lowest levels of the model will not be at the sea-level but at the level of the terrain at that grid point. The orography is at 1 degree resolution and is based on the GLOBE data set (Martin et al., 2006). The differences between the terrain heights are smoothly reduced until the model top which is of uniform height.

In HadGEM1 horizontal data is based on an Arakawa C-grid (Arakawa and Lamb, 1977). An Arakawa C-grid is a grid with the zonal winds, meridional winds and thermodynamics all staggered and is found to work well with semi-implicit time stepping and gives the best geostrophic adjustments for atmospheric flows (Martin et al., 2006). The vertical grid is a Charney Phillips grid where the momentum and thermodynamics are staggered (Martin et al., 2006). Semi-Lagrangian advection is designed to take advantage of features of Lagrangian and Eulerian advection schemes. Eulerian schemes evaluate change from a fixed grid point but are vulnerable to computational instabilities. To prevent these instabilities requires a short time step and increases computational costs. In contrast Lagrangian advection evaluates change while moving with one of the changing properties, such as a particle of a fluid. This is more stable but leads to an uneven distribution of information.

The mixture of a regular grid from Eulerian advection and the long time steps of Lagrangian advection is desirable and reduces computational costs (Davies et al., 2005). The time step of the model is constrained by computational requirements, the desired accuracy of the model, the resolution of the model and the parametrisations used in the model (Davies et al., 2005).

### **3.1.2 Radiation**

The radiation code used in HadGEM1 is similar to the code used in HadCM3 with several small updates (Martin et al., 2006). A decision made during the formulation of the radiation code is that it should be available for use independently of the model (Edwards and Slingo, 1996). The radiation code runs in a two stream mode for both longwave and shortwave radiation. A two stream mode is one where the radiation is calculated in two distinct directions, downwards and upwards.

### **3.1.3 Microphysics and Precipitation**

The microphysics and precipitation scheme used within HadGEM1 is described in Wilson and Ballard (1999). The scheme is a mixed phase scheme with water split into the four following categories: liquid water, water vapour, ice and rain. The transfers between these categories are controlled by physical equations which contain particle size information (Martin et al., 2006). The precipitation scheme takes several inputs from the model including temperature; and ice water, liquid water and water vapour mixing ratios. Ice contains information on both snow and hail within the model. Precipitation is calculated from a sequential series of processes that are initiated by ice falling from one level to another and ending with autoconversion from liquid water to rain. The processes are shown in Figure 3.1 and their transfer terms are detailed in the appendix of (Wilson and Ballard, 1999).

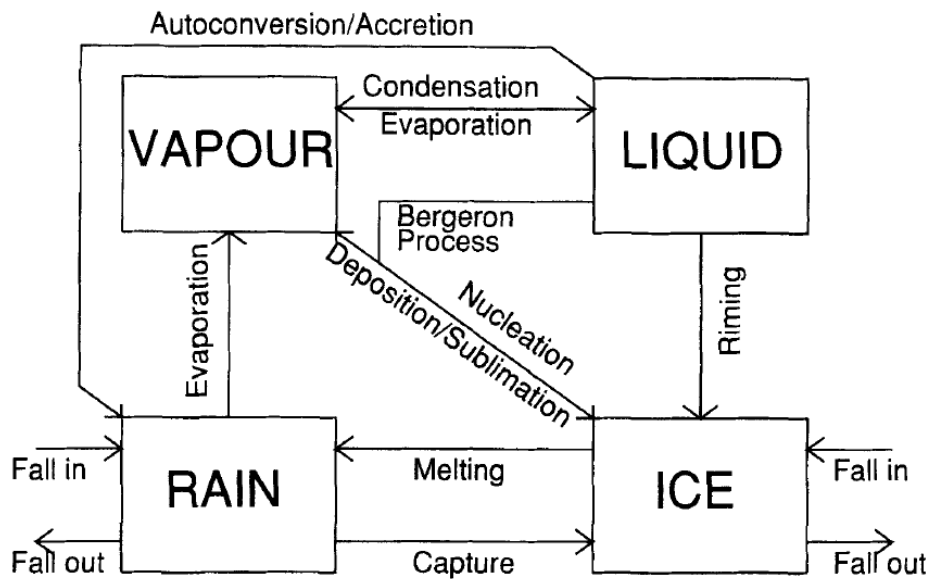


FIGURE 3.1: A diagram of the scheme used within HadGEM1 to move water within the atmosphere system. Boxes show the four phases of water within the model and arrows show the transfer mechanisms simulated. Image copied from Wilson and Ballard (1999).

### 3.1.4 Aerosol Processes

Aerosols in the model include an interactive sulphate scheme, a simple sea salt scheme, a biomass burning scheme and a black carbon scheme (Martin et al., 2006). The interactive sulphate scheme and the simple diagnostic sea salt scheme are described in Jones et al. (2001). The number of sea-salt aerosol particles is determined by the wind-speed at 10 m above the sea surface and exponentially falls with height. The sulphate scheme is much more detailed than the sea salt scheme and contains both dimethyl sulphide and sulphur dioxide oxidation terms in addition to both dry and wet deposition. Two size bins of aerosol are used within the model; small (associated with Aitken mode) and large (for accumulation mode) with radii of 24 nm and 95 nm respectively. Black Carbon (BC) within the model is represented by three quantities. The BC is either ‘Fresh’, ‘Aged’ or ‘Within cloud’. The BC is aged to show the changes as a result of oxidation or the addition of hygroscopic materials. Fresh or Aged BC is not subject to wet deposition but can be captured by cloud droplets and then precipitated out (Roberts and Jones, 2004).

The biomass burning scheme in HadGEM1 is very similar to the BC scheme (Martin et al., 2006). Particle sizes, and tracers for emissions from biomass burning are described in Davison et al. (2004). Within the biomass burning scheme the particles progress from ‘Fresh’ to ‘Aged’, as with the BC scheme the biomass particles are assumed to be hydrophobic but able to be scavenged by cloud droplets. Both the first and second indirect effect of aerosols on climate are modelled within HadGEM1 (see Section 1.3.3 for a description of the first and second indirect effects).

### **3.1.5 Boundary layer**

The boundary layer scheme contains adiabatic conservation of variables and is described in detail in Lock (2001). The convective boundary layer is considered well mixed as a result of constantly overturning thermal currents. The diurnal cycle within the model is found to be weak, while being strongly influenced by solar radiation. In previous work if an air parcel were to subside from the free troposphere it would appear to push an unresolved inversion into a lower grid box. This appears to cause a drying of the boundary layer and have a significant impact on the representation of stratocumulus clouds. The new subsidence scheme balances moisture more successfully and in turn improves the model ability to show stratocumulus cloud layers. The model is tested at the resolution used by HadCM3 and is found to be closer to reality while still requiring further work to accurately represent stratocumulus clouds. The model is able to show the breakup of a stratocumulus deck into trade cumulus (Lock, 2001).

### **3.1.6 Convection**

The convection scheme within the model is used to represent the motion of air parcels. As the model grid size is significantly larger than individual clouds the clouds are parametrised into a convection scheme. The scheme is based on a heavily modified version of a mass flux scheme detailed in Gregory and Rowntree

(1990). In the case of convection appearing in the model the boundary layer is capped at the cloud base and a mass flux scheme is used (Martin et al., 2006).

### 3.1.7 Ocean

The ocean model within HadGEM is coupled to the atmosphere to allow feedbacks of temperature, ice content and evaporation to be utilised in more detail. Coupling of the atmosphere and ocean models is described in Johns et al. (2006). The ocean model has a resolution of  $1^\circ$  zonally everywhere and  $1^\circ$  meridionally between  $30^\circ$  and the poles. In the region between  $30^\circ$  N and  $30^\circ$  S the resolution increases towards the equator where it reaches  $\frac{1}{3}^\circ$ . The vertical grid of 40 levels has spacings of 10 m near the surface and increasing to 345 m in the deep ocean to a maximum depth at 5.4 km. The increase in oceanic resolution from HadCM3 to HadGEM1 leads to an improved bathymetric map. Where the resolution of the ocean obstructs a narrow channel it is artificially opened to give a more realistic representation.

With the differing resolutions of the atmosphere and the ocean, the data have to be interpolated to move from one to the other. Fluxes from land, ocean and sea ice are computed independently and then weighted to generate a grid box leading to a blurred coastline (Johns et al., 2006).

## 3.2 Comparison with datasets

A comparison of model and observational results allows insights into the strengths and weaknesses of the model. The comparison in this section is performed in addition to the work undertaken by model developers. For this comparison the annual average sea surface temperature (SST) and precipitation fields are used and the model is based on a working configuration with the atmospheric carbon dioxide concentration set to 379 ppm, which was the mean over the time for analysis.. The



model is run for 10 years under 2010 conditions, with lowered carbon dioxide levels and the average over the 10 years analysed.

### 3.2.1 Sea surface temperature

The sea surface temperature field is an output that the model produces directly and the comparison data is available from NOAA Physical Sciences Division<sup>1</sup>. The derivation of the data is explained in Reynolds et al. (2002). The original dataset requires interpolation from 1° resolution to match the model resolution detailed in Section 3.1.1. The global average sea surface temperatures are 291.1 K and 291.5 K for the model and observations respectively. As can be seen from Figure 3.2 large portions of the oceans are within 2 K of the recorded data. In the northern hemisphere there are issues near the Gulf Stream and the Kuroshio Current. There are several issues near Western coasts where the model is warmer than the dataset. The model is warm at the Chilean coast which would indicate El Niño conditions. However the majority of the southern Pacific exhibits La Niña behaviour with cooler tropics north of warmer subtropics, particularly between 120° W and 180° W.

### 3.2.2 Precipitation

Precipitation is a complex quantity within the model and has to be parametrised to account for subgrid scale events. The CPC Merged Analysis of Precipitation (CMAP) dataset is generated using several satellite sources and NCEP/NCAR re-analysis data. A full description of the derivation of the dataset can be found in Xie and Arkin (1997). As is shown in Figure 3.3 the model can be seen to struggle across much of the tropics and also near mountainous coasts. However the model is within 1 mm/day for large portions of the globe. The model is on average 0.4 mm/day wetter than the CMAP dataset with a globally averaged precipitation rate

---

<sup>1</sup>[www.esrl.noaa.gov/psd/data/gridded/data.noaa.oisst.v2.html](http://www.esrl.noaa.gov/psd/data/gridded/data.noaa.oisst.v2.html)

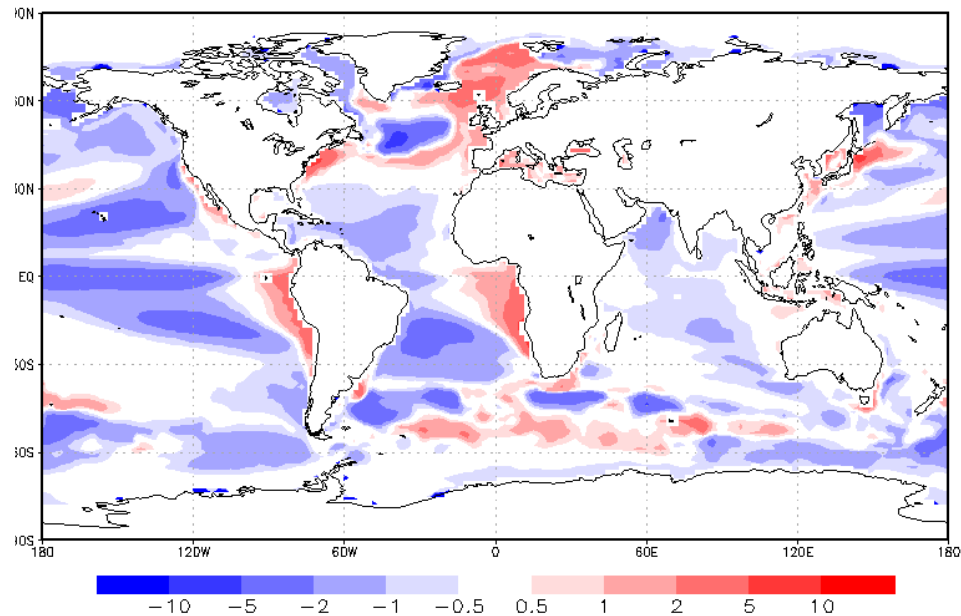


FIGURE 3.2: Difference between HadGEM1 and NOAA recorded annual average sea surface temperature (K).

of 3.12 mm/day compared to 2.78 mm/day from CMAP. The model appears to under predict rainfall in monsoon regions such as India, the northern Amazon and the Sahel. The model is also drier than CMAP over Antarctica which would result in lower snowfall and may impact on local temperatures.

### 3.3 Summary

In this chapter the HadGEM1 global climate model is introduced. HadGEM1 is the successor to the HadCM3 climate model and contains several major and minor changes (Martin et al., 2006). Major changes within the model include a new dynamical core, new aerosol parametrisation and boundary layer schemes. The new dynamical core in HadGEM1 doubles the horizontal and vertical resolution of the model which leads to an increase in number of grid cells by a factor of eight when compared with HadCM3 (Martin et al., 2006). The radiation scheme is based on the Edwards - Slingo code after a modification which allows faster computation (Cusack et al., 1999; Edwards and Slingo, 1996). The cloud microphysics, precipitation

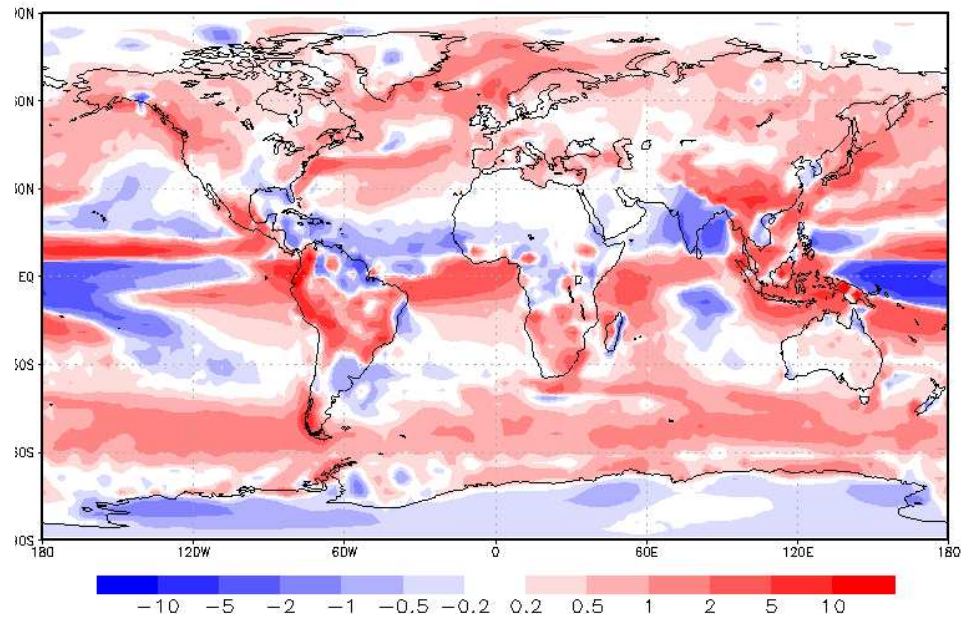


FIGURE 3.3: Difference between HadGEM1 model annual average precipitation and CMAP observed and modelled precipitation (mm/day).

and convection schemes are parametrised (Gregory and Rowntree, 1990; Wilson and Ballard, 1999).

The atmosphere within HadGEM is coupled to an ocean model which runs at a significantly higher resolution. This resolution difference leads to a blending of grid boxes where atmospheric and ocean fields interact (Johns et al., 2006). The HadGEM1 model is run at an atmospheric resolution of  $1.25^\circ$  latitude and  $1.875^\circ$  longitude with an uneven vertical grid of 38 levels which has a lid at 39 km. The oceanic resolution is  $1^\circ$  zonally everywhere and  $1^\circ$  meridionally between  $30^\circ$  and the poles. In the tropics the meridional resolution increases smoothly to  $\frac{1}{3}^\circ$ .

An example simulation from the HadGEM1 model is compared with long term observational datasets for both sea surface temperature and precipitation. The example shows several regions where the model struggles to replicate recorded data. However there are also large areas where the model performs well.

## **Chapter 4**

# **Geoengineering, comparison of results with previous work**

Before performing new simulations it is important to understand how the HadGEM1 model compares with previous results. Many MCB publications show a climate change scenario and a geoengineered scenario. This enables two comparisons, one on the expected impacts of increasing greenhouse gas concentrations and one where the effectiveness of MCB to reduce these impacts is assessed.

### **4.1 Experiment description**

The HadGEM1 model is used to simulate several climate scenarios as described in Table 4.1. Each simulation is run for 70 years with the final 20 years analysed. The simulations are started from predicted 2020 levels of atmospheric carbon dioxide. In some of the simulations the atmospheric carbon dioxide levels change with time. A graph showing the change in carbon dioxide concentration against time is shown in Figure 4.1. For the MCB scenarios, two seeding maps are developed and these are shown in Figure 4.2. Figure 4.2(a) shows the three regions of persistent marine stratocumulus clouds used to investigate MCB in Jones et al. (2009, 2011); Latham

Experiment name	Carbon dioxide fraction (ppm)	Seeding scheme
CON	440	None
2CO <sub>2</sub>	440 + 1 %/year, held at 560	None
MCB3_2CO <sub>2</sub>	440 + 1 %/year, held at 560	Three regions, Figure 4.2(a)
MCBA_2CO <sub>2</sub>	440 + 1 %/year, held at 560	All ocean, Figure 4.2(b)
MCB3	440	Three regions, Figure 4.2(a)
MCBA	440	All ocean, Figure 4.2(b)

TABLE 4.1: The various climate scenario simulations run using HadGEM1 to investigate the climate effects of geoengineering via MCB. Where CON is the Control simulation and 2CO<sub>2</sub> gradually increases carbon dioxide levels to double preindustrial levels. MCB3\_2CO<sub>2</sub> and MCBA\_2CO<sub>2</sub> are geoengineering simulations using MCB in the same atmospheric conditions as 2CO<sub>2</sub>. MCB3 and MCBA are MCB simulations run in the control atmosphere without the effects of doubling preindustrial carbon dioxide. The carbon dioxide fractions are graphed in Figure 4.1.

et al. (2012, 2008). The regions in Figure 4.2(a) are known as three region seeding for the remainder of this work. Figure 4.2(b) shows the all sea seeding area which covers all marine regions and is used in Latham et al. (2008). The turquoise regions indicate the seeded areas. When seeding is switched on the CDNC is set to  $375 \text{ cm}^{-3}$  which is the same value as used in Jones et al. (2009, 2011); Latham et al. (2012, 2008), for all model levels between 0 km and 3 km. The first two experiments (CON and 2CO<sub>2</sub>) are designed to allow investigation into the impacts of climate change brought on by a continual increase in carbon dioxide until double preindustrial levels are reached. In addition to these initial experiments there are two MCB scenarios investigating the cumulative effects of increasing carbon dioxide while using MCB, (MCB3\_2CO<sub>2</sub> and MCBA\_2CO<sub>2</sub>). Two further experiments (MCB3 and MCBA) are initiated to investigate the effects of MCB on a control atmosphere. For the control simulations the control case is held at constant projected 2020 levels of carbon dioxide (440 ppm). Preindustrial levels are defined as 280 ppm (Forster et al., 2007).

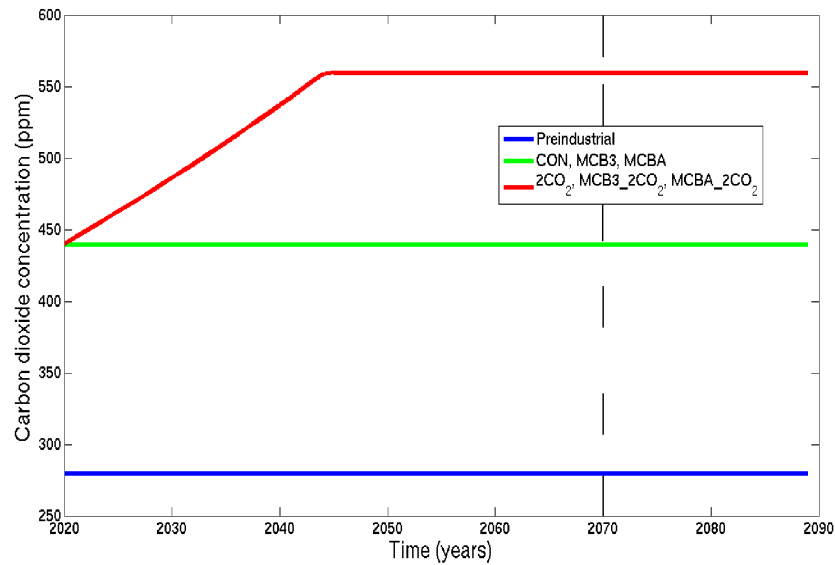
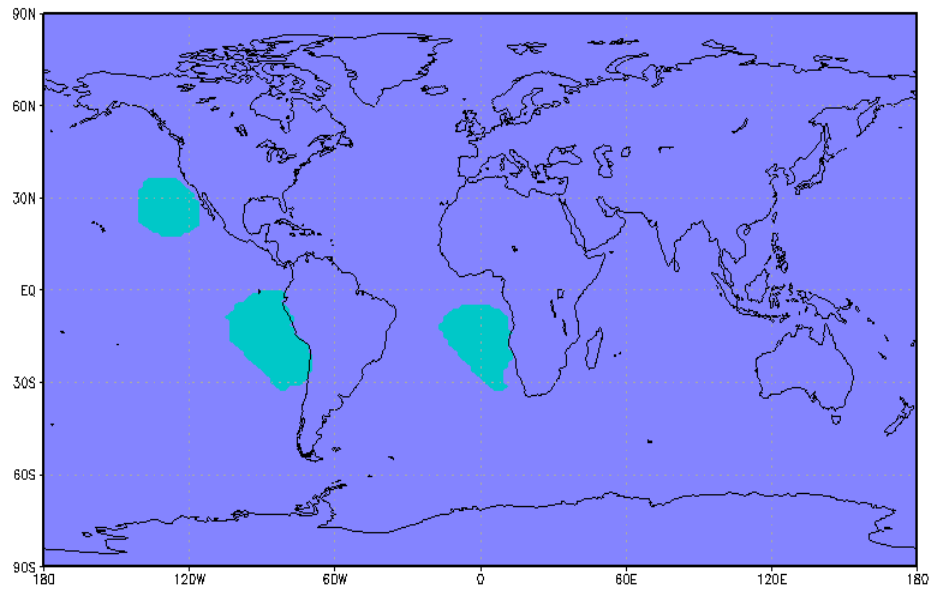


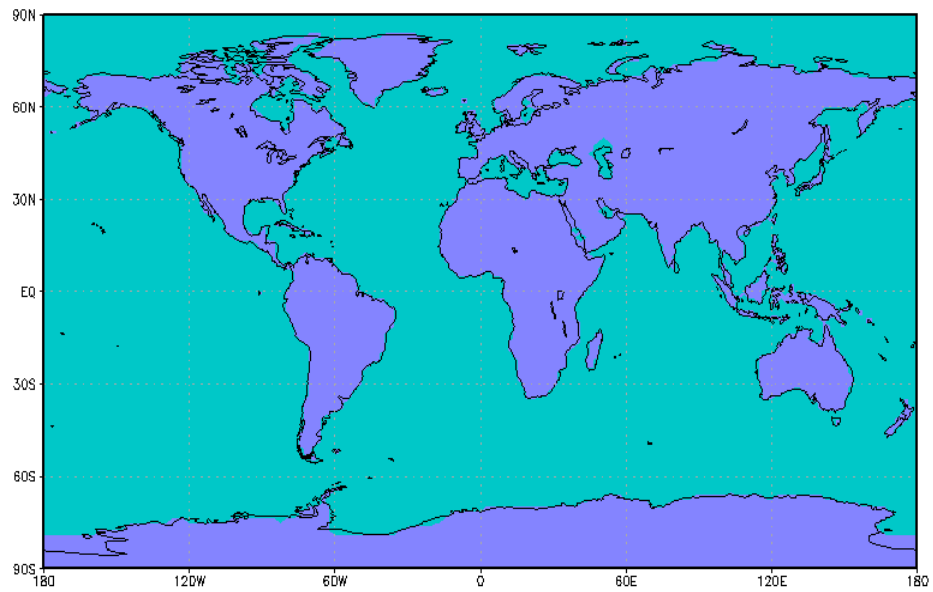
FIGURE 4.1: Carbon dioxide levels used in the simulations described in Table 4.1. The green line shows the carbon dioxide fraction in control atmospheres, the red line shows the carbon dioxide fraction in double preindustrial carbon dioxide concentration atmospheres and the blue line shows the preindustrial carbon dioxide level of 280 ppm. The vertical dashed black line shows the start of the analysis period for the simulations.

## 4.2 Previous work

In this section the results from previous publications on MCB are compared with this work. Four publications are examined in detail Jones et al. (2009, 2011) using the HadGEM2 suite Rasch et al. (2010) and Bala et al. (2011) using the NCAR CCM suite. The experiments differ either in terms of the seeding method or the time period within the simulation analysed. The differences between the models used in Bala et al. (2011); Jones et al. (2009, 2011); Rasch et al. (2010) and this work are detailed in Appendix A. A comparison with the results in Latham et al. (2008) is not performed as the model used by Latham et al. (2008) is an atmosphere only model. A comparison of the commonly included fields is shown in Section 4.2.1 before an investigation of publication specific fields in Section 4.2.2. The similarities and differences between the four publications and this work are shown in Table 4.2. The work in Jones et al. (2009) and Jones et al. (2011) uses the IPCC A1B simulation as a scenario based on the A1 scenario which includes rapid economic growth and



(a) Seeding map used in experiments MCB3.2CO<sub>2</sub> and MCB3. This mask covers approximately 5 % of the ocean surface.



(b) Seeding map used in experiments MCBA.2CO<sub>2</sub> and MCBA. This mask covers 100 % of the ocean surface.

FIGURE 4.2: Seeding maps used in the simulations described in Table 4.1. Turquoise regions indicate the area of the marine atmosphere seeded to a CDNC of  $N=375 \text{ cm}^{-3}$ .



a peak in population near 2050. The A1B scenario assumes a balance between fossil intensive and non fossil-intensive energy sources (Solomon et al., 2007).

### **4.2.1 Temperature, precipitation and sea ice cover**

The three most commonly displayed results are surface air temperature, precipitation rate and sea ice cover. A table of these published fields is shown in Table 4.3. Jones et al. (2009) do not present global mean results and is therefore omitted. Overall when the predicted changes shown in Table 4.3 are compared with the expected impacts shown in Figure 1.7 it can be seen the MCB would reduce the impacts of increasing greenhouse gas levels on the climate system.

#### **4.2.1.1 Surface temperature**

The temperature results from Figure 4.3 are displayed on different scales. However all show a greater than average increase in temperatures in the Arctic. A key point of these results is the sensitivity of the models to polar amplification which is described in Section 1.2.2. The warming in the Antarctic is not as uniform as in the Arctic; however it is still reasonably consistent across all four simulations. All results appear to find an approximately 1 K increase in temperature over the tropical oceans. The change in Arctic temperatures within the models ranges from 4 K to 8 K which is likely to be dependent on the atmospheric carbon dioxide concentrations in the simulations.

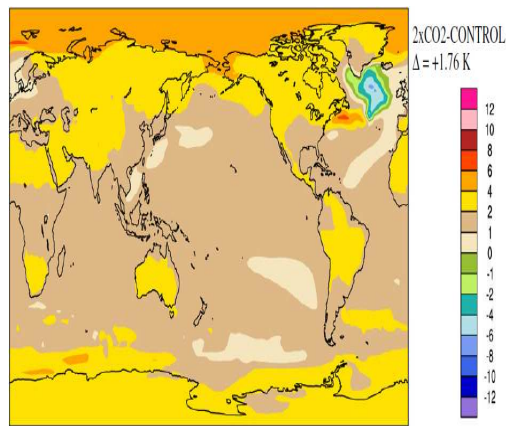
Rasch et al. (2010), shown in Figure 4.4(b) seed by setting the CDNC to 1000  $\text{cm}^{-3}$  in either 20 % or 70 % of the ocean surface. Bala et al. (2011) shown in Figure 4.4(d) reduced the effective radius of all oceanic cloud droplets to 11.5  $\mu\text{m}$ . The 70 % results (in Rasch et al. (2010)) from Figure 4.4(b) are comparable with results from MCBA\_2CO<sub>2</sub> shown in Figure 4.4(f). Both of these figures show heating off Greenland and Japan with a strong cooling in the Arctic. The strong temperature changes shown in Figure 4.4(f) are non-physical and have to be treated carefully.

Publication	Model	Resolution	CO <sub>2</sub>	Seeding strategy	Analysis time
Jones et al. (2009)	HadGEM2	1.25° x 1.875°	A1B	As Figure 4.2(a)	Final 30 of 60 years
Jones et al. (2011)	HadGEM2	1.25° x 1.875°	A1B	As Figure 4.2(a)	Equal temperature
Rasch et al. (2010)	NCAR CCSM	1.9° x 2.5°	710 ppm	20, 30, 40, 70 % sea surface	Final 20 of 100 years
Bala et al. (2011)	NCAR CAM 3.5	1.9° x 2.5°	800 ppm	Change in $r_{eff}$ of oceanic CCN	Final 40 of 70 years
This work	HadGEM1	1.25° x 1.875°	As Table 4.1	As Figures 4.2(a) 4.2(b)	Final 20 of 70 years

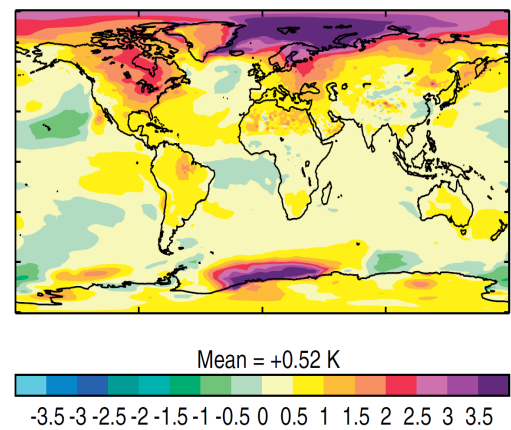
TABLE 4.2: The model, resolution, background atmospheric conditions, seeding mechanisms and analysis time used in four publications on MCB and this work.

Field	Jones et al. (2011)	Rasch et al. (2010)	Bala et al. (2011)	This work
Surface Temperature (K)	+0.52	+1.8	+2.4	+0.82
Precipitation (mm/day)	-0.048	+0.1	+5.0	+0.028
Sea ice cover	-7.4x10 <sup>-3</sup>	NH -20 % SH -36 %	-34 %	-6.9x10 <sup>-3</sup>
Surface Temperature (K)	-0.02	<b>20 %</b> +0.82 <b>70 %</b> -0.39	+0.06	<b>5 %</b> -0.05 <b>100 %</b> -6.5
Precipitation (mm/day)	-0.072	<b>20 %</b> +0.01 <b>70 %</b> -0.08	-1.3	<b>5 %</b> -0.049 <b>100 %</b> -0.58
Sea ice cover	-4.7x10 <sup>-3</sup>	<b>40 %</b> NH -9 % SH -8 % <b>70 %</b> NH -2 % SH +20 %	+1.1 %	<b>5 %</b> -1.8x10 <sup>-3</sup> <b>100 %</b> +4.3x10 <sup>-2</sup>

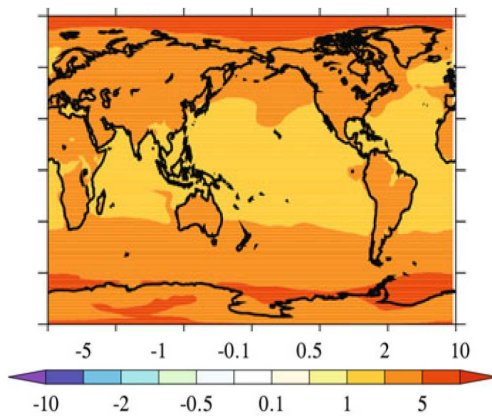
TABLE 4.3: Numerical results from several fields as presented in publications on the climate impacts of increasing greenhouse gas concentrations (above the line) or geoengineering in an increased greenhouse gas concentration atmosphere (below the line). Sea ice values for Rasch et al. (2010) and Bala et al. (2011) are percentage changes relative to the control simulation and not changes in the total ice cover. Both Rasch et al. (2010) and this work have multiple seeding fractions, therefore the fraction of the ocean seeded is shown in bold next to the values they apply to.



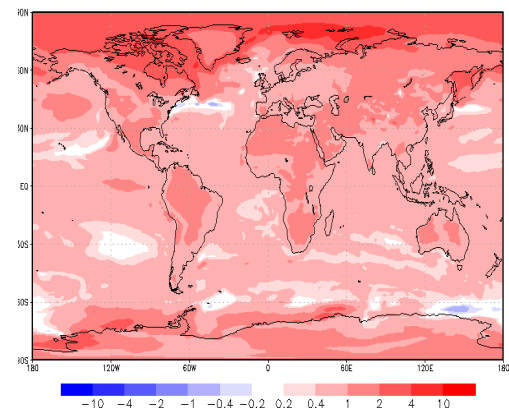
(a) Difference in surface temperature (K) in an increased carbon dioxide concentration atmosphere as shown in Rasch et al. (2010). Range -12 K to 12 K.



(b) Difference in surface temperature (K) in an increased greenhouse gas concentration atmosphere as shown in Jones et al. (2011). Range -3.5 K to 3.5 K.



(c) Difference in surface temperature (K) in an increased carbon dioxide concentration atmosphere as shown in Bala et al. (2011). Range -10 K to 10 K.



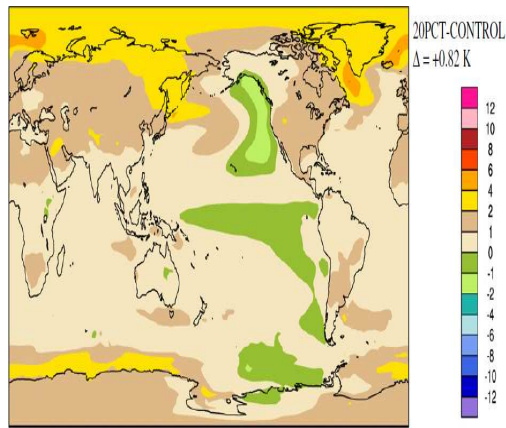
(d) Difference in surface temperature (K) between simulations 2CO<sub>2</sub> and CON as described in Table 4.1. Range -10 K to 10 K.

FIGURE 4.3: Comparison of effects of increased greenhouse gas concentrations on surface temperature (K) from Bala et al. (2011); Jones et al. (2011); Rasch et al. (2010) with this work.

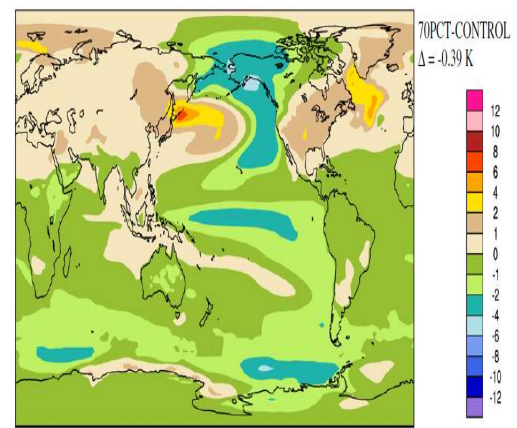
Results in Figures 4.4(c) and 4.4(e) show the effects of three region seeding in an increased carbon dioxide atmosphere. Jones et al. (2011) found a stronger heating of the Arctic and less cooling under seeded regions when compared with this work.

#### 4.2.1.2 Precipitation

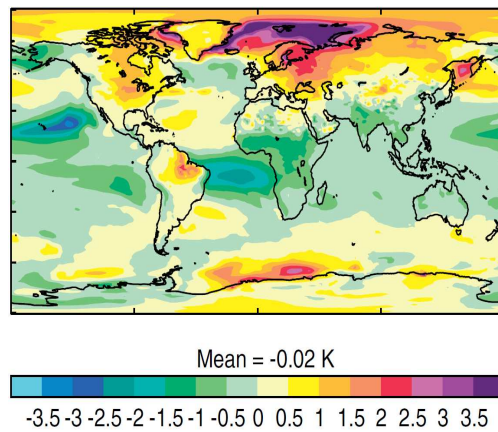
Figures 4.5 and 4.6 show the model results for precipitation changes as a result of increasing carbon dioxide and geoengineering via three region MCB. Precipitation



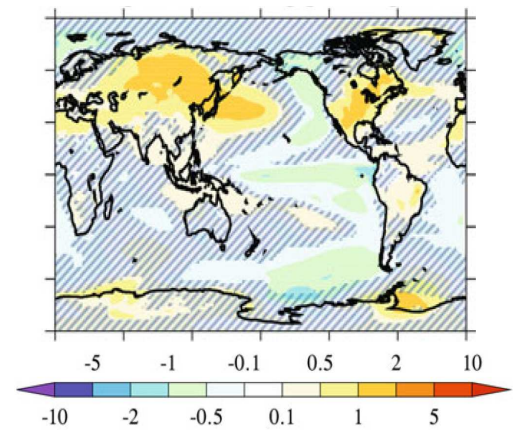
(a) Difference in surface temperature (K) in an increased carbon dioxide concentration atmosphere with 20 % seeding MCB as shown in Rasch et al. (2010). Range -12 K to 12 K.



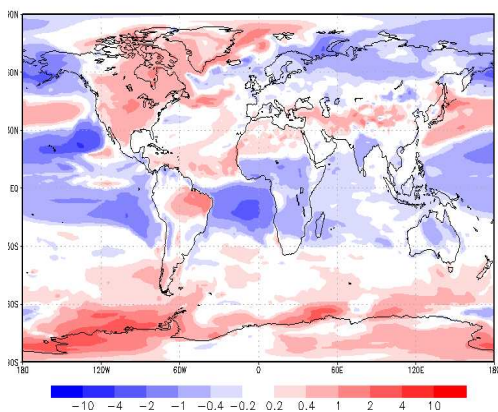
(b) Difference in surface temperature (K) in an increased carbon dioxide concentration atmosphere with 70 % seeding MCB as shown in Rasch et al. (2010). Range -12 K to 12 K.



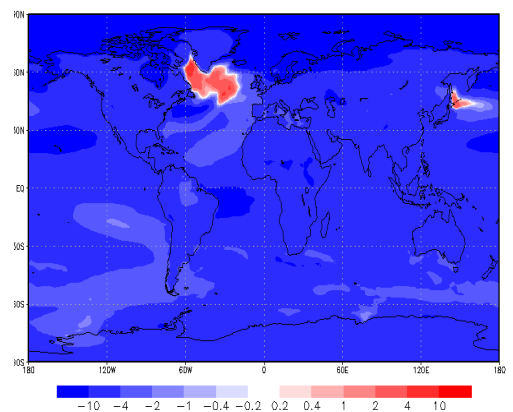
(c) Difference in surface temperature (K) in an increased greenhouse gas concentration atmosphere with three region seeding as shown in Jones et al. (2011). Range -3.5 K to 3.5 K.



(d) Difference in surface temperature (K) in an increased carbon dioxide concentration atmosphere with MCB as shown in Bala et al. (2011), hatched areas are not significant at the 1 % level. Range -10 K to 10 K.



(e) Difference in surface temperature (K) between simulations MCB3.2CO<sub>2</sub> and CON as described in Table 4.1. Range -10 K to 10 K.



(f) Difference in surface temperature (K) between simulations MCBA.2CO<sub>2</sub> and CON as described in Table 4.1. Range -10 K to 10 K.

FIGURE 4.4: Comparison of effects of seeding in an increased greenhouse gas concentrations on surface temperature (K) from Bala et al. (2011); Jones et al. (2011); Rasch et al. (2010) with this work.



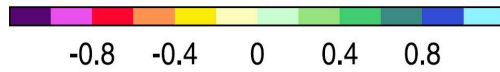
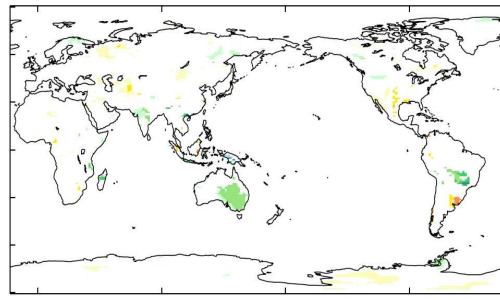
is a poorly handled quantity within GCMs as many of the contributory factors act on subgrid scales and require parametrisation instead of explicit calculation (See Section 3.1.3). Results from Jones et al. (2009) and Jones et al. (2011) are displayed in Figures 4.5(a) and 4.5(c). The results from Jones et al. (2009) and Jones et al. (2011), despite using the same model, and seeding mechanism, are quite different. The differences between the results in Jones et al. (2009) and Jones et al. (2011) are due to the differences in initial conditions and analysis time. Jones et al. (2011) finds a reduction in precipitation over the Amazon brought on by increasing carbon dioxide, whereas Jones et al. (2009) does not. Changes in Australian rainfall are also not consistent between Jones et al. (2009) to Jones et al. (2011). The results from Rasch et al. (2010) match the results from the simulations in Table 4.1 closely as shown in Figures 4.5(b) and 4.5(e). Results from Bala et al. (2011) have a much more significant change in tropical rainfall. The results from this work, (Figure 4.5(e)) show the largest changes in tropical precipitation. However these results should be treated with care as HadGEM1 is known to struggle at reproducing tropical rainfall patterns (See Section 3.2.2).

The changes in precipitation as a result of three region seeding are shown in Figures 4.6(a), 4.6(c) and 4.6(e). In Jones et al. (2009) and Jones et al. (2011) the Amazon region suffers a reduction in precipitation while there is an increase over much of Africa and Australia. The results shown in Figure 4.6(e) agrees with these findings. However without data over the oceans in Jones et al. (2009) and Jones et al. (2011) a full comparison is difficult. Rasch et al. (2010) (Figure 4.6(b)) shows changes of up to 8 mm/day over the tropics but less drying of the Amazon, furthermore unlike previous results there is an increase in precipitation over India and a decrease in Africa. A change in oceanic cloud droplet size results in an increase in rainfall over the majority of the world's rain forests and drying over parts of Indonesia and the eastern tip of South America (Bala et al., 2011). These results are consistent with the all-sea seeding results shown in Figure 4.6(f). However the reduction of rainfall in Figure 4.6(f) covers the entire Amazon instead of the small area in Figure 4.6(d). From these results it appears seeding generally increases rainfall

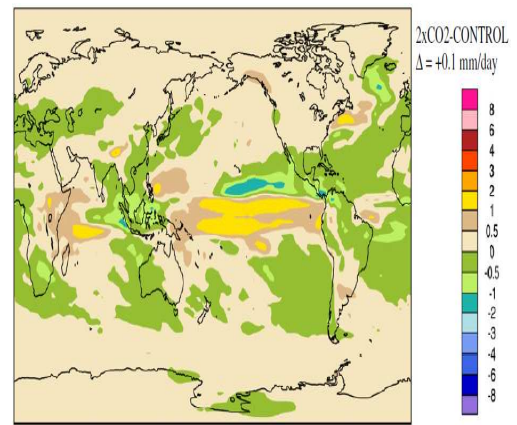
over the desert areas of Africa and Australia while reducing rainfall in the Amazon, depending on the simulations performed. Work done by Jones et al. (2009) indicates that seeding over the South Atlantic is responsible for this reduction in rainfall. The seeding method in Rasch et al. (2010) selects the clouds with the lowest droplet number for each month and then simulates seeding those clouds to a CDNC of  $1000 \text{ cm}^{-3}$ . The seeded area in Rasch et al. (2010) is north of the South Atlantic region used by Jones et al. (2009, 2011) and this work. An image showing the seeding regions used in Rasch et al. (2010) can be found in the supplementary material for their paper.

#### **4.2.1.3 Sea ice cover**

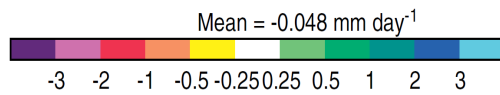
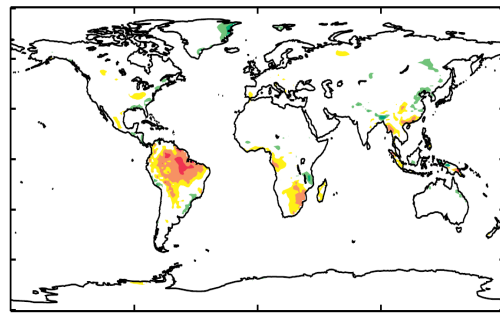
Descriptions of the impacts on sea ice cover are not included in all papers, in contrast with precipitation or surface temperature. Ice-albedo feedbacks within polar amplification imply that is an important field (See Section 1.2.2). Furthermore, there are various questions about the impact on both wildlife and human interests. Jones et al. (2011) and Rasch et al. (2010) investigate the impacts of MCB on sea ice cover. Sea ice cover responds to the surface temperature and this can be most clearly seen in Figures 4.7(b) and 4.7(d) when compared with the temperature fields in Figures 4.3(b) and 4.3(d). In Jones et al. (2011) the warming north of Norway and east of the Antarctic peninsular is matched by the change in ice cover, Figures 4.3(b) and 4.7(b). This work finds similar responses between ice cover and temperature change but does not produce such a significant result in Antarctica. The sea ice minima for both poles are published in Rasch et al. (2010) using the months of September in the northern hemisphere and March in the southern hemisphere. In Rasch et al. (2010) the carbon dioxide concentration is doubled for the entire 100 year run while in the present work gradually increases carbon dioxide concentration, this in turn leads to a slower change in ice cover. This is also true for the work in Jones et al. (2011) where the IPCC A1B scenario (Randall et al., 2007) increased carbon dioxide by 2 %/yr as rather than the 1 %/yr shown in Table 4.1.



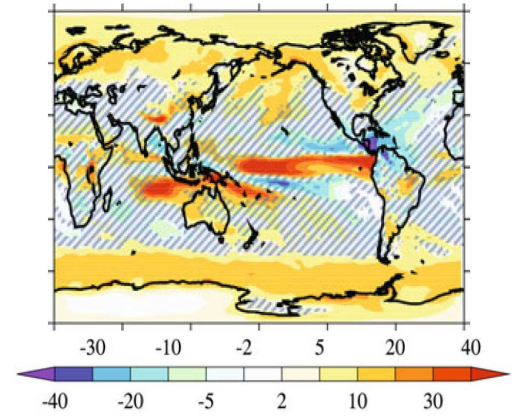
(a) Difference in precipitation rate (mm/day) in an increased greenhouse gas concentration atmosphere as shown in Jones et al. (2009). Range -0.8 mm/day to 0.8 mm/day.



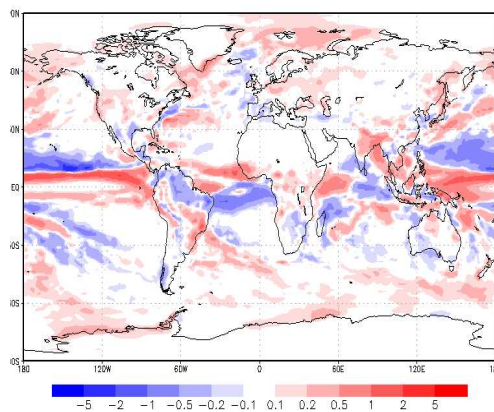
(b) Difference in precipitation rate (mm/day) in an increased carbon dioxide concentration atmosphere as shown in Rasch et al. (2010). Range -8 mm/day to 8 mm/day.



(c) Difference in precipitation rate (mm/day) in an increased greenhouse gas concentration atmosphere as shown in Jones et al. (2011). Range -3 mm/day to 3 mm/day.



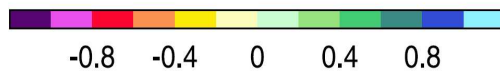
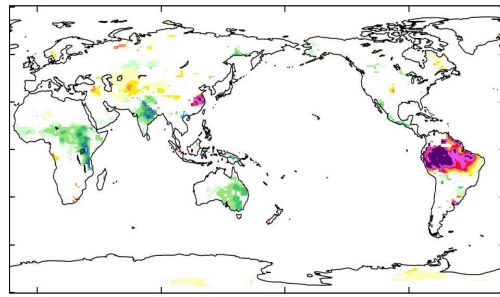
(d) Difference in precipitation rate (cm/year) in an increased carbon dioxide concentration atmosphere as shown in Bala et al. (2011), hatched areas are not significant at the 1% level. Range -40 cm/year to 40 cm/year.



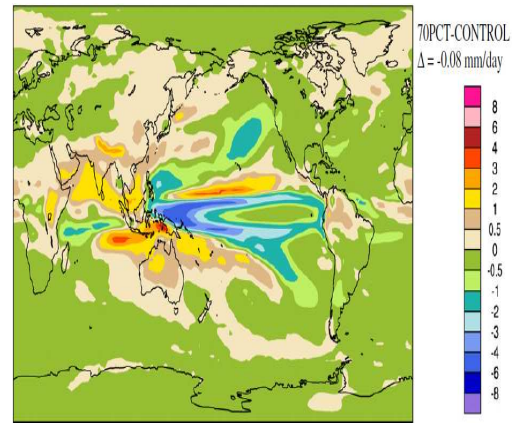
(e) Difference in precipitation rate (mm/day) between simulations 2CO<sub>2</sub> and CON as described in Table 4.1. Range -5 mm/day to 5 mm/day.

FIGURE 4.5: Comparison of effects of increased greenhouse gas concentrations on precipitation (mm/day except Bala et al. (2011) cm/year) rate from Bala et al. (2011); Jones et al. (2009, 2011); Rasch et al. (2010) with this work.

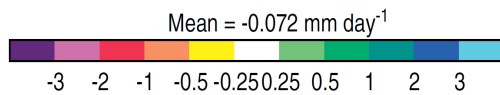
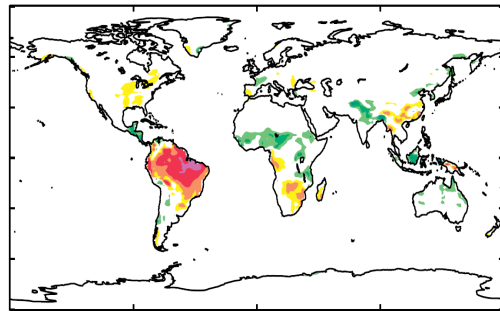




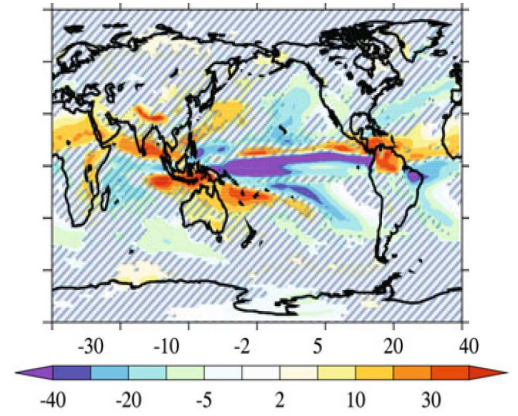
(a) Difference in precipitation rate (mm/day) in an increased greenhouse gas concentration atmosphere with three region seeding as shown in Jones et al. (2009). Range -0.8 mm/day to 0.8 mm/day.



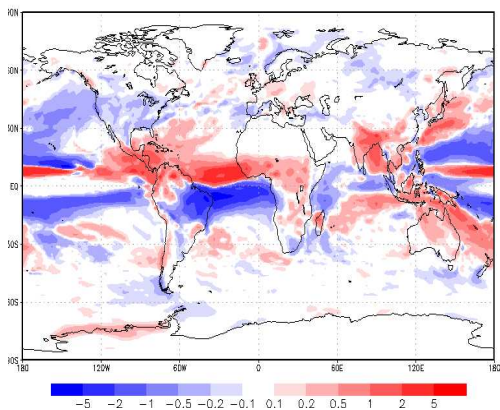
(b) Difference in precipitation rate (mm/day) in an increased carbon dioxide concentration atmosphere with MCB as shown in Rasch et al. (2010). Range -8 mm/day to 8 mm/day.



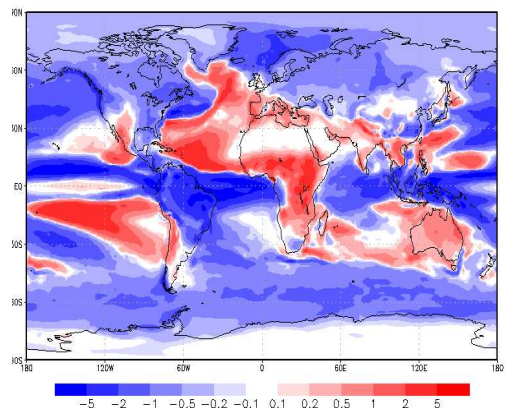
(c) Difference in precipitation rate (mm/day) in an increased greenhouse gas concentration atmosphere with three region seeding as shown in Jones et al. (2011). Range -3 mm/day to 3 mm/day.



(d) Difference in precipitation rate (cm/year) in an increased carbon dioxide concentration atmosphere with MCB as shown in Bala et al. (2011), hatched areas are not significant at the 1 % level. Range -40 cm/year to 40 cm/year.



(e) Difference in precipitation rate (mm/day) between simulations MCB3.2CO<sub>2</sub> and CON as described in Table 4.1. Range -5 mm/day to 5 mm/day.



(f) Difference in precipitation rate (mm/day) between simulations MCBA.2CO<sub>2</sub> and CON as described in Table 4.1. Range -5 mm/day to 5 mm/day.

FIGURE 4.6: Comparison of effects of seeding in an increased greenhouse gas concentration atmosphere on precipitation (mm/day except Bala et al. (2011) cm/year) rate from Bala et al. (2011); Jones et al. (2009, 2011); Rasch et al. (2010) with this work.

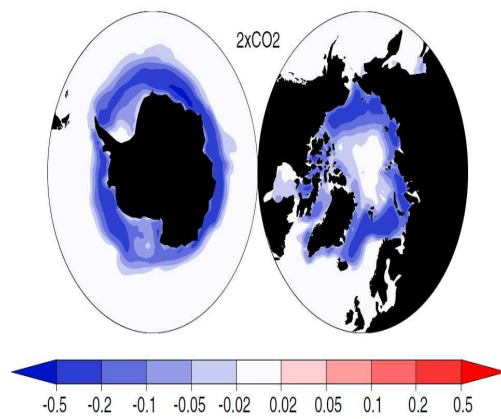
A comparison of the impacts of MCB on ice cover between the experiments in Table 4.1 and Rasch et al. (2010) is poor as the seeding quantities are very different. This study seeds either 5 % or 100 % of the marine atmosphere whereas Rasch et al. (2010) seeds either 40 % or 70 % of the marine atmosphere. Furthermore as described in Table 4.2 the work in Rasch et al. (2010) has a much higher atmospheric carbon dioxide concentration than the experiments in Table 4.1 which leads to larger warming of polar regions, see Figures 4.3(a) and 4.3(d). The impacts of seeding 40 % of the marine atmosphere in Rasch et al. (2010) and 5 % of the marine atmosphere in this work on ice cover are similar, see Figures 4.8(c) and 4.7(c). The 100 % seeding results shown in Figure 4.8(f) do not have the losses in ice cover found in the 70 % results from Figure 4.8(e). Both Jones et al. (2011) and this work find that seeding reduces the ice loss. As a result of the higher carbon dioxide concentration in Jones et al. (2011) the reduction in ice loss is not as large. As can be seen from both Figures 4.8(a) and 4.8(b) there is still ice loss north of Norway.

## **4.2.2 Radiative fields**

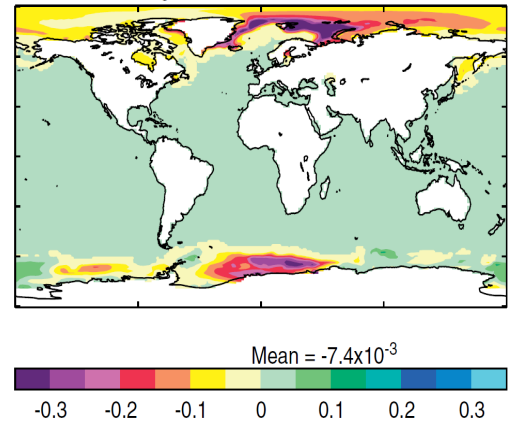
Radiative flux difference and albedo are analysed in Jones et al. (2011) and Bala et al. (2011) respectively. In this section two more comparisons are made to further establish consistency with Bala et al. (2011); Jones et al. (2011).

### **4.2.2.1 Radiative flux difference**

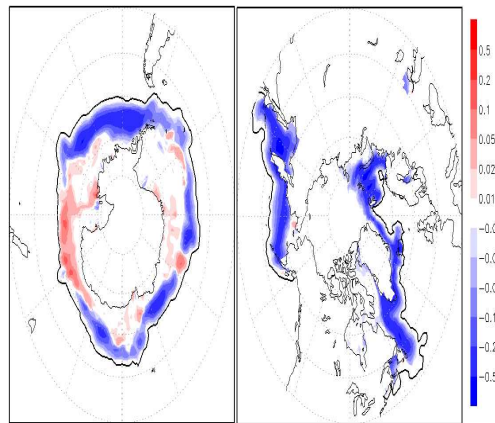
The radiative flux difference is not a true radiative forcing as energy is lost to the climate system in the form of surface heating, melting ice or warming the oceans. The radiative flux difference is the difference in energy flux between the downwelling shortwave (solar) radiation and the upwelling shortwave and longwave radiation. The results shown in Figure 4.9(a) show the change in radiative flux perturbation as a result of MCB over a ten year period from 2019-2028 in Jones et al. (2011).



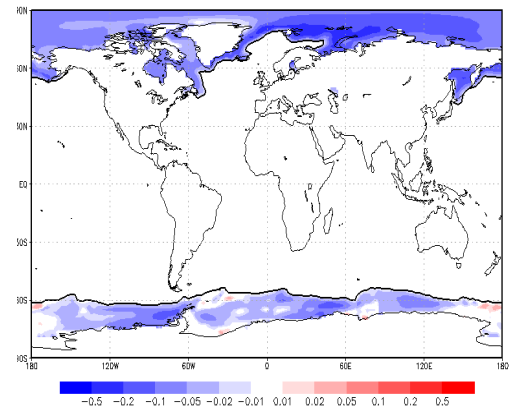
(a) Difference in minimum polar ice cover in an increased carbon dioxide concentration atmosphere as shown in Rasch et al. (2010). Range -0.5 to 0.5.



(b) Difference in global ice cover in an increased greenhouse gas concentration atmosphere as shown in Jones et al. (2011). Range -0.3 to 0.3.



(c) Difference in minimum polar ice cover between simulations  $2\text{CO}_2$  and CON as described in Table 4.1. Range -0.5 to 0.5.

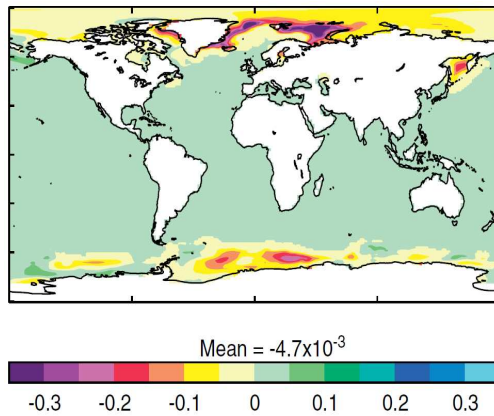


(d) Difference in global ice cover between simulations  $2\text{CO}_2$  and CON as described in Table 4.1. Range -0.5 to 0.5.

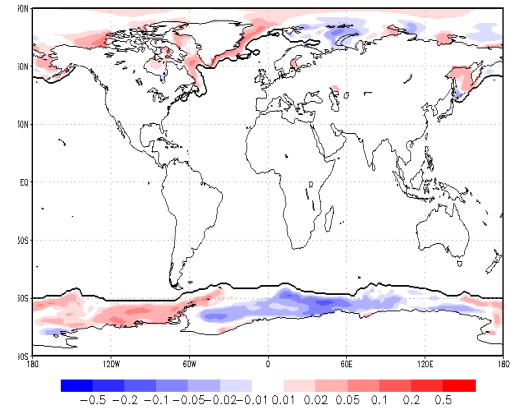
FIGURE 4.7: Comparison of effects of increased greenhouse gas concentrations on sea ice cover from Jones et al. (2011); Rasch et al. (2010) with this work.

Figure 4.9(b) shows the radiative flux difference at the top of the atmosphere for the final 20 years of the 70 year simulations and the effects of the three seeding regions can easily be seen. As the results in Figure 4.9(b) are taken from the end of the simulations and is not at the same time as in Jones et al. (2011) a numerical comparison is difficult as the amount of energy transferred to the land or ocean is unknown. In the present work there appears to be a spreading of the reduction in the radiative flux difference, this is probably due to clouds being formed in the seeding regions off the coasts of Namibia, Peru and California and then advected by tropical easterlies.

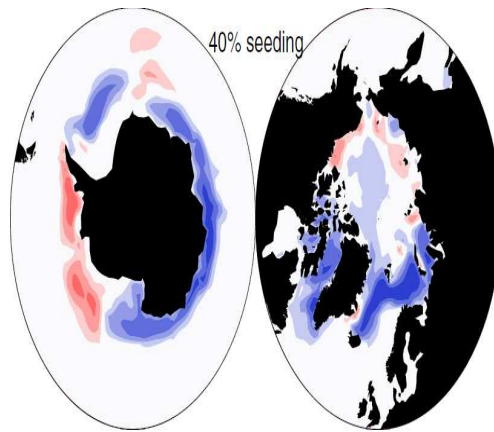




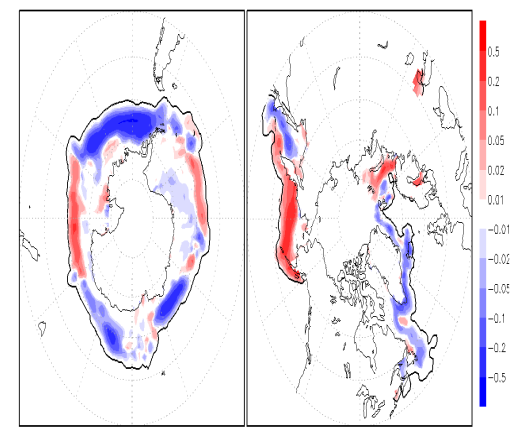
(a) Difference in global ice cover in an increased greenhouse gas concentration atmosphere with three region seeding as shown in Jones et al. (2011). Range -0.3 to 0.3.



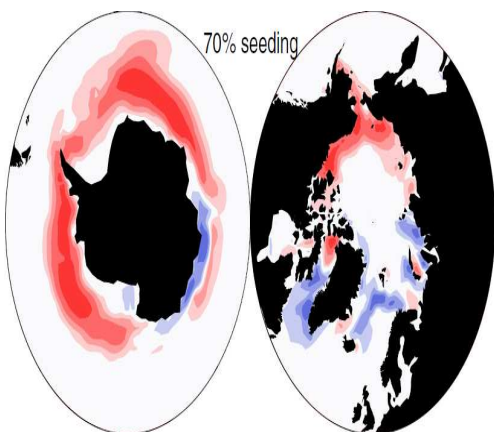
(b) Difference in global ice cover between simulations MCB3.2CO<sub>2</sub> and CON as described in Table 4.1. Range -0.5 to 0.5.



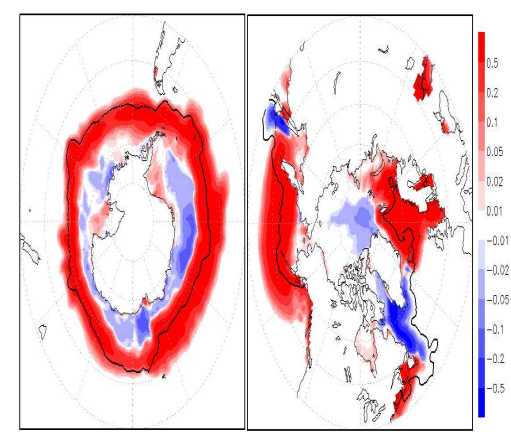
(c) Difference in minimum polar ice cover in an increased carbon dioxide concentration atmosphere with 40 % seeding as shown in Rasch et al. (2010). Range -0.5 to 0.5.



(d) Difference in minimum polar ice cover between simulations MCB3.2CO<sub>2</sub> and CON as described in Table 4.1. Range -0.5 to 0.5.

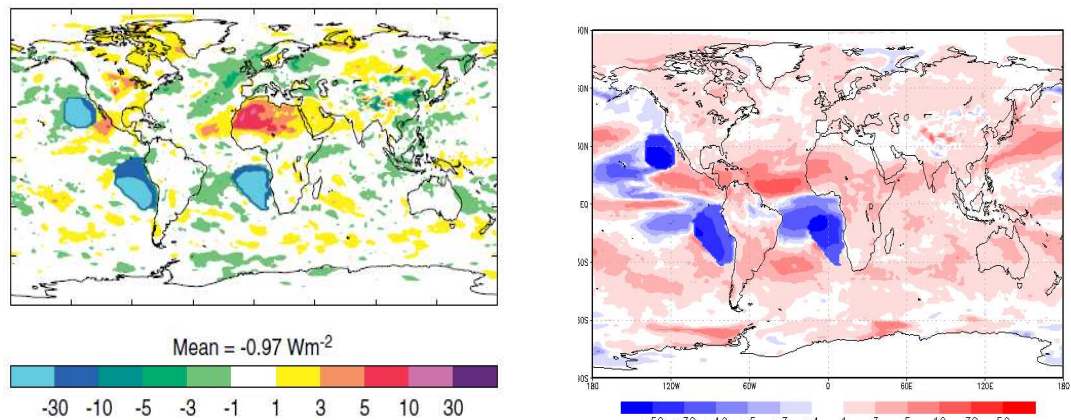


(e) Difference in minimum polar ice cover in an increased carbon dioxide concentration atmosphere with 70 % seeding as shown in Rasch et al. (2010). Range -0.5 to 0.5.



(f) Difference in global ice cover between simulations MCB3.2CO<sub>2</sub> and CON as described in Table 4.1. Range -0.5 to 0.5.

FIGURE 4.8: Comparison of effects of MCB in an increased greenhouse gas concentration atmosphere on sea ice cover from Jones et al. (2011); Rasch et al. (2010) with this work.



(a) Change in radiative flux difference ( $\text{W m}^{-2}$ ) as a result of MCB in and increased greenhouse gas concentration atmosphere as shown in Figure 1.b of Jones et al. (2011). Range  $-30 \text{ W m}^{-2}$  to  $30 \text{ W m}^{-2}$ .

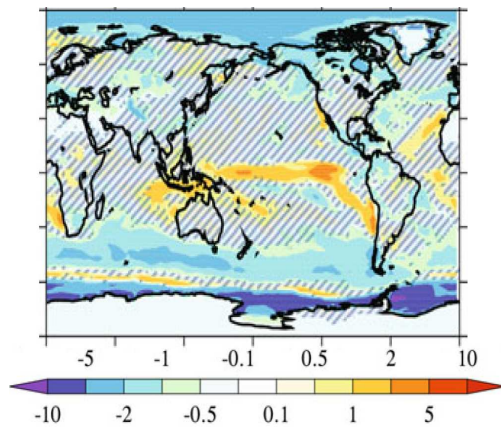
(b) Change in radiative flux difference ( $\text{W m}^{-2}$ ) between simulations MCB3.2CO<sub>2</sub> and CON as described in Table 4.1. Range  $-50 \text{ W m}^{-2}$  to  $50 \text{ W m}^{-2}$ .

FIGURE 4.9: Comparison of effects of MCB in an increased greenhouse gas concentrations atmosphere on radiative flux difference ( $\text{W m}^{-2}$ ) between Jones et al. (2011) and this work.

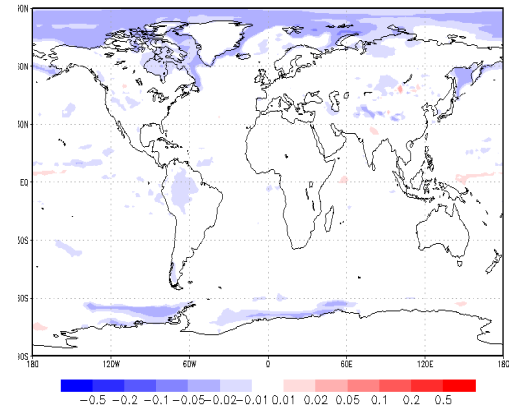
#### 4.2.2.2 Albedo

Changes in global albedo were initially mentioned in earlier publications on geoengineering on a global scale eg (Latham, 1990), later work (eg. Bala et al. (2011)) investigates the local scale albedo changes as a result of modifying cloud microphysics. The albedo is defined as the ratio of upwelling to downwelling radiation at the top of the atmosphere. Figures 4.10(a) and 4.10(b) show the impacts of increasing carbon dioxide on albedo. Figures 4.10(a) and 4.10(b) are fairly consistent with both showing a reduction in albedo in polar regions which can be attributed to sea ice loss and even be part of a feedback mechanism, such as Polar Amplification (see Section 1.2.2).

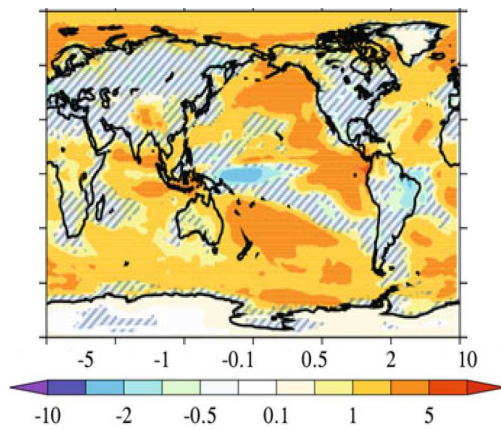
The seeding method differs between the present work and Bala et al. (2011) and therefore the albedo can be expected to change in a different manner. The results from Bala et al. (2011) shown in Figure 4.10(c) show small changes in the albedo, generally between 2 % and 5 %. The results are in contrast with the present work (Figure 4.10(d)) where albedo changes are regularly between 20 % and 50 %. It should be noted however the results in Bala et al. (2011) (Figure 4.10(c)) are for



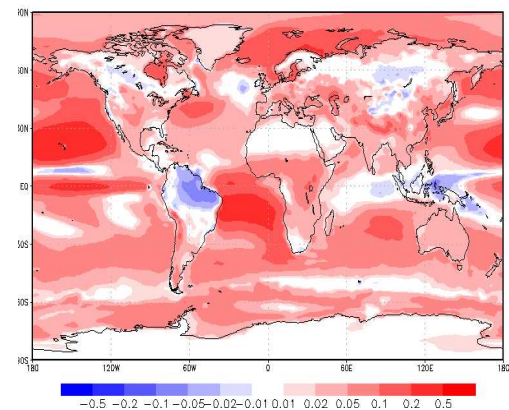
(a) Change in albedo in an increased carbon dioxide concentration atmosphere as shown in Bala et al. (2011). Range -10 % to 10 %.



(b) Change in top of atmosphere albedo between simulations 2CO<sub>2</sub> and CON as described in Table 4.1. Range -0.5 to 0.5.



(c) Change in albedo in as a result of seeding in an increased carbon dioxide concentration atmosphere as shown in Bala et al. (2011). Range -10 % to 10 %.



(d) Change in top of atmosphere albedo between simulations MCBA\_2CO<sub>2</sub> and CON as described in Table 4.1. Range -0.5 to 0.5.

FIGURE 4.10: Comparison of effects on albedo in increased carbon dioxide concentration atmospheres with and without seeding between (Bala et al., 2011) and this work.

a simulation designed to return global average temperatures to that of a control simulation whereas the temperature changes between MCBA\_2CO<sub>2</sub> and CON cool global surface temperatures by 6.5 K.

### 4.3 Discussion

Six experiments are used to investigate the climate impacts of MCB. Three of these experiments simulate an increase in the carbon dioxide concentrations within the atmosphere while the remaining three hold carbon dioxide levels static at predicted 2020 levels. A comparison of the outputs enables investigation into the effects of increasing carbon dioxide levels or the ability of MCB to return to a control level climate state in an increased carbon dioxide atmosphere. The comparisons between the experiments in Table 4.1 are discussed in detail in Chapters 5 and 6.

The experiments in Table 4.1 are an extension of previously published studies on the impacts of MCB. Preceding simulations vary, either by using a different model or seeding scheme or atmospheric conditions. The experiments in Table 4.1 utilise the lowest greenhouse gas levels when compared with Bala et al. (2011); Jones et al. (2009, 2011); Rasch et al. (2010) and hence will result in smaller differences from the control when simulating climate change. The changes in greenhouse gas levels for Bala et al. (2011); Jones et al. (2009, 2011); Rasch et al. (2010) and the present work are discussed in Section 4.2. The A1B simulations described in the IPCC 4th Assessment report (Randall et al., 2007), specifically an atmospheric carbon dioxide concentration increase of above 1 %/yr, this in addition to the contribution by other greenhouse gases is larger than the 1 %/yr shown in Table 4.1. The differences between the models used in Bala et al. (2011); Jones et al. (2009, 2011); Rasch et al. (2010) and this work are described in Appendix A. The seeding strategy employed in previous works also varies, with Bala et al. (2011) changing the size of cloud droplets over the entire ocean and Rasch et al. (2010) selects the optimum 20 %, 40 %, 70 % of the ocean to seed. The work in Jones et al. (2009, 2011) instead seeds three regions of persistent marine stratocumulus clouds as shown in Figure 4.2(a). This work investigates the three region seeding as in Jones et al. (2009, 2011); Latham et al. (2008) and shown in Figure 4.2(a) while also investigating the climatic responses to all-sea seeding.



The differences in seeding strategy, atmospheric conditions, simulation length and model choice all have an impact on the results. A higher level of greenhouse gases leads to more rapid climate change, while over simulating a longer length of time allows the climate to approach and equilibrium. The variations in model choice are the work of a large intercomparison project and are not discussed here. Despite the differences between the greenhouse gas concentrations, seeding strategy and simulation length the results in Figures 4.3 4.5 and 4.7 show that the impacts of climate change are consistent among Bala et al. (2011); Jones et al. (2009, 2011); Rasch et al. (2010).

In each case the surface temperature increases significantly at the poles while remaining closer to the control in the tropics (See Section 1.2.2 on Polar Amplification in the climate). MCB is generally able to reduce the global temperatures that are increased by greenhouse gases. However the effectiveness of MCB in polar regions is uncertain. Work by Rasch et al. (2010) gives differences in polar temperatures of +4 K near Greenland under 20 % seeding while using 70 % seeding there are regions of the North Pacific cooled by up to 10 K.

The precipitation changes in an increased greenhouse gas concentration atmosphere are more complex. However an increase is generally found and attributed to a higher volume of evaporation brought on by higher surface temperatures. The impacts of MCB on precipitation are shown in Figure 4.6 where the results indicate that MCB does reduce precipitation. Furthermore it appears that the reduction in precipitation increases with increasing the area of the ocean seeded by MCB.

The ice cover results also show a decline both in minimum and annual average extent, see Figure 4.7. With changes in temperatures there is an associated change in ice cover where results from this work compare well with previous publications.

The changes in radiative properties such as the albedo and the radiative flux difference appear to be consistent. Figure 4.10 shows the change in albedo as a result of doubling carbon dioxide levels and the impacts of changing sea ice cover can be seen in both work by Bala et al. (2011) and this work.

## 4.4 Summary

This chapter reports an investigation into the ability of the HadGEM1 coupled atmosphere-ocean model to simulate MCB and the suitability of the experiments described in Table 4.1. These experiments are designed to investigate the impacts of climate change or MCB. Impacts of MCB are described in Chapter 5 and 6.

There are several predicted consequences of climate change as a result of changing greenhouse gas levels. In the publications by Jones et al. (2009, 2011) the simulations follow the A1B path outlined by the IPCC in Randall et al. (2007), while in Rasch et al. (2010) and Bala et al. (2011) carbon dioxide levels are doubled at the start of the simulations. In the simulations described in Table 4.1 only carbon dioxide changes with time while retaining static levels of other greenhouse gases. The maximum temperature change under increasing greenhouse gas concentrations is found in Bala et al. (2011) (+2.4 K) and the minimum is found in Jones et al. (2009) (+0.52 K). This work is in the lower part of the range of temperature changes at +0.82 K while the work in Rasch et al. (2010) finds an increase of 1.8 K. The variations in the climate change simulations are also present in the MCB simulations where different seeding strategies are employed for several simulation lengths. The simulations detailed in Table 4.1 are shown to be consistent with previous publications on the effects of MCB on the climate system in a climate change atmosphere. The consistency between this work and previous publications is not complete and there are several differences in polar temperature and sea ice cover. Furthermore there are significant differences in the precipitation results over the Amazon between this work and work by Rasch et al. (2010), where the work in Rasch et al. (2010) find changes of under 1 mm/day for 70 % seeding and this work finds a reduction of over 5 mm/day.

## **Chapter 5**

# **The Impacts of Marine Cloud Brightening on the Polar regions and the Meridional Heat Flux**

Marine cloud brightening is designed to reduce incoming solar radiation and allow the climate to reach a new equilibrium as described in Section 1.4.3.5. The increase in greenhouse gas concentrations causes more longwave radiation to be retained in the climate system while also having secondary impacts such as ocean acidification. Altering the radiative balance of the atmosphere may counteract the radiative changes brought on by increasing greenhouse gas concentrations. It is shown in previous work that MCB cannot restore the climate to a preindustrial greenhouse gas concentration climate (Bala et al., 2011; Jones et al., 2009, 2011; Rasch et al., 2010). The work in Section 5.2 is based upon work in Parkes et al. (2012).

### **5.1 Climate impacts of Marine Cloud Brightening**

In Section 5.1.2 the changes to the climate as a result of doubling preindustrial atmospheric carbon dioxide concentrations are investigated. From those results

Experiment name	Carbon dioxide fraction (ppm)	Seeding scheme
CON	440	None
2CO <sub>2</sub>	440 + 1 %/year, held at 560	None
MCB3_2CO <sub>2</sub>	440 + 1 %/year, held at 560	Three regions, Figure 4.2(a)
MCBA_2CO <sub>2</sub>	440 + 1 %/year, held at 560	All ocean, Figure 4.2(b)

TABLE 5.1: Section of Table 4.1 used to assess the climate impacts of MCB. Where CON is the Control simulation and 2CO<sub>2</sub> gradually increases carbon dioxide levels to double preindustrial levels. MCB3\_2CO<sub>2</sub> and MCBA\_2CO<sub>2</sub> are geoengineering simulations using MCB in the same atmospheric conditions as 2CO<sub>2</sub>. The carbon dioxide fractions are graphed in Figure 4.1.

it is possible to establish the expected effects of continued use of fossil fuels. In Section 5.1.3 the impacts of seeding three regions of marine stratocumulus clouds in an atmosphere with double carbon dioxide concentrations are investigated. This section provides an insight into the possible side effects of a frequently postulated MCB scenario and the ability of MCB to return the atmosphere to the control conditions. A further scenario involves seeding the entire marine atmosphere and this is investigated in Section 5.1.4. In addition a process is proposed to provide an explanation for the link between the tropical seeding and polar impacts of MCB. The simulations used in this investigation are shown in Table 5.1, which contains a subset of the information from Table 4.1.

### 5.1.1 Variable selection

MCB in this work is simulated within the HadGEM1 climate model with a forced change in the CDNC. The CDNC is calculated in each model level up to 39 km above the surface. Results from the VOCALs-REx field campaign shows that the base of the stratocumulus deck is generally at an altitude of 1000 m and is between 300 m and 500 m thick as shown in Bretherton et al. (2010) and Chapter 2 of this work. The model produces a value for CDNC when cloud is present and gives a Not-a-Number (NaN) result otherwise. Within the experiments noted in Table 5.1, the model atmosphere is seeded between 0 km and 3 km. To provide CDNC results

within the stratocumulus deck, plots from the model level between 1 km and 1.2 km are selected.

Changes in the microphysical properties of the clouds, result in changes in related fields such as shortwave forcing and precipitation rate. HadGEM1 uses parametrisation to simulate the impacts of aerosol particles on clouds as described in Section 3.1.4. Within the model it is therefore possible to record a change in both cloudiness and precipitation as a result of changing microphysical variables.

The change in the cloud cover and precipitation rates have an impact on surface temperatures. The temperature field is involved in a positive feedback with the cloud field as described in Section 1.3. Temperature changes can also have an effect on the ocean below the cloud deck and the movement of cooled waters is linked to changes in ice cover. The precipitation pattern is also dependent on the temperature as a reduction in temperature reduces the amount of energy available to evaporate water. The shortwave forcing is also dependent on ice cover and a reduction in ice cover would result in a reduction in shortwave forcing.

The change in temperatures and the modification of the ocean circulation could have an impact on sea ice cover. In each section all results are compared to the control simulation where carbon dioxide levels are held at 2020 levels (440 ppm). The numerical results from the plots detailed in Sections 5.1.2, 5.1.3 and 5.1.4 are shown in Table 5.2.

### **5.1.2 Impact of doubling preindustrial carbon dioxide concentrations**

The doubling of preindustrial carbon dioxide concentrations within the model does not involve direct modification of the CDNC. Instead the only difference between the 2CO<sub>2</sub> and CON simulations is the increasing carbon dioxide levels which follow the red line in Figure 4.1. The changes occur instead as a result of feedbacks within the model. Example feedbacks include the sea ice-albedo feedback discussed in

Field	CON	2CO <sub>2</sub> - CON	MCB3_2CO <sub>2</sub> - CON	MCBA_2CO <sub>2</sub> - CON
CDNC at 1 km (cm <sup>-3</sup> )	44.1	+0.52	+4.36	+189
Shortwave forcing (W m <sup>-2</sup> )	-243	-0.70	+0.37	+14
Surface temperature (K)	288	+0.77	-0.12	-6.7
Precipitation (mm/day)	3.13	+0.035	+0.0068	-0.44
Ice cover (N) (10 <sup>6</sup> km <sup>2</sup> )	11.5	-3.2	+0.55	+23
Ice cover (S) (10 <sup>6</sup> km <sup>2</sup> )	10.1	-1.3	-0.75	+8.1

TABLE 5.2: Numerical results detailing the global annual average control levels and the differences in the simulations described in Table 5.1.

Section 1.2.2 where an increase in polar temperatures reduces sea ice cover and reduces the shortwave forcing. Another consequence of global warming is the increase in precipitation due to the increased evaporation of water as a result of increasing temperatures. There are minimal changes in CDNC between the 2CO<sub>2</sub> and CON simulations as shown in Figure 5.1(a), however the shortwave forcing is shown to reduce significantly in Figure 5.1(b).

The model simulated polar amplification of temperatures as a result of doubling atmospheric carbon dioxide concentrations is shown in Figure 5.1(c). Doubling atmospheric carbon dioxide concentrations increases the Arctic temperatures significantly more than in the tropics as shown in Figure 5.1(c). While the global average temperature change is +0.77 K there is an area of the Arctic where the change is over 6 K. There is also an increase of between 3 K and 4 K over the Antarctic. Polar amplification of temperature is described as the ratio of the change in 75° - 90° N temperature and the change in global average temperature (Holland and Bitz, 2003). The HadGEM1 model produces polar amplification and as such the temperature changes are greater in polar regions and this has an associated impact on ice cover. In the comparison between the CON and 2CO<sub>2</sub> simulations this value is found to be 3.8, i.e. the model temperatures in polar regions (between 75° N and 90° N) increase by 3.8 K for each 1 K of increase in global average temperatures. Associated with the increase in surface temperatures (Figure 5.1(c)) there is an increase in precipitation rate. The increase in precipitation rate is due to the increase in evaporation brought on by the increase in surface temperature. The majority of precipitation changes are in the tropics, where increases of over 1 mm/day are found over the Indian subcontinent and the Brazilian South Atlantic coast.

To give a more detailed view of changes to the sea ice cover the plots are shown in a polar stereographic projection. Despite the simulations showing ice in and around Japan, this is unlikely to happen in reality, therefore model results in this region have to be considered carefully. The reduction in sea ice cover as a result of increased polar temperatures is shown in Figures 5.1(e) and 5.1(f) and is found to be  $4.5 \times 10^6$  km<sup>2</sup>. The Arctic ice losses are in the same regions as the temperature increases

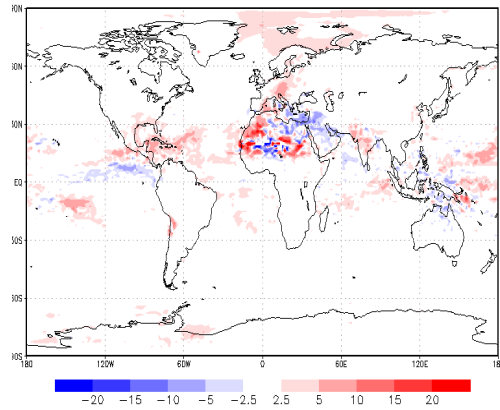


as from Figure 5.1(c). These results are a model of the potential future climate assuming that atmospheric carbon dioxide levels increase steadily until they reach double preindustrial levels at which point they become stable.

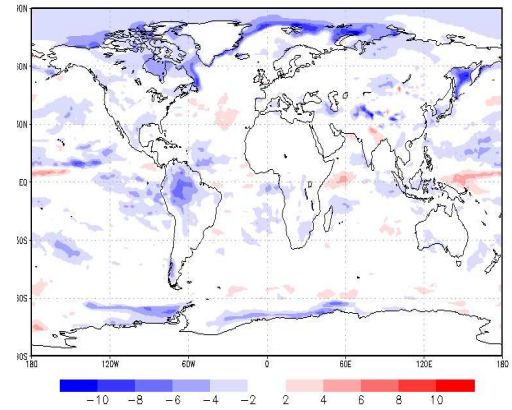
### **5.1.3 Impact of seeding three regions of marine clouds in a double carbon dioxide atmosphere**

Figure 5.2(a) shows the change in CDNC as a result of MCB in three regions in a double carbon dioxide atmosphere. The three seeded regions from Figure 4.2(a) can be clearly seen where the difference in droplet number is over  $300 \text{ cm}^{-3}$ . The large number of droplets in the red regions deplete the liquid water and therefore prevents natural droplet formation downstream of the three seeded regions. In contrast to this, there is an increase in droplet number over Indonesia and the tropical West Pacific. The change in global shortwave forcing as a result of MCB is  $+0.37 \text{ W m}^{-2}$  with the seeding regions subject to changes as large as  $50 \text{ W m}^{-2}$  as shown in Figure 5.2(b). There is also a reduction in shortwave forcing of  $20 \text{ W m}^{-2}$  in the most easterly regions of South America which could in turn warm the area. The reduction in shortwave forcing over the Amazon is a result of the liquid water in the atmosphere being used to form clouds in the South Atlantic as opposed to over the Amazon (Jones et al., 2009). There is also a small reduction (between  $2.5 \text{ W m}^{-2}$  and  $5 \text{ W m}^{-2}$ ) in shortwave forcing over most of the ocean, this is a result of the change in liquid water available to clouds outside of the seeded regions as evaporation rates are reduced with surface temperatures decreases.

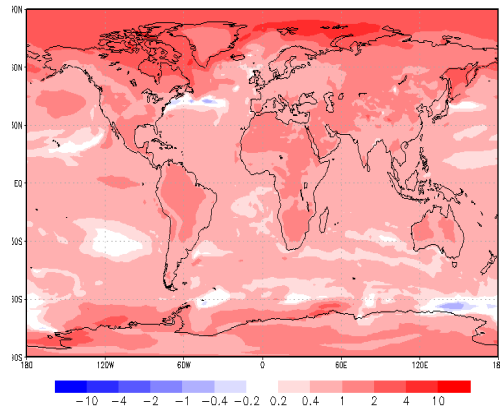
The increase in temperature over the Antarctic in the  $2\text{CO}_2$  is reduced by 1 K compared with Figure 5.1(c) when MCB is deployed in three regions as shown in Figure 5.2(c). The three regions underneath the stratocumulus clouds are shown to cool noticeably and this could have an impact upon marine life. The reduction in cloud forcing in Figure 5.2(b) over the Amazon is reflected in the change in temperature where there is an increase of up to 1 K. The change in temperature as a result of doubling carbon dioxide is  $+0.77 \text{ K}$ , however in an atmosphere with the



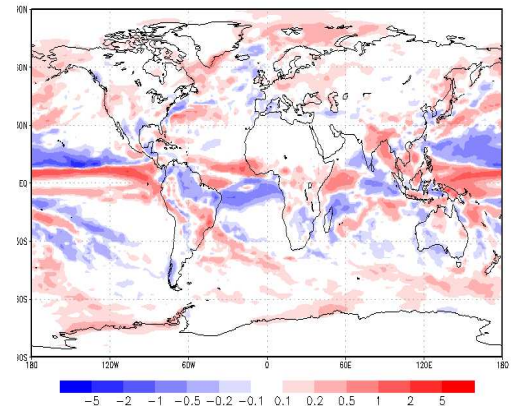
(a) Change in CDNC between the 2CO<sub>2</sub> and CON simulations (cm<sup>-3</sup>).



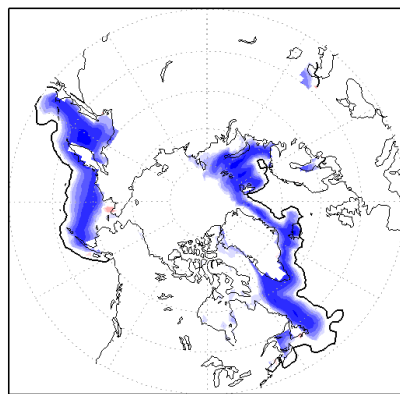
(b) Change in shortwave forcing at the top of the atmosphere between the 2CO<sub>2</sub> and CON simulations (W m<sup>-2</sup>).



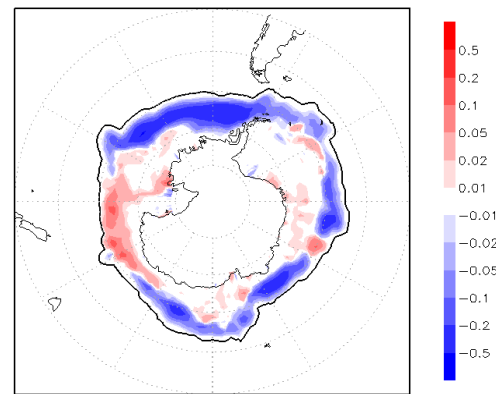
(c) Change in surface temperature between the 2CO<sub>2</sub> and CON simulations (K). This figure uses the same data as Figure 4.3(d).



(d) Change in precipitation rate between the 2CO<sub>2</sub> and CON simulations (mm/day). This figure uses the same data as Figure 4.5(e).



(e) Change in North polar ice cover between the 2CO<sub>2</sub> and CON simulations, contour showing the CON ice limit. This figure uses the same data as Figure 4.7(d).



(f) Change in South polar ice cover between the 2CO<sub>2</sub> and CON simulations, contour showing the CON ice limit. This figure uses the same data as Figure 4.7(d).

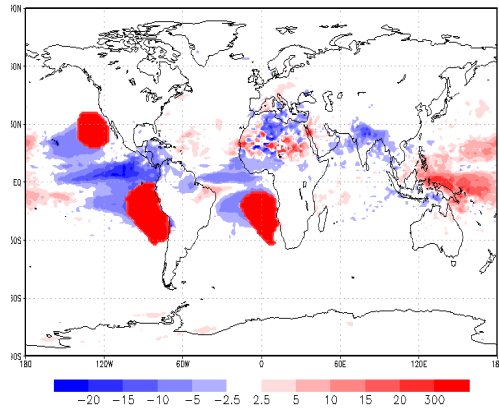
FIGURE 5.1: Comparison of the CDNC (cm<sup>-3</sup>), shortwave forcing (W m<sup>-2</sup>), surface temperature (K), precipitation rate (mm/day) and polar ice cover between the 2CO<sub>2</sub> and CON simulations described in Table 5.1.

three regions of MCB the temperature is found to be 0.12 K lower than in the control scenario.

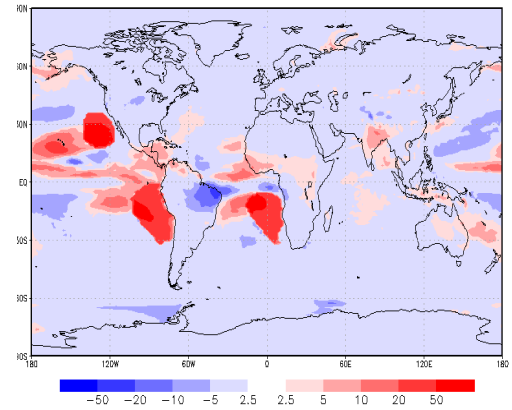
Cooling is non-uniform but is found to have an impact on the polar ice cover (See Figures 5.2(e) and 5.2(f)). In the northern hemisphere there is growth in sea ice relative to the control simulation and the losses in the southern hemisphere are found to be significantly reduced. The redistribution of ice acts to close the Northwest passage at the Bering Sea while unfreezing the waters near Greenland. Doubling atmospheric carbon dioxide concentrations leads to a loss of  $5.5 \times 10^6 \text{ km}^2$  of sea ice across the globe. In a double carbon dioxide atmosphere with three region MCB this loss in ice cover is reduced to  $0.2 \times 10^6 \text{ km}^2$ .

#### **5.1.4 Impact of seeding the entire marine atmosphere in a double carbon dioxide atmosphere**

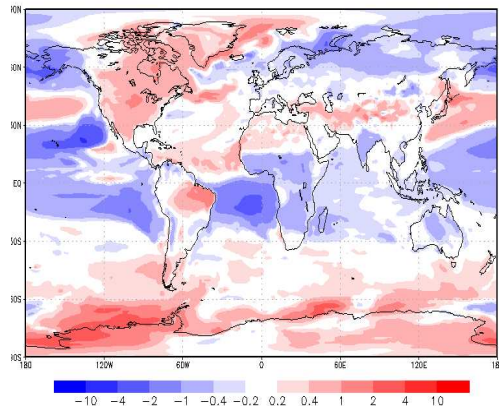
Figure 5.3(a) shows the difference in CDNC between MCBA\_2CO<sub>2</sub> and CON. In MCBA\_2CO<sub>2</sub> the seeding is simulated across all ocean shown in Figure 4.2(b). As a result of the seeding the continents of Africa, Europe and South America all see a reduction in CDNC, with localised effects also impacting South Australia, the Indian sub-continent and the Western United States. The reduction in CDNC over continental areas is a result of the model only identifying CDNC when clouds are present. The water vapour that is used to form continental clouds in the CON simulation appears to be used to form clouds over the ocean. In South East Asia and North Australia there is an increase in CDNC due to seeded air parcels being advected from the oceans. There is a further decrease in CDNC over the Sahara which may result in a change in precipitation over the desert area. As can be seen in Figure 5.3(b) there are three areas with a large change to the shortwave forcing. The two areas in the South Atlantic and North Pacific match recommended seeding regions from Figure 4.2(a). However, they do not exhibit the same behaviour seen at the limits of the seeding regions in Figure 5.2(b). This is due to the lack of any sharp change in CDNC at the edges of the seeding region in MCB3\_2CO<sub>2</sub>. There



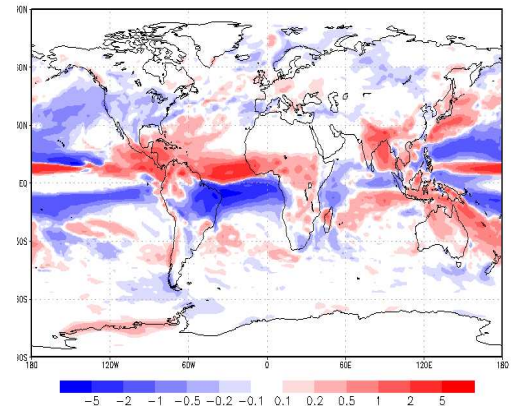
(a) Change in CDNC between the MCB3.2CO<sub>2</sub> and CON simulations (cm<sup>-3</sup>).



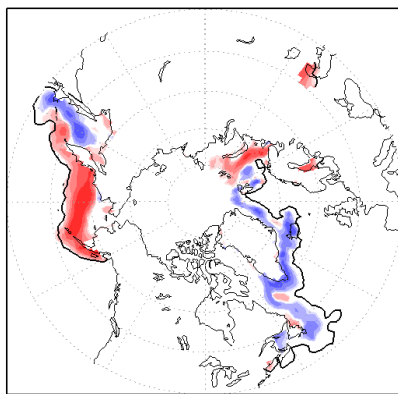
(b) Change in shortwave forcing at the top of the atmosphere between the MCB3.2CO<sub>2</sub> and CON simulations (W m<sup>-2</sup>).



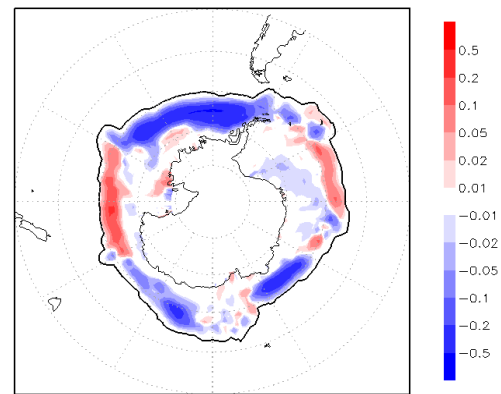
(c) Change in surface temperature between the MCB3.2CO<sub>2</sub> and CON simulations (K). This figure uses the same data as Figure 4.4(e).



(d) Change in precipitation rate between the MCB3.2CO<sub>2</sub> and CON simulations (mm/day). This figure uses the same data as Figure 4.6(e).



(e) Change in North polar ice cover between the MCB3.2CO<sub>2</sub> and CON simulations, contour showing the CON ice limit. This figure uses the same data as Figure 4.8(d).



(f) Change in South polar ice cover between the MCB3.2CO<sub>2</sub> and CON simulations, contour showing the CON ice limit. This figure uses the same data as Figure 4.8(d).

FIGURE 5.2: Comparison of the CDNC (cm<sup>-3</sup>), shortwave forcing (W m<sup>-2</sup>), surface temperature (K), precipitation rate (mm/day) and polar ice cover between the MCB3.2CO<sub>2</sub> and CON simulations described in Table 5.1.

is a peak of  $120 \text{ W m}^{-2}$  in the Pacific equatorial shortwave forcing and an increase in the southern Indian Ocean. The changes in shortwave forcing over land are small in magnitude in comparison with the ocean changes. Despite this there is a reduction in shortwave forcing ( $20 \text{ W m}^{-2}$ ) over the Amazon indicating that the region is reflecting away less energy, this is due to a reduction in cloud levels and may lead to vegetation loss as shown in Jones et al. (2009).

Seeding the entire ocean results in substantial changes in precipitation over the entire globe with reductions of between 0.1 mm/day and 2.0 mm/day over several continents. These reductions could have a severe impact on the rainforests. In contrast to this there is an increase in precipitation over Africa, India and Australia which could alleviate droughts and promote agriculture.

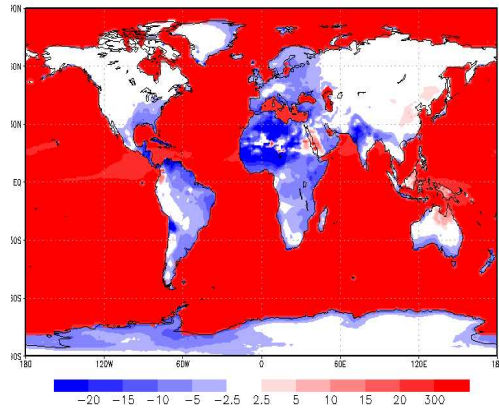
Under the influence of MCB over the entire ocean the majority of the surface has a reduction in temperature of between 2 K and 10 K, this can be seen in Figure 5.3(c). There is a significantly larger decrease in temperature in the Norwegian sea. This appears to be part of a dipole with a large increase in temperature found south of Greenland. These changes in temperature could have an impact on ocean life.

There is an increase in sea ice cover of  $31 \times 10^6 \text{ km}^2$  compared with the Control simulation which further contributes to the shortwave forcing. There is an increase in the southern hemisphere ice cover out to  $55^\circ \text{ S}$ , while in the northern hemisphere the Baltic and Caspian Seas become ice locked.

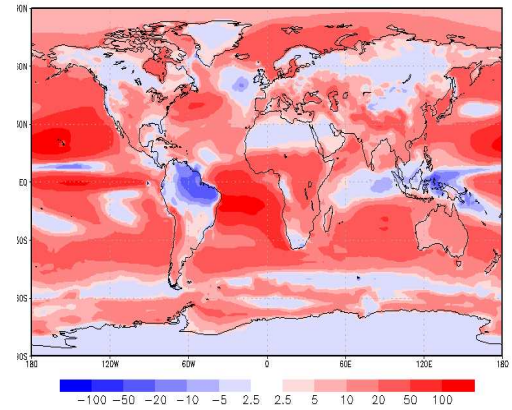
## 5.2 Meridional Heat Flux

The MHF is the process for the transfer of energy from the tropics to the poles. Currents within the atmosphere and ocean work to restore thermal equilibrium essentially by pumping heat towards the poles from the tropics. The ocean is postulated to contribute roughly 2 PW of the 5 PW MHF (Wunsch, 2005). A change in the MHF is a process proposed in this work to link changes in the tropics with changes in polar regions. If the Earth were a solid with no atmosphere or ocean

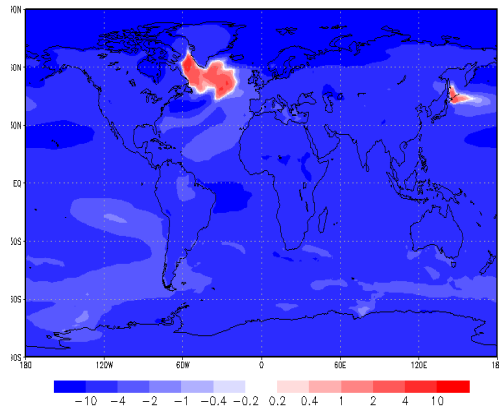




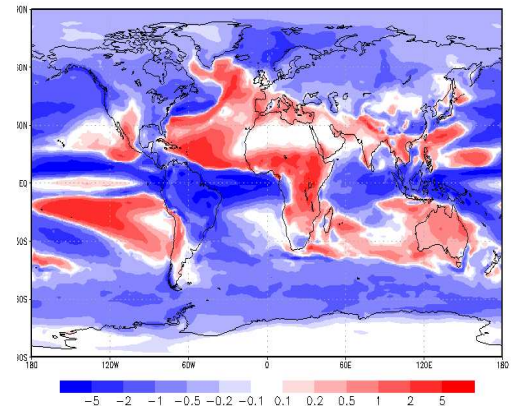
(a) Change in CDNC between the MCBA.2CO<sub>2</sub> and CON simulations (cm<sup>-3</sup>).



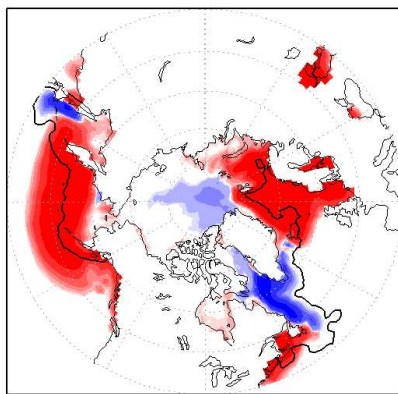
(b) Change in shortwave forcing at the top of the atmosphere between the MCBA.2CO<sub>2</sub> and CON simulations (W m<sup>-2</sup>).



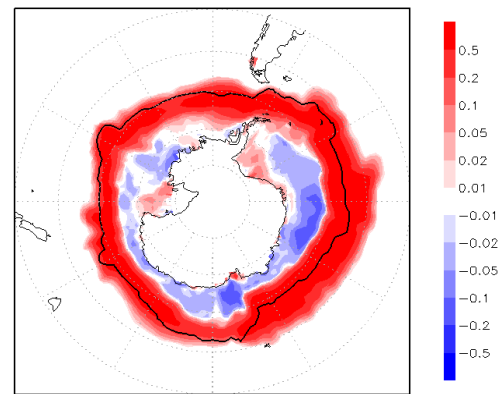
(c) Change in surface temperature between the MCBA.2CO<sub>2</sub> and CON simulations (K). This figure uses the same data as Figure 4.4(f).



(d) Change in precipitation rate between the MCBA.2CO<sub>2</sub> and CON simulations (mm/day). This figure uses the same data as Figure 4.6(e).



(e) Change in North polar ice cover between the MCBA.2CO<sub>2</sub> and CON simulations, contour showing the CON ice limit. This figure uses the same data as Figure 4.8(f).



(f) Change in South polar ice cover between the MCBA.2CO<sub>2</sub> and CON simulations, contour showing the CON ice limit. This figure uses the same data as Figure 4.8(f).

FIGURE 5.3: Comparison of the CDNC (cm<sup>-3</sup>), shortwave forcing (W m<sup>-2</sup>), surface temperature (K), precipitation rate (mm/day) and polar ice cover between the MCBA.2CO<sub>2</sub> and CON simulations described in Table 5.1.

then the energy incoming at the tropics could only be transferred using conduction through the surface or radiation back to space. With the presence of fluids such as an atmosphere or ocean then the possibility of transport of energy polewards exists (Wunsch, 2005). The MHF can be calculated for the atmosphere, ocean or as a sum of both (Trenberth and Caron, 2001; Wunsch, 2005). The method for calculating the total MHF is described in Section 5.2.1.

### 5.2.1 Meridional Heat Flux in HadGEM1

The motion of energy from the tropics to the poles can be calculated in several ways. For this work the method from Trenberth and Caron (2001) is used. Within this method the atmospheric and oceanic heat fluxes are components of the overall radiative MHF; removing the need to integrate over the full atmospheric and oceanic depths while still retaining influences from both. In Trenberth and Caron (2001) the Earth Radiation Budget Experiment (ERBE) dataset is used to calculate the MHF of the climate system which is then split into atmospheric and oceanic components.

The calculation of the MHF cannot be performed in the same manner as evaluating temperature or precipitation as it is not a standard output from HadGEM1. A zonal mean of the radiative flux difference (see Section 4.2.2.1) at the top of the atmosphere is found, this is shown in Figures 5.4(a) and 5.4(b). Figure 5.4(a) is copied from Figure 2 (a) of Wunsch (2005) and shows the radiative flux difference at the top of the atmosphere from the ERBE dataset. Figure 5.4(b) is the HadGEM1 equivalent of Figure 5.4(a).

Latitude bands are loops around the globe with steps in the zonal direction they are defined by the model grid or by the grid of data interpolation. This value is then multiplied by the area of each latitude band. This results in a flux of energy out of the atmosphere which is generally found to be close to  $10^{14}$  W. These results are shown in Figures 5.4(c) and 5.4(d). Figure 5.4(c) is copied from Figure 2 (b) of Wunsch (2005) and shows the latitude weighted energy flux out of the top of



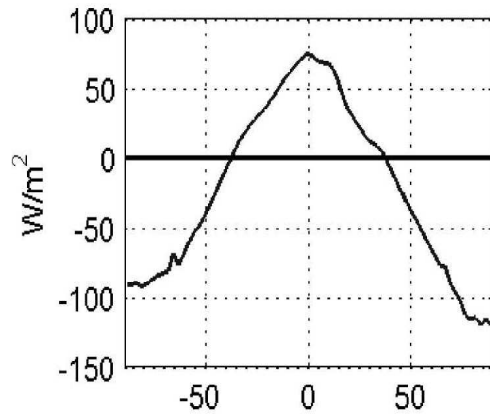
the atmosphere. Figure 5.4(d) is the HadGEM1 equivalent of Figure 5.4(c) and is interpolated to match the ERBE dataset resolution, (see below for details).

The final calculation is to sum the values from the South pole to the North pole. This results in the sinusoidal shape as clearly seen in Figures 5.4(e) and 5.4(f). The dotted line on both Figures 5.4(e) and 5.4(f) shows the result from taking the values from the North Pole to the South Pole, this shows the error in the accumulation at the Equator (Wunsch, 2005). If the climate system is balanced then the dashed line would overlay the solid line. The difference shows the excess energy in the climate system which is responsible for climate changes (Wunsch, 2005).

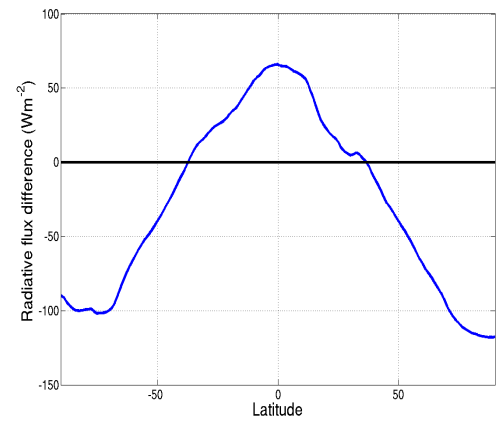
The model data used for this comparison is the final 20 years from the CON simulation described in Table 4.1. Figures 5.4(a) and 5.4(b) appear to be quite similar with the model having a slightly larger range of values between the tropics and the poles. To produce Figure 5.4(d) the data from Figure 5.4(b) is interpolated from the HadGEM1 model grid (See Section 3.1.1) to 2.5° square grid used by the ERBE dataset. The interpolation enables a direct comparison between the results in Figures 5.4(c) and 5.4(d). If the original grid spacing is retained the HadGEM results shows a larger number of smaller fluxes. In Figures 5.4(e) and 5.4(f) the shape of the MHF is predicted well by the model however the imbalances are of different magnitudes. This is possibly due to the model being able to collect all the data simultaneously and not be dependent on point measurements. The simulation in CON is run for 70 years allowing the climate system to approach equilibrium (Parkes et al., 2012).

### **5.2.2 Changes in the MHF as a result of MCB**

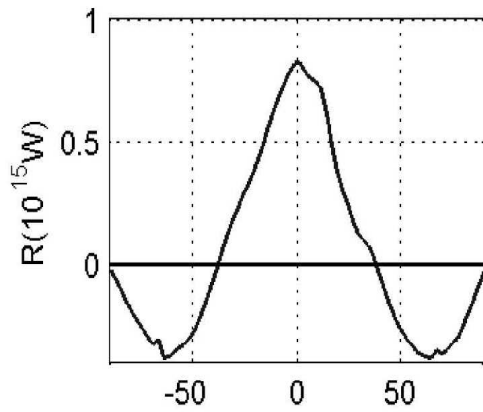
The link between the changes in the CDNC to the impacts on polar regions is shown in stages in the results in Sections 5.1.3 and 5.1.4. With an increase in CDNC, the clouds become more reflective and thus cool the atmosphere and waters below which are then moved by existing oceanic currents. The proposed mechanism that allows MCB to exert an effect on the poles is a change in MHF. The results shown in



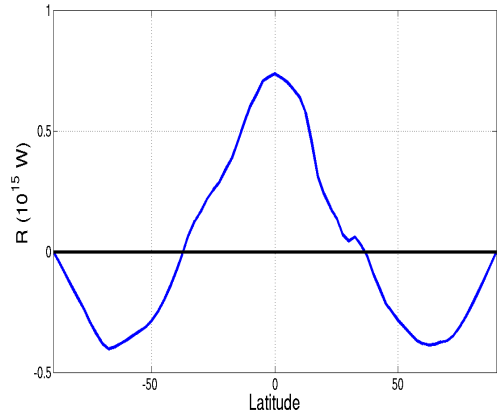
(a) Sum of average incoming and outgoing radiation recorded by the ERBE dataset ( $\text{W m}^{-2}$ ). Image copied from Wunsch (2005).



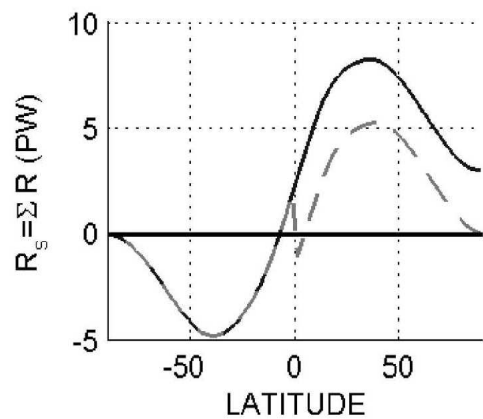
(b) Zonal mean plot of the radiative flux difference at the top of the atmosphere in HadGEM1 ( $\text{W m}^{-2}$ ).



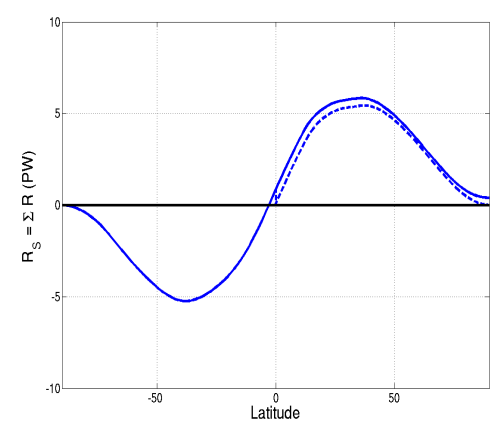
(c) The data from Figure 5.4(a) multiplied by the area in each latitude band (W). Image copied from Wunsch (2005).



(d) The equivalent of Figure 5.4(c) where the data from Figure 5.4(b) is interpolated to the same resolution as the ERBE dataset.



(e) The accumulation from the South to North poles of the data in Figure 5.4(c) (PW). The dotted line shows the value from North to South poles with a jump at the Equator signifying the imbalances in the system. Image copied from Wunsch (2005).



(f) The accumulation from the South to North poles of the data in Figure 5.4(d) (PW). The dotted line shows the value from North to South poles with a jump at the Equator signifying the imbalances in the system.

FIGURE 5.4: A comparison of the radiative flux difference at the top of the atmosphere ( $\text{W m}^{-2}$ ), the latitude weighted radiative power (W) and the radiative MHF (PW) for the ERBE dataset in Wunsch (2005) and this work.

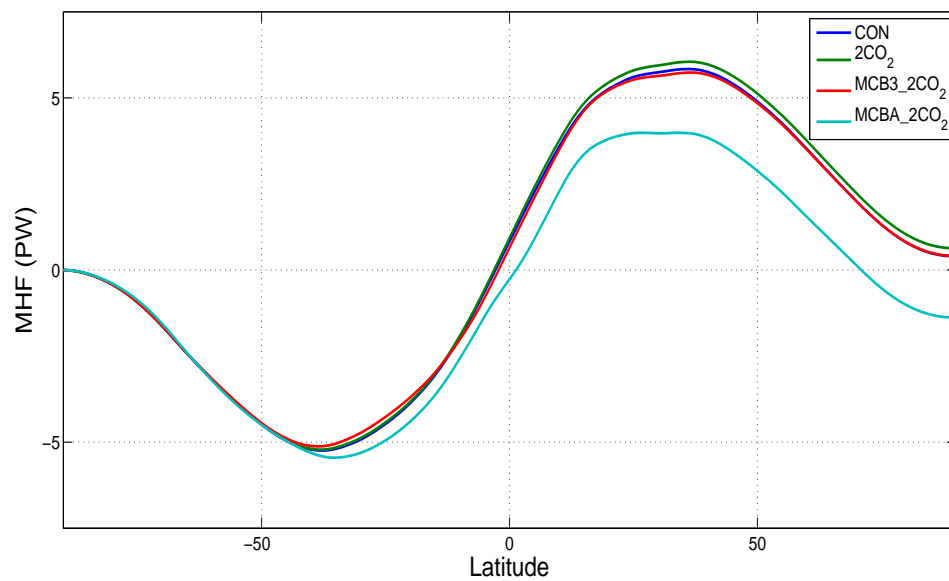


FIGURE 5.5: The total radiative MHF (PW) calculated for four climate simulations described in Table 4.1.

Figure 5.5 all exhibit the expected sinusoidal shape of a MHF. The most noticeable change is the significant reduction in the MHF from MCBA\_2CO<sub>2</sub>. MCBA\_2CO<sub>2</sub> reduces the maximum MHF to 3.98 PW from 5.84 PW in CON. This is a significant reduction from the double preindustrial carbon dioxide levels found in 2CO<sub>2</sub> which increases the maximum MHF to 6.05 PW (Parkes et al., 2012). The maximum MHF in MCB3\_2CO<sub>2</sub> is 5.73 PW which contributes to the slight cooling found in comparison with CON, this is consistent with the polar ice extent plots shown in Figures 5.2(e) and 5.2(f).

### 5.3 Discussion and Summary

An investigation is performed into the impacts of MCB using the HadGEM1 climate model. Within the model the climate system is modified by increasing the CDNC in selected maritime regions. It is shown that the fields such as cloud droplet number concentration have an effect on shortwave forcing and precipitation rate. Furthermore these changes in the temperatures are shown to have an impact on the surface temperature and polar ice cover.

The results from comparing CON and 2CO<sub>2</sub> indicate how changes to the global average carbon dioxide concentration affects both temperature and precipitation rates. However it is noted that the reliability of GCM precipitation predictions in tropical regions is low, Section 3.2.2. When a comparison of MCB3\_2CO<sub>2</sub> or MCBA\_2CO<sub>2</sub> with CON is performed it is possible to assess the climate impact of the MCB scheme in question and its ability to restore an original climate state while in an increased carbon dioxide atmosphere.

The results shown in Sections 5.1.3 and 5.1.4 show the ability of two MCB schemes (three region and whole ocean) to restore the original climate state. In particular the surface temperature and precipitation rate results are of interest as the former is a regularly used metric (Bala et al., 2011; Jones et al., 2011) and the latter is a commonly cited issue with MCB (Bala et al., 2011; Jones et al., 2009, 2011; Rasch et al., 2010). These results show that MCB is capable of restoring global average surface temperatures or reducing them beyond the control state while also reducing precipitation rates by 0.44 mm/day in the case of MCBA\_2CO<sub>2</sub>.

The calculation of the MHF is done in stages as shown in Section 5.2.1 where the results from HadGEM1 are compared to the results from the ERBE dataset calculated in Trenberth and Caron (2001). The zonal average model radiation balance is shown to be in good agreement with the satellite dataset. The amount of energy moved polewards by the MHF is shown to increase with increasing carbon dioxide levels. The final value of the MHF is shown to be in good agreement with observed satellite results whereby the northernmost value should equal zero. This is not the case in the satellite data and the differences are attributed to errors or warming the climate (Wunsch, 2005). The quality of model results is attributed to the model ability to record data from all points simultaneously instead of the temporal and physical restrictions brought on by satellite data recording.

It is suggested here that a change in the MHF is the process that allows MCB to exert an influence on polar regions while seeding in the tropics. This change in MHF in the case of MCB3\_2CO<sub>2</sub> is shown to be close to the magnitude of the change brought about by doubling carbon dioxide concentrations in the atmosphere. The

reduction in MHF is shown to be significantly larger under the entire ocean seeding scenario (MCBA\_2CO<sub>2</sub>).

Future work on the impact of MCB on the MHF could be undertaken to identify the relative contribution of the atmospheric or oceanic MHF as modified by MCB. As the atmosphere and ocean have different response times it is important to identify which flux is modified as this will have an impact on any deployment of MCB.

## **Chapter 6**

# **Impacts of MCB on two aspects the tropical climate**

Marine cloud brightening is focused in the tropics and subtropics where incoming solar radiation is at its greatest. As detailed in Chapter 5 modifications to the tropical radiation balance lead to changes in polar temperatures and ice fractions. In this chapter the impacts of MCB on the tropics are investigated.

### **6.1 Tropical cyclones**

Depending on their geographical location tropical cyclones have several different names including hurricane, typhoon, cyclonic storm, tropical storm and tropical depression. There are seven regions where cyclogenesis is a regular occurrence each with their own season. These seven locations are the North Atlantic, Northwest Pacific, Northeast Pacific, Southwest Pacific, North Indian, Southeast Indian and Southwest Indian ocean basins. A table with the tropical cyclone season and the names used to describe these storms is shown in Table 6.1. Where possible this work uses the geographically correct term for each cyclonic system and otherwise uses tropical cyclone for general cases. Tropical cyclones are a heavily

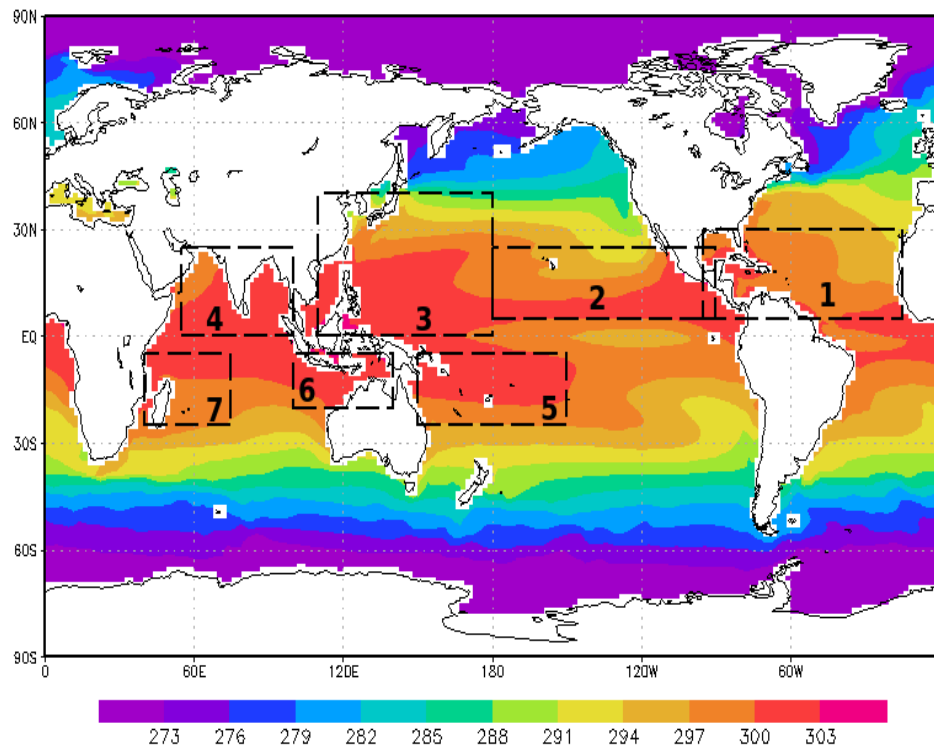


FIGURE 6.1: Locations of seven oceanic basins where investigations are performed into the effectiveness of using MCB as a tool to reduce the intensity of tropical cyclones. Contoured data shows annual average sea surface temperature (K) from the CON simulation described in Table 4.1.

Ocean basin	Number	Season	Peak season	Cyclone name
North Atlantic	1	June - November	August - October	Hurricane
Northeast Pacific	2	May - November	August - September	Hurricane
Northwest Pacific	3	April - January	June - November	Typhoon
North Indian	4	April - December	May, November	Cyclonic storm
Southwest Pacific	5	November - April	December - March	Tropical cyclone
Southeast Indian	6	November - April	December - March	Tropical cyclone
Southwest Indian	7	November - April	December - March	Tropical cyclone

TABLE 6.1: The tropical cyclone season, peak season and basin specific name for several ocean basins. The numbers relate to the numbered basins in Figure 6.1.

researched topic as they are responsible for significant loss of human life as a result of windstorms, floods or landslides. A plot showing the analysis regions for each cyclone basin is shown in Figure 6.1.



### 6.1.1 Life cycle

Formation of tropical cyclones, also known as cyclogenesis, is dependent on several contributory factors. Convection powers tropical cyclones, to maintain convection suitable for forming a tropical cyclone the following conditions need to be met; the surface temperature is required to be above  $26.5^{\circ}\text{C}$ , there must be a sufficiently humid mid troposphere and the storm is required to be a sufficient distance from the Equator to provide angular momentum from the Coriolis force (Gray, 1968). Tropical cyclones require warm waters to a depth of at least 50 m to power the convective systems and therefore any MCB approach requires cooling to the same depth. Winds and waves on the ocean surface encourage mixing while any surface waters that are cooled become denser than the warmer waters below and will sink until they reach an equilibrium depth. These conditions provide an unstable atmosphere which can be disturbed by a low pressure system and form a cyclone. An example low pressure system would be a convective storm moving East during the African monsoon season. To prevent the breakup of the cyclone there is a requirement for low vertical wind shear. While a tropical cyclone can be formed when each of these conditions is satisfied, there is no guarantee of cyclogenesis (Gray, 1968).

While conditions persist it is possible for a tropical cyclone to deepen, whereby the low pressure at the centre of the storm is further reduced. This deepening is sometimes accompanied with the creation of an eye at the centre of the storm, an example eye is shown in Figure 6.2. The path of a tropical cyclone is governed by the large scale atmospheric winds (Gray, 1968). The Coriolis force acts to move a storm polewards while prevailing winds have an Easterly direction. When a storm moves away from the tropics it is often moved by the Westerlies (trade winds) over extra-tropical waters. Tropical cyclones can also interact with other systems including other cyclones. A particular example of this is when two cyclones merge to form a single system (Fujiwhara, 1921).



FIGURE 6.2: A photograph of Hurricane Isabel (2003) in the Atlantic Ocean where the eye can clearly be seen at the centre of the image. Photograph taken by Astronaut Ed Lu aboard the International Space Station. Image released to the public domain by NASA.

Tropical cyclones weaken and dissipate into low pressure systems when the conditions to continue convection break down. This includes landfall where the humidity, latent heat flux and surface temperatures can drop significantly. If a tropical cyclone moves over a patch of ocean with insufficient temperature the convective processes weaken and the storm begins to lose energy (Tuleya, 1994).

### **6.1.2 Impacts**

Tropical cyclones are powerful phenomena with the ability to do significant damage to coastal regions. In some cases a tropical cyclone can persist for several days inland and cause further damage (Tuleya, 1994). Much of the damage done is a result of windspeeds and flooding associated with high rainfall. The high water levels can also lead to mudslides which do further damage. Several well documented

storms are known to have caused deaths and property damage in recent years including Hurricane Katrina (2005) in the United States of America, Typhoon Muifa (2004) in the Philippines and Hurricane Ike (2008) in both the Caribbean and the United States of America.

### **6.1.3 Impacts of climate change and MCB on surface temperatures in tropical cyclone basins**

Climate change is discussed as a potential reason for an observed increase in the amount of power dissipated by North Atlantic Hurricanes (Holland, 1997). Much of this increase in power is attributed to an increase in sea temperatures as a result of global warming (Bender et al., 2010; Emanuel, 2005; Knutson et al., 2010; Mann and Emanuel, 2006; Webster et al., 2005; Wu et al., 2010). There are predictions that global warming leads to a reduction in the frequency of tropical cyclones (Held and Zhao, 2011). With the results of (Held and Zhao, 2011) combined with the work in Bender et al. (2010); Emanuel (2005); Knutson et al. (2010); Webster et al. (2005); Wu et al. (2010) it is predicted that as a result of climate change there will be a fewer storms, each of which will dissipate a larger amount of power. It is however argued by Kossin et al. (2007) that the increase in energy dissipation found in Webster et al. (2005) is not correct as the upward trend in energy is not found in longer records. Therefore Kossin et al. (2007) states that the changes can only be applied to North Atlantic hurricanes.

It is shown in Sections 5.1.3 and 5.1.4 that MCB is capable of restoring control climate temperatures while in a double preindustrial carbon dioxide atmosphere. Work from Dare and McBride (2011) found that more than 93 % of tropical cyclones' formation happened where sea surface temperatures (SSTs) are over 26.5°C. It is suggested that MCB can cool surface oceans this can reduce the energy available to tropical cyclones and therefore reduce their intensity. The suggestion of using MCB to reduce tropical cyclone intensity is not related in any way to seeding the cyclones directly with the aim of dispersing them. MCB instead as shown in

Experiment name	Carbon dioxide fraction (ppm)	Seeding scheme
CON	440	None
2CO <sub>2</sub>	440 + 1 %/year, held at 560	None
MCB3	440	Three regions, Figure 4.2(a)
MCBA	440	All ocean, Figure 4.2(b)
MCB3_2CO <sub>2</sub>	440 + 1 %/year, held at 560	Three regions, Figure 4.2(a)
MCBA_2CO <sub>2</sub>	440 + 1 %/year, held at 560	All ocean, Figure 4.2(b)

TABLE 6.2: The various climate scenario simulations run using HadGEM1 to investigate the climate effects of geoengineering via MCB. Where CON is the Control simulation and 2CO<sub>2</sub> gradually increases carbon dioxide levels to double preindustrial levels. MCB3 and MCBA are MCB simulations run in the control atmosphere without the effects of doubling preindustrial carbon dioxide. MCB3\_2CO<sub>2</sub> and MCBA\_2CO<sub>2</sub> are geoengineering simulations using MCB in the same atmospheric conditions as 2CO<sub>2</sub>. This is a reordered version of Table 4.1.

Chapter 5 relies on changing the temperature of the oceans. These cooled waters are then moved by existing oceanic currents and reduce temperatures across the globe. Each of the seven ocean basins is analysed in turn during the peak tropical cyclone season using the simulations in Table 4.1. Table 6.2 is a reordered copy of Table 4.1 and is shown here for completeness.

An investigation into the temperature changes brought on by the changes detailed in Table 6.2 is divided into three sections. Section 6.1.3.1 investigates the impact of increasing atmospheric carbon dioxide fractions by comparing the temperature results between CON and 2CO<sub>2</sub>. Section 6.1.3.2 investigates the impacts of MCB on temperatures in tropical cyclone basins. The results in Section 6.1.3.3 show the impact of MCB in an increased carbon dioxide atmosphere on the sea surface temperatures in tropical cyclone basins.

### **6.1.3.1 Impacts of increasing greenhouse gas concentrations on sea surface temperatures in tropical cyclone basins**

A comparison between the CON and 2CO<sub>2</sub> simulations allows an investigation into the projected changes in sea surface temperature as a result of increasing atmospheric carbon dioxide concentrations. An increase in temperature is likely to result

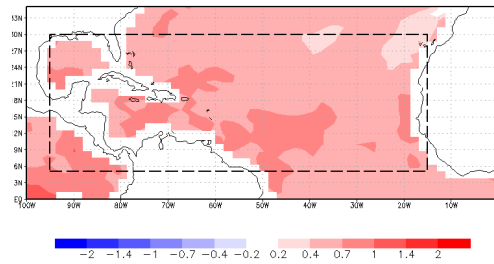
in fewer higher intensity tropical cyclones (Bender et al., 2010; Held and Zhao, 2011; Knutson et al., 2010; Webster et al., 2005; Wu et al., 2010).

The results from Figure 6.3 show that each of the seven tropical cyclone basins analysed are subject to an increase in sea surface temperatures as a result of increasing atmospheric carbon dioxide concentrations. The surface temperature during the tropical cyclone season for all seven basins increases in temperature by between 0.4 K and 0.7 K. The basins which record the largest change in sea surface temperature are the Northeast Pacific and North Atlantic basins which are warmed by 0.63 K and 0.62 K respectively. The basin where the change in temperature is smallest is the Southwest Pacific (Figure 6.3(e)) where the increase in sea surface temperature is 0.44 K.

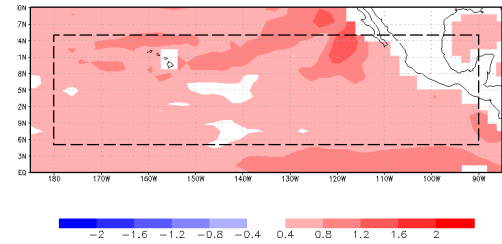
#### **6.1.3.2 Impacts of MCB on sea surface temperatures in tropical cyclone basins**

The results for changes in sea surface temperatures for the seven tropical cyclone basins described in Figure 6.1 and Table 6.1 are shown in Figures 6.4 and 6.5. In Figures 6.4 and 6.5 the results comparing MCB3 and CON are in the left panels with the results comparing MCBA and CON in the right panels. The order of results is the same as shown in Table 6.1.

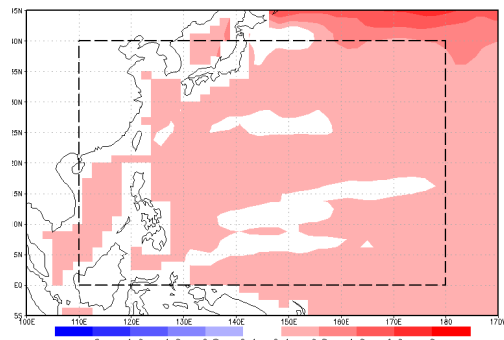
In the comparison between MCB3 and CON the change in surface temperature is always negative with the exception of the Northeast corner of the Pacific Typhoon region shown in Figure 6.4(e), this may be due to circulation changes related to the permanent La Niña (ENSO cool phase) brought on by three region MCB. In the results shown in Figure 6.4(a) there are regions with little to no change in temperature surrounded by areas where cooling is present. Despite the lack of seeding in the Indian ocean the results in Figures 6.4(g), 6.5(c) and 6.5(e) show cooling of between 0.4 K and 0.8 K over the majority of each regions. This cooling is caused by the existing oceanic currents advecting water from the seeded regions (see



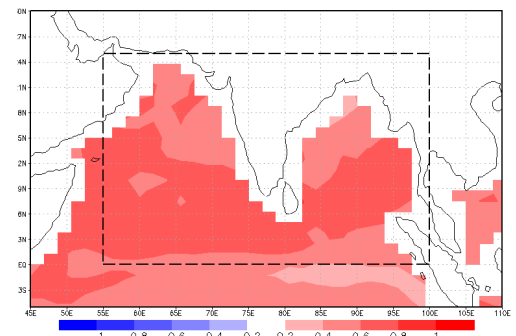
(a) Comparison between MCB3 and CON SST (K) during peak North Atlantic Hurricane season.



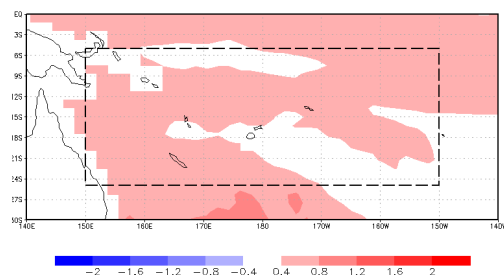
(b) Comparison between MCBA and CON SST (K) during peak Northeast Pacific Hurricane season.



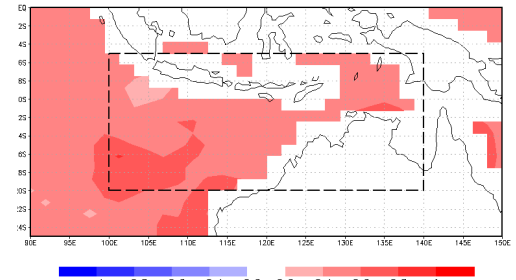
(c) Comparison between MCB3 and CON SST (K) during peak Northwest Pacific Typhoon season.



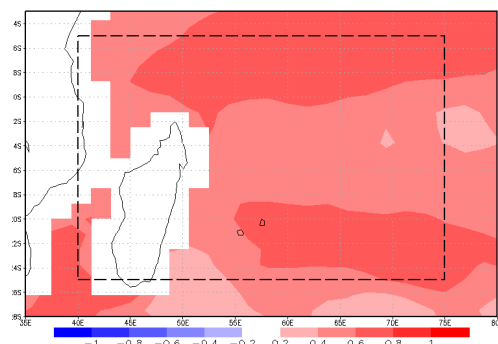
(d) Comparison between MCBA and CON SST (K) during peak North Indian Cyclonic storm season.



(e) Comparison between MCB3 and CON SST (K) during peak Southwest Pacific Tropical storm season.



(f) Comparison between MCBA and CON SST (K) during peak Southeast Indian Tropical storm season.



(g) Comparison between MCB3 and CON SST (K) during peak Southwest Indian Tropical storm season.

FIGURE 6.3: Change in SST (K) during peak tropical cyclone season for the seven tropical cyclone basins described in Figure 6.1. For each plot the dashed box shows the tropical cyclone basin of interest.



Figure 4.2(a)) to other areas. The oceanic currents carrying cooled water to remote regions is investigated in Chapter 5 where the Meridional Heat Flux is shown to change with MCB.

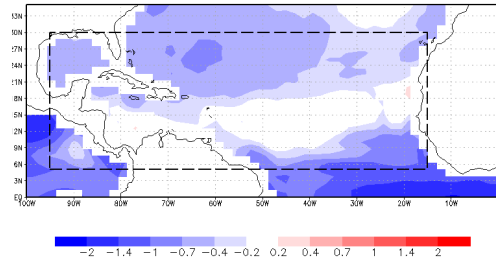
The results from comparing MCBA and CON show a much larger reduction in temperature in all seven basins. Seeding of a tropical cyclone would not happen under realistic deployment of MCB as tropical cyclones create significant amounts of sea spray and would render the flux from a ship in the local area negligible.

### **6.1.3.3 Impacts of MCB in an increased carbon dioxide atmosphere on sea surface temperatures in tropical cyclone basins**

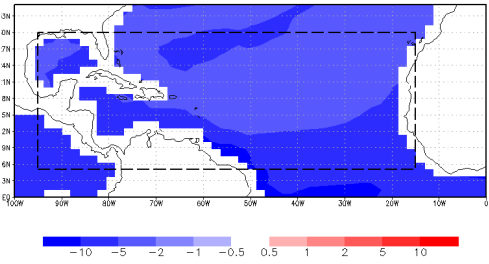
The results in Sections 6.1.3.1 and 6.1.3.2 investigate the impacts of increasing greenhouse gas concentrations and MCB on tropical cyclones independently. This section investigates the impacts of concurrent increases in greenhouse gases with marine cloud brightening. The plots in Figures 6.6 and 6.7 are in the same order as Figures 6.4 and 6.5. In Figures 6.6 and 6.7 the comparison between MCB3\_2CO<sub>2</sub> and CON is on the left and the comparison between MCBA\_2CO<sub>2</sub> and CON is on the right.

The impacts of three region MCB in an increased carbon dioxide concentration atmosphere is cooling in six of the seven tropical cyclone basins, the exception being the North Atlantic. In the North Atlantic the temperature changes across much of the analysed region are close to the control however the south of the region is subject to a small warming of between 0.3 K and 0.7 K. The warming in the south of the North Atlantic hurricane development region (Figure 6.6(a)) would lend extra energy to any tropical storms or hurricanes. Tropical storms that propagate from African Easterly waves often follow the southern edge of the hurricane development region and the results here indicate that three region MCB would not ameliorate the warming brought on by increasing atmospheric greenhouse gas concentrations. The warming in the north of the Northwest Pacific typhoon development region (Figure 6.6(e)) is not in the primary storm track and would not result in an increase

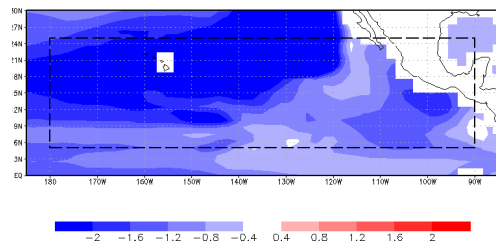




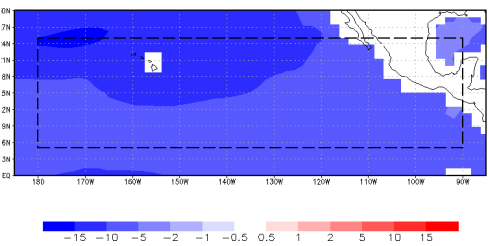
(a) Comparison between MCB3 and CON SST (K) during peak North Atlantic Hurricane season.



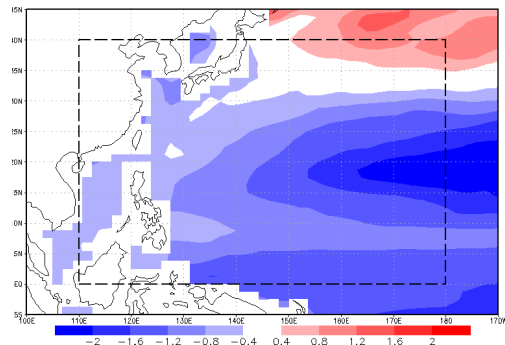
(b) Comparison between MCBA and CON SST (K) during peak North Atlantic Hurricane season.



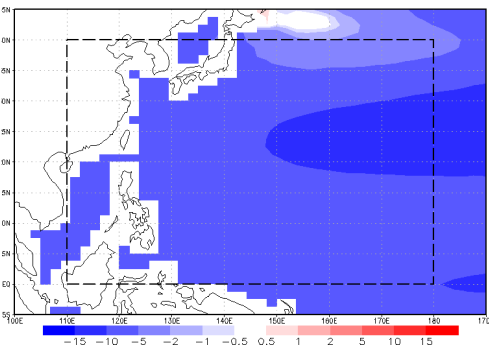
(c) Comparison between MCB3 and CON SST (K) during peak Northeast Pacific Hurricane season.



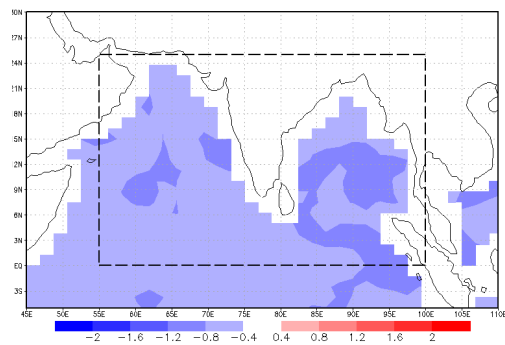
(d) Comparison between MCBA and CON SST (K) during peak Northeast Pacific Hurricane season.



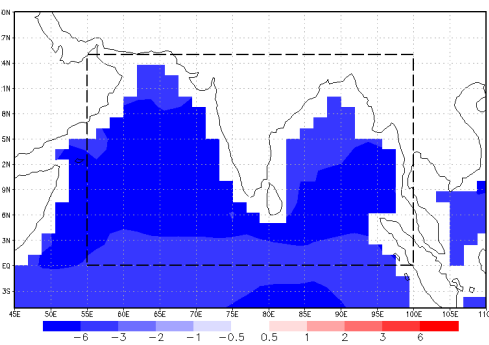
(e) Comparison between MCB3 and CON SST (K) during peak Northwest Pacific Typhoon season.



(f) Comparison between MCBA and CON SST (K) during peak Northwest Pacific Typhoon season.

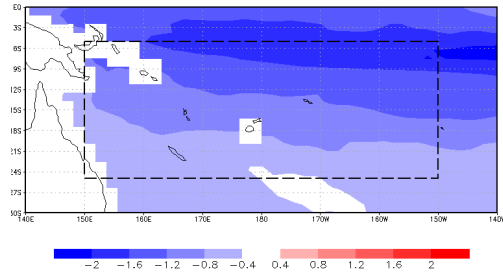


(g) Comparison between MCB3 and CON SST (K) during peak North Indian Cyclonic storm season.

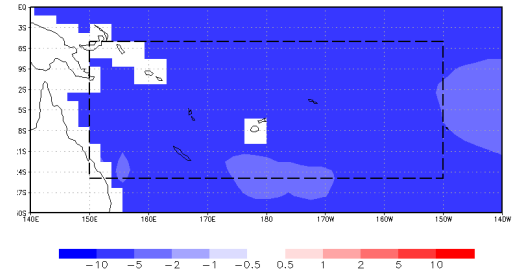


(h) Comparison between MCBA and CON SST (K) during peak North Indian Cyclonic storm season.

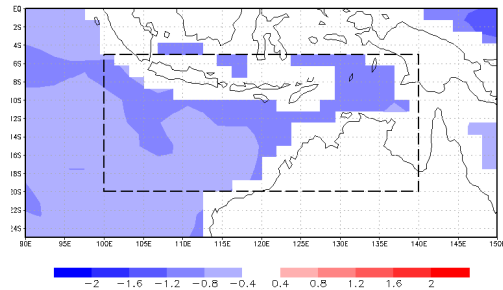
FIGURE 6.4: Change in SST (K) during peak tropical cyclone season for the North Atlantic, Northeast Pacific, Northwest Pacific and North Indian ocean basins as a result of MCB in three regions (left panels) or MCB over the entire ocean surface (right panels). For each plot the dashed box shows the tropical cyclone basin of interest.



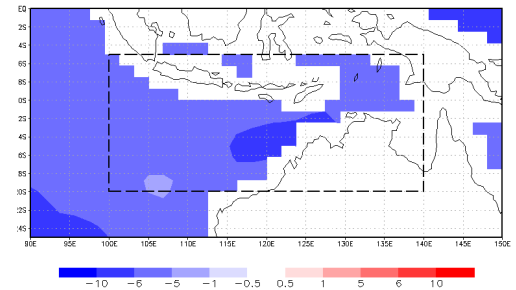
(a) Comparison between MCB3 and CON SST (K) during peak Southwest Pacific Tropical storm season.



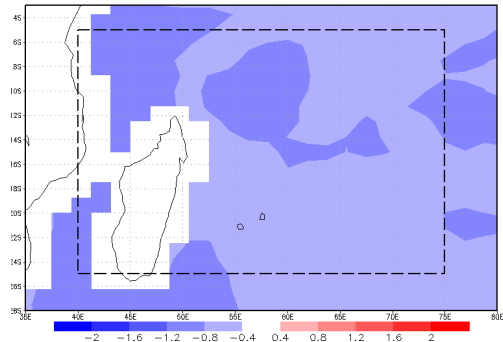
(b) Comparison between MCBA and CON SST (K) during peak Southwest Pacific Tropical storm season.



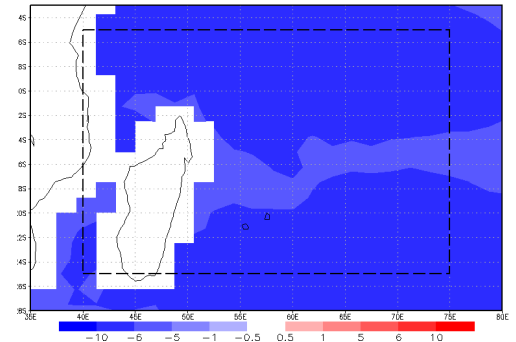
(c) Comparison between MCB3 and CON SST (K) during peak Southeast Indian Tropical storm season.



(d) Comparison between MCBA and CON SST (K) during peak Southeast Indian Tropical storm season.



(e) Comparison between MCB3 and CON SST (K) during peak Southwest Indian Tropical storm season.



(f) Comparison between MCBA and CON SST (K) during peak Southwest Indian Tropical storm season.

FIGURE 6.5: Change in SST (K) during peak tropical cyclone season for the Southwest Pacific, Southeast Indian and Southwest Indian ocean basins as a result of MCB in three regions (left panels) or MCB over the entire ocean surface (right panels). For each plot the dashed box shows the tropical cyclone basin of interest.

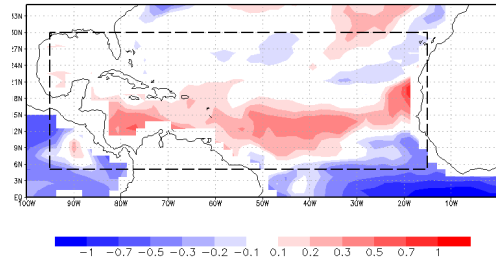
in typhoon energy. The remaining five tropical cyclone basins (Northeast Pacific, North Indian, Southwest Pacific, Southeast Indian and Southwest Indian) each are cooled between 0.28 K and 1.1 K with a maximum cooling found in the Northeast Pacific ocean basin (see Table 6.3). The stronger cooling found in the Northeast Pacific ocean basin is a result of the close proximity of the North Pacific seeding region shown in Figure 4.2(a).

The comparison between MCBA\_2CO<sub>2</sub> and CON shows a strong cooling across all seven tropical cyclone basins with a maximum cooling of 8.1 K found in the Northeast Pacific basin. The smallest cooling is found in the North Atlantic, indicating that this region warms more readily in a double carbon dioxide atmosphere.

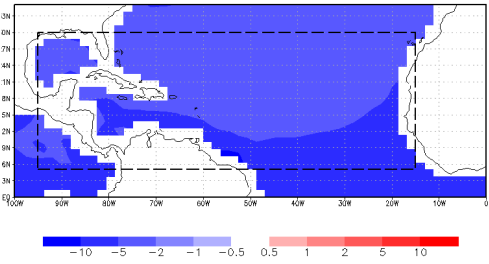
#### **6.1.4 Discussion and summary of the impacts of climate change and MCB on tropical cyclones**

An investigation into the effectiveness of using MCB to alter tropical cyclone intensity has been carried out using the HadGEM1 climate model. It is shown in several publications that tropical cyclone formation is dependent on multiple factors including the temperature of the waters below the cyclonic system (Dare and McBride, 2011; Gray, 1968; Holland, 1997). Furthermore it is shown that the increase in global average temperatures brought on by climate change results in fewer higher intensity tropical cyclones (Bender et al., 2010; Knutson et al., 2010; Webster et al., 2005; Wu et al., 2010). Tropical cyclones however form during a specific season which is dependant on location. To account for this the temperature results are averaged over the most active months of each tropical cyclone season. The average change in surface temperatures for each ocean basin are shown in Table 6.3.

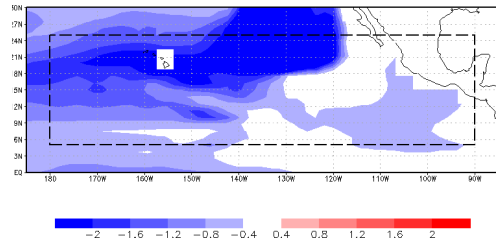
The results shown in Figures 6.6 and 6.7 show that during peak tropical cyclone seasons the surface temperatures can be cooled using MCB while in an increased carbon dioxide concentration atmosphere. Several publications show that MCB is capable of reducing sea surface or surface temperatures while in an atmosphere



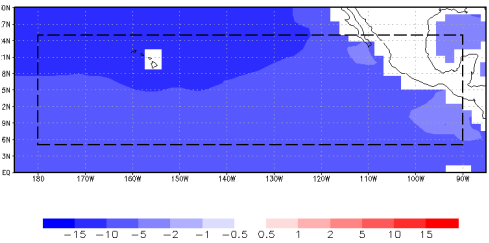
(a) Comparison between MCB3 and CON SST (K) during peak North Atlantic Hurricane season.



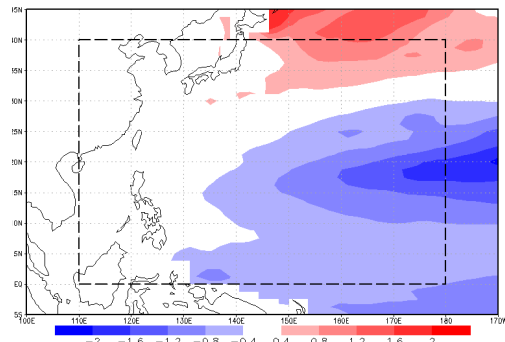
(b) Comparison between MCBA and CON SST (K) during peak North Atlantic Hurricane season.



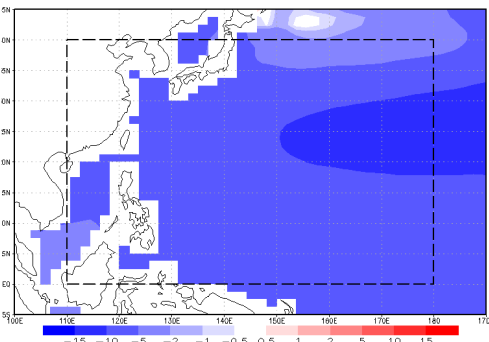
(c) Comparison between MCB3 and CON SST (K) during peak Northeast Pacific Hurricane season.



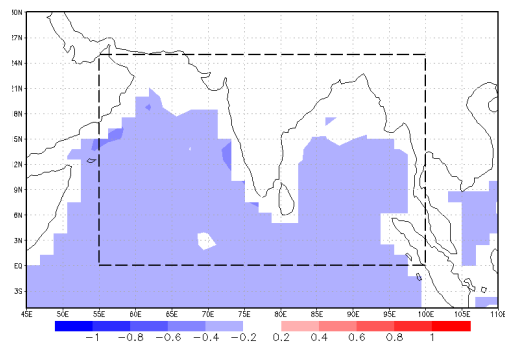
(d) Comparison between MCBA and CON SST (K) during peak Northeast Pacific Hurricane season.



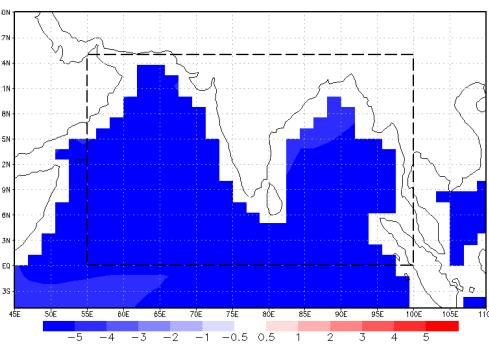
(e) Comparison between MCB3 and CON SST (K) during peak Northwest Pacific Typhoon season.



(f) Comparison between MCBA and CON SST (K) during peak Northwest Pacific Typhoon season.

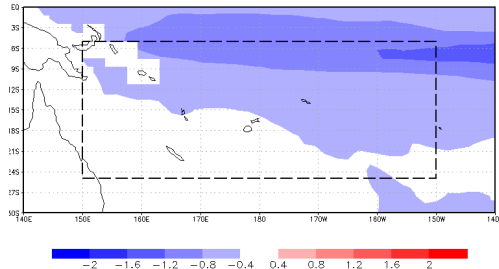


(g) Comparison between MCB3 and CON SST (K) during peak North Indian Cyclonic storm season.

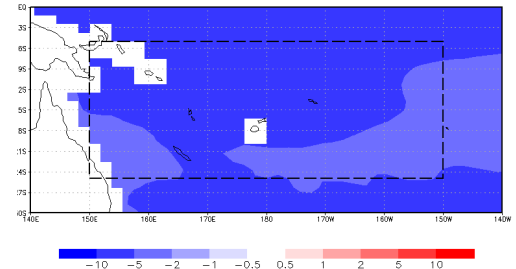


(h) Comparison between MCBA and CON SST (K) during peak North Indian Cyclonic storm season.

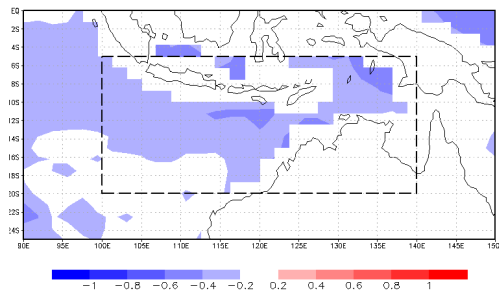
FIGURE 6.6: Change in SST (K) during peak tropical cyclone season for the North Atlantic, Northeast Pacific, Northwest Pacific and North Indian ocean basins as a result of MCB in three regions (left panels) or MCB over the entire ocean surface (right panels) in an increased carbon dioxide atmosphere. For each plot the dashed box shows the tropical cyclone basin of interest.



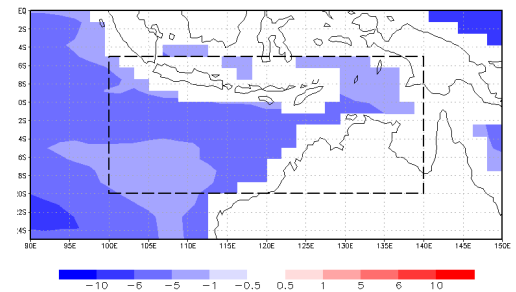
(a) Comparison between MCB3 and CON SST (K) during peak Southwest Pacific Tropical storm season.



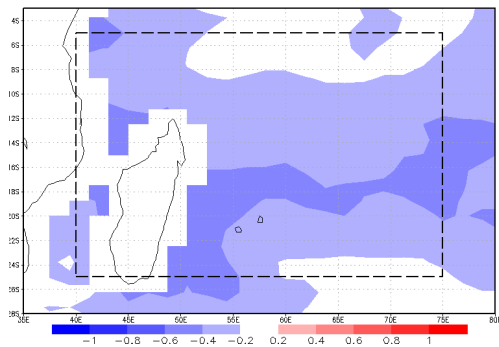
(b) Comparison between MCBA and CON SST (K) during peak Southwest Pacific Tropical storm season.



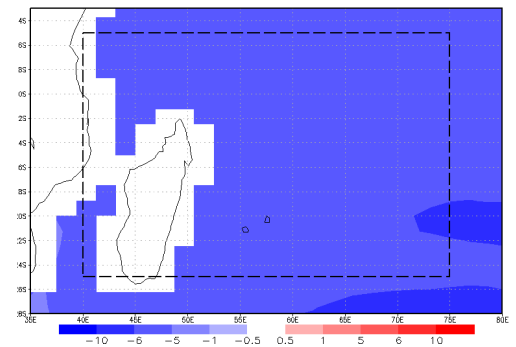
(c) Comparison between MCB3 and CON SST (K) during peak Southeast Indian Tropical storm season.



(d) Comparison between MCBA and CON SST (K) during peak Southeast Indian Tropical storm season.



(e) Comparison between MCB3 and CON SST (K) during peak Southwest Indian Tropical storm season.



(f) Comparison between MCBA and CON SST (K) during peak Southwest Indian Tropical storm season.

FIGURE 6.7: Change in SST (K) during peak tropical cyclone season for the Southwest Pacific, Southeast Indian and Southwest Indian ocean basins as a result of MCB in three regions (left panels) or MCB over the entire ocean surface (right panels) in an increased carbon dioxide atmosphere. For each plot the dashed box shows the tropical cyclone basin of interest.

with increasing carbon dioxide concentrations (Bala et al., 2011; Jones et al., 2009, 2011; Rasch et al., 2010). Results from Figures 6.6 and 6.7 are consistent with published results while focusing on peak tropical cyclone seasons. As can be seen in Table 6.3 MCB3 is capable of cooling surface waters between 0.5 K and 2.0 K which could lead to a reduction in the available energy for forming tropical cyclones. The results from MCBA are much larger in magnitude with cooling values of between 5.5 K and 9.0 K.

Future work on the topic of impacts on tropical cyclones by MCB could use a combination of climate model results and tropical cyclone forecast model results. The oceanic and atmospheric outputs from a climate model are potential inputs for the tropical cyclone forecast model to allow a deeper understanding of the impacts of MCB on tropical cyclone formation and development.

## **6.2 Coral bleaching**

Coral reefs are structures built over long timescales by colonies of corals. Corals are small invertebrates that form a calcium based exoskeleton as they grow. The build up of the exoskeletons eventually forms a reef, the largest group of which is the Great Barrier Reef to the northeast of Australia. Corals exist in a symbiotic relationship with algae within their cells, the corals provide nutrients to the algae which in turn photosynthesise energy from solar radiation and feed the coral. In times of stress, from temperature or acidity, corals will expell their algae and discolour to white (Kleypas et al., 2008; Lough, 2000). The discolouration is known as coral bleaching (Eakin et al., 2010; Hennessy et al., 2007). Corals reefs support large ecosystems, much like forests on land where the reef provides food, shelter and hunting grounds for several species ranging from sponges to sharks.

Ocean Basin	2CO <sub>2</sub> - CON	MCB3 - CON	MCBA - CON	MCB3_2CO <sub>2</sub> - CON	MCBA_2CO <sub>2</sub> - CON
North Atlantic	0.62 K	-0.46 K	-5.4 K	0.032 K	-4.8 K
Northeast Pacific	0.63 K	-1.9 K	-8.9 K	-1.1 K	-8.1 K
Northwest Pacific	0.51 K	-0.93 K	-7.6 K	-0.35 K	-7.2 K
North Indian	0.61 K	-0.74 K	-6.0 K	-0.28 K	-5.4 K
Southwest Pacific	0.44 K	-1.1 K	-5.9 K	-0.52 K	-5.4 K
Southwest Indian	0.57 K	-0.77 K	-6.1 K	-0.32 K	-6.1 K
Southeast Indian	0.54 K	-0.81 K	-5.5 K	-0.29 K	-5.5 K

TABLE 6.3: Difference in sea surface temperature (K) between five climate scenarios and a control in seven tropical cyclone development regions during peak tropical cyclone season.



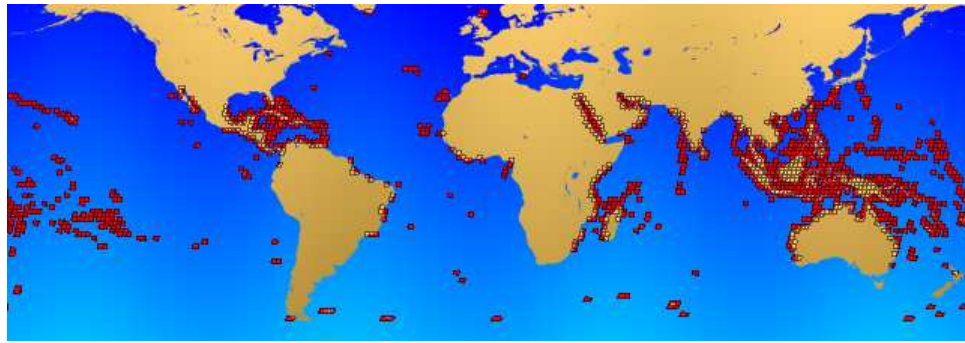


FIGURE 6.8: Location of coral reefs generated from data collected by the Millennium Coral Reef Landsat Archive project undertaken by NASA.

### 6.2.1 Coral reef locations

Coral reefs are generally found between  $30^\circ$  and the Equator with rarer cold and deep water corals found outside this region. As corals are dependent on both a flow of nutrients and sunlight they typically inhabit regions with agitated clear water. Figure 6.8 shows an image of all the reefs captured by a NASA survey between 1999 and 2003. Figure 6.8 shows that coral reefs are commonly found in the Caribbean, the rim of the Indian Ocean, in the South East Asian island chains and out into the Pacific ocean.

### 6.2.2 Impacts of climate change and MCB on sea surface temperatures in regions containing coral reefs

The results in Figure 6.9 show temperature changes in tropical regions as a result of either increasing carbon dioxide concentrations, geoengineering via MCB or both. The results from increasing atmospheric carbon dioxide concentrations shown in Figure 6.9(a) shows temperature increases of between 0.4 K and 1 K across all reef regions. The tropical cooling brought on by MCB3 in a control atmosphere reduces temperatures in reef regions by between 0.4 K and 1.4 K, while the MCBA results in temperature decreases of between 4 K and 6 K. Figures 6.9(d) and 6.9(e) show the results of MCB in an increased carbon dioxide concentration atmosphere.

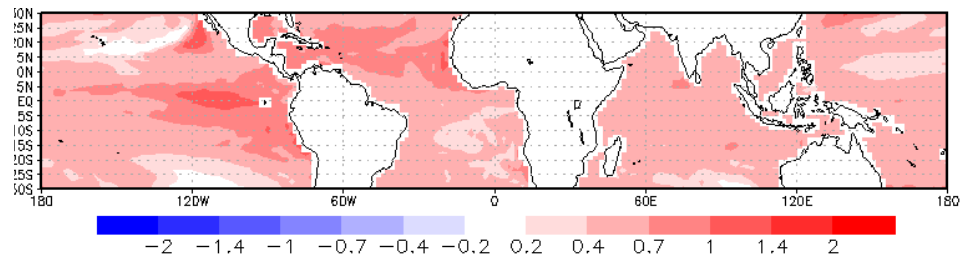
The comparison between MCB3\_2CO<sub>2</sub> and CON shows temperature differences in reef regions of between -0.7 K and +0.4 K with the Great Barrier Reef near Australia subject to temperature changes of less than 0.2 K. The stronger cooling brought on by all sea seeding in an increased carbon dioxide concentration atmosphere results in temperature changes of between -4 K and -6 K.

### **6.2.3 Discussion and summary of the impacts of climate change and MCB on regions containing coral reefs**

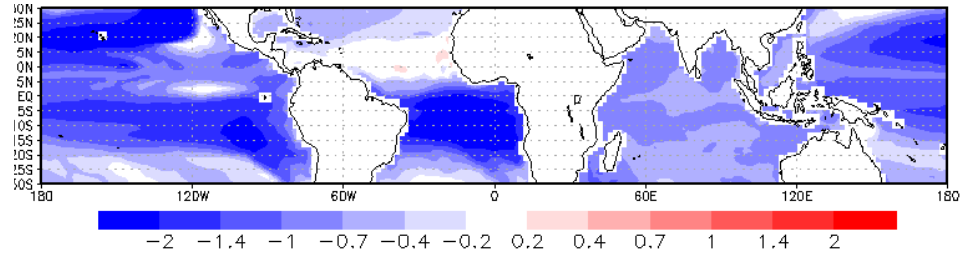
Following work on tropical cyclones, an investigation into temperate changes over coral reefs is performed using the HadGEM1 climate model. The vulnerability of corals to climate change and global warming in particular is noted in the IPCC 4th assessment report (Hennessy et al., 2007; Parry et al., 2007).

The results in Figure 6.9 show that increasing atmospheric carbon dioxide concentrations lead to an increase in tropical SSTs which in turn may cause thermal stress to corals. The warming brought on by increasing atmospheric carbon dioxide concentrations is mitigated by three region MCB (Figure 6.9(d)). Using all sea seeding to mitigate climate change may overcool the tropics and lead to further stress on the corals.

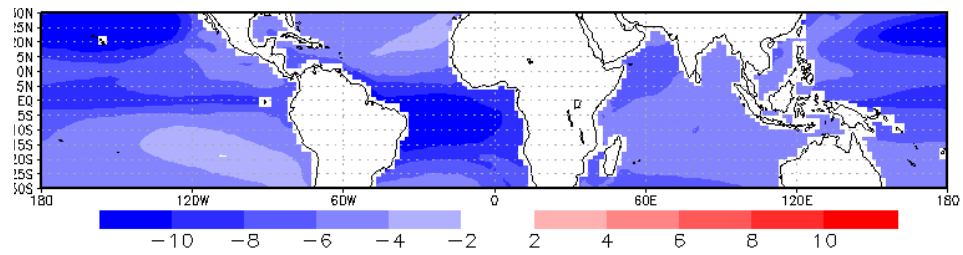
Corals are dependent on photosynthesis for a portion of their energy and therefore the increase in cloud cover as a result of MCB requires careful investigation. The results from three region seeding in an increased carbon dioxide concentration atmosphere indicate that MCB could reduce the thermal stress on corals and has the relative advantage of seeding over very few reefs. In contrast all sea seeding leads to a significant overcooling and involves seeding over all coral reefs a combination which may be very damaging to reefs and the surrounding ecosystems.



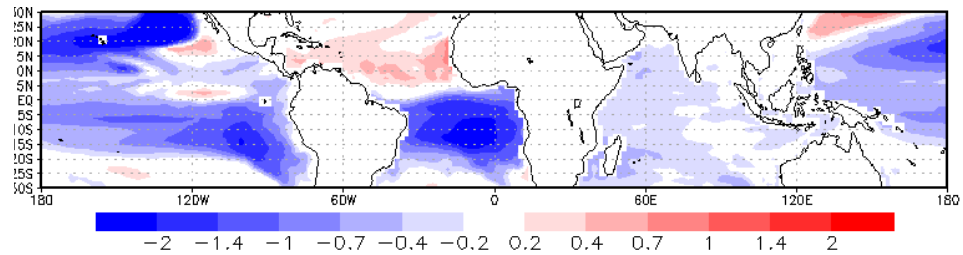
(a) Comparison between 2CO<sub>2</sub> and CON annual average SST (K) between 30° N and 30° S. This figure uses the same data as Figure 4.3(d).



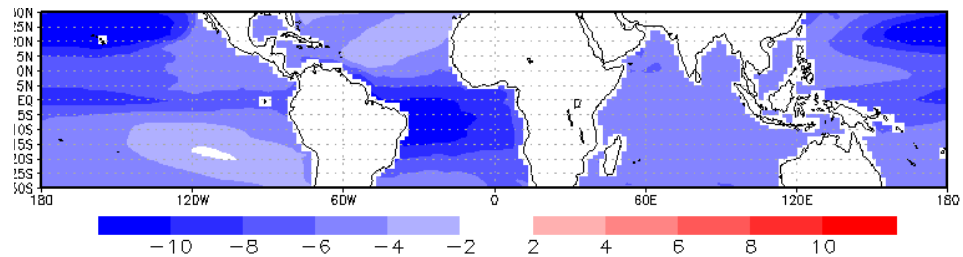
(b) Comparison between MCB3 and CON annual average SST (K) between 30° N and 30° S.



(c) Comparison between MCBA and CON annual average SST (K) between 30° N and 30° S.



(d) Comparison between MCB3.2CO<sub>2</sub> and CON annual average SST (K) between 30° N and 30° S. This figure uses the same data as Figure 4.4(e).



(e) Comparison between MCBA.2CO<sub>2</sub> and CON annual average SST (K) between 30° N and 30° S. This figure uses the same data as Figure 4.4(f).

FIGURE 6.9: Difference in annual average sea surface temperature (K) between five climate scenarios and a control scenario in tropical regions between 30° N and 30° S.

Expansions of the work on coral reefs, involves using dedicated models which can read in climate model outputs and predict with higher skills levels the impacts of either climate change or MCB on coral reefs (Private Communication Joanie Kelypas 2012).

## **Chapter 7**

# **Pseudo-random seeding in a climate model**

The HadGEM series of climate models is used to investigate MCB for fixed locations of seeding to assess the impacts of geoengineering (Jones et al., 2009, 2011; Latham et al., 2012, 2008). The results from Jones et al. (2009) indicate that seeding the South Atlantic Ocean leads to a significant reduction in precipitation over the Amazon region (see Section 4.2.1.1 for details). The results in Section 4.2.1.2 show an increase in Saharan precipitation is also possible after deployment of MCB. This chapter explores the hypothesis that it is possible to use MCB to target desired climate changes such as an increase in precipitation or a decrease in polar temperatures. The impact of MCB on precipitation patterns is a criticism of the method and is investigated in Bala et al. (2011); Jones et al. (2009, 2011); Latham et al. (2012); Rasch et al. (2010).

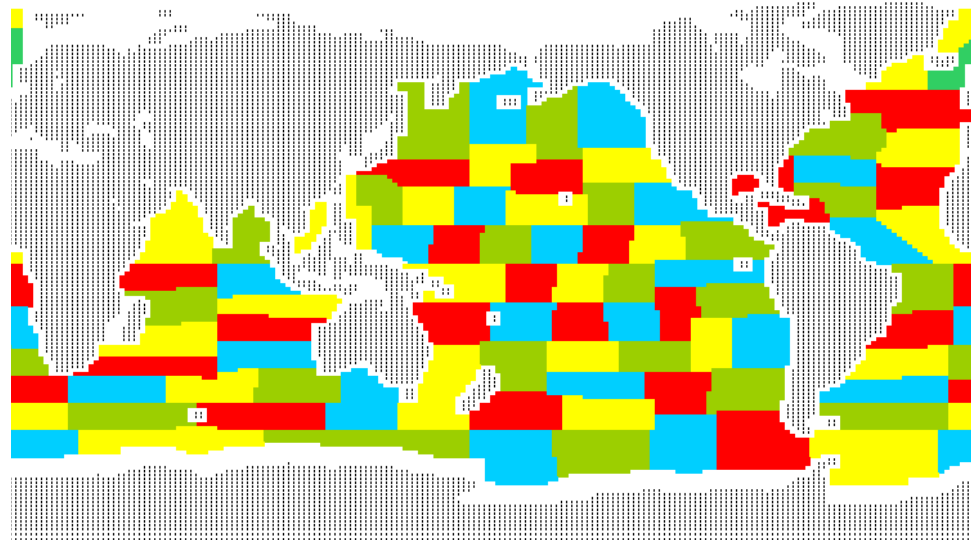
### **7.1 Method**

The principal concept used herein is that it is possible to pseudo-randomly seed multiple regions across the globe and then identify the signal from each region by

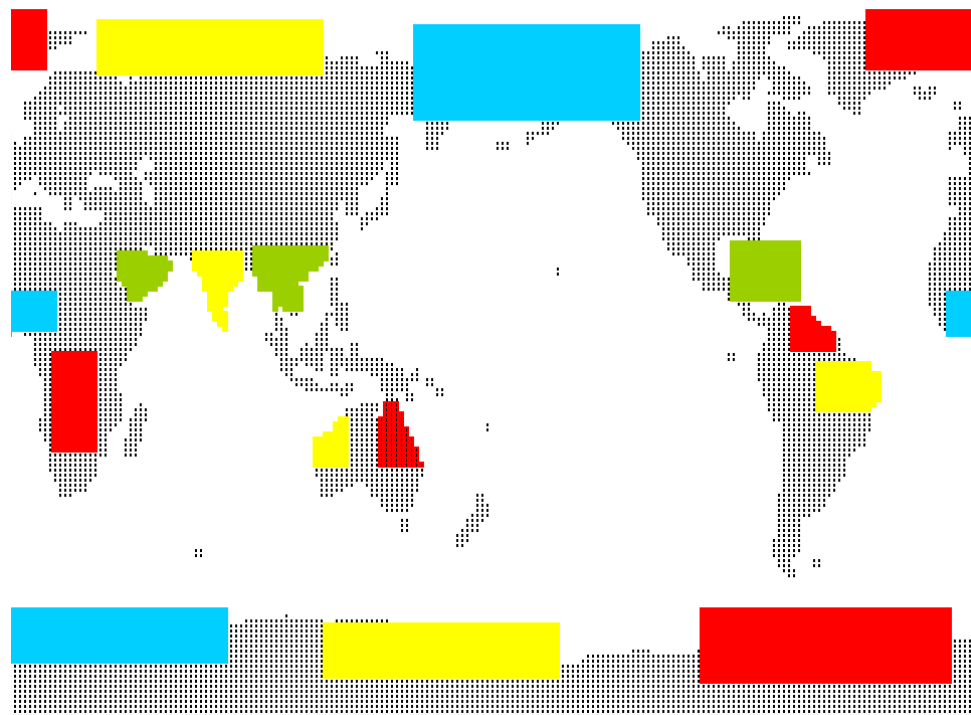
deconstructing the timeseries of the variable of interest in an analysis region (S. Salter Personal Communication 2011). Figure 7.1 shows the seeding and analysis masks used in this chapter. The seeding regions are designed to all be of similar size, with the exception of the two regions near Iceland where one region is split in two. The seeding regions do not match the seeding regions from previous studies such as Jones et al. (2009, 2011) or work in Chapters 4, 5 and 6. Multiple smaller regions are selected to allow more detailed investigations of transfer functions from remote regions to selected analysis regions. To perform the pseudo-random seeding on the 89 regions shown in Figure 7.1(a) the model is initially run normally for 20 years starting from a 2050 CON simulation start point (see Section 4.1) while outputting the mean CDNC every ten days. The model is then rerun with the CDNC values fixed at their ten day average values. The 89 seeding regions shown in Figure 7.1(a) are switched ‘on’ and ‘off’ using a unique pseudo-random sequence. When a region is ‘on’ the number of droplets is multiplied by 150 % and when it is ‘off’ the droplet number is reduced to 66 %. Figure 7.1(b) shows the analysis regions used in this chapter. The analysis regions are designed to cover areas of interest in both the poles and the tropics.

Figure 7.2 shows an example of this set up using randomly generated numbers between 0 and 150 as a substitute for the CDNC. The pseudo-random number sequences for this chapter are generated using the `Rand` function within the MATLAB software. In order to ensure the quality of results the pseudo-random simulations are run using eight different sets of pseudo-random numbers. For each pseudo-random set of values the second half of the track is the inverse of the first half to remove any biases. A step by step description of the method used is detailed in the bullet points below and is also shown in flow chart form in Appendix B.

- Calculate average results of the desired variable for both fixed and modified records over chosen analysis region, Figures 7.3(a) and 7.3(b)
- Subtract fixed record results from the modified record results to remove annual cycle, Figure 7.3(c)



(a) Image showing the 89 seeding areas used to investigate the effects of pseudo-random seeding in HadGEM1.



(b) Image showing the 16 analysis areas used to investigate the effects of pseudo-random seeding in HadGEM1.

FIGURE 7.1: Seeding and analysis maps used in development and analysis of pseudo-random seeding of a climate model.



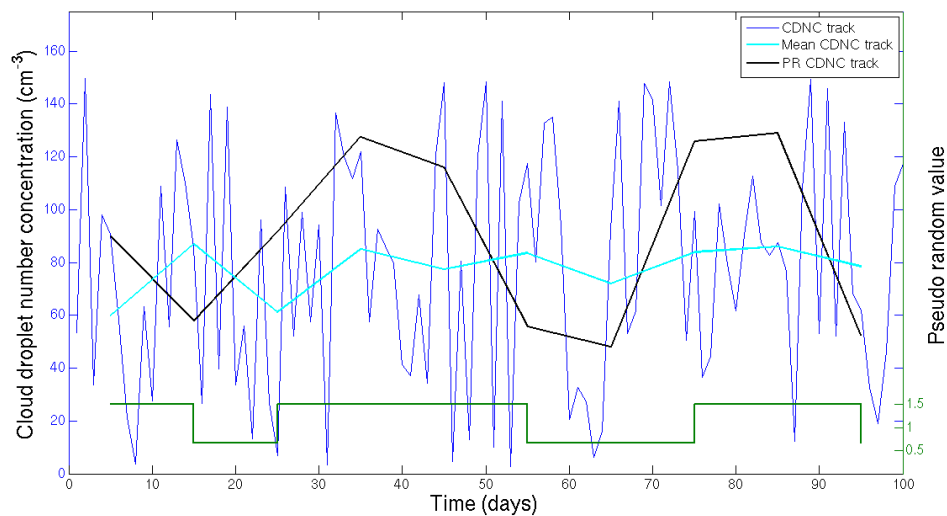


FIGURE 7.2: An example of randomly generated cloud droplet numbers (blue), the average of the random series (cyan), a pseudo-random sequence (green) and the average of the random sequence multiplied by the pseudo-random sequence (black).

- Subtract mean from remaining record to give new average of zero, Figure 7.3(d)
- While seeding is switched ‘on’ in the seeding region, invert the value in Figure 7.3(d) about zero, Figure 7.3(e)
- The value of the mean of the pseudo-random switched track (Figure 7.3(e)) divided by the seeding fraction (150 %) is the transfer function
- Mean the transfer functions over the eight pseudo-random runs
- Repeat method for each possible time lag up to six months
- Select largest magnitude value as the transfer function

A flow chart of this method is shown in Appendix B

For each seeding region there is a signal to every analysis region for the selected variable. Each signal requires individual extraction using the method detailed above (S. Salter Personal Communication 2011). An example set of plots showing the method for identifying the transfer function between a single analysis and seeding

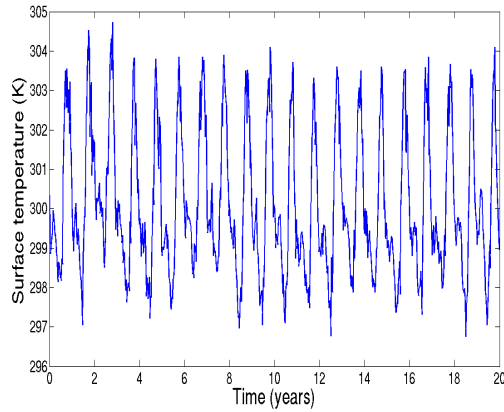
region is shown in Figure 7.3. Figures 7.3(a) and 7.3(b) show the 20 year temperature track for an example analysis region under control conditions and during one pseudo-random simulation. Figure 7.3(c) shows the difference between Figures 7.3(a) and 7.3(b) where the red line shows the mean value. Figure 7.3(d) is Figure 7.3(c) where the mean is subtracted from each point. Figure 7.3(e) shows the track from Figure 7.3(d) when the value is inverted about zero when the track from Figure 7.3(f) is 'on'. Figure 7.3(f) shows the sections of the simulation when the pseudo-random seeding is on. The final value of the transfer function is the average of the plot in Figure 7.3(e) divided by 150 %. Finding the predicted change in a quantity based on the transfer function requires a single calculation, the value of the transfer function is multiplied by the relative change in CDNC. For example doubling the CDNC is a 100 % increase, therefore the expected change in the quantity is 100 multiplied by the transfer function. The example shown in Figure 7.3 is for an instantaneous change however it is possible that there is an amount of time taken for a change in a seeding region to propagate to an analysis region. To account for a lag the switch which takes place in Figure 7.3(e) can be delayed by a number of time steps depending on the output frequency. The values shown in Sections 7.2.1 and 7.2.2 show the maximum transfer function across all possible time lags between 0 days and 180 days.

## 7.2 Climate model results

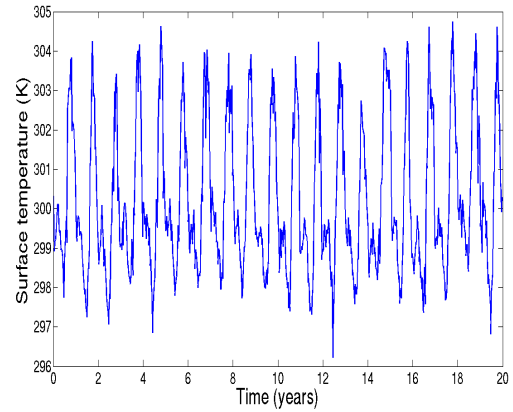
The results from the 10 day mean outputs are shown in Section 7.2.1. An improvement to the method is developed using daily output data and the results from this are shown in Section 7.2.2.

### 7.2.1 Results from 10 day mean data

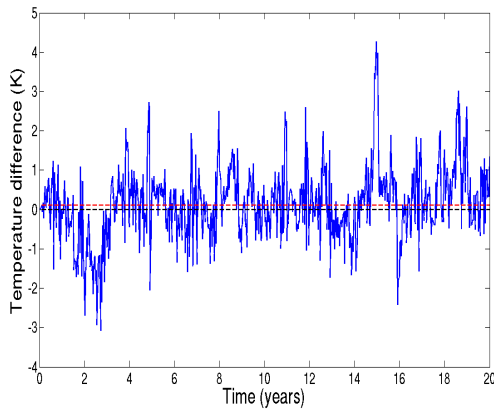
The Amazon region of South America is a large area which is considered to be at risk from precipitation reductions if MCB is deployed. Figure 4.6 shows results



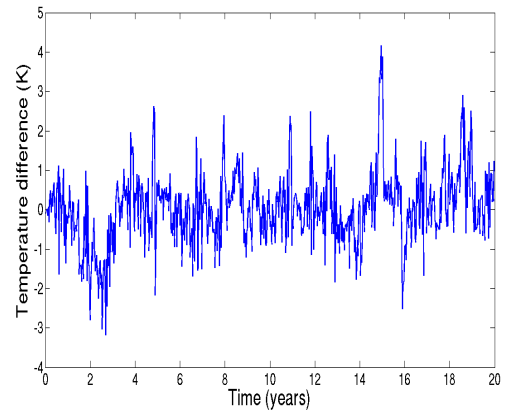
(a) An example temperature track from one analysis region during the Fixed CDNC simulation (K).



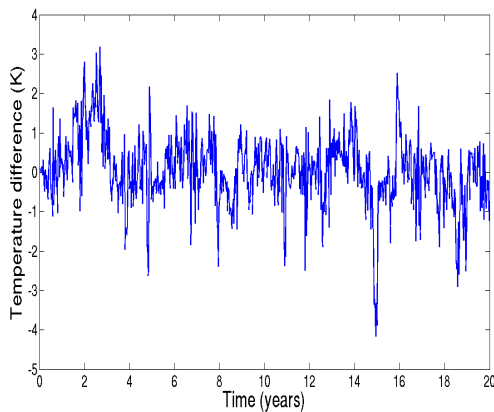
(b) An example temperature track from one analysis region during one of the pseudo-random CDNC simulations (K).



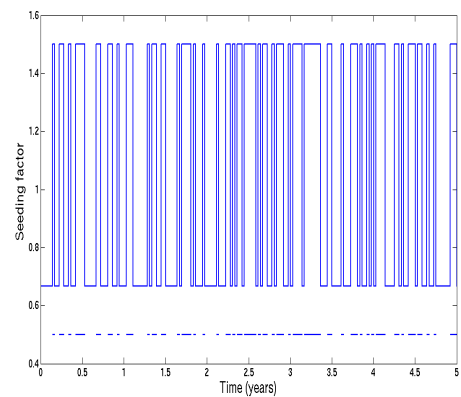
(c) The difference between the values in Figures 7.3(a) and 7.3(b) (K). The red dashed line shows the mean and the black dashed line shows zero.



(d) As Figure 7.3(c) except the mean is set to zero.



(e) As Figure 7.3(d) with the value switched about zero when the seeding is 'on' (K).



(f) Example section of the seeding track as used in Figure 7.3(e) to switch the average. The dashed line at the base of the plot indicates times when seeding is 'on'.

FIGURE 7.3: Example pseudo-random seeding result from the HadGEM1 climate model. Showing a temperature track from a Fixed CDNC simulation, a pseudo-random simulation. The difference between the tracks, the difference between the tracks with a mean of zero. The track after switching according to a pseudo-random number track and the pseudo-random number track used to perform the switching.

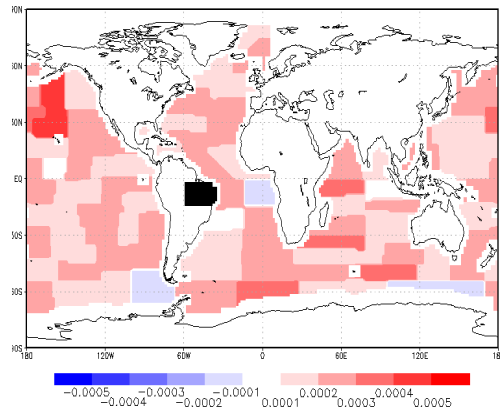
from various model simulations of MCB, all find a precipitation reduction over the Amazon. In particular the work by Jones et al. (2009) finds that seeding off the Namibian coast to be responsible for the precipitation reduction over the Amazon. To allow more detailed analysis here there are two analysis regions in the Amazon (see Figure 7.1(b)). Two regions are selected as results in Figure 4.6 show that precipitation reductions from MCB do not necessarily cover the entire Amazon region. In particular the results from Rasch et al. (2010), shown in Figure 4.6(d) have different results for the precipitation change in the northern and southern analysis regions of the Amazon.

Figures 7.4 and 7.5 show the maximum transfer function for precipitation as a result of pseudo-random seeding of 89 seeding regions. The results in Figures 7.4(a) and 7.4(b) show that seeding regions off the southwest coast of Africa does lead to a reduction in precipitation over the Amazon. However the seeding region with the highly negative transfer function differs depending on the area of the Amazon analysed. The results in Figures 7.4(a) and 7.4(b) do not match the results from Jones et al. (2009), where the present work finds changes to the Amazon that are dependent on seeding location within the South Atlantic. The results shown in Figures 7.5(c) and 7.5(d) contrast with results shown in Figure 4.6 where MCB generally leads to an increase in precipitation over Africa. The reduction found in precipitation is possibly due to the method selecting the largest magnitude change, or the seeding regions being different from previous simulations. The maximum magnitude precipitation changes over India in Figure 4.6 generally show a small increase depending on the location of the seeding. This is repeated in Figure 7.4(f) where seeding the Persian Gulf increases precipitation slightly over India. The results shown in Figure 7.4(d) indicate that Southeast Asia is likely to suffer a reduction in precipitation. The Arabian region (Figure 7.4(e)) is robust to changes in droplet number and appears unlikely to experience a change in precipitation as a result of MCB.

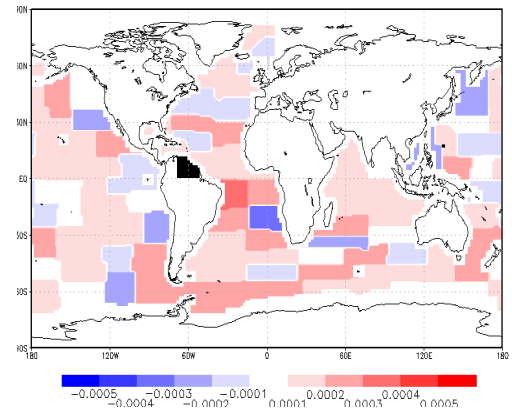
Figure 7.6 shows the transfer functions for surface temperature for the 89 seeding regions at six polar analysis regions. Work from Chapter 5 indicates that seeding in

tropical regions cools the poles. However the results in Chapter 5 are based upon long term seeding and not pseudo-random seeding. Within the ten day temperature plots a warming is found as a result of seeding many regions. The majority of seeding locations return an increase in the transfer function for temperature in Figures 7.6(b), 7.6(c) and 7.6(d). The results in Figures 7.6(e) and 7.6(f) shows that seeding is almost as likely to warm as they are to cool the Antarctic while Figure 7.6(a) does show cooling as a predominant feature. The plots in Figure 7.6 show little to no agreement with previous results as shown in Figure 4.4. However it is noted that the results in Figure 4.4 are in a double preindustrial carbon dioxide concentration atmosphere and the results in Figure 7.6 are in a control atmosphere.

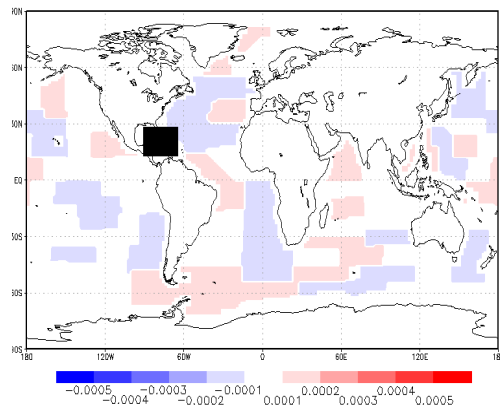
The results shown in Figures 7.4 and 7.5 show that some of the changes in precipitation from Figure 4.6 can be replicated as a transfer function using pseudo-random seeding, however results in Figure 7.6, when compared with Figure 4.4 indicate that the same is not true for temperature. There are also issues with regard to the magnitude of results. For example the precipitation transfer function between the Namibian coast and the North Amazon is found to be  $-0.0003 \text{ mm/day/ \% change in CDNC}$ . The results from Jones et al. (2009) find a reduction of up to  $1.2 \text{ mm/day}$  as a result of MCB in the South Atlantic. If the transfer function of  $-0.0003 \text{ mm/day/ \% change in CDNC}$  is correct then it implies a 4000 % change in CDNC ( $1.2 \text{ mm/day} / 0.0003 \text{ mm/day/ \% change in CDNC}$ ). A 4000 % increase is an increase by a factor of 40 in the value. The work in Jones et al. (2009) uses a fixed CDNC concentration of  $375 \text{ cm}^{-3}$ . If the value of  $375 \text{ cm}^{-3}$  is 40 times the control value then this implies a control value of less than  $10 \text{ cm}^{-3}$ . Using data from the Control simulation (see Table 4.1) the HadGEM1 CDNC is closer to  $50 \text{ cm}^{-3}$  which is much higher than the value predicted by the transfer function. These results are currently inconsistent and require further investigation.



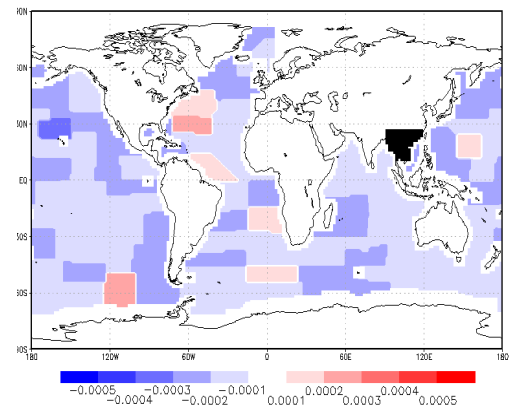
(a) Maximum transfer function to the South Amazon (black box) for 89 seeding regions. (mm/day/ % change in CDNC)



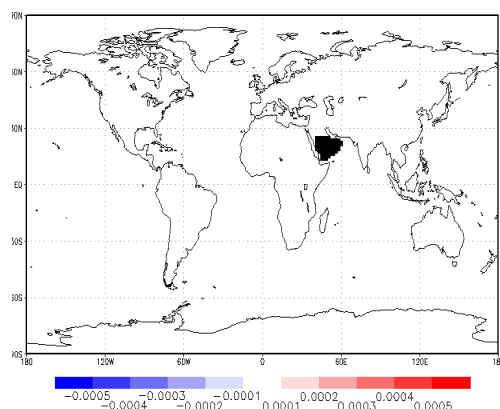
(b) Maximum transfer function to the North Amazon (black box) for 89 seeding regions. (mm/day/ % change in CDNC)



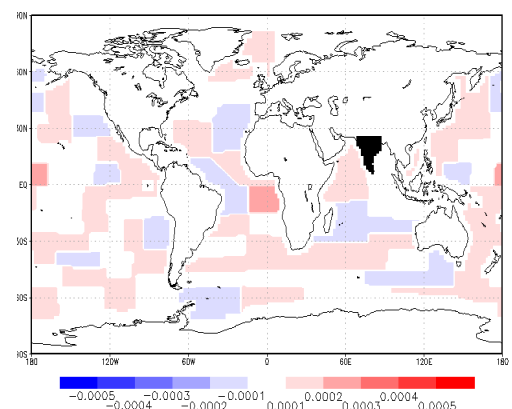
(c) Maximum transfer function to the Caribbean (black box) for 89 seeding regions. (mm/day/ % change in CDNC)



(d) Maximum transfer function to Southeast Asia (black box) for 89 seeding regions. (mm/day/ % change in CDNC)



(e) Maximum transfer function to Arabia (black box) for 89 seeding regions. (mm/day/ % change in CDNC)



(f) Maximum transfer function to India (black box) for 89 seeding regions. (mm/day/ % change in CDNC)

FIGURE 7.4: Transfer functions for ten day average precipitation within a climate model on two areas of South America, the Caribbean, Southeast Asia, Arabia and India. A doubling of CDNC in one seeding regions would result in a precipitation change of 100 times the transfer function. For example doubling the CDNC in the seeding area on the Angolan coast would lead to and increase in precipitation of 0.01 mm/day in the South Amazon.

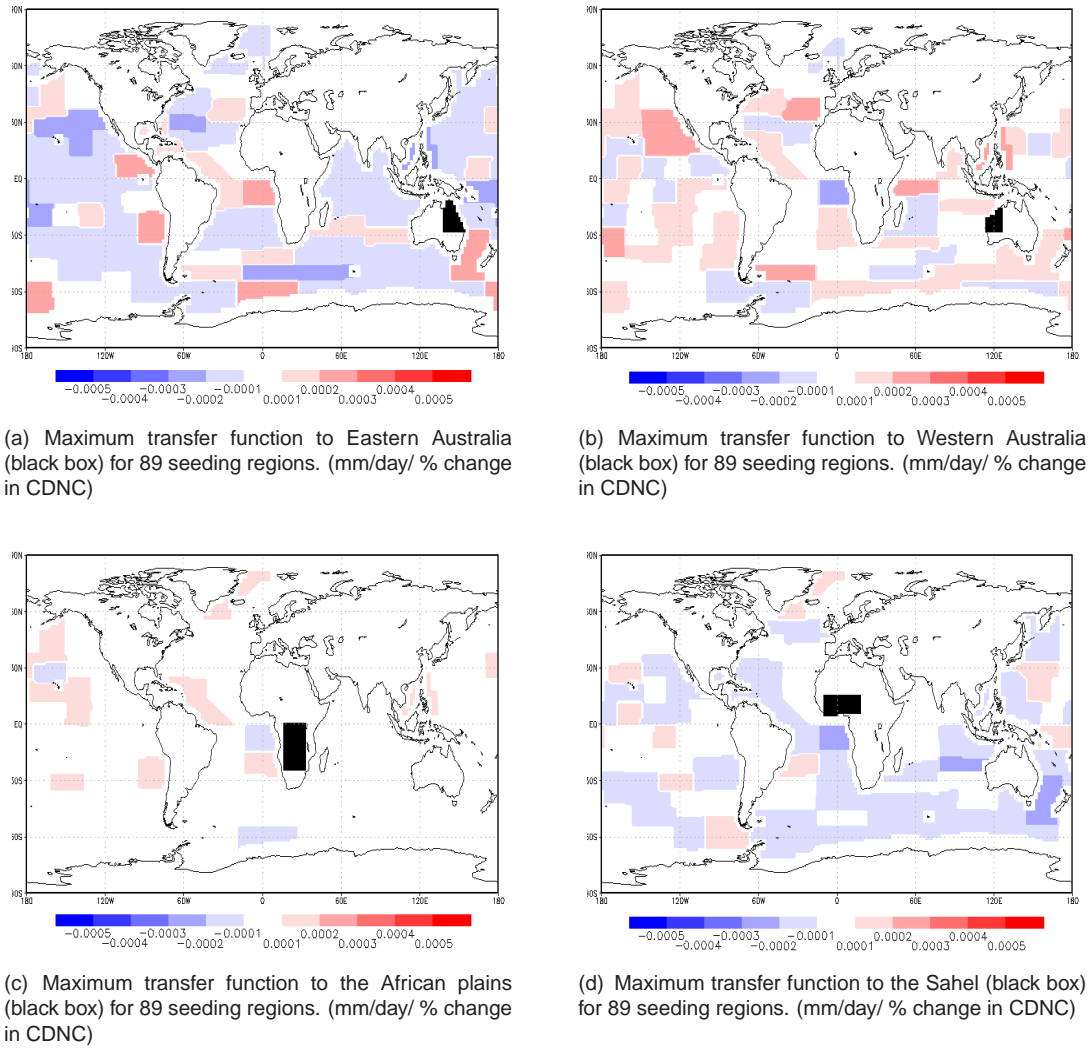
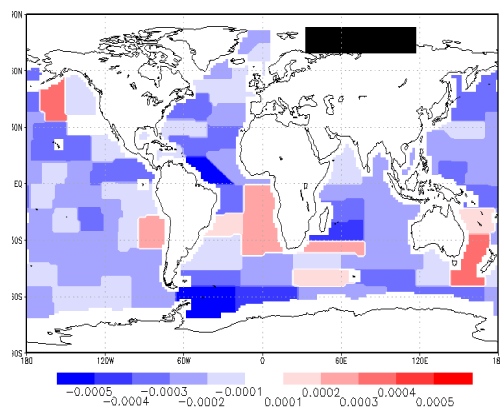


FIGURE 7.5: Transfer functions for ten day average precipitation within a climate model on two areas of Australia, the Sahel and African plains.

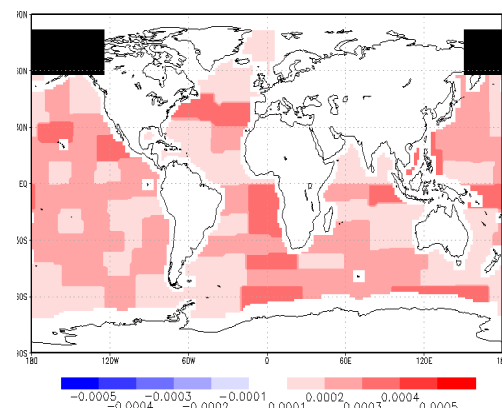
## 7.2.2 Results from 1 day mean data

The results in Section 7.2.1 do not replicate previous results for precipitation changes in the Amazon such as in Jones et al. (2009), this may be due to differences in the seeding regions or an issue with averaging over 10 days of results as described below. Furthermore the temperature results shown in Figure 7.6 do not replicate previous work. The method is repeated using daily precipitation data as it is possible that the ten day averages are masking results where the time lag is not wholly divisible by ten. If the lag between seeding and effect is five days then turning

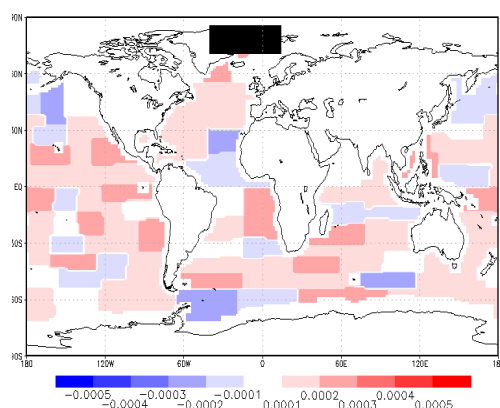




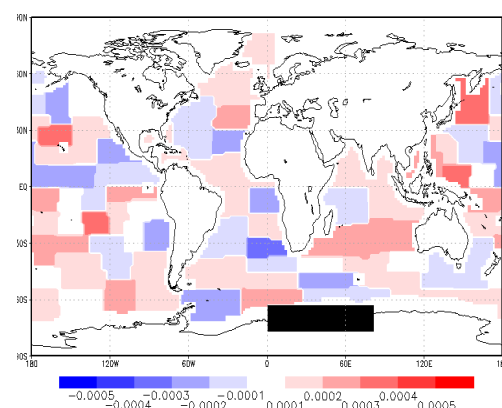
(a) Maximum transfer function in surface temperature over one region of the Arctic (Black box) for 89 seeding regions (K/ % Change in CDNC).



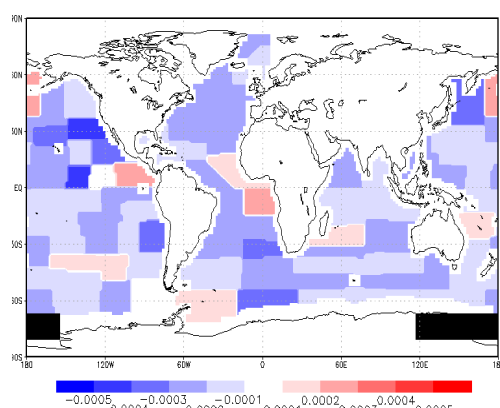
(b) Maximum transfer function in surface temperature over one region of the Antarctic (Black box) for 89 seeding regions (K/ % Change in CDNC).



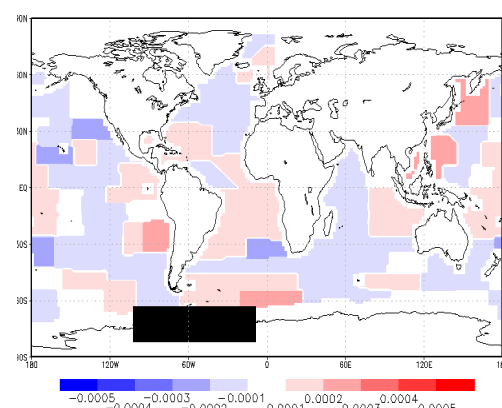
(c) Maximum transfer function in surface temperature over one region of the Arctic (Black box) for 89 seeding regions K/ % Change in CDNC).



(d) Maximum transfer function in surface temperature over one region of the Antarctic (Black box) for 89 seeding regions (K/ % Change in CDNC).



(e) Maximum transfer function in surface temperature over one region of the Arctic (Black box) for 89 seeding regions (K/ % Change in CDNC).



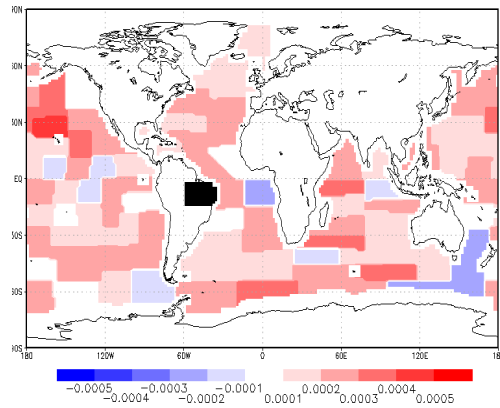
(f) Maximum transfer function in surface temperature over one region of the Antarctic (Black box) for 89 seeding regions (K/ % Change in CDNC).

FIGURE 7.6: Transfer functions for surface temperature within a climate model on six polar regions.

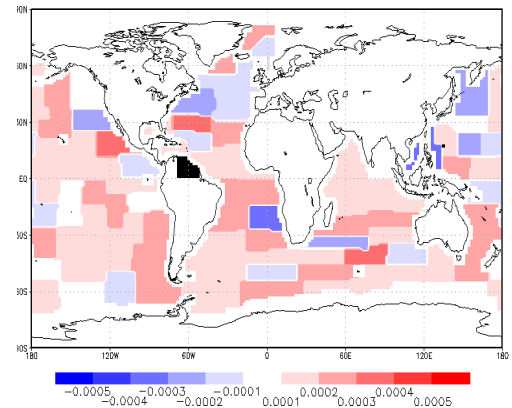
the seeding off after ten days leads to averaging over five days of seeding on and five days of seeding off. The potential overlap of results due to a lag between source and effect possibly reduces the magnitude of results. The ten day results shown in Figures 7.4 and 7.5 are repeated in the daily results shown in Figure 7.7 and 7.8. The transfer function for precipitation over two Amazon regions again does not repeat the general pattern of results from Jones et al. (2009) as shown in Figures 7.7(a) and 7.7(b). Using data from the one day results, it appears that regions in the Eastern Pacific no longer cause drying of the north Amazon analysis region while some seeding regions in the Central Pacific and Southern Oceans dry the south Amazon analysis region. As shown in Figure 7.8(d) there are now some regions which are found to increase precipitation over the Sahel analysis region when compared with Figure 7.5(d). However there is also an increase in the number and intensity of drying regions. The results over India shown in Figure 7.7(f) are not significantly different from the ten day average data in Figure 7.4(f). The daily results over Australia are similar to the ten day results as shown in a comparison between Figures 7.8(a) and 7.8(b) and Figures 7.5(a) and 7.5(b) however the daily results indicate that seeding the Pacific may lead to a drying in Eastern Australia. The Arabian peninsular is again robust to changes in CDNC and does not experience any identifiable changes (Figure 7.7(e)).

### **7.2.3 Inverse plotting from 1 day mean data**

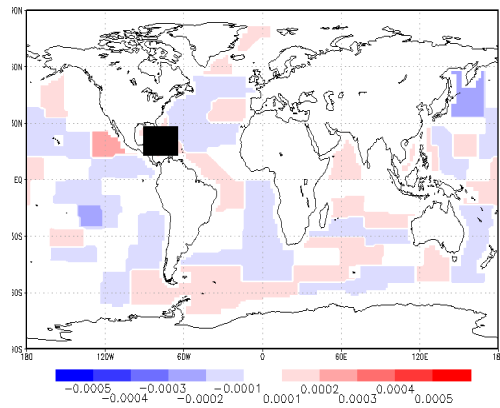
The data used to plot the results shown in Section 7.2.2 can be used to build inverse maps of results showing the impacts of any given seeding region on all analysis regions. The use of the inverse maps allows a direct comparison with the results shown in Figure 8 of Jones et al. (2009). A comparison of regions pseudo-randomly seeded in this work and the results from Jones et al. (2009) is shown in Figure 7.9. The seeding regions used in this work do not exactly match the ones used in Jones et al. (2009) however they are in similar areas. The results shown in Figures 7.9(a) and 7.9(b) have differences in precipitation changes over South America, Africa and



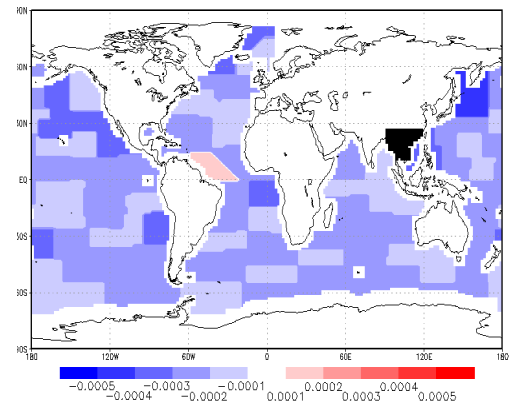
(a) Maximum transfer function to the South Amazon (black box) for 89 seeding regions. (mm/day/ % change in CDNC)



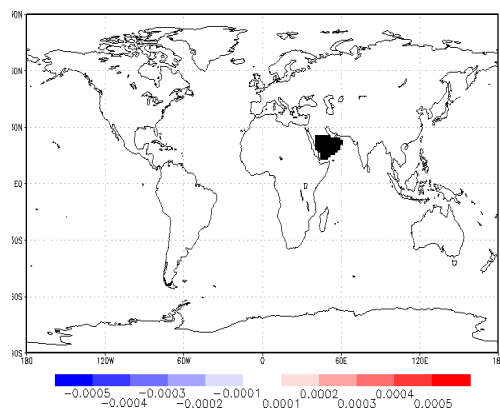
(b) Maximum transfer function to the North Amazon (black box) for 89 seeding regions. (mm/day/ % change in CDNC)



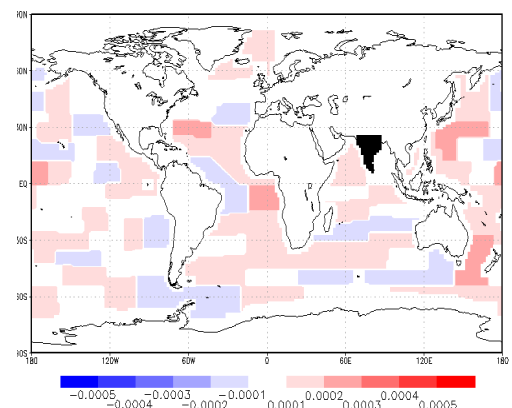
(c) Maximum transfer function to the Caribbean (black box) for 89 seeding regions. (mm/day/ % change in CDNC)



(d) Maximum transfer function to Southeast Asia (black box) for 89 seeding regions. (mm/day/ % change in CDNC)

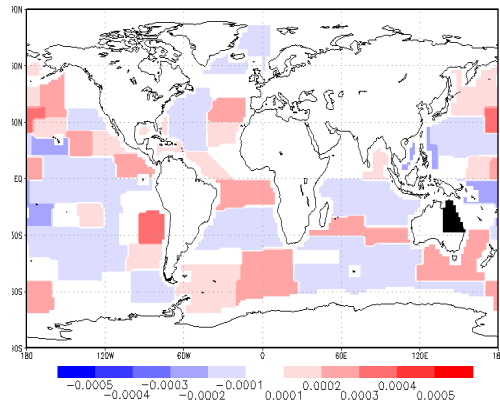


(e) Maximum transfer function to Arabia (black box) for 89 seeding regions. (mm/day/ % change in CDNC)

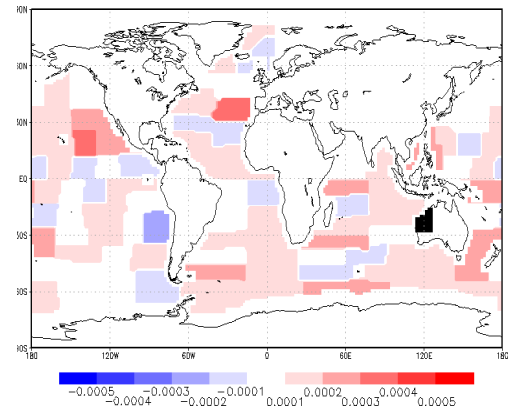


(f) Maximum transfer function to India (black box) for 89 seeding regions. (mm/day/ % change in CDNC)

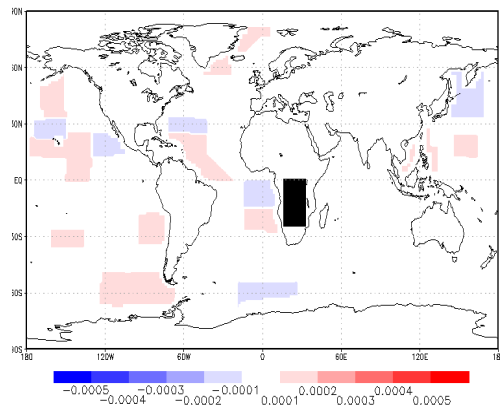
FIGURE 7.7: Transfer functions for daily average precipitation within a climate model on two areas of South America, the Caribbean, Southeast Asia, Arabia and India.



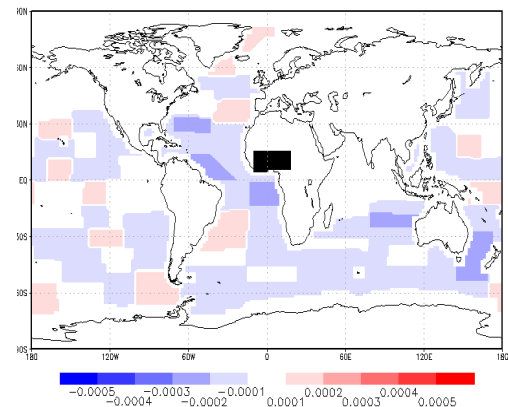
(a) Maximum transfer function to Eastern Australia (black box) for 89 seeding regions. (mm/day/ % change in CDNC)



(b) Maximum transfer function to Western Australia (black box) for 89 seeding regions. (mm/day/ % change in CDNC)



(c) Maximum transfer function to the African plains (black box) for 89 seeding regions. (mm/day/ % change in CDNC)



(d) Maximum transfer function to the Sahel (black box) for 89 seeding regions. (mm/day/ % change in CDNC)

FIGURE 7.8: Transfer functions for daily average precipitation within a climate model on two areas of Australia, the Sahel and African plains.

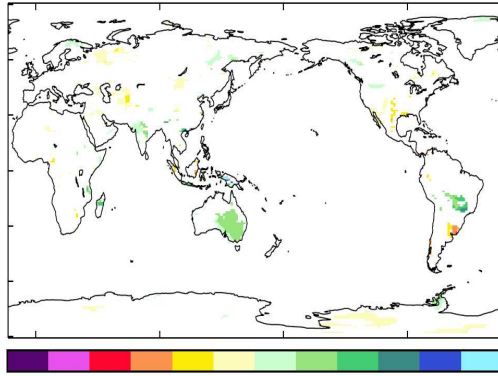
India when compare to Jones et al. (2009). Furthermore the sizeable changes in Eastern Australian precipitation found in Figure 7.9(a) are reversed in the pseudo-random results from Figure 7.9(b). The results for seeding the South Pacific, shown in Figures 7.9(c) and 7.9(d) are similar for many of the analysis regions shown in Figure 7.1(b), in that there are few sizable changes. In particular the results in Figure 7.9(d) only show a change in precipitation in Southeast Asia. The results shown in Figure 7.9(e) show that seeding the Namibian coast leads to a large reduction in Amazon rainfall. Using pseudo-random seeding the transfer function from the same region (Figure 7.9(f)) results in an increase in precipitation over

the Southern Amazon and the African plains and a decrease over the Northern Amazon. The results in Figure 7.9(f) do not match the results in Figure 7.9(e) for Arabia which is found to be robust to changes in the marine CDNC.

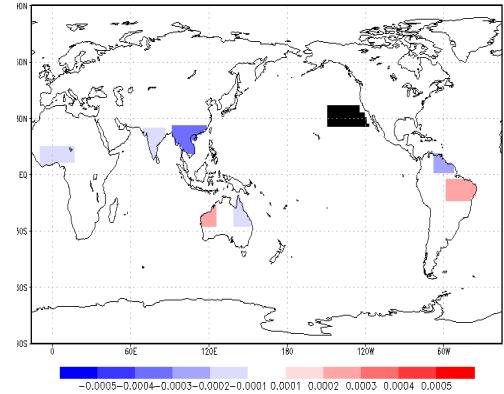
## 7.3 Discussion

A series of simulations are conducted to investigate the use of pseudo-random seeding within a GCM. Several publications show that MCB is capable of recovering some aspects of a control climate such as surface temperature or polar ice cover, however there are undesired side effects such as precipitation changes (Bala et al., 2011; Jones et al., 2009, 2011; Latham et al., 2012; Rasch et al., 2010). An example of an undesired outcome is the drying of the Amazon rain forest as found in Figure 8 (f) of Jones et al. (2009). The work in Jones et al. (2009) finds that seeding in the South Atlantic is responsible for the drying of the Amazon. Instead of running large numbers of simulations an approach using pseudo-random seeding is used here. With multiple seeding regions being turn 'on' or 'off' pseudo-randomly it is possible to reconstruct a map of impacts. To investigate the impacts of multiple seeding regions at once map 89 seeding regions and 16 analysis regions are defined, these maps are shown in Figures 7.1(a) and 7.1(b) respectively.

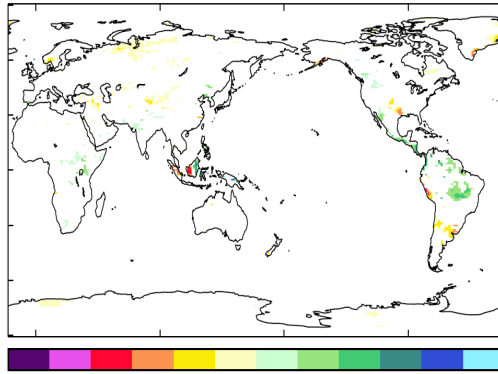
The seeding is switched 'on' or 'off' pseudo-randomly with a period of ten days. The transfer functions for precipitation are found to be inconsistent with previous results from Jones et al. (2009) with the South Amazon region no longer dried as a result of seeding the Namibian coast. Despite the encouraging results for identifying transfer functions of precipitation the temperature results proved inconclusive. As the temperature outputs are focused in polar regions it is possible that changes as a result of pseudo-random seeding requires a longer 'on' time to have an effect on the circulation and propagate.



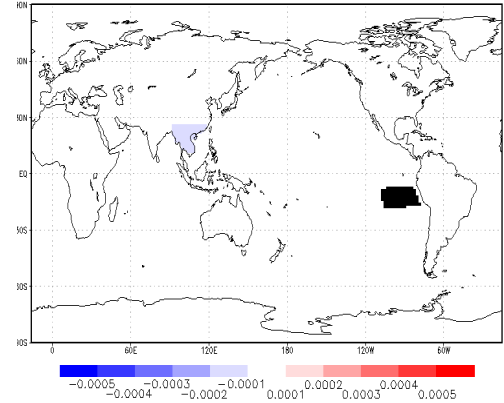
(a) Impacts of seeding the North Pacific to  $N=375 \text{ cm}^{-3}$ , copied from Jones et al. (2009).



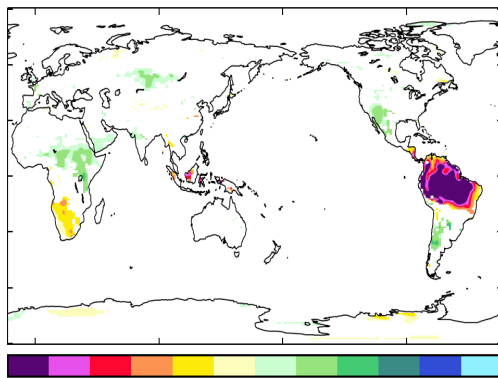
(b) Transfer function derived from pseudo-random seeding of the North Pacific (black box) on the 16 analysis regions.



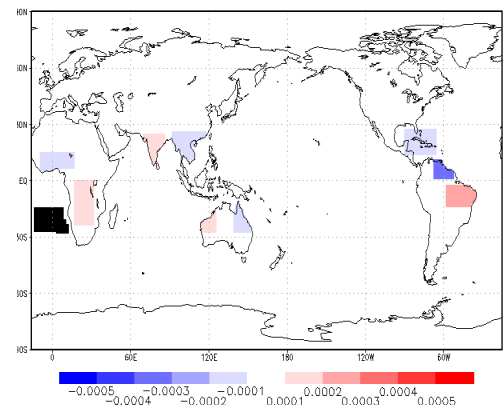
(c) Impacts of seeding the South Pacific to  $N=375 \text{ cm}^{-3}$ , copied from Jones et al. (2009).



(d) Transfer function derived from pseudo-random seeding of the South Pacific (black box) on the 16 analysis regions.



(e) Impacts of seeding the South Atlantic to  $N=375 \text{ cm}^{-3}$ , copied from Jones et al. (2009).



(f) Transfer function derived from pseudo-random seeding of the South Atlantic (black box) on the 16 analysis regions.

FIGURE 7.9: A comparison between seeding three regions permanently and pseudo-randomly. The fixed results are copied from Figure 8 of Jones et al. (2009). All results are for precipitation, with the left panels in mm/day and the right panels in mm/day/ % change in CDNC. Note the scale is symmetrical with asymmetric labelling to prevent overlapping numbers.

In the light of the ten day results the simulations are repeated using daily outputs of precipitation data. The transfer functions for precipitation calculated from daily output are shown in Figures 7.7 and 7.8. The transfer functions generated from daily average data are not significantly different from the ten day results, however they do show some changes in magnitude and sign. The size of the transfer functions for daily average precipitation are too small to replicate the results found in previous publications.

The use of inverse maps indicates that the transfer functions calculated from pseudo-random seeding do not match previous results. The lack of consistency with previous results indicates that improvements are needed in either the seeding or analysis techniques. The current results are based on eight pseudo-random simulations which are averaged and then plotted, an improvement could be to use of more simulations to reduce the impact of outliers. An increase of the seeding fraction from 150 % to 200 % or higher may ease identification of small signals.

## 7.4 Summary

An investigation into the possibility of creating a map of effects of MCB from multiple regions is undertaken using the HadGEM1 GCM. A number of regions are identified as seeding areas where MCB is applied pseudo-randomly with the impacts assessed at multiple analysis regions. Results from daily and ten day average precipitation results are found to be unable to replicate results from publications such as Jones et al. (2009). With the use of inverse maps a comparison of seeding regions is performed and it is found that pseudo-random seeding is unable to identify the same transfer functions as direct seeding. Furthermore transfer functions of temperature changes in polar regions are found to be contrary to previous results from Chapter 5. Possible improvements to the method used include running more simulations, or increasing amount of seeding performed. Furthermore analysis of



data other than the maximum magnitude result would allow more detailed understanding, see Section 8.3 for details.

# Chapter 8

## Conclusions

In this thesis an exploration of the impacts of changing CDNC on cloud albedo is performed using data from the VOCALs-REx field campaign. The HadGEM1 GCM is used to investigate two potential MCB scenarios in two different climate scenarios. Comparisons between the results from several simulations enabled an investigation into the climate impacts of MCB. Furthermore it is possible to assess the ability of MCB to reduce tropical cyclone intensity or reduce temperature changes in coral reef regions. In the final results chapter of this thesis a new approach is taken to derive transfer functions within the HadGEM1 model.

### 8.1 Major findings

Several questions are proposed in Section 1.5 and investigated throughout this work.

1. It is possible to use the HadGEM1 model to simulate MCB in a manner that is consistent with previous results.
  - a) The double carbon dioxide scenario used in this work is consistent with outputs from four previous publications on MCB.

- b) The HadGEM1 simulations shown in Chapter 4 are consistent with expected results and with previous publications. Several differences are found which are attributed to different initial conditions and methods.
- 2. A mechanism linking modification of the tropical radiation balance to changes in polar temperatures is investigated in Chapter 5.
  - a) The simulations conducted in Chapter 4 show cooling in polar regions larger than in the tropics, this agrees with work in previous publications including Bala et al. (2011); Jones et al. (2009, 2011); Rasch et al. (2010).
  - b) Changes in the meridional heat flux is identified as a potential mechanism for cooling the poles as a result of modifying the tropical radiation balance.
- 3. Tropical cyclones are shown to increase in intensity as a result of climate change. One driving factor for this is an increase in tropical temperature which provides more energy for convection. There is also an increase in temperature over the tropics which may impact coral reefs.
  - a) MCB is shown to decrease sea surface temperatures during peak tropical cyclone season for several tropical cyclone basins, which in turn reduces the energy available for convection and may reduce intensity of storms.
  - b) MCB reduces surface temperatures around coral reef regions and may prevent thermal stress which in turn can lead to coral bleaching, excessive cooling is possible and this in turn may damage the reefs.
- 4. Changes in precipitation can be found using pseudo-random seeding as shown in Chapter 7 including repetition of previous results.
  - a) Signals from pseudo-random seeding can be resolved using a climate model.
  - b) The comparison plots in Figure 7.9 show that the results of pseudo-random seeding are not consistent with results from Jones et al. (2009).

## 8.2 Implications of this work

MCB receives attention in the media and in scientific literature. Within the scientific literature there is work assessing the impacts and effectiveness of MCB within global atmosphere or climate models (Bala et al., 2011; Jones et al., 2009, 2011; Latham et al., 2008; Rasch et al., 2010). Each of these publications relies on an assumed change in CDNC as a result of geoengineering with little to no investigation of the engineering requirements. The engineering requirements and their impacts are instead investigated in publications such as Salter et al. (2008) and Korhonen et al. (2010). This work is not designed to investigate the conditions required to generate a set CDNC. Instead it makes the assumption that a desired value could be achieved.

The previous publications show that MCB is capable of cooling polar regions by predominantly seeding clouds in the tropics. A proposed mechanism for this cooling is a modification of the MHF; where energy that would be incident on the tropics is instead reflected back into space. This leads to a reduction in energy that is available for the MHF to propagate polewards. As the total radiative MHF is investigated in Chapter 5 an expansion would be to identify if the change in MHF is in the atmospheric or oceanic components as this has implications for deployment of MCB.

Under the assumptions detailed in Chapter 6 the results from the HadGEM1 climate model indicate that it is possible to reduce global SSTs. A reduction in SSTs therefore reduces the amount of energy available for convection within a tropical cyclone. The work in Chapter 6 also highlights an issue with MCB as it may be possible to overcool the ocean and add thermal stress to coral reefs. The results show that three region MCB in an increased carbon dioxide concentration atmosphere is most capable of retaining control temperatures.

It is shown in Chapter 7 that it is possible to calculate transfer functions within a climate model for a rapidly changing field such as precipitation. Transfer functions

for slowly changing fields such as temperature have not been found and this is a weakness of the method. Several signals are found using pseudo-random seeding however improvements are needed to replicate current results. As results in Chapter 5 indicate static seeding regions are most effective for MCB. It is possible that utilising results on transfer functions within a model can be done to identify the most optimal seeding areas with least undesired side effects.

### **8.3 Future work**

During work on this thesis several potential avenues of expansion have become apparent. With regard to modelling geoengineering or MCB there are multiple potential scenarios to investigate including the climate impacts of deploying multiple SRM techniques simultaneously or a combination of SRM and CDR techniques. As there is work on both the engineering and impacts aspects of MCB it may be possible to use the UKCA-mode coupled climate-chemistry-aerosol model to simulate seeding from a ship based source and assess the impacts on a global scale. The assumed value of cloud droplet number concentration used in Bala et al. (2011); Jones et al. (2009, 2011); Latham et al. (2008); Rasch et al. (2010) and this work would instead be calculated by the model. The dynamical feedbacks between the new clouds and the aerosol would also be simulated by the model as opposed to the offline winds and thermodynamics used in Korhonen et al. (2010).

As is mentioned in Sections 5.3 and 8.2, the work undertaken in Chapter 5 finds that cooling of polar regions as a result of MCB is possibly caused by a change in the MHF. An expansion of this work would include ascertaining which component of the MHF is modified by MCB.

The ability of global climate models to reproduce extreme weather events such as tropical cyclones is discussed in Chapter 8 of the IPCC Fourth Assessment report (Randall et al., 2007) where the coarse resolution is cited as a weakness. To expand on the work in Chapter 6 the use of a dedicated tropical cyclone forecast

model could be used to assess the impacts of MCB. MCB may also alter the relative humidity and wind shear in tropical cyclone basins. A tropical cyclone forecast model could assess the impacts of changes to wind shear and relative humidity on tropical cyclones with greater predictive skill than a climate model. The work in Chapter 6 can also be expanded with the use of a model dedicated to studying climate impacts on coral reef systems. Use of a dedicated model allows investigation of the combined effects of ocean acidification and global warming and the effectiveness of using MCB to prevent reef damage by cooling tropical waters.

Chapter 7 examines pseudo-random teleconnections within a GCM and shows the derivation of transfer functions within HadGEM1. The results in Chapter 7 are not consistent with previous work and expansions to the method could include new analysis regions and a possible change in seeding fraction. If reliable results can be found it would then be possible to identify seeding regions which do not lead to precipitation reductions over key regions such as the Amazon rainforest. Beyond optimal seeding regions it would also be possible to target MCB in a manner that increases precipitation over land in semi-arid regions.

## References

- Albrecht, B. A. (1989), “Aerosols, cloud microphysics, and fractional cloudiness”, *Science* , Vol. 245, pp. 1227–1230.
- Alexeev, V., Langen, P. and Bates, J. (2005), “Polar amplification of surface warming on an aquaplanet in ‘ghost forcing’ experiments without sea ice feed-backs”, *Climate Dynamics* , Vol. 24, Springer Berlin / Heidelberg, pp. 655–666. 10.1007/s00382-005-0018-3.
- Allen, G. and Abel, S. (2009), VAMOS Ocean-Climate-Atmosphere-Land Study: UK component, Technical report, VOCALS-UK.
- Alterskjær, K., Kristjánsson, J. E. and Seland, Ø. (2012), “Sensitivity to deliberate sea salt seeding of marine clouds observations and model simulations”, *Atmospheric Chemistry and Physics* , Vol. 12, pp. 2795–2807.
- Arakawa, A. and Lamb, V. R. (1977), “Computational design of the basic dynamical process of the ucla general circulation model”, *Methods in Computational Physics* , Vol. 17, pp. 173–265.
- Bala, G., Caldeira, K., Nemani, R., Cao, L., Ban-Weiss, G. and Shin, H.-J. (2011), “Albedo enhancement of marine clouds to counteract global warming: impacts on the hydrological cycle”, *Climate Dynamics* , Vol. 37, Springer-Verlag, pp. 915–931.
- Bao, L. and Trachtenberg, M. C. (2006), “Facilitated transport of CO<sub>2</sub> across a liquid membrane: Comparing enzyme, amine, and alkaline”, *Journal of Membrane Science* , Vol. 280, pp. 330 – 334.



- Bender, M. A., Knutson, T. R., Tuleya, R. E., Sirutis, J. J., Vecchi, G. A., Garner, S. T. and Held, I. M. (2010), "Modeled impact of anthropogenic warming on the frequency of intense atlantic hurricanes", *Science* , Vol. 327, pp. 454–458.
- Borg, L. A. and Bennartz, R. (2007), "Vertical structure of stratiform marine boundary layer clouds and its impact on cloud albedo", *Geophysical Research Letters* , Vol. 34, AGU, pp. L05807–.
- Bretherton, C. S., Wood, R., George, R. C., Leon, D., Allen, G. and Zheng, X. (2010), "Southeast pacific stratocumulus clouds, precipitation and boundary layer structure sampled along 20° s during vocals-rex", *Atmospheric Chemistry and Physics* , Vol. 10, pp. 10639–10654.
- Brovkin, V., Petoukhov, V., Claussen, M., Bauer, E., Archer, D. and Jaeger, C. (2009), "Geoengineering climate by stratospheric sulfur injections: Earth system vulnerability to technological failure", *Climatic Change* , Vol. 92, pp. 243–259.
- Caldeira, K. and Wood, L. (2008), "Global and arctic climate engineering: numerical model studies", *Philosophical Transactions of the Royal Society A: Mathematical, Physical and Engineering Sciences* , Vol. 366, pp. 4039–4056.
- Canadell, J. G. and Raupach, M. R. (2008), "Managing forests for climate change mitigation", *Science* , Vol. 320, pp. 1456–1457.
- Christensen, M. W. and Stephens, G. L. (2011), "Microphysical and macrophysical responses of marine stratocumulus polluted by underlying ships: Evidence of cloud deepening", *Journal of Geophysical Research* , Vol. 116, p. D03201.
- Claeys, M., Graham, B., Vas, G., Wang, W., Vermeylen, R., Pashynska, V., Cafmeyer, J., Guyon, P., Andreae, M. O., Artaxo, P. and Maenhaut, W. (2004), "Formation of secondary organic aerosols through photooxidation of isoprene", *Science* , Vol. 303, pp. 1173–1176.
- Collins, W. D., Bitz, C. M., Blackmon, M. L., Bonan, G. B., Bretherton, C. S., Carton, J. A., Chang, P., Doney, S. C., Hack, J. J., Henderson, T. B., Kiehl, J. T., Large,

- W. G., McKenna, D. S., Santer, B. D. and Smith, R. D. (2006), "The community climate system model version 3 (ccsm3)", *Journal of Climate*, Vol. 19, American Meteorological Society, pp. 2122–2143.
- Crutzen, P. (2006), "Albedo enhancement by stratospheric sulfur injections: A contribution to resolve a policy dilemma?", *Climatic Change*, Vol. 77, Springer Netherlands, pp. 211–220. 10.1007/s10584-006-9101-y.
- Curry, J. A., Schramm, J. L., Rossow, W. B. and Randall, D. (1996), "Overview of arctic cloud and radiation characteristics", *Journal of Climate*, Vol. 9, American Meteorological Society, pp. 1731–1764.
- Cusack, S., Edwards, J. M. and Crowther, J. M. (1999), "Investigating k distribution methods for parameterizing gaseous absorption in the hadley centre climate model", *Journal of Geophysical Research*, Vol. 104, AGU, pp. 2051–2057.
- Dare, R. A. and McBride, J. L. (2011), "The threshold sea surface temperature condition for tropical cyclogenesis", *Journal of Climate*, Vol. 24, American Meteorological Society, pp. 4570–4576.
- Davies, T., Cullen, M. J. P., Malcolm, A. J., Mawson, M. H., Staniforth, A., White, A. A. and Wood, N. (2005), "A new dynamical core for the met office's global and regional modelling of the atmosphere", *Quarterly Journal of the Royal Meteorological Society*, Vol. 131, John Wiley & Sons, Ltd., pp. 1759–1782.
- Davison, P. S., Roberts, D. L., Arnold, R. T. and Colvile, R. N. (2004), "Estimating the direct radiative forcing due to haze from the 1997 forest fires in indonesia", *Journal of Geophysical Research*, Vol. 109, AGU, p. D10207.
- Diaz, R. J. and Rosenberg, R. (2008), "Spreading dead zones and consequences for marine ecosystems", *Science*, Vol. 321, pp. 926–929.
- Donohoe, A. and Battisti, D. S. (2011), "Atmospheric and surface contributions to planetary albedo", *Journal of Climate*, Vol. 24, pp. 4402–4418.

- Droplet Measurement Technologies (2009), Cloud droplet probe (cdp) manual, Technical report, Droplet Measurement Technologies Inc.
- Eakin, C. M., Morgan, J. A., Heron, S. F., Smith, T. B., Liu, G. and 63 other authors (2010), "Caribbean corals in crisis: Record thermal stress, bleaching, and mortality in 2005", *PLoS ONE*, Vol. 5, Public Library of Science, p. e13969.
- Edwards, J. M. and Slingo, A. (1996), "Studies with a flexible new radiation code. i: Choosing a configuration for a large-scale model", *Quarterly Journal of the Royal Meteorological Society*, Vol. 122, pp. 689–719.
- Emanuel, K. (2005), "Increasing destructiveness of tropical cyclones over the past 30 years", *Nature*, Vol. 436, Nature Publishing Group, pp. 686–688.
- FAAM (2011), Broadband radiometers, Technical report, Faculty of Airborne Atmospheric Measurement.
- Forster, P., Ramaswamy, V., Artaxo, P., Berntsen, T., Betts, R., Fahey, D., Haywood, J., Lean, J., Lowe, D., Myhre, G., Nganga, J., Prinn, R., Raga, G., Schulz, M. and Dorland, R. V. (2007), Changes in atmospheric constituents and in radiative forcing, in S. Solomon, D. Qin, M. Manning, Z. Chen, M. Marquis, K. Averyt, M. Tignor and H. Miller, eds, 'Climate Change 2007: The Physical Science Basis. Contribution of Working Group I to the Fourth Assessment Report of the Intergovernmental Panel on Climate Change', Cambridge University Press, Cambridge, United Kingdom and New York, NY, USA.
- Fujiwhara, S. (1921), "The natural tendency towards symmetry of motion and its application as a principle in meteorology", *Quarterly Journal of the Royal Meteorological Society*, Vol. 47, John Wiley & Sons, Ltd, pp. 287–292.
- Global Warming and Ice Ages: I. Prospects for Physics-Based Modulation of Global Change.* (1997).
- Govindasamy, B. and Caldeira, K. (2000), "Geoengineering earth's radiation balance to mitigate CO<sub>2</sub> induced climate change", *Geophysical Research Letters*, Vol. 27, pp. 2141–2144.

- Govindasamy, B., Caldeira, K. and Duffy, P. (2003), "Geoengineering earth's radiation balance to mitigate climate change from a quadrupling of  $\text{CO}_2$ ", *Global and Planetary Change*, Vol. 37, pp. 158–168.
- Gray, W. M. (1968), "Global view of the origin of tropical disturbances and storms", *Monthly Weather Review*, Vol. 96, pp. 669–700.
- Gregory, D. and Rowntree, P. R. (1990), "A mass flux convection scheme with representation of cloud ensemble characteristics and stability-dependent closure", *Monthly Weather Review*, Vol. 118, American Meteorological Society, pp. 1483–1506.
- Haman, K. E. (2009), "Simple approach to dynamics of entrainment interface layers and cloud holes in stratocumulus clouds", *Quarterly Journal of the Royal Meteorological Society*, Vol. 135, John Wiley & Sons, Ltd., pp. 93–100.
- Hanson, H. P. (1991), "Marine stratocumulus climatologies", *International Journal of Climatology*, Vol. 11, John Wiley & Sons, Ltd., pp. 147–164.
- Held, I. M. and Zhao, M. (2011), "The response of tropical cyclone statistics to an increase in  $\text{CO}_2$  with fixed sea surface temperatures", *Journal of Climate*, Vol. 24, American Meteorological Society, pp. 5353–5364.
- Hennessey, K., Fitzharris, B., Bates, B., Harvey, N., Howden, S., Hughes, L., Salinger, J. and Warrick, R. (2007), Australia and new zealand, in 'Climate Change 2007: Impacts, Adaptation and Vulnerability. Contribution of Working Group II to the Fourth Assessment Report of the Intergovernmental Panel on Climate Change', Cambridge University Press, Cambridge, UK.
- Hogan, R. J., Grant, A. L. M., Illingworth, A. J., Pearson, G. N. and O'Connor, E. J. (2009), "Vertical velocity variance and skewness in clear and cloud-topped boundary layers as revealed by doppler lidar", *Quarterly Journal of the Royal Meteorological Society*, Vol. 135, John Wiley & Sons, Ltd., pp. 635–643.
- Holland, G. J. (1997), "The maximum potential intensity of tropical cyclones", *Journal of the Atmospheric Sciences*, Vol. 54, pp. 2519–2541.

- Holland, M. M. and Bitz, C. M. (2003), "Polar amplification of climate change in coupled models", *Climate Dynamics*, Vol. 21, Springer Berlin / Heidelberg, pp. 221–232. 10.1007/s00382-003-0332-6.
- Hudson, S. R. (2011), "Estimating the global radiative impact of the sea ice-albedo feedback in the arctic", *Journal of Geophysical Research*, Vol. 116, AGU, p. D16102.
- Johns, T. C., Durman, C. F., Banks, H. T., Roberts, M. J., McLaren, A. J., Ridley, J. K., Senior, C. A., Williams, K. D., Jones, A., Rickard, G. J., Cusack, S., Ingram, W. J., Crucifix, M., Sexton, D. M. H., Joshi, M. M., Dong, B.-W., Spencer, H., Hill, R. S. R., Gregory, J. M., Keen, A. B., Pardaens, A. K., Lowe, J. A., Bodas-Salcedo, A., Stark, S. and Searl, Y. (2006), "The new hadley centre climate model (hadgem1): Evaluation of coupled simulations", *Journal of Climate*, Vol. 19, American Meteorological Society, pp. 1327–1353.
- Jones, A., Haywood, J. and Boucher, O. (2009), "Climate impacts of geoengineering marine stratocumulus clouds", *Journal of Geophysical Research*, Vol. 114, AGU, pp. D10106–.
- Jones, A., Haywood, J. and Boucher, O. (2011), "A comparison of the climate impacts of geoengineering by stratospheric  $\text{so}_2$  injection and by brightening of marine stratocumulus cloud", *Atmospheric Science Letters*, Vol. 12, John Wiley & Sons, Ltd., pp. 176–183.
- Jones, A., Haywood, J., Boucher, O., Kravitz, B. and Robock, A. (2010), "Geoengineering by stratospheric  $\text{so}_2$  injection: results from the met office hadgem2 climate model and comparison with the goddard institute for space studies model", *Atmospheric Chemistry and Physics*, Vol. 10, pp. 5999–6006.
- Jones, A., Roberts, D. L., Woodage, M. J. and Johnson, C. E. (2001), "Indirect sulphate aerosol forcing in a climate model with an interactive sulphur cycle", *Journal of Geophysical Research*, Vol. 106, AGU, pp. 20293–20310.

- Kleypas, J. A., Danabasoglu, G. and Lough, J. M. (2008), "Potential role of the ocean thermostat in determining regional differences in coral reef bleaching events", *Geophysical Research Letters* , Vol. 35, AGU, p. L03613.
- Knutson, T. R., McBride, J. L., Chan, J., Emanuel, K., Holland, G., Landsea, C., Held, I., Kossin, J. P., Srivastava, A. K. and Sugi, M. (2010), "Tropical cyclones and climate change", *Nature Geoscience* , Vol. 3, Nature Publishing Group, pp. 157–163.
- Korhonen, H., Carslaw, K. S. and Romakkaniemi, S. (2010), "Enhancement of marine cloud albedo via controlled sea spray injections: a global model study of the influence of emission rates, microphysics and transport", *Atmospheric Chemistry and Physics* , Vol. 10, pp. 4133–4143.
- Kossin, J. P., Knapp, K. R., Vimont, D. J., Murnane, R. J. and Harper, B. A. (2007), "A globally consistent reanalysis of hurricane variability and trends", *Geophysical Research Letters* , Vol. 34, AGU, pp. L04815–.
- Koven, C. D., Ringeval, B., Friedlingstein, P., Ciais, P., Cadule, P., Khvorostyanov, D., Krinner, G. and Tarnocai, C. (2011), "Permafrost carbon-climate feedbacks accelerate global warming", *Proceedings of the National Academy of Sciences* , Vol. 108, pp. 14769–14774.
- Lackner, K. S. (2009), A physics perspective on energy supply and climate change - prediction, mitigation and adaptation., in 'Proceedings of the W.E. Heraeus Seminar, 26 -29 May 2008, Physikzentrum Bad Honnef.'
- Lackner, K. S., Ziock, H.-J. and Grimes, P. (1999), Carbon dioxide extraction from air: Is it an option, in 'Proceedings of the 24th International Conference on Coal Utilization and Fuel Systems', pp. 885 – 896.
- Lampitt, R., Achterberg, E., Anderson, T., Hughes, J., Iglesias-Rodriguez, M., Kelly-Gerreyn, B., Lucas, M., Popova, E., Sanders, R., Shepherd, J., Smythe-Wright,

- D. and Yool, A. (2008), "Ocean fertilization: a potential means of geoengineering?", *Philosophical Transactions of the Royal Society A: Mathematical, Physical and Engineering Sciences* , Vol. 366, pp. 3919–3945.
- Lance, S., Brock, C. A., Rogers, D. and Gordon, J. A. (2010), "Water droplet calibration of the cloud droplet probe (cdp) and in-flight performance in liquid, ice and mixed-phase clouds during arcpac", *Atmospheric Measurement Techniques* , Vol. 3, pp. 1683–1706.
- Latham, J. (1990), "Control of global warming?", *Nature* , Vol. 347, pp. 339–340.
- Latham, J. (2002), "Amelioration of global warming by controlled enhancement of the albedo and longevity of low-level maritime clouds", *Atmospheric Science Letters* , Vol. 3, John Wiley & Sons, Ltd., pp. 52–58.
- Latham, J., Bower, K., Choularton, T., Coe, H., Connelly, P., Cooper, G., Craft, T., Foster, J., Gadian, A., Galbraith, L., Iacovides, H., Johnston, D., Launder, B., Leslie, B., Meyer, J., Neukermans, A., Ormond, B., Parkes, B., Rasch, P., Rush, J., Salter, S., Stevenson, T., Wang, H., Wang, Q. and Wood, R. (2012), "Marine cloud brightening", *Philosophical Transactions of the Royal Society A (In press)* , Vol. -, pp. —.
- Latham, J., Rasch, P., Chen, C.-C., Kettles, L., Gadian, A., Gettelman, A., Morrison, H., Bower, K. and Choularton, T. (2008), "Global temperature stabilization via controlled albedo enhancement of low-level maritime clouds", *Philosophical Transactions of the Royal Society A: Mathematical, Physical and Engineering Sciences* , Vol. 366, pp. 3969–3987.
- Lawson, R. P., O'Connor, D., Zmarzly, P., Weaver, K., Baker, B., Mo, Q. and Jonsson, H. (2006), "The 2d-s (stereo) probe: Design and preliminary tests of a new airborne, high-speed, high-resolution particle imaging probe", *Journal of Atmospheric and Oceanic Technology* , Vol. 23, American Meteorological Society, pp. 1462–1477.



- Lee, S. and Penner, J. (2011), "Dependence of aerosol-cloud interactions in stratocumulus clouds on liquid-water path", *Atmospheric Environment*, Vol. 45, pp. 6337–6346.
- Lenton, T. M. and Vaughan, N. E. (2009), "The radiative forcing potential of different climate geoengineering options", *Atmospheric Chemistry and Physics*, Vol. 9, pp. 5539–5561.
- Lock, A. P. (2001), "The numerical representation of entrainment in parameterizations of boundary layer turbulent mixing", *Monthly Weather Review*, Vol. 129, American Meteorological Society, pp. 1148–1163.
- Lough, J. M. (2000), "Unprecedented thermal stress to coral reefs?", *Geophysical Research Letters*, Vol. 27, AGU, pp. 3901–3904.
- Lunt, D. J., Ridgwell, A., Valdes, P. J. and Seale, A. (2008), "'sunshade world': A fully coupled gcm evaluation of the climatic impacts of geoengineering", *Geophysical Research Letters*, Vol. 35, AGU, pp. L12710–.
- MacMynowski, D. G., Keith, D. W., Caldeira, K. and Shin, H.-J. (2011), "Can we test geoengineering?", *Energy and Environmental Science*, Vol. 4, The Royal Society of Chemistry, pp. 5044–5052.
- Makisara, K., Meinander, M., Rantasuo, M., Okkonen, J., Aikio, M., Sipola, K., Pylkkii, P. and Braam, B. (1993), Airborne imaging spectrometer for applications (aisa), in 'Dig. IGARSS', Vol. 2, pp. 479–481.
- Mann, M. E. and Emanuel, K. A. (2006), "Atlantic hurricane trends linked to climate change", *Eos, Transactions of the American Geophysical Union*, Vol. 87, AGU, pp. –.
- Martin, G. M., Bellouin, N., Collins, W. J., Culverwell, I. D., Halloran, P. R., Hardiman, S. C., Hinton, T. J., Jones, C. D., McDonald, R. E., McLaren, A. J., O'Connor, F. M., Roberts, M. J., Rodriguez, J. M., Woodward, S., Best, M. J., Brooks, M. E., Brown, A. R., Butchart, N., Dearden, C., Derbyshire, S. H.,

- Dharssi, I., Doutriaux-Boucher, M., Edwards, J. M., Falloon, P. D., Gedney, N., Gray, L. J., Hewitt, H. T., Hobson, M., Huddleston, M. R., Hughes, J., Ineson, S., Ingram, W. J., James, P. M., Johns, T. C., Johnson, C. E., Jones, A., Jones, C. P., Joshi, M. M., Keen, A. B., Liddicoat, S., Lock, A. P., Maidens, A. V., Manners, J. C., Milton, S. F., Rae, J. G. L., Ridley, J. K., Sellar, A., Senior, C. A., Totterdell, I. J., Verhoef, A., Vidale, P. L. and Wiltshire, A. (2011), "The HadGEM2 family of Met Office Unified Model climate configurations", *Geoscientific Model Development*, Vol. 4, pp. 723 – 757.
- Martin, G. M., Ringer, M. A., Pope, V. D., Jones, A., Dearden, C. and Hinton, T. J. (2006), "The Physical Properties of the Atmosphere in the New Hadley Centre Global Environmental Model (HadGEM1). Part I: Model Description and Global Climatology", *Journal of Climate*, Vol. 19, American Meteorological Society, pp. 1274–1301.
- Martin, J. H. (1990), "Glacial-interglacial co<sub>2</sub> change: The iron hypothesis", *Paleoceanography*, Vol. 5, AGU, pp. 1–13.
- Naidoo, R., Balmford, A., Costanza, R., Fisher, B., Green, R. E., Lehner, B., Malcolm, T. R. and Ricketts, T. H. (2008), "Global mapping of ecosystem services and conservation priorities", *Proceedings of the National Academy of Sciences*, Vol. 105, pp. 9495–9500.
- Painemal, D. and Zuidema, P. (2011), "Assessment of modis cloud effective radius and optical thickness retrievals over the southeast pacific with vocals-rex in situ measurements", *Journal of Geophysical Research*, Vol. 116, AGU, pp. D24206–.
- Parkes, B., Gadian, A. and Latham, J. (2012), "The effects of marine cloud brightening on seasonal polar temperatures and the meridional heat flux", *ISRN Geophysics (In press)*, Vol. 2012, pp. –.
- Parry, M.L., Canziani, O., Palutikof, J. and Co-authors (2007), Technical summary, in 'Climate Change 2007: Impacts, Adaptation and Vulnerability. Contribution of Working Group II to the Fourth Assessment Report of the Intergovernmental Panel on Climate Change', Cambridge University Press, Cambridge, UK.

- Rahn, D. A. and Garreaud, R. (2010), "Marine boundary layer over the subtropical southeast pacific during vernal-rain part 1: Mean structure and diurnal cycle", *Atmospheric Chemistry and Physics* , Vol. 10, pp. 4491–4506.
- Randall, D. A. and Suarez, M. J. (1984), "On the dynamics of stratocumulus formation and dissipation", *Journal of the Atmospheric Sciences* , Vol. 41, pp. 3052–3057.
- Randall, D., Coakley, J., Fairall, C., Kropfli, R. and Lenschow, D. (1985), "Outlook for research on sub-tropical marine stratiform clouds - response", *Bulletin of the American Meteorological Society* , Vol. 66(7), pp. —.
- Randall, D., Wood, R., Bony, S., Colman, R., Fiechter, T., Fyfe, J., Kattsov, V., Pitman, A., Shukla, J., Srinivasan, J., Stouffer, R., Sumi, A. and Taylor, K. (2007), Climate models and their evaluation., in 'Climate Change 2007: The Physical Science Basis. Contribution of Working Group I to the Fourth Assessment Report of the Intergovernmental Panel on Climate Change', Cambridge University Press, Cambridge, United Kingdom and New York, NY, USA.
- Rasch, P. J. and Kristjánsson, J. E. (1998), "A comparison of the ccm3 model climate using diagnosed and predicted condensate parameterizations", *Journal of Climate* , Vol. 11, American Meteorological Society, pp. 1587–1614.
- Rasch, P. J., Latham, J. and Chen, C.-C. J. (2010), "Geoengineering by cloud seeding: influence on sea ice and climate system", *Environmental Research Letters* , Vol. 4, p. 045112.
- Rasch, P. J., Tilmes, S., Turco, R. P., Robock, A., Oman, L., Chen, C.-C. J., Stenchikov, G. L. and Garcia, R. R. (2008), "An overview of geoengineering of climate using stratospheric sulphate aerosols", *Philosophical Transactions of the Royal Society A: Mathematical, Physical and Engineering Sciences* , Vol. 366, pp. 4007–4037.

- Read, D., Beerling, D., Cannell, M., Cox, P., Curran, P., Grace, J., Ineson, P., Jarvis, P., Malhi, Y., Powlson, D., Shepherd, J. and Woodward, I. (2001), The role of land carbon sinks in mitigating global climate change, Technical Report 10/01.
- Redfield, A. C. (1934), On the proportions of organic derivations in sea water and their relation to the composition of plankton, *in* R. Daniel, ed., 'James Johnstone Memorial Volume.', University Press of Liverpool, pp. 177–192.
- Reynolds, R. W., Rayner, N. A., Smith, T. M., Stokes, D. C. and Wang, W. (2002), "An improved in situ and satellite sst analysis for climate", *Journal of Climate*, Vol. 15, American Meteorological Society, pp. 1609–1625.
- Ricke, K. L., Morgan, M. G. and Allen, M. R. (2010), "Regional climate response to solar-radiation management", *Nature Geoscience*, Vol. 3, Nature Publishing Group, pp. 537–541.
- Ringer, M. A., Martin, G. M., Greeves, C. Z., Hinton, T. J., James, P. M., Pope, V. D., Scaife, A. A., Stratton, R. A., Inness, P. M., Slingo, J. M. and Yang, G.-Y. (2006), "The physical properties of the atmosphere in the new hadley centre global environmental model (hadgem1). part ii: Aspects of variability and regional climate", *Journal of Climate*, Vol. 19, American Meteorological Society, pp. 1302–1326.
- Roberts, D. L. and Jones, A. (2004), "Climate sensitivity to black carbon aerosol from fossil fuel combustion", *Journal of Geophysical Research*, Vol. 109, AGU, pp. D16202–.
- Robock, A., Oman, L. and Stenchikov, G. L. (2008), "Regional climate responses to geoengineering with tropical and arctic so<sub>2</sub> injections", *Journal of Geophysical Research*, Vol. 113, AGU, pp. D16101–.
- Salter, S., Sortino, G. and Latham, J. (2008), "Sea-going hardware for the cloud albedo method of reversing global warming", *Philosophical Transactions of the Royal Society A: Mathematical, Physical and Engineering Sciences*, Vol. 366, pp. 3989–4006.

- Segrin, M. S., Coakley, J. A. and Tahnk, W. R. (2007), "Modis observations of ship tracks in summertime stratus off the west coast of the united states", *Journal of the Atmospheric Sciences* , Vol. 64, American Meteorological Society, pp. 4330–4345.
- Seitz, R. (2011), "Bright water: hydrosols, water conservation and climate change", *Climatic Change* , Vol. 105, Springer Netherlands, pp. 365–381.
- Slingo, A., Nicholls, S. and Schmetz, J. (1982), "Aircraft observations of marine stratocumulus during jasin", *Quarterly Journal of the Royal Meteorological Society* , Vol. 108, John Wiley & Sons, Ltd, pp. 833–856.
- Smith, R. N. B. (1990), "A scheme for predicting layer clouds and their water content in a general circulation model", *Quarterly Journal of the Royal Meteorological Society* , Vol. 116, John Wiley & Sons, Ltd, pp. 435–460.
- Solomon, S., Qin, D., Manning, M., Chen, Z., Marquis, M., Averyt, K., M.Tignor and Miller, H. (2007), Summary for policymakers, *in* S. Solomon, D. Qin, M. Manning, Z. Chen, M. Marquis, K. Averyt, M.Tignor and H. Miller, eds, 'Climate Change 2007: The Physical Science Basis. Contribution of Working Group I to the Fourth Assessment Report of the Intergovernmental Panel on Climate Change', Cambridge University Press, Cambridge, United Kingdom and New York, NY, USA.
- Sorooshian, A., Feingold, G., Lebsock, M. D., Jiang, H. and Stephens, G. L. (2010), "Deconstructing the precipitation susceptibility construct: Improving methodology for aerosol-cloud precipitation studies", *Journal of Geophysical Research* , Vol. 115, AGU, pp. D17201–.
- Spectral Imaging Ltd. (2009), Aisa dual hyperspectral sensor, Technical report, Spectral Imaging Ltd.
- Stephens, G. L. (1978), "Radiation profiles in extended water clouds. ii: Parameterization schemes", *Journal of the Atmospheric Sciences* , Vol. 35, American Meteorological Society, pp. 2123–2132.

- Stevens, B., Vali, G., Comstock, K., Wood, R., Van Zanten, M. C., Austin, P. H., Bretherton, C. S. and Lenschow, D. H. (2005), "Pockets of open cells and drizzle in marine stratocumulus", *Bulletin of the American Meteorological Society*, Vol. 86, American Meteorological Society, pp. 51–57.
- Stolaroff, J. K., Keith, D. W. and Lowry, G. V. (2008), "Carbon dioxide capture from atmospheric air using sodium hydroxide spray", *Environmental Science & Technology*, Vol. 42, pp. 2728–2735. PMID: 18497115.
- The Royal Society (2009), *Geoengineering the Climate*, The Royal Society.
- Tilmes, S., Garcia, R. R., Kinnison, D. E., Gettelman, A. and Rasch, P. J. (2009), "Impact of geoengineered aerosols on the troposphere and stratosphere", *Journal of Geophysical Research*, Vol. 114, AGU, pp. D12305–.
- Trenberth, K. E. and Caron, J. M. (2001), "Estimates of meridional atmosphere and ocean heat transports", *Journal of Climate*, Vol. 14, American Meteorological Society, pp. 3433–3443.
- Tuleya, R. E. (1994), "Tropical storm development and decay: Sensitivity to surface boundary conditions", *Monthly Weather Review*, Vol. 122, American Meteorological Society, pp. 291–304.
- Twohy, C. H., Petters, M. D., Snider, J. R., Stevens, B., Tahnk, W., Wetzel, M., Russell, L. and Burnet, F. (2005), "Evaluation of the aerosol indirect effect in marine stratocumulus clouds: Droplet number, size, liquid water path, and radiative impact", *Journal of Geophysical Research*, Vol. 110, AGU, pp. D08203–.
- Twomey, S. (1974), "Pollution and the planetary albedo", *Atmospheric Environment*, Vol. 8, pp. 1251–1256.
- Twomey, S. (1977), "The influence of pollution on the shortwave albedo of clouds", *Journal of the Atmospheric Sciences*, Vol. 34, American Meteorological Society, pp. 1149–1152.

- Volodin, E. M., Kostrykin, S. V. and Ryaboshapko, A. G. (2011), "Climate response to aerosol injection at different stratospheric locations", *Atmospheric Science Letters*, Vol. 12, John Wiley & Sons, Ltd., pp. 381 – 385.
- Wang, H. and Feingold, G. (2009), "Modeling mesoscale cellular structures and drizzle in marine stratocumulus. part i: Impact of drizzle on the formation and evolution of open cells", *Journal of the Atmospheric Sciences*, Vol. 66, American Meteorological Society, pp. 3237–3256.
- Webster, P. J., Holland, G. J., Curry, J. A. and Chang, H.-R. (2005), "Changes in tropical cyclone number, duration, and intensity in a warming environment", *Science*, Vol. 309, pp. 1844–1846.
- Wilson, D. R. and Ballard, S. P. (1999), "A microphysically based precipitation scheme for the uk meteorological office unified model", *Quarterly Journal of the Royal Meteorological Society*, Vol. 125, John Wiley & Sons, Ltd, pp. 1607–1636.
- Wood, R. and Bretherton, C. S. (2004), "Boundary layer depth, entrainment, and decoupling in the cloud-capped subtropical and tropical marine boundary layer", *Journal of Climate*, Vol. 17, American Meteorological Society, pp. 3576–3588.
- Wood, R., Comstock, K. K., Bretherton, C. S., Cornish, C., Tomlinson, J., Collins, D. R. and Fairall, C. (2008), "Open cellular structure in marine stratocumulus sheets", *Journal of Geophysical Research*, Vol. 113, AGU, pp. D12207–.
- Wood, R., Mechoso, C. R., Bretherton, C. S., Weller, R. A., Huebert, B., Straneo, F., Albrecht, B. A., Coe, H., Allen, G., Vaughan, G., Daum, P., Fairall, C., Chand, D., Gallardo Klenner, L., Garreaud, R., Grados, C., Covert, D. S., Bates, T. S., Krejci, R., Russell, L. M., de Szoeke, S., Brewer, A., Yuter, S. E., Springston, S. R., Chaigneau, A., Toniazzo, T., Minnis, P., Palikonda, R., Abel, S. J., Brown, W. O. J., Williams, S., Fochesatto, J., Brioude, J. and Bower, K. N. (2011), "The vamos ocean-cloud-atmosphere-land study regional experiment (vocals-rex): goals, platforms, and field operations", *Atmospheric Chemistry and Physics*, Vol. 11, pp. 627–654.



- Wu, L., Tao, L. and Ding, Q. (2010), "Influence of sea surface warming on environmental factors affecting long-term changes of atlantic tropical cyclone formation", *Journal of Climate* , Vol. 23, American Meteorological Society, pp. 5978–5989.
- Wunsch, C. (2005), "The total meridional heat flux and its oceanic and atmospheric partition", *Journal of Climate* , Vol. 18, American Meteorological Society, pp. 4374–4380.
- Xie, P. and Arkin, P. A. (1997), "Global precipitation: A 17-year monthly analysis based on gauge observations, satellite estimates, and numerical model outputs", *Bulletin of the American Meteorological Society* , Vol. 78, American Meteorological Society, pp. 2539–2558.
- Xue, H. and Feingold, G. (2006), "Large-eddy simulations of trade wind cumuli: Investigation of aerosol indirect effects", *Journal of the Atmospheric Sciences* , Vol. 63, American Meteorological Society, pp. 1605–1622.

## **Appendix A. Differences between climate models**

In Chapter 3 it is noted that HadGEM1 is the successor to the HadCM3 model (Martin et al., 2006). In Chapter 4 the work of Bala et al. (2011); Jones et al. (2009, 2011); Rasch et al. (2010) is compared with this work. The HadGEM2 model used in Jones et al. (2009, 2011) is an updated version of the HadGEM1 model used in this work. The HadGEM2 model is described in Martin et al. (2011). The appendix of Martin et al. (2011) contains tables which describe the changes between HadGEM1 and HadGEM2. The CCM3 used in Bala et al. (2011); Rasch et al. (2010) is the NCAR Community Climate Model version 3 and is described in Collins et al. (2006). The similarities and differences between the HadCM3, HadGEM1, HadGEM2 and NCAR CCM3 models are shown in Tables 1 and 2.

Component	HadCM3	HadGEM1	HadGEM2	NCAR CCM3
Horizontal resolution	2.5° Latitude, 3.75° Longitude	1.25° Latitude, 1.875° Longitude	1.25° Latitude, 1.875° Longitude	1.9° Latitude, 2.5° Longitude
Vertical resolution	19 levels (Lorenz grid)	38 levels (Charney-Phillips)	38 levels (Charney-Phillips)	26 levels (Sigma grid)
Dynamics	Eulerian advection	Semi Lagrangian advection	Semi Lagrangian advection	Finite volume dynamical core
Radiation	Edwards and Slingo (1996)	Edwards and Slingo (1996)	Edwards and Slingo (1996) and aerosol improvements	Updated two stream scheme interacting with water vapour
Boundary layer	Local Richardson number mixing	Non-local Richardson number mixing in BL	Improved on HadGEM1 see Martin et al. (2011)	Prognostic treatment of detrainment, mixing and advection
Microphysics	Senior and Mitchell (1993)	Wilson and Ballard (1999)	Wilson and Ballard (1999)	Rasch and Kristjánsson (1998)
Convection	Mass flux scheme Gregory and Rowntree (1990)	Revised scheme based on Grant and Brown (1999)	Improved on HadGEM1 see Martin et al. (2011)	Mass flux scheme

TABLE 1: The similarities and differences between climate models HadCM3, HadGEM1, HadGEM2 and the NCAR CCM3. HadCM3 was the precursor to HadGEM1 (See Chapter 3) and HadGEM1, HadGEM2 and the NCAR CCM3 were used for comparison in Chapter 4. HadCM3 and HadGEM1 described in Martin et al. (2006), HadGEM2 in Martin et al. (2011), CCSM3 in Collins et al. (2006).

Part one of table continued in Table 2.

Component	HadCM3	HadGEM1	HadGEM2	NCAR CCM3
Aerosols	Interactive sulphate scheme	Jones et al. (2001); Roberts and Jones (2004)	Improved on HadGEM1 see Martin et al. (2011)	Perscribed sulphur, sea salt, dust and black carbon
Clouds	Smith (1990)	Cusack et al. (1999); Smith (1990)	Improved on HadGEM1 see Martin et al. (2011)	Single moment scheme
Horizontal resolution (Ocean)	1.25° Latitude, 1.25° Longitude	1° Latitude, 1° Longitude, Tropical Longitude increases to $\frac{1}{3}^{\circ}$	1° Latitude, 1° Longitude, Tropical Longitude increases to $\frac{1}{3}^{\circ}$	1° Latitude, 1° Longitude
Vertical resolution (Ocean)	20 levels	40 levels	40 levels	40 levels

TABLE 2: The similarities and differences between climate models HadCM3, HadGEM1, HadGEM2 and the NCAR CCM3. HadCM3 was the precursor to HadGEM1 (See Chapter 3) and HadGEM1, HadGEM2 and the NCAR CCM3 were used for comparison in Chapter 4. HadCM3 and HadGEM1 described in Martin et al. (2006), HadGEM2 in Martin et al. (2011), CCSM3 in Collins et al. (2006).

Part two of table continued from Table 1.

## Appendix B. Flow chart of method used in Chapter 7

The method used in Section 7.1 is shown in Flow chart form in Figure 1.

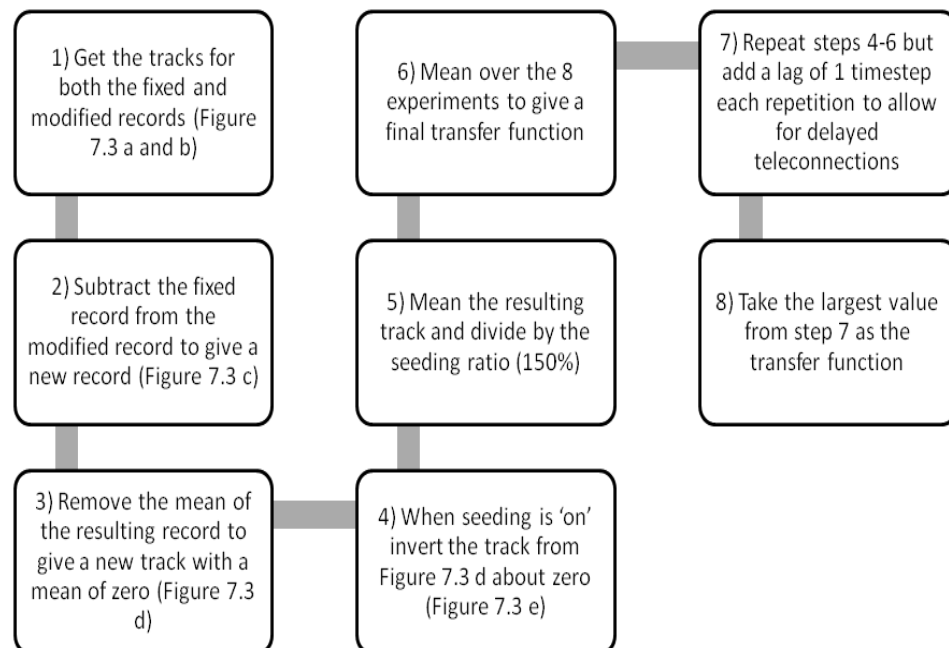


FIGURE 1: A flowchart showing the method used in Chapter 7 for analysis of transfer functions in the HadGEM1 GCM.